UNIVERSIDAD COMPLUTENSE DE MADRID

FACULTAD DE CIENCIAS FÍSICAS

Departamento de Física Teórica II

TESIS DOCTORAL

Measurement of the neutron capture cross section of the ^{235}U at the n_TOF facility

Medida de la sección eficaz de captura neutrónica del ^{235}U en la instalación n_TOF

MEMORIA PARA OPTAR AL GRADO DE DOCTOR

PRESENTADA POR

Javier Balibrea Correa

Directores

Emilio Mendoza Cembranos
Daniel Cano Ott

Madrid, 2018

Universidad Complutense de Madrid

Departamento de Física Teórica II

UNIVERSIDAD
COMPLUTENSE
MADRID

DOCTORAL THESIS

Madrid 2017

Measurement of the neutron capture cross section of the ^{235}U at the n_TOF facility
Medida de la sección eficaz de captura neutrónica del ^{235}U en la instalación n_TOF

Javier Balibrea Correa

javier.balibrea@externos.ciemat.es

Supervised by:

Dr. Emilio Mendoza Cembranos (CIEMAT)
Dr. Daniel Cano Ott (CIEMAT)

A Marta

Acknowledgments

I would like to thanks to all the people that help me along all this period. Specially to my supervisors, Emilio and Dani, for the opportunity, theirs strong support, great patience, enthusiastic passion, knowledge and guidance within all the process.

To all the members of the n_TOF collaboration who helped me a lot during my long visits at CERN with special mention to: Carlos, Massimo, Nicola, Fede, Frank, Jorge, Christina, Thanos, Michi, Álvaro, Daniela, Paco, Cesar, etc.

To all my colleagues at CIEMAT for their grateful help during this period: Daniel López, Paco Alvarez, David, Trino, Merche, Enrique, Pablo, Aczel, Miriam, Vicente, Marina, Gabriel, Joaquin,, Claudia, Paco Feria, Julio, Laura, Cayetano, Unai, Aris, Manuel, Paco Martín-Fuertes, Juan Blázquez, Iván, etc.

También agradecer a todas las personas que han estado a lo largo camino hasta llegar aquí. A mi familia por el esfuerzo, paciencia, ayuda y comprensión en todos estos años. A mis padres y mis hermanos, Rosa y Rogelio, Alex y Pablo. A mis abuelos, con un cariño especial a mi abuelo Salva por enseñarme los cimientos de la ciencia. A todos mis tios. A mis suegros y mi cuñada José, Lidia y Lidia. Y como no a mi amiga Marta Sabaté por todos los momentos compartidos durante el doctorado.

Gracias a todos.

Marta, no tengo palabras para agradecer todo lo que has hecho por mi a lo largo de todos estos años. Muchisimas gracias por compartir tu vida conmigo y hacerme feliz.

'The first principle is that you must not fool yourself and you are the easiest person to fool.'
R. P. Feynman

Contents

Chapter 1

Introduction

The aim of this manuscript is to present the analysis and results of the ^{235}U neutron capture cross-section measurement performed at the CERN n_TOF facility, in the neutron energy range from 0.2 to 200 eV.

Chapter 1 is dedicated to the purpose behind this measurement (section 1.1)and the theoretical framework of the neutron-induced nuclear reactions (section 1.2). Furthermore, the process of obtaining the neutron capture cross-section for a fissile isotope is explained at the end of the chapter (section 1.3).

In chapter 2 we describe the experimental facility (section 2.1), the experimental setup (section 2.2), the ^{235}U targets (section 2.3) and the experimental configurations used during this measurement (section 2.4).

Chapter 3 describes the analysis performed on the experimental data and the procedure for obtaining the ^{235}U(n,γ) cross-section.

Chapter 4 is dedicated to presenting the results obtained and a comparison with the evaluated neutron libraries and other experiments.

Finally, Chapter 5 will present the summary, conclusions and future work suggested by this measurement.

1.1 Motivation

This measurement is strongly influenced by the design of new critical nuclear systems such as the Gen-IV reactors [1] and the management of the resulting waste from existing nuclear reactors. For this reason, a brief introduction to sustainable energy is given in the section 1.1.1 while the importance of nuclear cross-sections in the design of new critical nuclear systems and strategies for nuclear waste management are described in the section 1.1.2.

1.1.1 The nuclear energy overview

The incredible growth of industrialized and developing countries in recent decades has greatly increased the demand for, and supply of, primary energy on a global basis, necesitating the improvement of existing energy sources and the design and development of new efficient energy power sources [3].

The rapid increase of primary energy supply in the period from 1971 to 2014 is shown in Fig. 1.1. While the demand for energy in OECD countries (Organization for Economic Co-operation and Development *https://www.oecd.org/*) is slowly increasing, the substantial development of NON-OECD countries, led by China, has driven primary energy demand to the extremely high levels of today [3].

To meet this demand for energy, countries have developed combined energy programs which rely on coal, oil, hydro, natural gas and nuclear power. More recently, these programs have included renewable energy sources. With regards to energy production from nuclear sources, since the instigation of the first

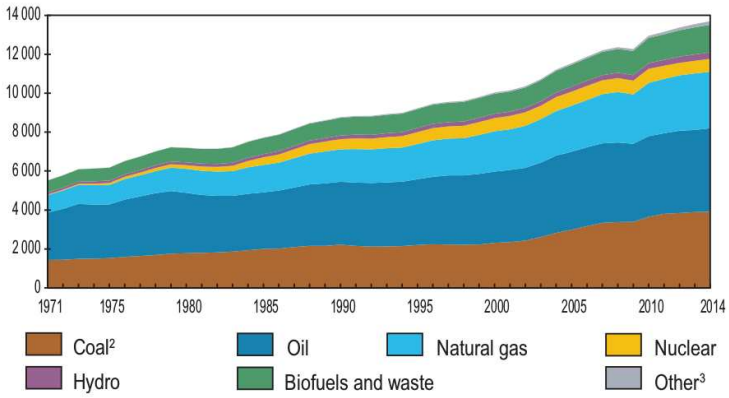

Figure 1.1: World-wide total primary energy supply in the period from 1971 to 2014 by fuel (Mtoe) [3].

commercial nuclear power plant at the end of the 1950s, many countries have been developing their own nuclear energy programs. The oil crisis in the early seventies encouraged the development of these programs in most industrialized countries including Canada, Spain, France, Italy, Japan and Germany, to be followed by Mexico, Brazil, Taiwan and Korea. However, the accident that occurred at the Chernobil reactor in 1987 slowed their construction in the 1990s as a result of safety concerns.

Energy production by nuclear plants from 1970 to the present has increased rapidly, as shown in Fig. 1.2. This is mainly due to the OECD countries [3], which possess most of the existing nuclear power plants as indicated in the table 1.1. More than 30% of nuclear energy is produced by the United States, followed by France at 17.2%, and the Russian Federation at 7.1%. These three countries represent more than 50% of worldwide energy production by nuclear reactors. In total, the energy production by nuclear power plants represents 10% of the total global electrical energy production.

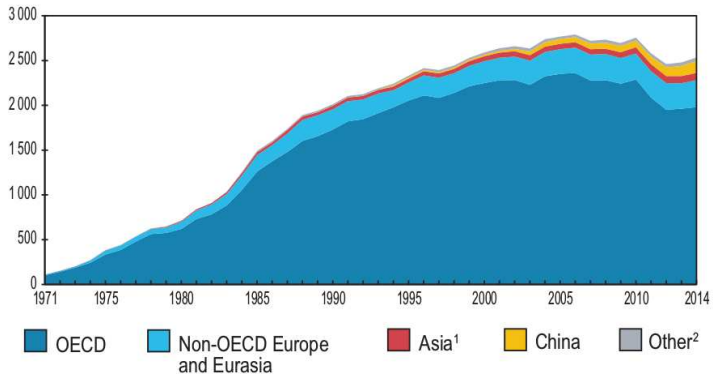

Figure 1.2: Nuclear energy production in the period from 1971 to 2014 by regions in terawatthours (TWh) [3].

With regards to Europe, there are a total of 186 nuclear power plants with 163.685 MWe of installed electric net capacity in operation and 13.696 MWe under construction, which is distributed in 15 plants in 6 countries [4] as shown in the table 1.2.

The electricity generated by nuclear energy occupies an important position in E.U countries, with France

Country	Produced (TWh)	Net installed Capacity (GW)	% of nuclear production in total
United States	831 (32.8%)	99	19.2
France	436 (17.2%)	63	78.4
Russian Federation	181 (7.1%)	25	17.0
Korea	156 (6.2%)	21	28.7
People's Rep. of China	133 (5.2%)	24	2.3
Canada	108 (4.3%)	14	16.4
Germany	97 (3.8%)	14	15.6
Ukraine	88 (3.5%)	13	48.6
Sweden	65 (2.6%)	9	42.3
United Kingdom	64 (2.5%)	-	19.0
Rest of the world	376 (14.8%)	60	9.4
World	**2535 (100%)**	**384**	**10.7**

Table 1.1: Produced, net installed nuclear reactors capacity and % of nuclear production in total domestic electricity generation of the different countries (2014) [3].

Country	in operation number	in operation net capacity (MWe)	under construction number	under construction net capacity (MWe)
Belarus	-	-	2	2.218
Belgium	7	1.926	-	-
Czech Republic	6	3.930	-	-
Finland	4	2.752	1	1.600
France	58	63.130	1	1.630
Germany	8	10.799	-	-
Hungary	4	1.889	-	-
Netherlands	1	482	-	-
Romania	2	1.300	-	-
Russia	36	26.557	7	5.468
Slovakia	4	1.814	2	880
Slovenia	1	688	-	-
Spain	7	7.121	-	-
Sweden	10	9.651	-	-
Switzerland	5	3.333	-	-
Ukraine	15	13.107	2	1.900
United Kingdom	15	8.918	-	-
total	**186**	**163.685**	**15**	**13.696**

Table 1.2: Summary of nuclear power plants under construction and in operation in Europe (2016) [4].

holding the top position at 76.3% followed by the Ukraine with 56.4%, Slovakia with 55.9% and Hungary with 52.7% [4].

The consistent projections of the annual international outlook report from the U. S. Energy Information Administration (2016) [5], which provides a reliable forecast of energy consumption, focuses exclusively on marketed energy. The projections provided by this report are used by international agencies, governments, trade associations, and other decision makers to plan their strategies and plans for the future.

The report indicates the rising level of demand for energy over the next three decades, led by strong increases in demand in countries outside the OECD. China and India account for more than half of the world's total increase in energy consumption in the projection period from 2012 to 2040. Total world energy consumption is expected to rise from the current 549 quadrillion British thermal units (Btu) to 815 quadrillion Btu in 2040. This represents an increase of more than 48%, mostly due to non-OECD countries, whose economic polices are driving a strong demand for energy. This increase is represented in the left hand panel of Fig. 1.3, which shows the current and forecast energy consumption for the following decades up to 2040.

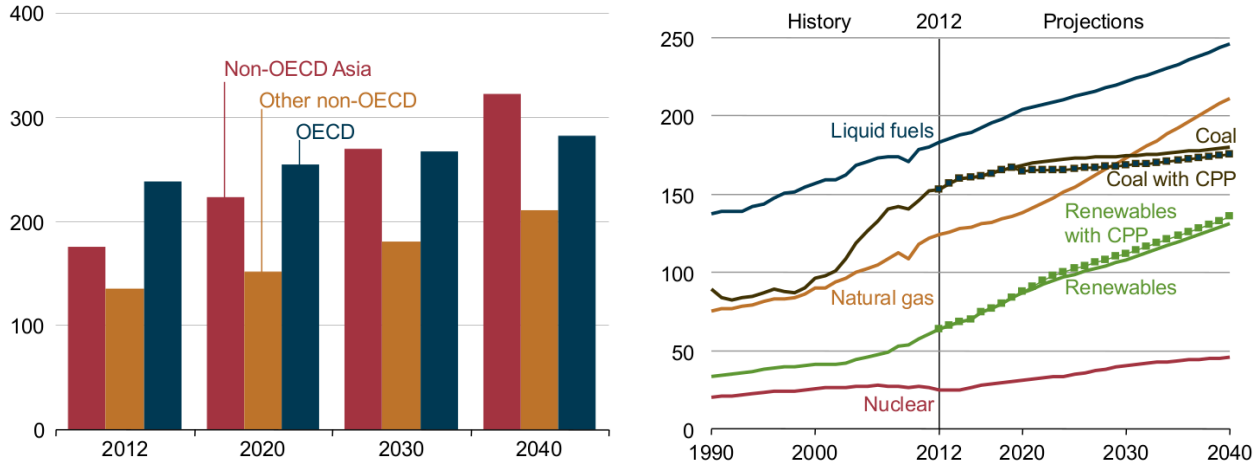

Figure 1.3: In the left hand panel: projection of energy consumption, in Btu, for the period from 2012 to 2040. In the right hand panel: projection of energy consumption by energy source in Btu from 1990 to 2040 [5].

Renewable energy production is the fastest growing energy source as projected over the 2012-2040 period. In general, this energy production source will grow by an average of 2.6%/year. Nuclear power is the second fastest growing energy source, with an average growth rate of 2.3%/year over this period, as is shown in the right hand panel of Fig. 1.3.

Electricity has been the fastest growing form of energy consumption for many decades, as it will continue to be in the future. The net generation of electricity will increase by 69%, from 21.6 trillion kilowatthours (kWh) in 2012 to 36.5 trillion kWh in 2040. Long-term global prospects continue to improve for generation from renewable energy sources and nuclear power due to the commitment from different countries to reduce greenhouse emissions.

Electricity generation from nuclear power plants is estimated to increase from 2.1 trillion kWh in 2012 to 4.5 trillion kWh in 2040. Virtually all of the projected net expansion of installed nuclear power capacity will occur in the non-OECD region, in particular the addition of 139 gigawatts (GW) of nuclear capacity in China from 2012 to 2040.

The current and forecast energy demand from nuclear plants requires the improvement of existing critical nuclear systems by refining their efficiency, and the development of new advanced nuclear reactors

such as GEN-IV nuclear reactors [1] or Accelerated Driver Systems (ADS) [6, 7, 8].

1.1.2 The ^{235}U neutron cross sections and nuclear energy applications

Nuclear technology and cross sections of the ^{235}U

The potential benefits of advanced reactors such as Gen-IV reactors [1] and Accelerated Driven Systems (ADS) [6, 7, 8] are many and varied and include improved levels of efficiency in the use of fuel, a reduction in the amount of waste following the process, and the ability to recycle part of the present reactor waste, both producing energy and reducing the radio-toxicity of fuel elements. Sustainable nuclear energy production requires a dedicated and ambitious research program over the entire breadth of nuclear science, including the improvement of existing neutron-induced cross-section reaction data [6].

In contrast to current nuclear power reactors, which are clearly limited by existing parameters, the advanced systems under consideration for the coming decades will be required to achieve comparable or even better performance than existing ones. This represents a challenge in view of the considerable feedback and optimization that has benefited the latter. Therefore, the viability of new designs will depend more than ever on the quality of the underlying physics: experiments and computational simulations of high quality are needed before we can convince ourselves that the boundary conditions of sustainability can indeed be met. This difficult task can directly be translated into (i) considerable challenges regarding basic nuclear data, neutronics, material science, thermohydraulics, fuel fabrication, reprocessing and partitioning, the coupling of all these aspects (multi-physics), and modern quality-assured software that will replace the current suite of reactor simulation codes in both research and industry, and (ii) many requirements in terms of 'missing' experimental data, facilities and demonstration plants.

The first crucial ingredient for reactor and fuel cycle analysis is nuclear data. When designing or assessing the safety of a reactor system, nuclear data for a wide range of reactions and materials needs to be known. Energy production, radiation damage, radioactivity and related matters all result from interactions between particles (usually neutrons) and nuclei; a precise simulation of these nuclear reactions is necessary to predict the system characteristics with sufficient accuracy. Therefore, in contemporary simulations, a major role is played by the uncertainty of nuclear data, which in a reactor system analysis can be propagated throughout the entire simulation scheme and may eventually lead to uncertainties regarding key performance parameters of the simulated designs and the associated fuel cycle.

In order to improve existing nuclear plants and design new ones, designers and physicists must address many variants of these plants and perform extensive calculations to estimate the performance of the critical nuclear system. To formulate accurate and reliable estimates, these studies should incorporate the most accurate and reliable nuclear data and neutron cross-sections, compiled in evaluated libraries such as ENDF/B-VII.1 [9], JENDL-4.0a [10] or JEFF-3.2 [11]. These evaluated libraries are tested against relevant experimental benchmark data, thus validating current knowledge of nuclear cross-sections and nuclear data. These major evaluated libraries predict the measured criticality of nuclear systems extremely well (for many assemblies, although not for all of them). However, such good performance in integral testing creates a false sense of optimism [12]. In particular, a more careful evaluation of the integral testing comparisons, and the fundamental and evaluated cross-section data, indicates a number of problems:

- **Compensating errors**: Significant compensating errors must be present in most if not all nuclear data evaluations. These embody compensating errors distributed between the roles of fission (cross-sections, average number of prompt neutrons, and neutron spectra), capture, inelastic scattering and elastic scattering. A major challenge to our community is to remove these compensating errors from the evaluated libraries by the precise new experimental measurements of neutron-induced cross-sections and other nuclear data.

- **Calibration**: Calibration has been used in some cases in the evaluated databases to better match measured criticality of integral systems. Thus, agreement between simulated and measured criticality,

k_{eff}, is not as impressive as it might seem, though of course a common set of evaluated data was used for all of the neutronic simulations of different critical assemblies. Where a certain amount of calibration was undertaken, it usually involved a reasonable degree of physics assumptions and was not entirely ad-hoc, and cross-sections were usually adjusted within their uncertainty levels. Thus, a high certainty degree of adjustment between the simulation and the experimental data is obtained.

- **Discrepancies**: The discrepancies between different evaluated libraries reflect discrepancies amongst various measurements, and also differences in theory, model parameters and code calculations. Thus, new nuclear data must be included to improve and correct this situation.

Quantity measured	Author	Year	Neutron energy period (eV)	Reference
$\eta(E_n)$	H. Palevsky *et al.*	1956	0.01 - 0.9	[13]
$\eta(E_n)$	J. R. Smith *et al.*	1957	0.1 - 9.0	[14]
$\sigma_\gamma(E_n)$	G. de Saussure *et al.*	1966	0.4 - 62.0	[15]
$\int \sigma_\gamma(E_n)$	G. de Saussure *et al.*	1966	10.0- 1800.0	[15]
$\eta(E_n$	F.D. Brooks *et al.*	1966	0.9 - 200	[16]
$\int \sigma_\gamma(E_n)$	F.D. Brooks *et al.*	1966	10 - 200	[16]
$\sigma_\gamma(E_n)$	R.B. Perez *et al.*	1973	8.0 - 200.0	[17]
$\int \sigma_\gamma(E_n)$	G.V. Muradyan *et al.*	1977	100 - 20000	[18]
$\alpha_R(E_n)$	G.V. Muradyan *et al.*	1985	2.0 - 32.0	[19]
$\eta(E_n)$	H. Weigmann *et al.*	1990	0.001 0.4	[20]
$\sigma_\gamma(E_n)$	M. Jandel *et al.*	2012	4.0 - $8{\cdot}10^6$	[32]
$\sigma_\gamma(E_n)$	C. Guerrero *et al.*	2012	-	[23]

Table 1.3: List of $^{235}U(n,\gamma)$ cross section measurements retrieved from the EXFOR database [24] overlapping in some region with the neutron energy range of this work.

Over the years, great efforts have been made to obtain reliable neutron-induced cross-sections of the ^{235}U, which are the most important physical constants in nuclear energy applications. In particular, for the neutron capture cross-section there are several measurements in the neutron resonance region as shown in the table 1.3. The neutron-induced cross-sections for this isotope are very important, not only for major nuclear thermal reactors but also for Fast Breeder Reactors (FBRs) because many critical experiments for FBRs have been performed at critical assemblies where UO_2 fuels were used as driver fuels. The experimental data obtained at such critical assemblies has a great impact on design work for FBRs. Recent studies show that calculated sodium void reactivity values for BFS experiments underestimate the experimental results by 30-50% [25]. These significant discrepancies not only exceed the target accuracy of 20% for a FBR design but also negatively affect the design accuracy estimated with the cross-section adjustment and bias factor techniques.

The epithermal neutron capture cross-section of ^{235}U was investigated within the framework of the Working Party on International Nuclear Data Evaluation Co-operation (WPEC) [27, 28]. As a result, the Oak Ridge National Laboratory (ORNL) group revised the resolved resonance parameters, which are currently used by all major libraries. However, recent analyses of fast-neutron cores with U fuels reveal very poor predictions for neutronic characteristics. The calculated over experimental ratio, C/E, values of sodium-voided reactivity for BFS are much less than 1.0 except for JENDL-3.2 which adopted a different evaluation. Moreover, the C/E values of criticalities for Fast Critical Assemblies (FCA) IX-series experiments [28, 29], where neutron spectra were varied with U fuels, largely depend on the spectrum shape as shown in the left hand panel of Fig. 1.4. The reproduction of these critical assemblies leads to the conclusion that the ^{235}U(n,γ) cross-section could be overestimated in the neutron energy range from 100 eV to 2 keV as was suggested by the Japanese nuclear data community [9].

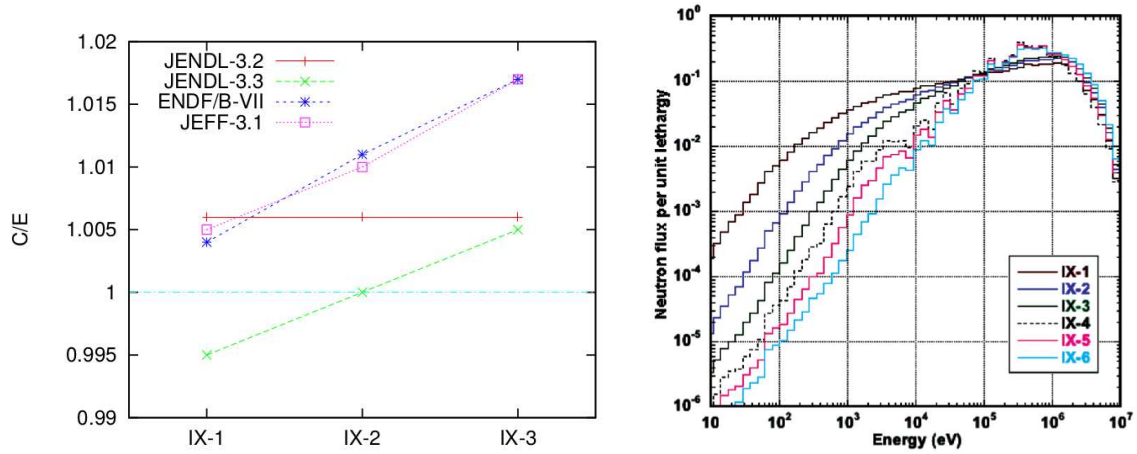

Figure 1.4: In the left hand panel, calculated experimental ratio C/E criticality values for the different FCA-IX benchmarks experiments and evaluated libraries. In the right hand panel, neutron flux for the different FCA-IX criticality experiments. The figures has been obtained from [26, 28].

The (FCA) IX-series experiments, used as benchmark experiments, have a great impact on the design of new nuclear reactors. The poor knowledge regarding neutron cross-sections may not only produce inadequate reproduction of the critical assemblies experimental data, but may also introduce bias into the neutron cross-sections of other isotopes by the bias compensation mentioned before [9].

In addition to this, post irradiated experiments analysis of the nuclear fuel in Pressurized Water Reactors (PWRs) shows a small over-estimation of ^{235}U cross-section predictions and systematic underestimation of ^{236}U build-up [30], suggesting an increment of 10% of the ^{235}U neutron capture cross-section in the epithermal neutron energy range [25].

Therefore, there is a required accuracy for the ^{235}U neutron capture cross reflected in the High Priority Request List [26] of the International Atomic Energy Agency (IAEA). This accuracy as a function of the neutron energy range is presented in the table 1.4.

Neutron energy interval	Accuracy target (%)
100 eV - 1 keV	5
1keV -30 keV	8
30 keV - 1 MeV	3

Table 1.4: Required accuracy of the ^{235}U neutron capture cross-section as indicated by the High Priority Request List of the Nuclear Energy Agency [26].

To tackle the discrepancies in the neutron cross-section data of the major nuclides, the IAEA CIELO pilot project [12, 31] is re-evaluating the major nuclides that are important for the nuclear applications: ^{1}H, ^{16}U, ^{235}U, ^{238}U and ^{239}Pu. The main goal of this project is the production of improved, and validated, evaluated nuclear data files. In particular, for the ^{235}U isotope, the main objectives are summarized as follows:

- **Resolved Resonance Parameters:** All the existing libraries adopted the resolved resonance parameters for ^{235}U from ORNL. The upper energy boundary of the resolved region, which is 2.25 keV, was lowered to 500 eV in JENDL-4.0 and point-wise cross-sections are provided in the 500 eV to 2.25

keV energy range based on the previous resolved resonance parameter set from a previous evaluation. Hence, the cross sections below 500 eV in all the libraries are identical. New work on ^{235}U is needed to resolve a number of existing problems [27] with the addition of new experimental data from different reaction channels such as radiative neutron capture or neutron capture to fission cross-section (α) data.

- **Radiative Capture:** The neutron capture cross-section in the resolved resonance region is given by the resonance parameters from ORNL. In the fast energy range, although unresolved resonance parameters were also provided by ORNL, the evaluations are based on available experimental data from critical assemblies and other experiments. The evaluation in ENDF/B-VII.1 is based on an analysis of measured capture and α-value (capture to fission ratio) data above 2.25 keV. ROSFOND adopted ENDF/B-VII.1 and JEFF-3.1 adopted ENDF/B-VI.8, which resulted in very similar cross-sections above 25 keV. Questions associated with the ^{235}U capture cross-section should be resolved, especially in the 0.5 – 2 keV energy range where the recent JENDL-4.0 evaluation lowered the cross-section by more than 25% based on integral reactor (sodium void) testing [28, 29]. This analysis led to increased capture compared to ENDF and JEFF in the 3–5 keV region, and for 100–1000 keV. New data measured at Los Alamos National Neutron Science Center (LANSCE) by Jandel et al [32] with the DANCE detector partly supports the Japanese conjecture (from 1 to 5 keV), but also suggests that a ∼10% capture increase is needed from 10 to 70 keV for all evaluations. Recent measurements by Danon*et al.*at RPI also support a lower capture cross-section in the 100 eV – 2 keV region.

- **Inelastic Scattering:** From the threshold to several MeV, there are significant differences between JENDL-4 and ENDF/B-VII.1 (JEFF- 3.1 is the same as ENDF/B-VI) up to 50 keV, exhibiting differences in the treatment of the low-lying rotational band built upon the isomeric state. All evaluations are significantly higher than some of the measurements in the 1–2 MeV range.

- **Average Number of Neutrons per Fission $\bar{\nu}$:** The ENDF/B-VII.1 $\bar{\nu}$ evaluation comes from a covariance analysis of the measured data, though in the fast region the evaluation was modified slightly (within the parameters of uncertainty) to optimize a match to the fast critical assembly benchmarks.

The work presented in this manuscript focuses on the framework for improving the neutron capture cross-section at low neutron energy and improve current knowledge of the resonance parameters of the ^{235}U isotope.

1.2 The neutron cross-section theory

The microscopic neutron cross-section, $\sigma(\mathrm{E}_n)$, is a physical magnitude that quantifies the interaction probability of a neutron with a specific nucleus. If we consider a beam of neutrons with intensity $\mathrm{I}(\mathrm{E}_n)$ (neutrons/cm^2/s) incident on a very thin plate of a given isotope with area A (cm^2), density of nuclei N (nuclide/cm^3) and thickness Δx (cm), then the reaction rate $\mathrm{R}(\mathrm{E}_n)$ (interactions/cm^2/s) must be proportional to the intensity of the neutron beam ($\mathrm{I}(\mathrm{E}_n)$) and the number of target nuclei (N·Δx·A):

$$R(E_n) \propto I(E_n) \cdot N \cdot \Delta x \cdot A \tag{1.1}$$

The constant of proportionality is the neutron cross-section, $\sigma(\mathrm{E}_n)$ with area dimensions:

$$R(E_n) = \sigma(E_n) \cdot I(E_n) \cdot N \cdot \Delta x \cdot A \tag{1.2}$$

Typically, for any target nuclei, there are several neutron-induced reactions permitted such as elastic scattering, neutron capture and neutron components and thus, the total cross-section $\sigma_{tot}(\mathrm{E}_n)$ is the sum of the partial cross-sections:

$$\sigma_{tot}(E_n) = \sigma_{el}(E_n) + \sigma_{\gamma}(E_n) + \sigma_{fiss}(E_n) + .. \tag{1.3}$$

Typically, the neutron cross-section is expressed in 'barns' (1 barns=10^{-24}cm^2). The neutron cross-section depends on the incident neutron energy and demonstrates large variations from one isotope to another, but some general characteristics are applicable for all the nuclei:

- The more nucleons are involved in the target nuclei, the finer is the resonance structure. Typical level spacings observed in neutron reactions are of the order of MeV for light isotopes, keV for medium-weight and eV for heavy nuclei with the exception of magic nuclei such as the ^{208}Pb.
- The neutron capture and elastic scattering reactions can take place for any neutron energy without any energy threshold. For fissile isotopes, there is no fission threshold such as exists for the ^{235}U or ^{239}Pu. Thus, for these isotopes, neutron-induced fission reactions can take place for any neutron energy. Other reactions have energy thresholds, with exceptions such as ^{6}Li(n,α)t or ^{10}B(n,α)^{7}Li.

Elastic scattering, neutron capture and neutron-induced fission have the same neutron energy structure and can be divided into four neutron energy periods:

- The Thermal and Epithermal Region: From the thermal point up to the first resonance, the neutron cross-section demonstrates a behavior: $\sigma(\mathrm{E}_n) \sim 1/\sqrt{E_n}$. This is true for all reaction channels except for neutron elastic scattering.
- The Resolved Resonance Region (RRR): From the first resonance (typically in the eV region for heavy nuclei) up to a certain neutron energy value depending on the target nuclei (typically keV region for heavy nuclei). For this neutron energy period, the resonant structure is present with large variations between the peaks and valleys of the resonances. All the reaction channels appear at the same neutron energy, since the neutron resonances are levels from the compound nuclei, as will be shown later.
- The Unresolved Resonance Region (URR): Above a certain neutron energy, the neutron resonance width is comparable to the average resonance spacing. In this case, the experimental resolution cannot distinguish between the resonances despite the neutron resonances not overlapping completely. For this neutron energy period, the parameters of the individual resonances cannot be well determined.
- The High Energy Region: Above a certain neutron energy, the resonant structure cannot be observed any more. In addition, more reaction channels are permitted due to the energy threshold of the reaction.

1.2.1 The compound nucleus and the R-matrix theory

The neutron resonances observed in the microscopic neutron cross-sections are understood through the compound nucleus model, first discussed by Niels Bohr in 1939 [35]. The idea behind the model is that the neutron-induced reaction takes place in two steps:

- During the first step, the neutron and the target nuclei form a compound nucleus with excitation energy, E^*, defined as:

$$E^* = S_n + \frac{A}{A+1} E_n \tag{1.4}$$

  Where A is the mass number of the target nuclei, E_n is the kinetic energy of the incident neutron and S_n is the neutron separation energy of the compound nucleus. The observed resonances correspond to quasi-stationary levels or neutron resonances defined by its excitation energy E^*, half life τ, spin J, and parity Π.

- The formed compound nucleus in the excited quasi-stationary level decay via the opened channels such as the radiative channel, (n,γ); the fission channel (n,f) or the elastic scattering. The decay path is assumed to be independent of the way that the compound nucleus was formed.

In the model, the total neutron cross-section for a given isotope is related to the absorption probability of the incident neutron. The resonances have, as a good approximation, a Breit-Wigner shape [36] determined by the resonance parameters: energy E_0 and a set of partial widths related to the decay probability through different mechanisms: capture Γ_γ, fission Γ_f and scattering Γ_n, for example. The sum of all widths, $\Gamma_{tot} = \sum_c \Gamma_c$ is a quantity related to the lifetime of the quasi-stationary level, defined by the Heisenberg Uncertainty Principle $\tau = h/\Gamma_{tot}$. The theory behind the compound nucleus is the R-matrix theory introduced by Wigner and Eisenbud [37, 38]. For further and detailed information of the R-Matrix theory consult the references [39, 40].

1.2.2 The neutron radiative capture process

In accordance with the compound nucleus model, when a neutron is captured by a (n,γ) process, after the formation of the compound nucleus it decays from the excited nuclear level to the ground or metastable nuclear level by the emission of γ-ray and electron particles. The resulting electromagnetic cascade produced in the process is the signature used at n_TOF facility for the determination of the neutron capture cross-section. In order to obtain the amount of neutron capture reactions which occur during the measurement, the determination of the detection efficiency of the detector used is necessary and is achieved by the reproduction of the experimental electromagnetic cascades by Monte Carlo techniques.

For the exact reproduction of these electromagnetic cascades, it is necessary to know the exact nuclear level scheme of the compound nucleus at this high excitation energy (E^*=S_n+E_n) as well as all the branching ratios and information related to the conversion electrons for each possible decay path. From the practical point of view it is impossible to know all the information needed for the exact reproduction of the electromagnetic cascade. For this reason, the experimental nuclear scheme measured at low excitation energy is used and completed by a statistical model from a specific excitation energy up to the excitation energy of the resonance. A brief summary of the theoretical basis will be provided in this section. For further information, consult the references [42, 43, 44, 45, 46].

In the model most widely used for the generation of electromagnetic cascades [47, 48], the radiation width $\Gamma_{a\gamma b}$, is defined as the probability of a γ-ray decay from a level with energy E_a to another with excitation energy E_b. The expectation value of this partial radiation width for a given radiation type X (electric or magnetic) and multipolarity L is assumed to be (following the Fermi's golden rule [49]):

$$\bar{\Gamma}^{(XL)}_{a\gamma b} = f^{(XL)}(E_\gamma)E_\gamma^{2L+1}/\rho(E_a, J_a^{\pi_a}) \tag{1.5}$$

where $\rho(E, J^\pi)$ is the nuclear density for states with J^π and $f^{(XL)}(E_\gamma)$ is the Photon Strength Function (PSF) whose only dependence is assumed to be with the γ-ray energy and not with properties of the initial and final nuclear levels. This is the so-called Hypothesis of Brinck.

There are different models for the density of nuclear levels up to these high excitation energies such as the Back Shifted Fermi Gas. For further information, consult the references [50, 51, 52]. The Digl description of the nuclear level density [52] uses the following expression:

$$\rho(E, J) = \frac{1}{24\sqrt{2}} \frac{2J+1}{\sigma^3 a^{1/4}} \frac{exp\left[2(a(E-\Delta))^{1/2} - J(J+1)/2\sigma^2\right]}{(E-\Delta+t)^{5/4}} \tag{1.6}$$

where t is the thermodynamic temperature defined by $E\text{-}\Delta = at^2\text{-}t$, σ is the spin cut-off parameter and a and Δ are the parameters of the model.

The PSF functions are usually parametrized by the Standard Lorentzian or the Enhanced Generalized Lorentzian (EGLO). The Lorentzian Shape functions are described by three parameters, the resonance point, E_r; the decay width, Γ_r; and the probability normalization σ_r. The values of these three parameters must be adjusted from the comparison of the experimental data with the statistical cascade model.

1.2.3 The neutron induced fission process

From the classical point of view, the behavior of the nuclei in the fission process [33] is analogous to the behavior of a drop of mercury that is divided into two smaller drops. In a heavy nucleus such as the ^{235}U, one nucleon situated in the inner part of the nucleus is in constant and violent motion due to the attraction of the rest of the nucleons, but since it is totally surrounded by other nucleons, the net force applied is zero. This is not the case of a nucleon close to the surface of the nucleus, where due to the short range of the nuclear force and because there are no nucleons 'outside', the net force applied to the nucleon is balanced to the inside; thus, the nucleon is pulled towards the center of the nucleus.

As a consequence, on average, the nucleus has a spherical shape similar to the mercury drop. The classical image of the heavy nucleus is that of a bubble whose surface is oscillating, but generally with a spherical shape. If the amplitude of these oscillations becomes too great, the nucleus can split in two. This is known as the liquid drop model [53], and offers a clear and intuitive picture of a heavy nucleus.

Certain isotopes such as the ^{246}Cm or ^{252}Cf can fission spontaneously even without any outside influence, but this is a rare event. The probability of fissioning for a given nucleus increases as energy is added from some outside source. With the classical picture of the process, we can imagine that the nucleus gains energy (excitation energy), oscillating more violently until reaching a certain 'critical energy' where the fission probability increases and the fission process take place, dividing the nucleus into two smaller nuclei. For this reason, the fission process can be seen as a threshold energy process. A nucleus below this excitation threshold is unlikely to de-excite itself by fissioning instead of another process such as radiative decay. Typically, the excitation energy needed to open the fission reaction channel for a heavy nucleus is one such as the ^{235}U ~4-5 MeV.

The liquid drop model is the simplest model of fission. The reality is that in addition to the fission barrier from the liquid model, there are nuclear shell corrections, giving a more complicated but fashionable description of the fission process and phenomena such as the double-humped barrier. This is illustrated in Fig. 1.6, where on the x axis is presented the quadrupolar moment of the nucleus (deformation) and on the y axis the excitation energy. As is shown, there are two minimums in the fission barrier due to the shell corrections, thus producing fission isomers. The simplest way to explain this is that there are two different configurations of the nucleons in the nucleus with the same excitation energy but with different shapes.

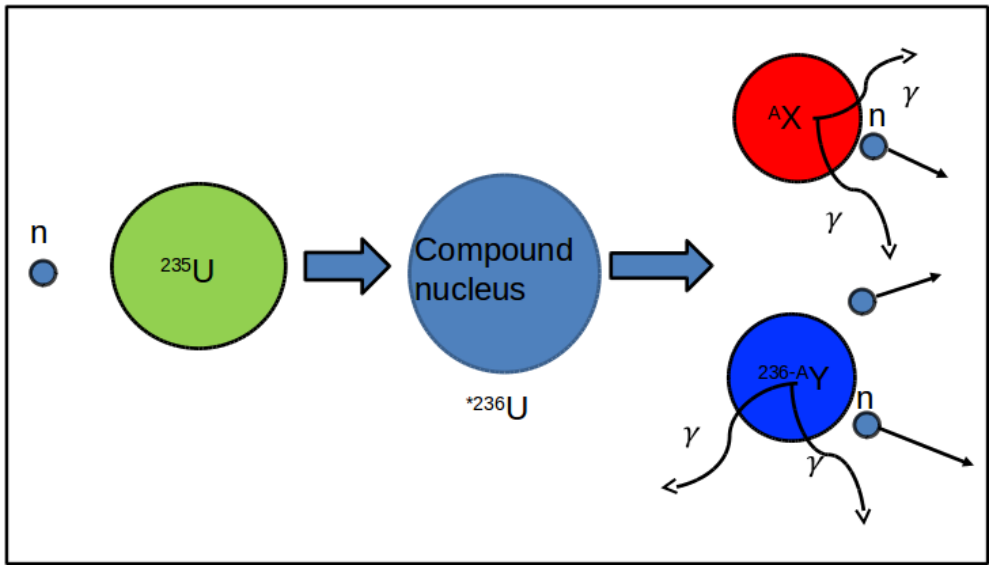

Figure 1.5: Schematic plot of the fission process. The formation of the compound nucleus and decay to fission fragments with the emission of prompt neutrons and γ-rays.

The neutron-induced fission reaction is explained within the framework of the compound nucleus model [53]. Just after the neutron reaches the target nucleus, the compound nucleus is formed at a nuclear level with excitation energy, E^* defined by:

$$E^* = E_n + S_n \tag{1.7}$$

If this energy is above the fission threshold (barrier), the fission reaction is energetically possible; thus the fission reaction channel is open. Even if the excitation energy is not sufficient, there is the probability of nuclei fissioning by a tunnel effect, but this is highly suppressed. There are some nuclei such as the ^{235}U where the excitation energy of the compound nucleus formed by the system neutron+target is above the fission barrier, even without the kinetic energy of the incident neutron. Therefore, the (n,f) channel is always energetically possible. These nuclei are termed fissile nuclei, such as the ^{235}U or the ^{239}Pu.

In the fission process, not only are fission fragments emitted with a high kinetic energy, but also neutrons and γ-rays, known as prompt fission γ-ray cascades. Because the fission fragments are produced in a high excited nuclear state with high angular moments and excitation energy, the fission products decay immediately, emitting neutrons and γ-rays. A schematic picture of the neutron- induced fission process is shown in Fig. 1.5.

The total energy released during fission, Δ(E), is easily derived from the energy conservation law of the neutron+target system before and after neutron-induced fission. That is:

$$\Delta(E) = E_n + \left(M_0 - \sum_i M_i \right) c^2 \tag{1.8}$$

where E_n is the kinetic energy of the incident neutron, M_0 is the mass of the compound nucleus given by the sum of the target mass M_{targt} and the mass of the neutron, m_n; M_i is the mass of the individual primary fission fragments and c the speed of light. The total energy released per fission will vary from one fission to the next depending on the fission products formed, but in average the energy released per fission of the ^{235}U with thermal neutrons is about 200 MeV.

The released energy in the fission process is distributed among the fission fragments as excitation and kinetic energy, the kinetic energy of the fission neutrons and the prompt γ-rays. The rest is released over a long period of time after the fission occurs as β-decay, retarded neutron emission and γ decay of the residual nuclei.

Reaction	Δ(E) (MeV)	TKE (MeV)	$\bar{\nu}$	m_γ
$n_{th}+^{233}U$	~200	172	2.492	9
$n_{th}+^{235}U$	~200	171	2.418	8
$n_{th}+^{239}Pu$	~200	177	2.108	7

Table 1.5: Total released energy $\Delta(E)$, kinetic energy of the fission fragments (TKE), average number of prompt emitted neutrons $\bar{\nu}$ and average number of prompt γ-rays in neutron induced fission reaction with some isotopes.

Typically, for neutron-induced fission reactions with different isotopes, the total energy released has similar values, kinetic energy of the fission fragments, and average number of neutrons and γ-ray emitted as is shown in the table 1.5.

For fissile isotopes, the fission cross-section is larger than the capture cross-section. This fact, added to the large amount of prompt γ-rays and fission neutrons emitted (table 1.5) causes a large background inherent to the ^{235}U targets that must be accurately subtracted for the calculation of the neutron capture cross-section, thus complicating the measurement of the neutron radiative capture reaction.

The double-humped barrier and the fission isomers

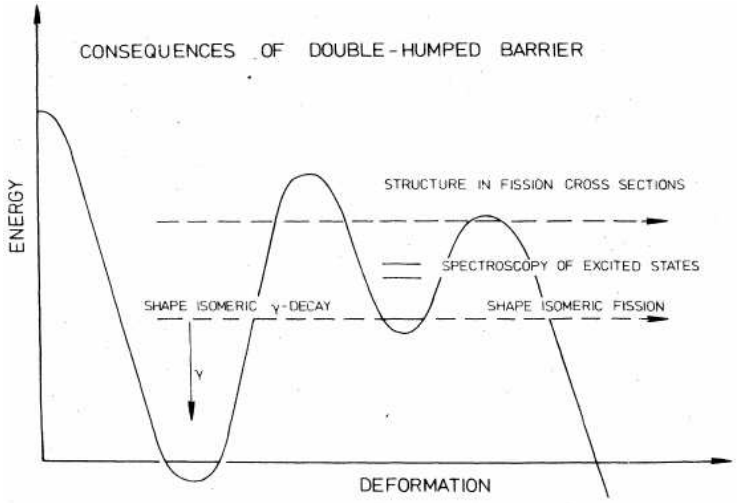

Figure 1.6: Typical double-humped fission barrier for an actinide isotope. The quadrupolar momentum (deformation) is shown on the x axis and on the y-axis, the excitation energy of the system.

One of the immediate consequences of the double-humped barrier in fissile isotopes is the existence of fission isomers. Fission isomers are excited nuclear states which decay by spontaneous fission or γ de-excitation to the ground state after population in a nuclear reaction [54]. The half-lives presently known range from 5 ps to 14 ms, depending on the height of the barrier depths, and their width. All fission isomers are located in the actinide region with proton numbers of Z=92-97 and N=141-151, respectively.

For Z>97, the half-lives become too short to be observable with current techniques, while Z<92 shape isomeric γ decay rather than fission, presumably becoming dominant. Quantitatively, of course, the exact boundaries of this region depend on the sensitivity of the experimental techniques used.

The double-humped character of the nuclear potential energy as a function of the deformation arises from the superposition of a macroscopic smooth liquid drop part and a shell correction, as was mentioned previously [56, 57]. Oscillations in this shell correction as a function of deformation lead to two minimums in the potential barrier energy; thus, the ground state of the isomer nuclei is located at a deformation of ε_2=0.6, 2-3 MeV above the first. In the specific case of the ^{235}U+n system, the difference between the ground state of the system and the first isomeric ground state is only 1 MeV due to the ^{236}U nucleus being a double-closed shell nucleus.

This concept explains the observable consequences listed in Fig. 1.6. The nuclei caught in the second minimum can either tunnel through the outer barrier (isomeric fission), or can decay back to the first minimum (isomeric γ decay). There will be a spectrum of low-lying excited states built on the ground state in the second well, which can studied, at least in principle, by 'conventional' spectroscopic methods [54].

Proceeding higher up in the level of excitation energy to the barrier region via the kinetic energy of the neutron, intermediate structures occur in the neutron-induced fission cross-sections. These consist mainly of two types:

- A broad structure in the neutron-induced fission cross-section caused by 'transmission resonances'.
- A fine structure in the neutron-induced fission cross-section seen as a clustering of neutron resonances.

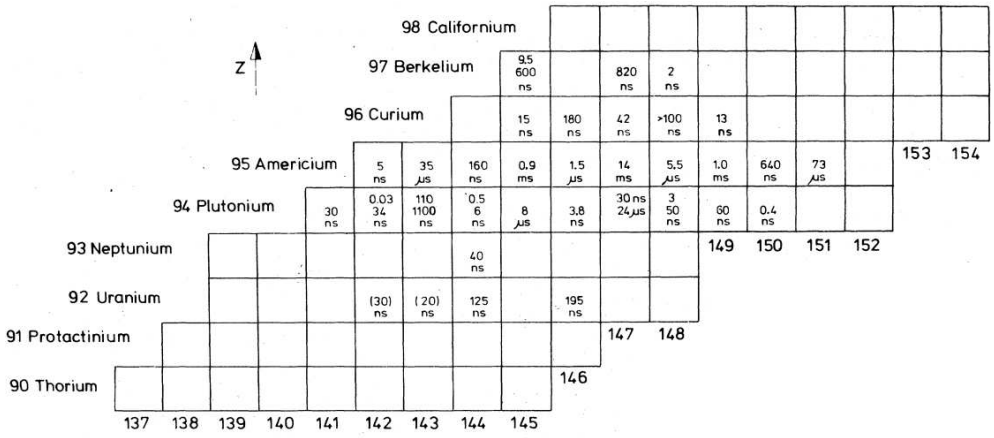

Figure 1.7: Experimental isomeric states detected in the actinide region 92<Z<97. The half-life of those nuclei is given in ns. The figure has been taken from [56].

The detailed behavior of these neutron-induced fission cross-sections together with the information on isomers is used to extract the barrier heights [55]. Following any nuclear reaction which excites an actinide nucleus above the fission barrier, the probabilities of prompt fission, of decay back into the first minimum and of trapping in the region of the second minimum, are in the order of 0.9, 0.1 and 10^{-5}-10^{-4}, respectively [56]. A detailed investigation of the properties of shape isomeric states therefore encounters tremendous experimental difficulties.

Present knowledge is mostly restricted to the identification of isotopes, half-lives, and in some cases, excitation energies of the states decaying by spontaneous fission. In accordance with Britt, 1973, the actinide region of the char of nuclei seen in Fig. 1.7, shows, at least, 33 fission isomers between U and Bk with half-lives ranging from 10^{-11} to 10^{-2} sec.

1.3 Measurement of capture cross-sections in fissile isotopes

The neutron capture cross-section, $\sigma_\gamma(E_n)$, is usually measured by detecting γ-ray cascades after the formation of the compound nucleus. For the fissile nucleus the probability of a neutron producing a fission reaction is, on average, greater than that of producing a neutron capture reaction. Moreover, since the resonances are the excited levels of the compound nucleus, both cross-sections have the same resonant structure as a function of the neutron energy as shown in Fig. 1.8. In addition, the amount of γ-ray emitted in a fission reaction is larger than in a (n,γ) reaction. Thus, measuring (n,γ) reactions in fissile isotopes is challenging due to the fact that it competes with the fission reaction channel.

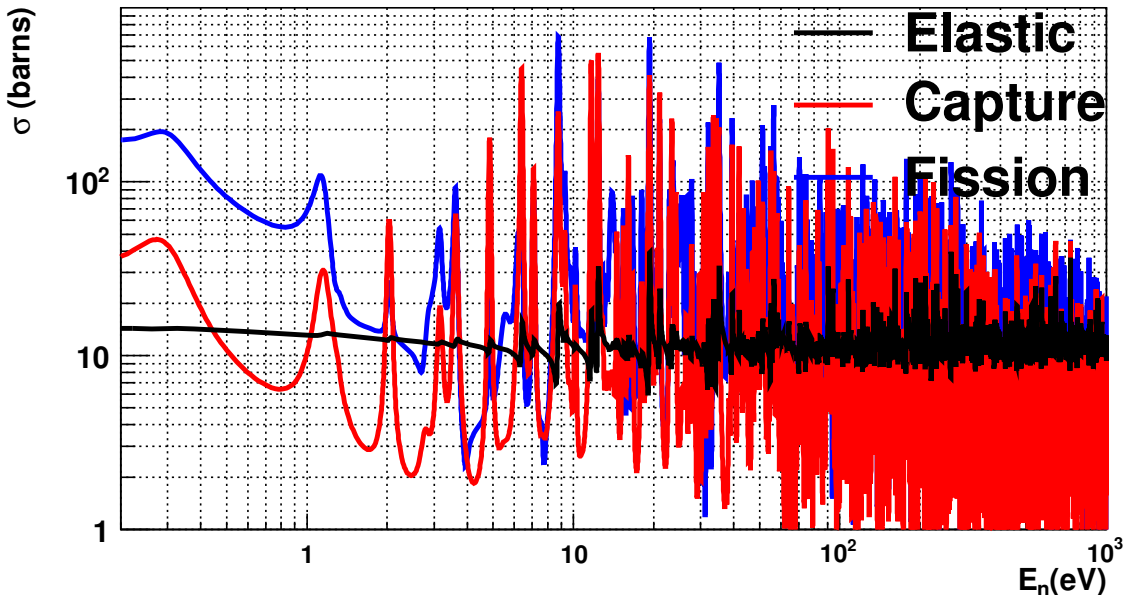

Figure 1.8: ^{235}U(n,f), ^{235}U(n,γ) and ^{235}U(n,n) cross section obtained from the evaluated library ENDF/B-VII.1 in the neutron energy range from 0.2 eV to 1 keV.

To accomplish the subtraction of the prompt fission background for the measurement of the ^{235}U(n,γ) cross-section, the fission tagging technique [15, 17, 23, 32] has been used. The main idea of the technique is to measure simultaneously the fission and capture reaction channels by means of fission and electromagnetic detectors respectively. By evaluating the time coincidence between both detection systems, the fission γ-ray cascades can be tagged. The idea was developed in the early 1960s at Los Alamos [15, 17] and modified in recent years at the n_TOF facility [23] and DANCE (Los Alamos) [32], with improved setups and detection systems. There are some difficulties inherent to the technique:

- The large amount of dead material intercepting the neutron beam: the fission tagging detectors, together with all the components of the fission chamber, must intercept the neutron beam, thus producing a large amount of background material which is detected by the γ-ray detector.
- The systematic uncertainties associated with the detection efficiencies: these parameters, critical for the determination of the ^{235}U(n,γ) cross-section, must be carefully determined as will be explained later in this section.

- The low count statistics: for high efficiency in detecting fission fragments via fission detectors, the use of very thin targets with low mass is required. Therefore, the capture to background ratio will be lower compared to thicker samples, and longer periods of measurement are required.

For the reasons explained previously, not all fission and γ-ray detectors are suitable for this technique. The methodology requires:

- High detection efficiency γ-ray detectors for (n,γ) cascades such as the segmented n_TOF Total Absorption Calorimeter (TAC) [58].
- High detection efficiency fission detectors for the (n,f) events, of low mass and sufficiently compact to fit inside the small fission chamber used in the experimental setup, such as Fission Tagging Micromegas detectors [59].

These two detection systems have been used for the experimental setup of this measurement as described in the section 2.2.

The microscopic neutron cross-section for any reaction channel cannot be measured directly. Instead, the observable measurement is the reaction yield, $Y_x(E_n)$, defined as the fraction of neutrons impinging on the target that produces reactions of the desired reaction channel. This magnitude, as with the neutron cross-section, strongly depends on the kinetic energy of the incident neutron. Thus, the reaction yield for any reaction channel x is determined experimentally as:

$$Y_x(E_n) = \frac{c_x(E_n)}{\phi_n(E_n)} \tag{1.9}$$

where $c_x(E_n)$ is the total number of channel reactions produced in the targets, and $\phi_n(E_n)$ is the total number of neutrons with kinetic energy E_n impinging on the sample under study. The total number of reactions of the channel produced in the targets is obtained from the difference between the total number of reactions measured, $c_{tot}(E_n)$, and the background, $c_{bkg}(E_n)$, divided by the detection efficiency of the specific reaction channel, $\varepsilon_x(E_n)$. Then, the equation 1.9 is written as:

$$Y_x(E_n) = \frac{c_{tot}(E_n) - c_{bkg}(E_n)}{\varepsilon_x(E_n)\phi_N(E_n)} \tag{1.10}$$

Theoretically, the reaction yield and the neutron cross-section are connected by the equation 1.11 when the multiple scattering effects are neglected [40]:

$$Y_x(E_n) = \frac{\sigma_x(E_n)}{\sigma_T(E_n)}\left(1 - e^{-n_s\sigma_T(E_n)}\right) \tag{1.11}$$

where $\sigma_x(E_n)$ and $\sigma_T(E_n)$ are the specific reaction channel x and the total neutron cross-sections, respectively. The thickness of the targets, n_s, is expressed in Atm/barn. Under the thin target approximation, which is equivalent to a low probability of interaction of the neutrons with the target sample, ($n_s \cdot \sigma_T(E_n) << 1$), the equation 1.11 leads to:

$$Y_x(E_n) \approx n_s\sigma_x(E_n) \tag{1.12}$$

which is valid for targets with low thickness and/or low neutron total cross-section. The background for the (n,γ) reaction channel (equation 1.10) in this particular case can be described as follows:

$$c_{bkg}(E_n) = c_{Fiss}(E_n) + c_{Other}(E_n) \tag{1.13}$$

where $c_{Fiss}(E_n)$ is the prompt fission background, defined as the background induced in the γ-ray detector several nanoseconds after the fission reaction occurs and $c_{Other}(E_n)$ is the remaining background.

The prompt fission background is determined by the fission tagging technique [23, 32], obtained from the number of coincidences between the fission and γ-ray detection systems, $c_{tagg}(E_n)$, divided by a factor labelled here as fission tagging detection efficiency, ε_f^*, which takes into account that not all fission events are tagged by the fission detection system. Then:

$$c_{Fiss}(E_n) = \frac{1}{\varepsilon_f^*} c_{tagg}(E_n) \tag{1.14}$$

The fission tagging detection efficiency, ε_f^*, and the fission detection efficiency, ε_f, are the same quantity; the probability of detecting a fission reaction with one of the detectors does not depend on whether it has been detected by the other [23]. Inserting Eq. 1.13 and Eq. 5.2 in Eq. 1.10, the neutron capture yield leads to:

$$\boxed{Y_\gamma(E_n) = \frac{c_\gamma(E_n)}{\phi_N(E_n)} = \frac{c_{tot}(E_n) - \frac{1}{\varepsilon_f^*} c_{tagg}(E_n) - c_{Other}(E_n)}{\varepsilon_\gamma(E_n)\phi_N(E_n)}} \tag{1.15}$$

and $\sigma_\gamma(E_n)$ is easily deduced from equation 1.12.

The fission tagging technique requires the simultaneous measurement of the neutron capture and neutron-induced fission reaction yields. Thus, the measurement can be interpreted as the measurement of the absolute ratio between both reaction yields. For small neutron energy periods:

$$\frac{Y_\gamma(E_n)}{Y_f(E_n)} = \frac{\frac{\sigma_\gamma(E_n)}{\sigma_T(E_n)}\left(1 - e^{-n_s\sigma_T(E_n)}\right)}{\frac{\sigma_f(E_n)}{\sigma_T(E_n)}\left(1 - e^{-n_s\sigma_T(E_n)}\right)} = \frac{\sigma_\gamma(E_n)}{\sigma_f(E_n)} = \alpha(E_n) \tag{1.16}$$

where $\alpha(E_n)$, the alpha ratio, is by definition the ratio between the neutron capture and the fission cross-sections. Experimentally, this quantity is determined as:

$$\boxed{\alpha(E_n) = \frac{Y_\gamma(E_n)}{Y_f(E_n)} = \frac{\varepsilon_f(E_n)}{\varepsilon_\gamma(E_n)} \frac{c_{tot}(E_n) - \frac{1}{\varepsilon_f^*} c_{tagg}(E_n) - c_{Other}(E_n)}{c_f(E_n)}} \tag{1.17}$$

where $c_f(E_n)$ is the total number of fissions detected by the fission detector. The background for this reaction channel has been neglected.

The measurement, presented as $\alpha(E_n)$ ratio (Eq. 1.17), constitutes an absolute value of the ratio between both reaction channels. Moreover, it minimizes systematic uncertainties since:

- It removes common errors associated with the determination of the shape and absolute value of the neutron fluence.
- It does not depend on the sample thickness, thus eliminating uncertainties associated with the possible inhomogeneities and mass of the samples under study.

On the other hand, the determination of the capture cross-section from the equation 1.15 has lower statistical uncertainties. In most cases, when neither the samples and/or the absolute value of the neutron fluence are accurately characterized, the neutron capture cross-section requires an external normalization, N_{norm}, thus increasing the systematic uncertainty in the determination of this quantity.

In the particular case of the ^{235}U isotope, the neutron-induced fission cross-section is accurately determined for some neutron energy periods, thus the $\alpha(E_n)$ ratio can be computed in those periods and used for the normalization of the neutron capture cross-section, as will be shown in the section 3.8. In this way, the systematic uncertainties associated with the target thickness, inhomogeneities and the absolute value of the neutron fluence are removed from the neutron capture cross-section.

In order to estimate the α-ratio sensitivity (and the neutron capture cross-section) of the fission tagging detection efficiency, ε_f^*, we propagate the uncertainty in this parameter to the α-ratio under the following assumptions:

- The contribution of other background sources, $c_{others}(E_n)$, has been neglected for this calculation.
- The TAC detection probability is similar for the γ-ray cascades from the (n,γ) and (n,f) processes.
- The (n,f) events are detected independently by both detection systems, thus the fission tagging detection efficiency and the fission detection efficiency are the same quantity: $\varepsilon_f = \varepsilon_f^*$.

Thus, the α-ratio sensitivity to ε_f^* parameter is:

$$\boxed{\frac{\Delta_{\varepsilon_f^*}(\alpha(E_n))}{\alpha(E_n)} \simeq \left(1 + \frac{\sigma_f(E_n)}{\sigma_\gamma(E_n)}\right) \frac{\Delta(\varepsilon_f^*)}{\varepsilon_f^*}} \tag{1.18}$$

In the case of the ^{235}U, $\sigma_f(E_n)/\sigma_\gamma(E_n)$ the ratio depends on the resonance but it is, on average, a factor of 2-3. Thus, for an uncertainty of 1% in the fission tagging detection efficiency parameter, this introduces to the α-ratio a systematic uncertainty of 3-4%. Therefore, the determination of this parameter is critical for the accurate calculation of the neutron capture cross-section.

Chapter 2

The ^{235}U(n,γ) cross section measurement

The measurements of the ^{235}U(n,γ) cross-section presented in this work were performed at the n_TOF facility using the segmented BaF_2 Total Absorption Calorimeter and the Fission Tagging Micromegas detectors. The aim of this chapter is to describe:

- Section 2.1: The n_TOF facility section.
- Section 2.2: The detectors and the experimental setup used for the measurement and the Data Acquisition System (DAQ).
- Section 2.3: The ^{235}U samples used for the measurement.
- Section 2.4: The experimental configurations used for the measurement of the ^{235}U(n,γ) cross-section.

2.1 The n_TOF facility at CERN

The construction of the n_TOF facility [60] was proposed by Rubbia *et al.* in 1998 [61] and built at CERN in 2001. The facility provides the astrophysics and nuclear technology scientific community with measurement of neutron cross-sections in the neutron energy range ranging from thermal up to several GeV. In this section, the principal characteristics of the facility will be briefly described. Extended reviews of the characteristics of the facility, performance and measurements carried out are available in the references [62, 63, 64, 65, 66, 67, 68].

The n_TOF facility is based on the 6 ns wide, 20 GeV pulsed proton beam delivered by the CERN's Proton Synchrotron (PS) with typically $7{\cdot}10^{12}$ or $4{\cdot}10^{12}$ protons per pulse (depending on whether the proton pulse delivered is dedicated or parasitic type), impinging on a lead spallation target, yielding about 300 neutrons per incident proton. A layer of water around the spallation target moderates the initially fast neutrons produced down to a white spectrum of neutrons, covering the full range of energies between meV and GeV [68].

The neutron bunches are spaced by multiples of 1.2 s, characteristic frequency of the PS cycle. This allows measurements to be made over long periods of flight without overlap between neutron pulses. The large energy range that can be measured at once is one of the key characteristics of the facility, although the high instantaneous neutron flux was designed specifically for measuring low mass and/or radioactive samples, minimizing the signal-to-background ratio. In the left hand panel of the figure 2.1 is shown a schematic picture of the n_TOF facility and the PS at CERN.

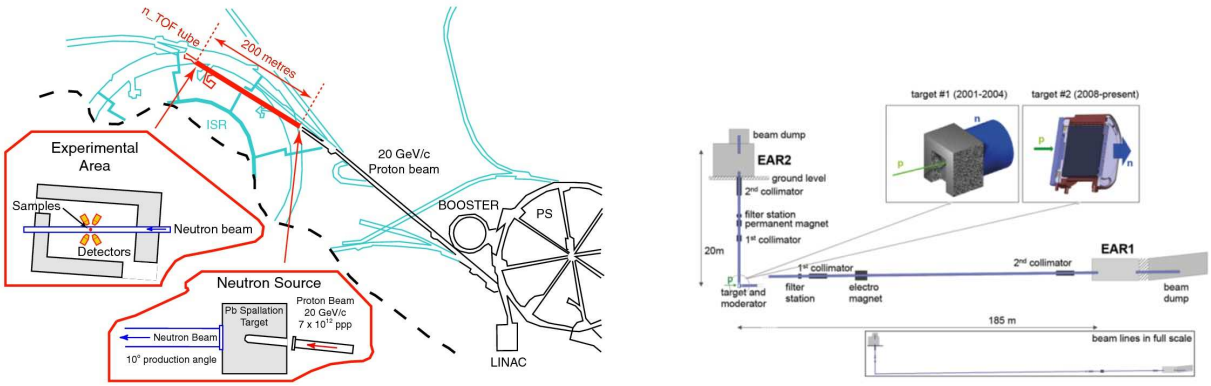

Figure 2.1: In the left hand panel, schematic picture of the n_TOF facility, the CERN's PS and that of the experimental area. In the right hand panel, a schematic picture of the facility, including the two neutron beam lines and the two experimental areas, EAR1 and EAR2.

The energy of the incident neutron is determined by the length of the flight technique. The neutrons, created at a time t_0 , travel from the spallation target to the experimental areas situated at a distance L where the reactions are detected by the experimental setup at time t_0+t. The velocity of the incident neutron is determined as v=L/(t_0+t) and its kinetic energy by the relativistic formula:

$$E_n = E_{tot} - m_n c^2 = (\gamma - 1)\, m_n c^2 = \left(\frac{1}{\sqrt{1 - v^2/c^2}} - 1 \right) m_n c^2 \tag{2.1}$$

where m_n is the neutron mass and c the light speed.

Two beam lines are in operation today. The first one, in existence since the opening of the facility, is a horizontal beam line with a large flight path (185 m) that leads to an experimental area (EAR1) where the experimental setups are mounted and the measurements of the neutron cross-sections are performed. The second one, operative since 2014, is a vertical beam line with a shorter flight path (20 m) that leads to another experimental area (EAR2) with a neutron flux about 25 times larger than the neutron flux in EAR1. For both neutron beam lines, collimators and magnets are placed between the spallation target and the experimental areas, which deflect the charged particles and scattered neutrons, thus reducing the amount of background in the experimental areas. In the right hand panel of Fig 2.1 is a schematic picture of the n_TOF facility, including both neutron beam lines, collimators and magnets.

In this manuscript we will refer only to the EAR1, where the experiment was performed.

The energy shape of the neutron flux in the experimental areas is determined using two fission chambers absolutely calibrated at PTB [69], Silicon Monitors based on ^{6}Li(n,α)t reactions, Micromegas detectors based on ^{235}U(n,f) and ^{10}B(n,α) reactions and Parallel Plate Avalanche Counters (PPACS) based on ^{235}U(n,f) reactions [70]. As a result of all the measurements, an evaluated flux is obtained as is shown in Fig 2.2. The differences observed between the neutron flux in 2009 and subsequent years are due to the presence of ^{10}B, dissolved this year for the reduction of the background produced in the ^{1}H(n,γ)^{2}H reactions of the neutron moderator of the spallation target.

Since the measurement of neutron-induced fission and neutron capture cross-sections is carried out in the experimental areas, two different collimators are used, the inner radius of the fission collimator being larger than that of the capture collimator due to the larger radius of the fission targets. For the capture measurements, the collimator used for such measurements provides a neutron beam with a spatial profile of 2 cm in diameter with a quasi-Gaussian spatial profile of σ ~0.77 cm in the energy range which is of

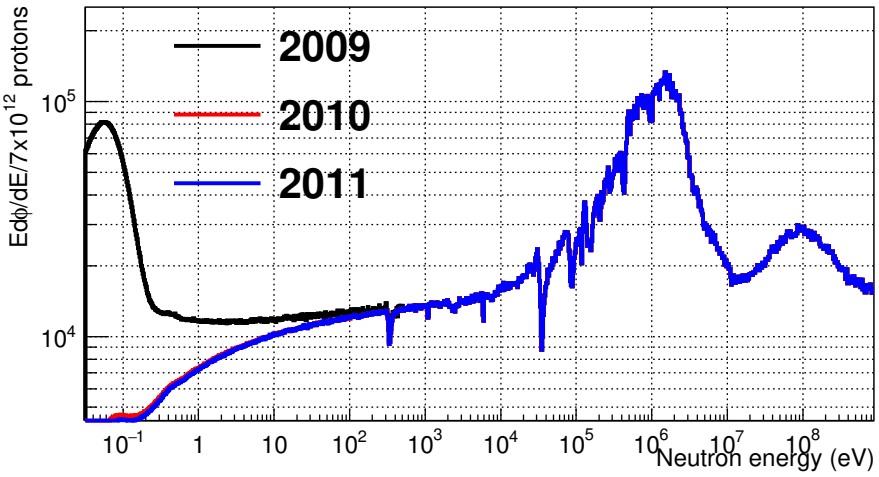

Figure 2.2: Evaluated neutron fluence in the EAR1 along the years: 2009 (solid black line), 2010 (solid red line) and 2011 (solid blue line).

interest to this work [71].

Since not all the neutrons are produced at the same time and position in the spallation target and the interactions of the neutrons with the moderator and other materials along the neutron beam line, there is an ambiguous distribution between the velocity and the time of flight. This probability distribution, also known as the Resolution function, R, needs to be accurately determined for the precise time of flight to energy conversion and analysis of the neutron cross-section data. The Resolution function is obtained by simulations and verified by the measurement of well-known neutron resonances. This probability distribution as a function of the true neutron energy, E_n, can be expressed by related quantities such as neutron energy, E, equivalent time, t, or equivalent distance, L, as is shown in figure 2.3. Thus:

$$R(E_n; E)dE = R_t(E_n; t)dt = R_L(E_n; L)dL \tag{2.2}$$

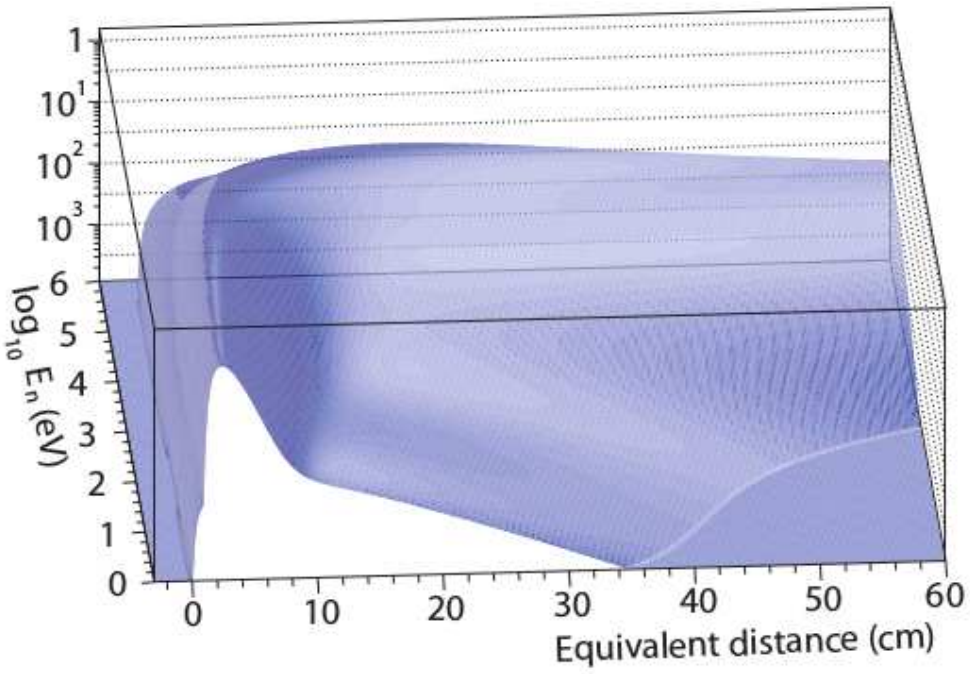

Figure 2.3: Resolution function of the n_TOF facility, expressed as equivalent distance traveled by each neutron as a function of its energy.

2.2 The experimental setup

During the ^{235}U(n,γ) cross-section measurement, five different types of detectors were used: (1) the n_TOF Total Absorption Calorimeter (TAC) [58] used to detect the capture reactions produced in the ^{235}U samples; (2) The Fission Tagging Micromegas Detectors (FTMG) [59], placed in the center of the TAC with the ^{235}U targets, were used for the measurement of the neutron-induced fission cross-section and the subtraction of the prompt-fission γ-ray background; (3) The Silicon Flux Monitors (SiMon) [72] used as intensity monitors of the neutron beam; (4) The Wall Current Monitor (WCM) [73] used to monitor the proton beam; (5) The Beam Current Transformer (BCT) [73] that registers the number of protons per pulse and is used for the same purpose as the WCM.

The signals of the of the first four detectors were recorded by the front-end n_TOF Data Acquisition System (DAQ) [74] and the BCT value is directly registered together with the rest of the data. All the detected signals recorded by the different detectors were analyzed offline by its dedicated pulse shape routines.

2.2.1 The Total Absorption Calorimeter

The γ-ray cascades following the (n,γ) reactions are detected by the Total Absorption Calorimeter (TAC), which is a 4π segmented array detector formed by 40 BaF_2 crystals [58] based on the design from Karlsruhe TAC [75]. There are 12 crystal of pentagonal shape and 28 crystals with a hexagonal shape. Each BaF_2 crystal is surrounded by two superposed layers of 0.1 mm thick each made from teflon and polished aluminum sheet for optimizing the light collection. The crystals are encapsulated in a 1 mm thickness of borated carbon fiber capsules for reduction in the amount of neutrons detected by the TAC. The assembly is coupled to a 5 inch Photonis XP4508B photomultiplier. The BaF_2 module is attached to an aluminum housing, integrated in a honeycomb structure, which holds the complete assembly as is shown in both panels of Fig. 2.5.For further information about the BaF_2 crystals and the TAC consult the references [34, 76].

The BaF_2 signals were recorded in the front-end n_TOF Data Acquisition System for the posterior offline analysis as is shown in Fig. 2.4 by the dedicated pulse shape routine [77].

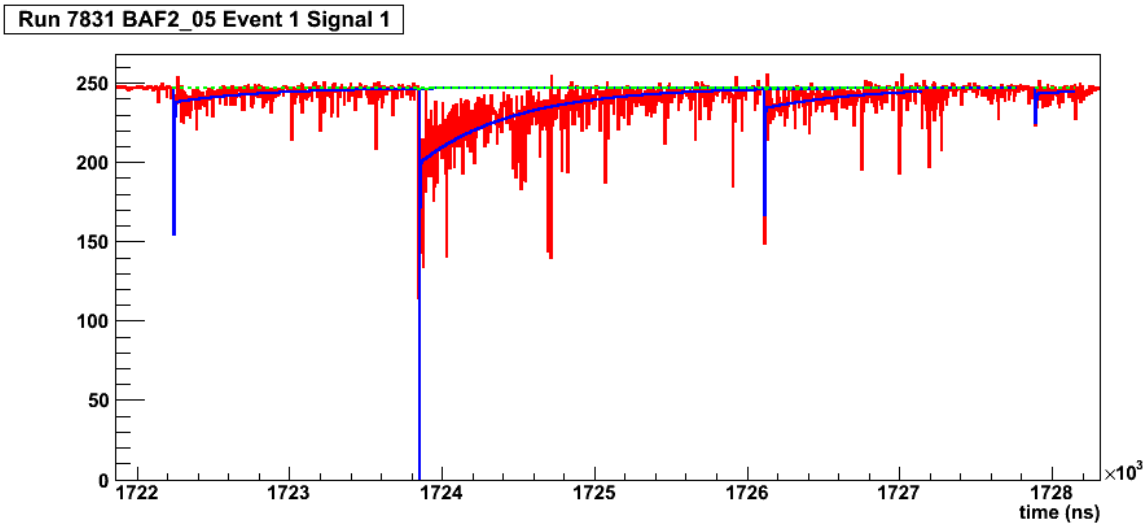

Figure 2.4: Raw buffer digitized from one BaF_2 detector (red solid line). The analyzed signals detected by the dedicated pulse shape routine are indicated by the solid blue line and the baseline by the dashed green line.

The entire structure, BaF_2 modules plus the honeycomb that holds the detectors, forms an spherical shell of 10 and 25 cm of inner and outer radius respectively, covering 95% of the solid angle. Between the fission chamber and the TAC was placed a polyethylene neutron absorber with an 18.8 cm diameter, 1.13 g/cm^3 density and enriched with natural Boron at 10%, in order to reduce the amount of scattered neutrons detected by the TAC. The borated neutron absorber surrounding the fission chamber is shown in the right hand panel of Fig. 2.3.

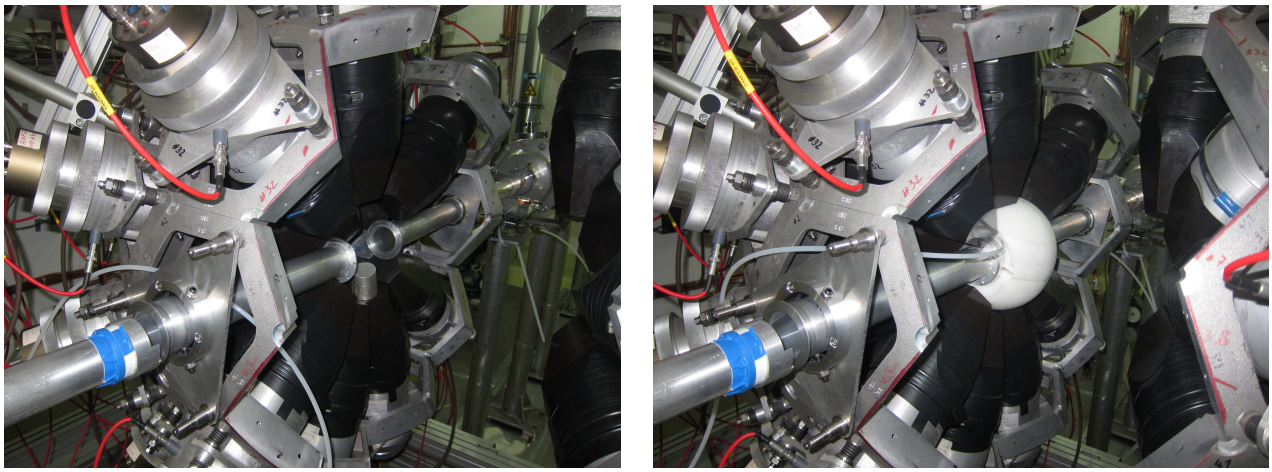

Figure 2.5: In the left hand panel, picture of the TAC empty during a calibration measurement with an Am/Be source. In the right hand panel, picture of the TAC with fission chamber in the center of the TAC surrounded by the borated neutron absorber.

The TAC was designed to detect in coincidence individual γ-rays emitted during the neutron capture process. The entire γ-ray cascade, which is emitted in several picoseconds, is detected in coincidence between the BaF_2 crystals using a time coincidence window of 20 ns.

The high TAC detection efficiency for the individual γ-rays permits the detection of the capture cascades with probabilities close to 100%, thus registering most of the γ-ray emitted after the nuclear reaction and its energies,E_γ. Thus, by the coincidence between the BaF_2 crystals, the TAC events are characterized by the number of BaF_2 crystals detected in coincidence, m_{cr}, and the total deposited energy of the event, E_{sum}, defined as the sum of all the detected deposited energy in the BaF_2 crystals. This high detection efficiency is scaled down to 60-70% when, during the analysis, some restrictions are applied to the detected events in order to improve the signal-to- background ratio.

2.2.2 The fission tagging micromegas detectors

The micromegas detector is a gaseous parallel plate detector [59, 78, 79] with three electrodes, cathode, micromesh and anode based on a relative simple detection principle. The detector is sensitive to the charged particles such as the α particles produced in the ^{10}B reactions or the fission fragments produced in neutron-induced fission reactions and X-rays. These detectors are used for hard radioactive environments such as nuclear reactors [80] due to their robustness and high resistance to radiation damage. The energy deposition of the incident charged particle produces ionization electrons in the gas that are amplified by the electric field applied.

The active volume of the detector is separated into two regions: the drift gap, formed by the region between the cathode, where calibration sources, the sample to be measured or neutron conversion samples

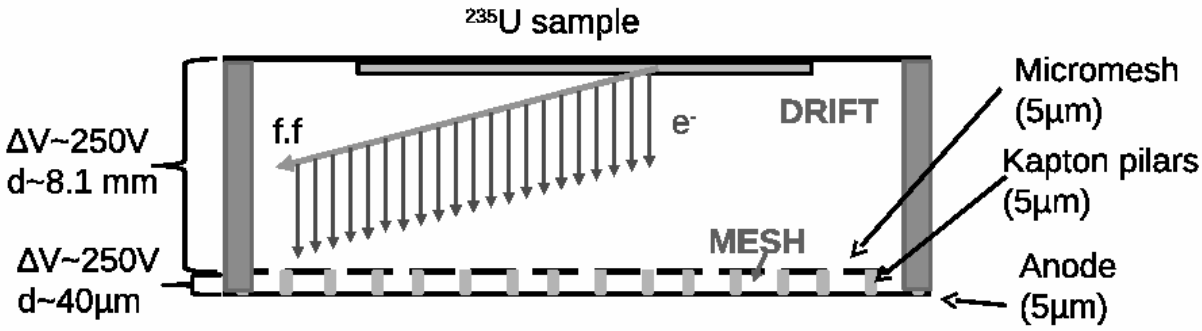

Figure 2.6: Schematic picture of the micromegas detector used for the fission tagging experiment. The gaseous detectors are divided into two regions: the drift gap, formed by the region between the cathode where the ^{235}U sample is placed and the micromesh; and the amplification gap, formed by the region situated between the micromesh and the anode plate.

are placed, and the micromesh; and the amplification gap, situated in the region between the micromesh and the anode plate. A schematic picture of the detector is shown in Fig. 2.6.

In the drift region, the low electric field applied (∼1 kV/cm) collects the ionization electrons towards the micromesh. In the amplification region, the high electric field applied (from 40 to 70 kV/cm) produces the multiplication of the incoming charge coming from the drift region by an avalanche process [78]. The amplified charge is finally collected by the anode plate, thus producing the electrical signal from the detector. The narrow separation between the micromesh and anode plate, typically 40-100 μm, controls the gain of the detector. Therefore, controlling the geometry of the space between the micromesh and the anode plate is crucial for energy resolution, as well as for the homogeneous collection and amplification of the charge produced.

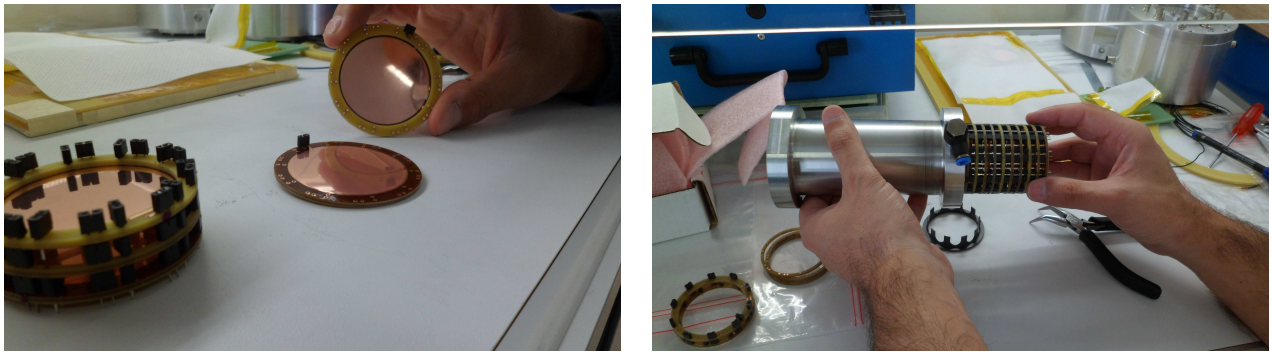

Figure 2.7: In the left hand panel, picture of the individual fission tagging micromegas detectors and the assembly of two fission tagging detectors. In the right hand panel, fission tagging micromegas assembly being placed inside the fission chamber.

The micromesh and the amplification region are produced by a chemical process that attacks a thin film made from copper and the kapton layers in order to obtain a grid of insulating kapton pillars with a thickness of the initial film. Therefore, the micromesh grid is a thin metallic copper foil, 5μm thick, composed by a hole grid with 25μm diameter and a distance between holes of 50μm. The uniform gap

between the micromesh and the anode is achieved by the small cylindrical insulating pillars created from the chemical process, fixed to the anode [59]. A schematic zoom of the amplification region of the micromegas is shown in Fig. 2.8.

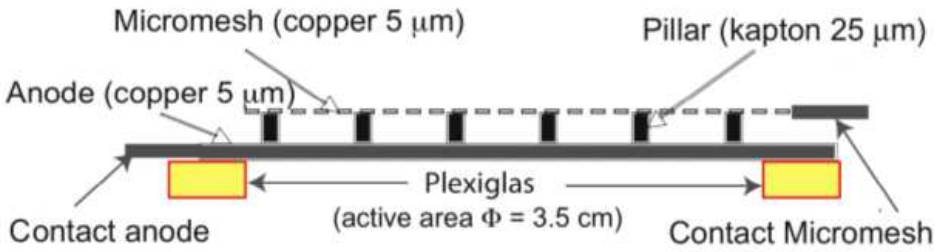

Figure 2.8: Zoom of the amplification region. The micromesh grid and the kapton pillars are shown in the top part of the figure. In the bottom part is shown the anode plate. The figure has been taken from [59].

Micromegas detectors are widely used for the monitoring of the neutron beam during the neutron cross-section measurement, using neutron converters such as ^{10}B, ^{6}Li or ^{235}U, and for the measurement of the neutron-induced charge particles cross-sections. The high transparency of these detectors and reduced amount of material required for the construction, produce low perturbations in the neutron beam, thus minimizing the amount of secondary particles and background produced by the interaction of the neutron beam. This is particularly important for the neutron capture measurements, where the background is a critical part of the analysis.

Fission Tagging Micromegas Detectors (FTMG) are a compact version of these versatile detectors. The diameter of FTMG is ϕ=60 mm, thus covering the entire neutron beam spatial profile, and the drift gap was 8.1 mm, this distance being a factor of two times less when compared to the micromegas detectors used as neutron beam monitors at the n_TOF facility. These reduced dimensions permit it to fit inside the sealed fission chamber as is shown in the right hand panel of Fig. 2.7. This small drift gap, as will be shown later, makes it impossible to completely stop the fission fragments. For the operation, the detectors were placed in a sealed fission chamber filled with a premixed gas of Ar+(10%)CF_4+(2%) iC_4H_{10} at atmospheric pressure (1 bar) as is shown in the right hand panel of Fig. 2.7. Due to the strict safety rules at CERN, the percentage of isobutane during the operation was low enough to be non-flammable.

The signal produced by the anode was shaped by a preamplifier-fast amplifier analogical system, producing signals of about 250 ns in width. These raw signals were recorded by the n_TOF DAQ at 100 MS/s as is shown in Fig. 2.9 in order to achieve neutron energies down to the thermal point.

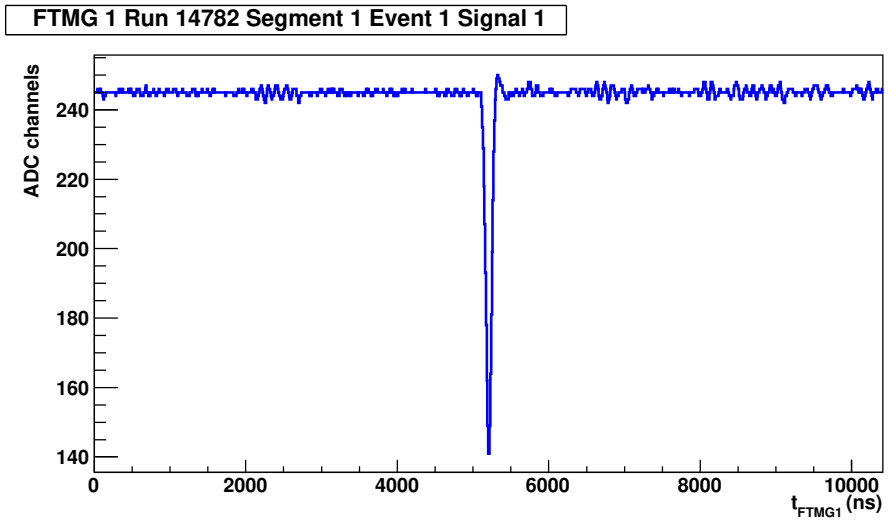

Figure 2.9: Raw buffer digitized from one FTMG detector. The recorded signal of a fission fragment is shown by the solid blue line. The time width of the signal is about 250 ns.

2.2.3 The neutron beam monitors

The intensity of the neutron flux during the measurement of the ^{235}U(n,γ) cross-section was monitored by three different detection systems:

- The Silicon Monitors (SiMons) [72], used to monitor the intensity of the neutron beam along the different experimental configurations.

  For the n_TOF facility, where the neutron beam is produced by spallation reactions, the accurate normalization could be achieved by recording the total number of protons impinging on the Pb target [73]. However, a precise relative normalization is also obtained by directly measuring the neutron beam using the well-known neutron cross-section of the reactions ^{6}Li(n,α)t.

  The SiMons is an array of four silicon detectors with a experimental setup designed to minimize the amount of material that intercepts the neutron beam as is shown in the schematic picture of Fig. 2.10. The ^{6}Li foil is inserted with a Mylar film in the neutron beam, where the reactions ^{6}Li(n,α)t are produced. The different detectors are placed outside the neutron beam at 45 degrees in respect to the norm of the neutron beam, detecting the resulting Tritium and α particles.

  The amplitude spectra detected by the four silicon detectors is shown in Fig.2.12. The upper part of the spectra correspond with the tritium detection peak while the plateau observed is due to the detection of the α particles. For further information about the detectors, their behavior and performance, consult the reference [72].

- The Wall Current Monitor (WCM) [81], is a system that generates a signal proportional to the intensity of the neutron beam, thus monitoring the intensity of the proton beam.

- The Beam Current Transformers (BCT) [81], also used to monitor the intensity of the proton beam, record the number of protons impinging on the spallation target. Both systems, the WCM and BCT, are independent, therefore giving reliable information about the proton beam intensity.

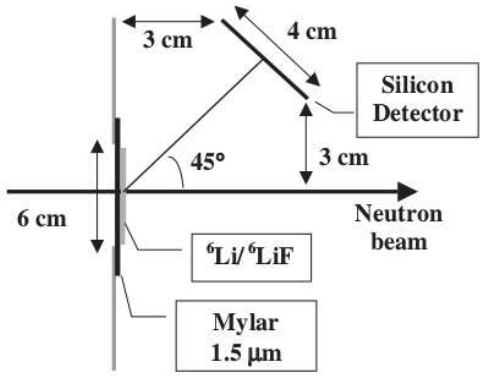

Figure 2.10: Schematic figure of the experimental setup of the SiMons at the n_TOF facility. The thin Mylar foil with the ^{6}Li target is inserted in the neutron beam and the array of silicon detectors is placed outside the neutron beam, minimizing the amount of dead material intercepting the neutron beam.

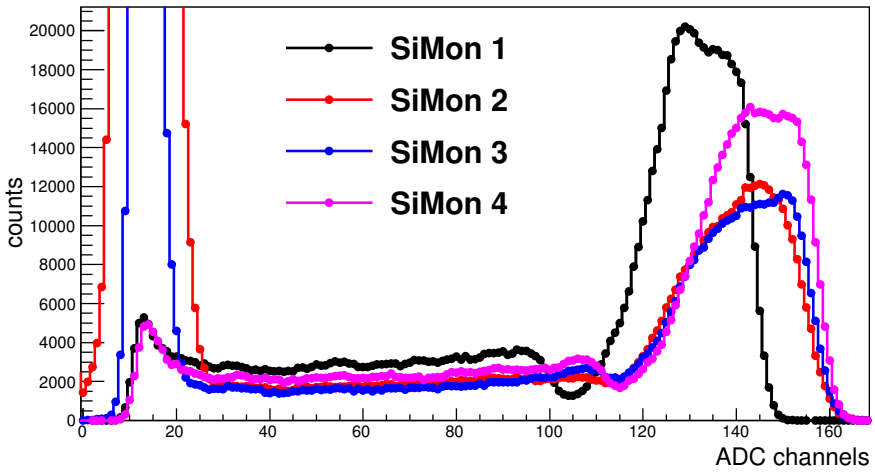

Figure 2.11: Amplitude spectra of the four Silicon Monitors used during the measurement of the $^{235}U(n,\gamma)$ cross section.

2.2.4 The data acquisition system

The entire experimental setup used during the measurement of the ^{235}U(n,γ) cross-section was completely recorded by the n_TOF Digital Acquisition System (DAQ) [74]. This system is based on Acqiris-DC270 Flash ADCs cards with 8 bits resolution, 1 GS/s of maximum sampling rate and maximum buffer memory capacity of 8 MB per channel. The sampling rate of the Flash ADCs is adapted to the signal time characteristic of the input detector and the time window required for the minimum neutron energy target of the measurement[1]. The trigger pulse, provided by the CERN PS, is delivered to the DAQ just before the incident proton pulse reaches the spallation target. This trigger signal is passed to all the available Flash ADCs cards, starting the acquisition and digitalizing each ADC channel up to the selected time window.

Figure 2.12: Front-end n_TOF DAQ formed by the Acqiris-DC270 flash ADCs cards used for the digitization of the signals of the detectors placed in the experimental area 1 (EAR1).

The entire digitized buffer of each ADC channel is then processed by an algorithm labeled as zero suppression that eliminates the pieces of the raw buffer where no detector signal is found, thereby reducing the amount of recorded data and eliminating the part of the buffer without any practical information. The rest of the buffer is stored in a binary file with global information such as the date, the number of protons reaching the spallation target, the pulse number present in the file, the type of incident proton pulse (dedicated, TOF, or parasitic, EASTC), and the temperature registered in the experimental area.

The large amount of useful raw data recored is then stored in the magnetic tapes of the CERN's CASTOR facility [82] for its posterior analysis with the dedicated pulse shape routines [77, 83]. The files with the raw buffers are saved in structures defined by runs, each one corresponding with the digitized data obtained between a start and stop of the DAQ.

For the measurement of the ^{235}U(n,γ) cross-section, the 40 BaF_2 detectors were recorded at 250 MS/s covering a total neutron energy range from several GeV down to 0.2 eV, which is the lower limit of this

[1]The possible sampling rate of the Acqiris-DC270 are 100 MS/s, 250 MS/s, 500MS/s and 1 GS/s, and the possible time windows 80 ms, 32 ms, 16 ms and 8 ms, respectively.

measurement. The FTMG detectors and the SiMons were recorded at 100 MS/s covering a large neutron energy period (down to below the thermal energies), but due to an undesirable registered signal generated by the CERN PS, the useful information is limited to 0.2 eV due to the limited memory of the Acquiris cars, 8 MB memory for each channel. The WCM were recorded at 250 MS/s, enough to extract the precise information about the incident proton pulse. In total, for the neutron capture cross-section of the ^{235}U, more than 50 detectors were recording at the same time with different sampling rates and time windows.

The stored data was analyzed by the dedicated pulse shape routines for each type of detector, resolving the pile-up which occurred and extracting the accurate information from the raw signals such as the time of flight, area, or amplitude.

2.3 The ^{235}U targets used for the measurement

Ten non-encapsulated U_3O_8 targets, highly enriched with ^{235}U isotope, were used during the measurement of the ^{235}U(n,γ) cross-section. The targets were manufactured at JRC-Geel [84] from the same batch of U oxide material produced for the samples used for neutron beam monitors [85]. The samples were produced by molecular plating technique in a polycetal molecular plating cell with a rotating Pt anode and were mounted on a Al foil of 0.03 mm thick. The aluminum backing was mounted on an aluminum ring with inner and outer diameters of 49 mm and 55 mm respectively. The diameter of the mask used for the preparation of the ^{235}U deposit was 42.00±0.03 mm. Hence, the active diameter of ^{235}U samples is the diameter of the mask. The superficial density of the ^{235}U targets is 300 μg/cm^2, standard for fission cross-section measurements, since this thickness permits the escape of the fission fragments from the samples. A picture of the ^{235}U target used during the measurement is shown in Fig. 2.13.

Figure 2.13: One of the ten ^{235}U samples used for the measurement of the ^{235}U(n,γ) cross section.

The batch of material used for the targets was of 99.934% enriched in ^{235}U. The isotopic composition was determined by mass spectrometry. The amount of ^{235}U in each sample was derived from the activity, as described in the reference [85]. In the table 2.1 is summarized the ^{235}U mass sample in mg, the superficial density in Atm/barns and the activity in Bq for the individual targets used during the measurement.

In order to verify if the use of the thin target approximation is possible, the following quantity has been calculated as a function of the neutron energy:

$$R(E_n) = \frac{1 - e^{-n\sigma_T(E_n)}}{n\sigma_T(E_n)} \tag{2.3}$$

where σ_T(E$_n$) is the total cross-section of the ^{235}U isotope as a function of the neutron energy and

Sample	mass (mg)	$n_{at} \cdot 10^{-7}$ (At/barn)	Activity (Bq)	expected CR (c/ms)
1	5.03±0.02	9.30±0.05	402.0±1	4.0
2	4.68±0.01	8.65±0.04	373.9±1	3.7
3	4.38±0.01	8.10±0.04	350.5±1	3.5
4	3.66±0.01	7.33±0.04	292.5±1	2.9
5	3.96±0.01	7.25±0.04	316.9±1	3.1
6	3.92±0.01	7.41±0.04	313.3±1	3.1
7	4.00±0.01	7.15±0.04	320.5±1	3.2
9	3.87±0.01	7.19±0.04	309.1±1	3.1
10	3.75±0.01	6.93±0.04	299.7±1	3.0
TOTAL	41.15±0.11	76.1±0.4		

Table 2.1: Summary of the targets used for the fission tagging experiment. In the columns are shown the determined amount of ^{235}U present in each sample, the superficial density and activity. The characterization of the ^{235}U targets were performed in 10/03/2012. In the last column of the table is shown the expected counting rate in the fission tagging micromegas detectors due to the α activity.

n is the superficial density in At/barn. The closer to unity that factor is, the better is the thin target approximation [2]. As is shown in Fig. 2.14, the thin target approximation is a very good approximation for this neutron cross-section since the deviations are smaller than 0.6% in the largest resonance.

[2] In the case of thin target, $n\sigma_T(E_n) << 1$, the exponential is reduced to $e^{-n\sigma_T(E_n)} \approx 1 - n\sigma_T(E_n)$ and the numerator is $R(E_n) \approx n\sigma_T(E_n)$.

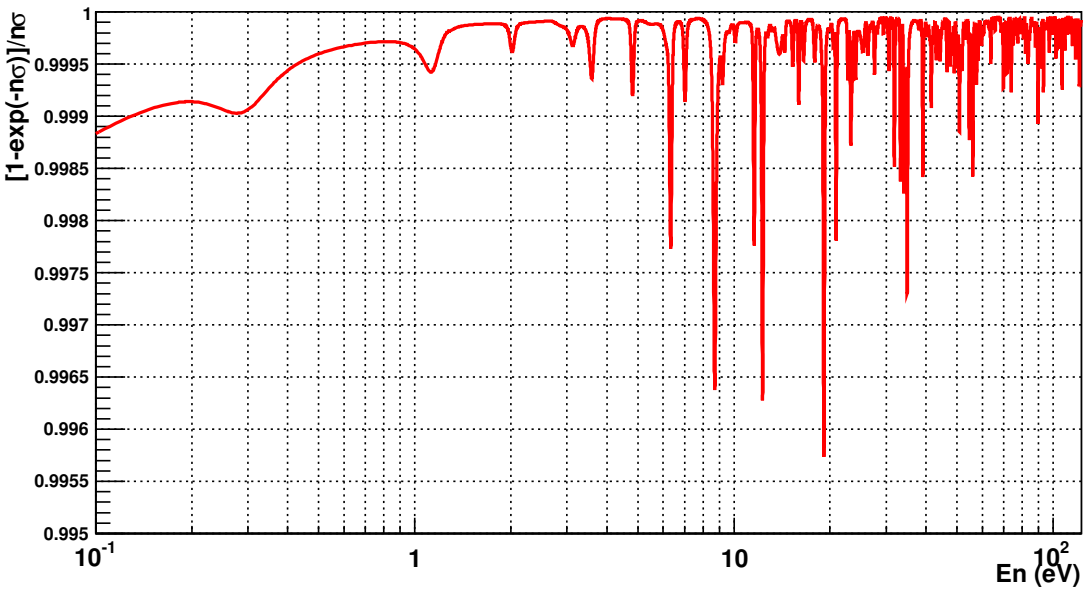

Figure 2.14: $R(E_n)$ as a function of the neutron energy for the validation of the thin target approximation. The total superficial density of the ^{235}U targets has been assumed as $n=7.6 \cdot 10^{-6}$ At/barn.

2.4 Experimental configurations for the measurement

During the measurement, the ^{235}U targets and FTMG were placed inside a sealed fission chamber specifically designed to fit inside the center of the TAC. The fission chamber, made from aluminum, was filled with a premixed gas Ar+(10%)CF_4+(2%) iC_4H_{10} at atmospheric pressure for the operation of the FTMG and sealed by two kapton windows. A picture of the fission chamber with half of the borated neutron absorber is shown in the left hand panel of Fig. 2.16.

In Fig. 2.15 a schematic picture of the experimental area is shown which plots the SiMon, the TAC with the FTMG chamber and the beam dump. The neutron beam line from the SiMons to the beam dump was in vacuum, with the exception of the center of the TAC where two kapton windows separate the beam line in vacuum from the sealed fission chamber.

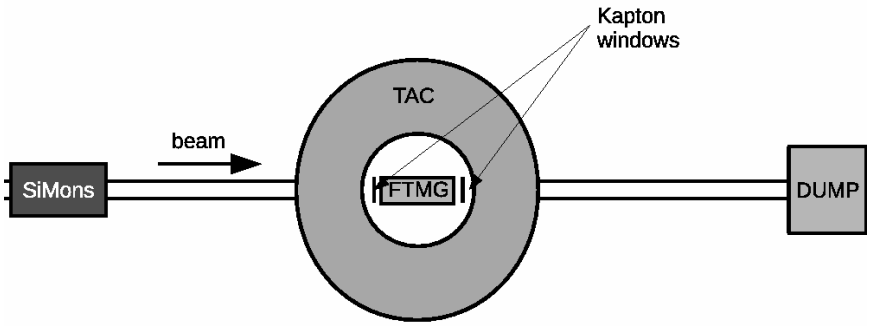

Figure 2.15: Schematic picture of the experimental setup used for the $^{235}U(n,\gamma)$ cross-section measurement showing the SiMons, the TAC, the fission chamber in the center of the TAC and the beam dump.

Two different experimental setups were used during the measurement:

- 2FTMG: In this experimental configuration, the ten ^{235}U samples were distributed in a stack of eight samples and another two encapsulated inside two FTMG. This setup, with a low FTMG fission detection efficiency (∼20%), aims to minimize the amount of dead material intercepting the neutron beam, thus reducing the background registered by the TAC and improving the signal-to-background ratio.

- 10FTMG: In this experimental configuration, the ten ^{235}U samples were encapsulated in ten FTMG, one per sample. With high FTMG fission detection efficiency (∼90%) and a substantial background, it aims to obtain an accurate prompt fission background subtraction, thus validating the technique and the data of the ^{235}U(n,γ) cross-section obtained from 2FTMG experimental configuration.

A schematic picture of the experimental configurations used for the measurement is shown in the right hand panel of Fig. 2.16.

The measurement was performed during a total of four full months of dedicated beam, from the end of June up to the end of October of 2012, with a total number of $\sim 4.0 \cdot 10^{18}$ protons. It must be said, however, that ∼30% of the measured data was not used at the end for the calculation of the neutron capture cross-section analysis, due to problems related with the alignment of the TAC with the neutron beam. The time calendar of the measurement, detailing the time periods, experimental configurations, and the number of protons dedicated to each period is shown in Fig. 2.17.

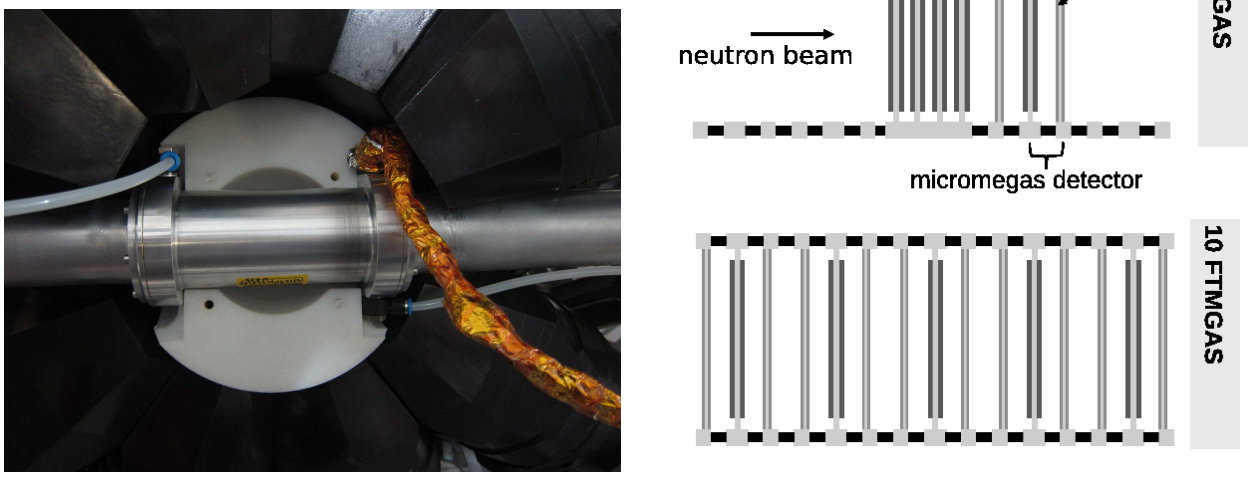

Figure 2.16: In the left hand panel is a picture of the sealed fission chamber in the center of the TAC with half of the borated neutron absorber. In the right hand panel, a schematic picture of the experimental configurations used for the measurement of the $^{235}U(n,\gamma)$ cross-section.

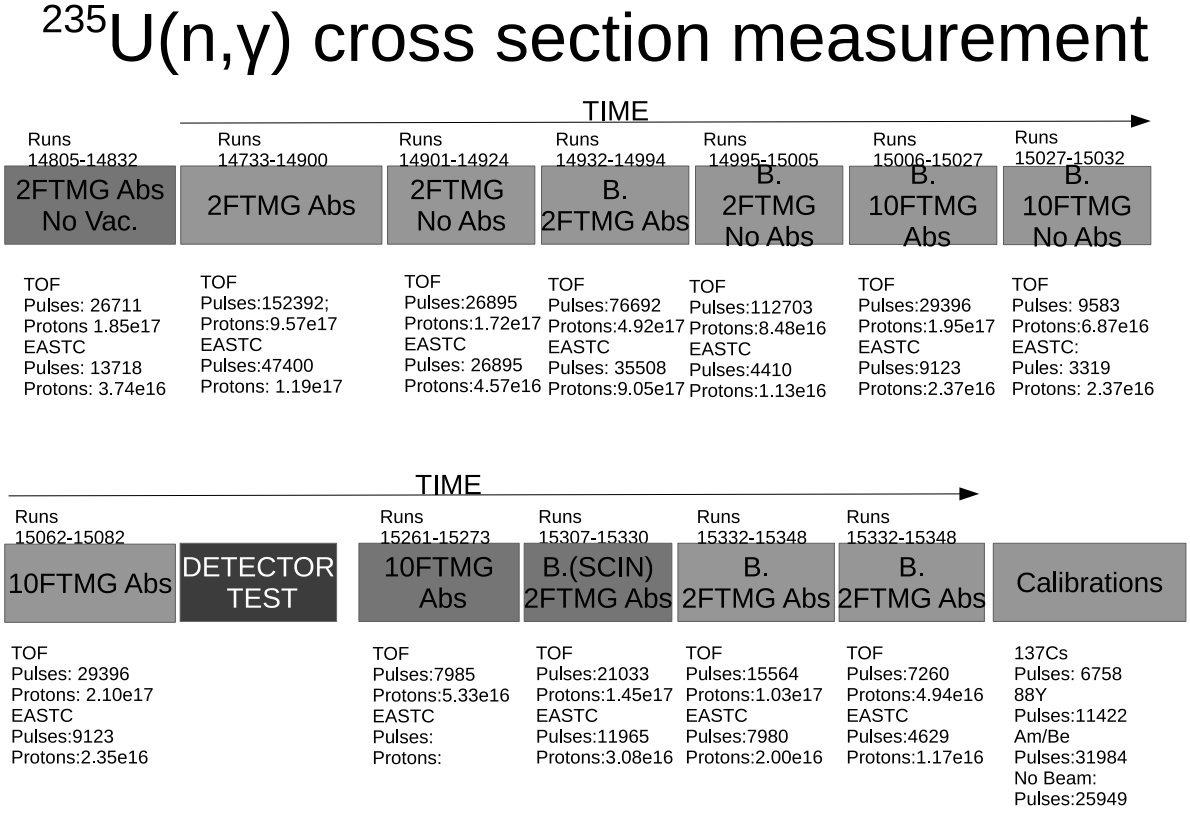

Figure 2.17: Detailed time calendar of the $^{235}U(n,\gamma)$ cross-section. The dedicated total number of protons and number of pules is shown for each period detailed.

Chapter 3

The procurement of the experimental cross-section

This chapter is devoted to describing the procedure followed in order to obtain the experimental ^{235}U(n,γ) cross-section from the experimental data. The procedure was described briefly in section 1.2, where it was shown that the experimental neutron capture cross- section in the thin target approximation, is calculated as:

$$\sigma_\gamma(E_n) = \frac{c_{tot}(E_n; E_{sum}, m_{cr}) - c_{bkg}(E_n; E_{sum}, m_{cr})}{N_{norm}\varepsilon_\gamma(E_n, E_{sum}, m_{cr})\phi_N(E_n)} \tag{3.1}$$

where $c_{tot}(E_n;E_{sum},m_{cr})$ is the total counting rate of the Total Absorption Calorimeter, $c_{bkg}(E_n;E_{sum},m_{cr})$ is the background determined, $\phi_N(E_n)$ is the neutron fluence, $\varepsilon_\gamma(E_n,E_{sum},m_{cr})$ is the detection efficiency and N_{norm} is the normalization factor for the neutron capture cross-section. All the variables (except N_{norm}) depend on the conditions applied to the TAC, m_{cr} and E_{sum}, and the kinetic energy of the incident neutron, E_n. Many of the tools and procedures needed for the analysis were developed in the past for the analysis of other measurements [34, 76, 86, 87, 88]. However, due to the fissile character of these nuclei, it was necessary to develop new tools for the FTMG and the coincidence analysis between both detection systems. The chapter is organized as follows:

- In section 3.1 the analysis of the individual BaF_2 detectors and the TAC is described.
- The section 3.2 is devoted to the analysis of the FTMG, including the new tools which have been developed for the instrumental/physics analysis of the detectors.
- The section 3.3 is devoted to describing the time coincidence analysis between the TAC and the FTMG.
- The section 3.4 is dedicated to the determination of the background detected by the TAC.
- The section 3.5 is devoted to the determination of the fission detection efficiency, ε_f and the fission tagging detection efficiency ε_f^*.
- In section 3.6 the determination of the TAC (n,γ) detection efficiency, ε_γ is explained.
- In the section 3.7 the determination of the neutron fluence shape $\phi_N(E_n)$ is considered.
- In the section 3.8 the normalization of the measurement is described.
- Section 3.9 is devoted to describing the dead time corrections applied to the TAC.

3.1 The Total Absorption Calorimeter

In this section we describe the instrumental analysis performed to the Total Absorption Calorimeter (TAC). The tools used for this analysis have been developed in the past for other measurements [34, 76] and will be described briefly in the following sections. The analysis performed is summarized as follows:

- The deposited energy calibration of the BaF_2 detectors, section 3.1.1, and the characterization of the deposited energy resolution of the BaF_2 crystals needed for the Monte Carlo simulations 3.1.2.
- The time calibration of the BaF_2 detectors 3.1.3 needed for the TAC events reconstruction.

3.1.1 Energy calibration of the BaF_2 modules

The energy calibration procedure of the BaF_2 modules is formed by three different well-defined parts: the α/γ/noise BaF_2 signal discrimination, the energy calibration by the use of the standard γ-ray calibration sources and the gain control of the different detector modules within the measurement. The results obtained for these three different parts will be shown in the following subsections.

The α/γ/noise signal discrimination

The BaF_2 scintillation process is characterized by two components whose time decay constants are different:

- The first one, labeled as the fast component, has a decay time constant of $\tau_{fast} \sim 0.7$ ns and is used for the determination of the timing of the detected signal.
- The second one, labeled as the slow component, has a decay time constant of $\tau_{slow} \sim 620$ ns and carries most of the information regarding the deposited energy detected in the BaF_2 [34, 76].

The relationship between the amplitude of the fast and slow components (A_{fast}/A_{slow}) permits the discrimination of the α and γ-ray particles. Electronic noise is removed efficiently from the analysis by the comparison of the real-time width of the detected signal, T_{real}, calculated from the dedicated BaF_2 pulse shape routine [77] to the expected one, and fixed by the decay time constant of the slow component $T_{expected}$ ~620 ns. Therefore, the pulse shape discrimination α/γ/noise is performed applying cuts to the ratio A_{fast}/Area and $T_{real}/T_{expected}$, where the variable Area is the area of the signal determined by the pulse shape routine. A detailed description of the dedicated BaF_2 pulse shape routine can be found in [77].

In Fig. 3.1 we can see the BaF_2 signal discrimination for detector number four in a dedicated measurement with the standard ^{137}Cs γ-ray calibration source. In the vertical axis of the diagrams we can see the ratio $T_{real}/T_{expected}$ for the discrimination of noise, and in the horizontal axis the ratio between the fast component and the total area of the BaF_2 signal, A_{fast}/Area, for the discrimination of the α/γ particles. We show the 2-dimensional plot for low amplitude signal in the top-left panel, and for the rest of the signals in the bottom-left panel. The γ-ray amplitude spectra obtained from the application of such conditions in the BaF_2 signals is shown as the red line in the upper-right panel of the same figure. Also in the same figure is the α-particle amplitude spectra, indicated as the blue line and the noise spectra as the green line color. The same discrimination process has been applied to the 40 BaF_2 modules, thus obtaining very good discrimination between the three components for all the detectors.

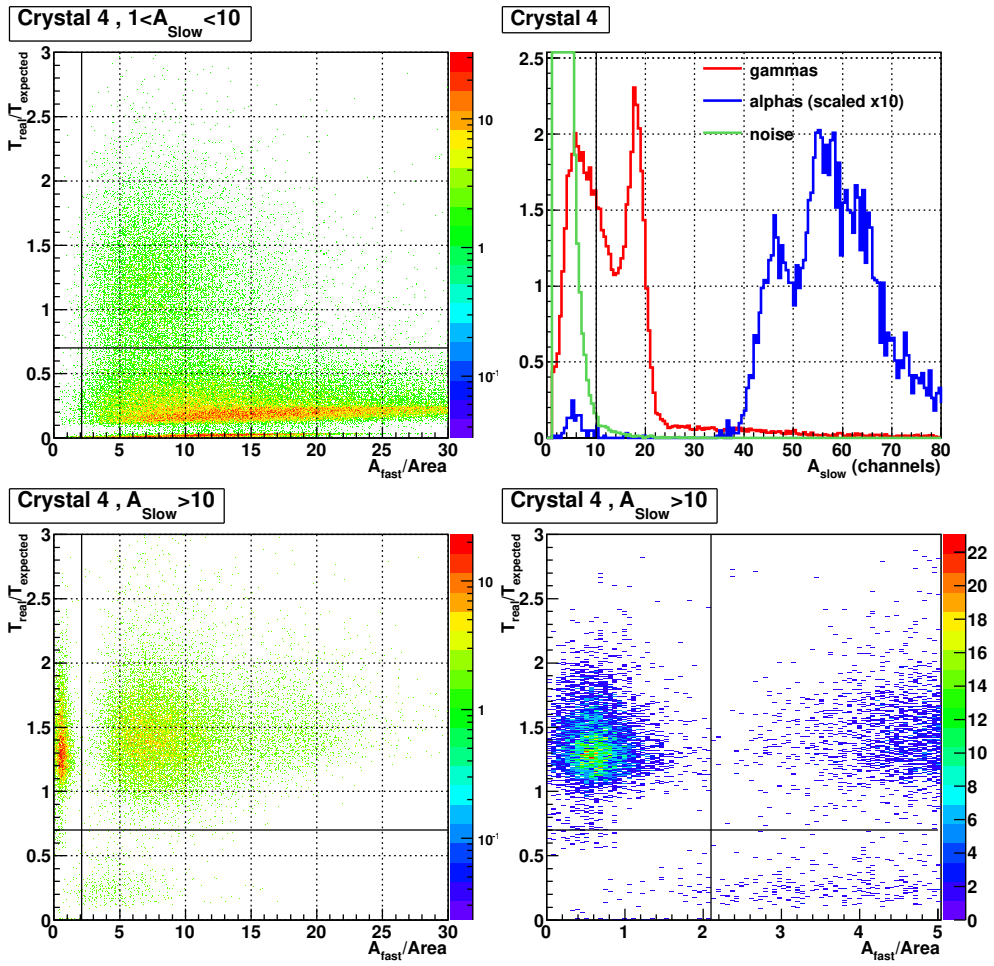

Figure 3.1: The α/γ/noise BaF_2 signal identification performed to the BaF_2 crystal number four in a dedicated measurement with the ^{137}Cs standard γ-ray calibration source.

Energy calibration using the γ-ray standard calibration sources

During the ^{235}U fission tagging experiment, periodical deposited energy calibrations of the BaF_2 modules were performed with the standard ^{137}Cs, ^{88}Y γ-ray calibration sources. As is explained in [34], the amplitude of the slow component A_{slow}, in good approximation, is proportional to the deposited energy in the BaF_2 detectors. Hence, the energy calibration in the detectors has been carried out by the correspondence of the slow amplitude to γ-ray energies peaks (E_γ) from standard calibration sources. This calculation has been repeated for all the individual BaF_2 detectors, calculating the position of the different γ-ray peaks observed during the dedicated measurement with the calibration sources. In order to obtain the centroid of the peaks, a Gaussian function plus an assumed linear background were used for the fit. In Fig. 3.2 can be seen an example of the correspondence obtained for the BaF_2 crystal number ten in two different calibration measurements: in the left hand panel this is shown for a ^{137}Cs γ-ray calibration source (E_γ= 667 keV) and in the right hand panel for a ^{88}Y γ-ray calibration source (E_γ= 882 keV,E_γ=1880 keV). The results of the fit performed for all the γ-ray peaks (gaussian + linear background) are indicated in both panels of Fig. 3.2 by the light blue line.

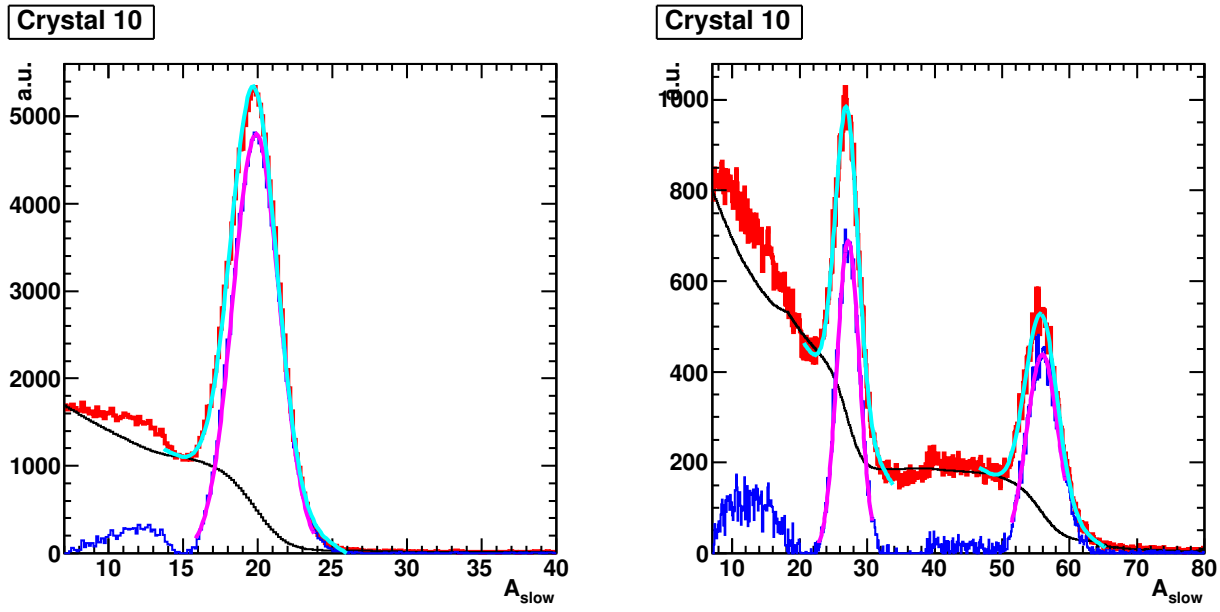

Figure 3.2: In the left hand panel, energy correspondence of the A_{slow} amplitude to the γ-ray peak of the ^{137}Cs calibration source is indicated. In the right hand panel can be seen energy correspondence of the A_{slow} amplitude to the two γ-ray peaks of the ^{88}Y calibration source.

Thus, the deposited energy calibration of the detectors is obtained by a linear fit of the correspondence obtained between the A_{slow} and the calibration sources γ-ray peaks.

Gain monitoring of the BaF_2 detectors within the measurement

The gain of the BaF_2 detectors has been monitored and corrected in the measurement of the α-decay spectra of the contaminant isotopes present in the crystals. The methodology was developed in the past for previous measurements; for further information consult [34, 87]. The results of this monitoring for 5 of the 40 BaF_2 detectors as a function of the run number is shown in Fig. 3.3. The gain variation observed in the BaF_2 detectors during the measurement does not exceed more than 5%.

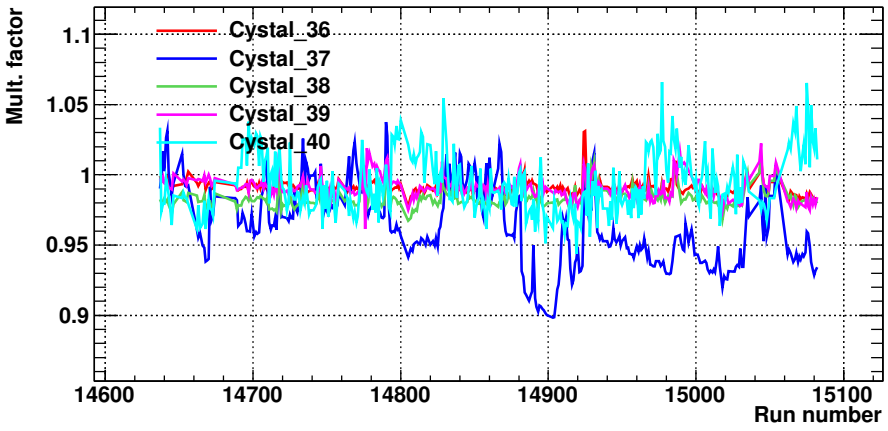

Figure 3.3: Gain monitoring for 5 of the 40 BaF_2 detectors within the $^{235}U(n,\gamma)$ measurement.

3.1.2 Energy resolution of the BaF_2 detectors

The characterization of the BaF_2 energy resolution as a function of the deposited energy, $R(E_\gamma)$, is necessary for the accurate Monte Carlo simulation of the TAC response to different particles and the calculation of the efficiency to the $^{235}U(n,\gamma)$ reaction as will be explained in the section 3.6. The values of the energy resolution obtained during the energy calibration process with standard calibration sources have been used for this purpose. The energy resolution, as a function of the γ-ray energy, has been modelled using the formula utilized in previous campaigns represented in the equation 3.2:

$$R(E_\gamma) = \frac{\Delta(E_\gamma)}{E_\gamma} = \frac{FWHM}{E_\gamma} = \sqrt{\alpha + \beta/E_\gamma} \tag{3.2}$$

where α and β are two free parameters used which fit the experimental energy resolution of the detectors [89].

The energy resolution at the energies γ-ray peaks (^{137}Cs and ^{88}Y) of the individual BaF_2 crystals are shown in the right hand panel of Fig. 3.4 and Fig. 3.5. The red line shown is the average energy resolution of all the BaF_2 detectors for the corresponding γ energy peak. The detectors with the worst energy resolution, 25 and 40, correspond with BaF_2 modules with the voltage divider badly adjusted, thus producing a considerably poor behavior in energy resolution and signal pulse shape.

The average energy resolution of the BaF_2 detectors is shown in the left hand panel of Fig. 3.4. The black points are the experimental average energy resolutions obtained at the energy of the γ-ray peaks and the red solid line is the model used to reproduce the energy resolution (Eq. 3.2).

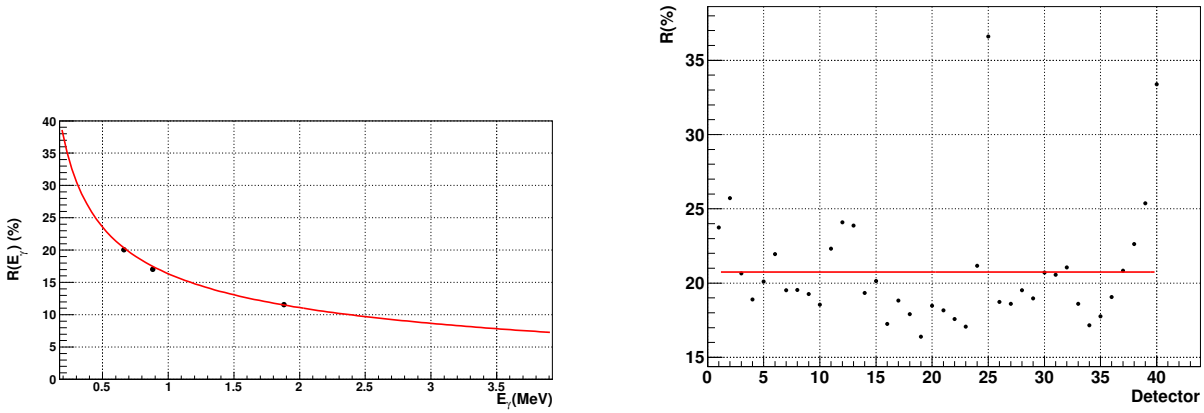

Figure 3.4: In the left hand panel is presented average energy resolution function of the BaF_2 as a function of the deposited energy. In the right hand panel, the black points are the experimental value of the energy resolution for the standard γ-ray calibration sources. The solid red line represents the model used for the energy resolution in the detectors. Energy resolution is obtained for the individual BaF_2 crystals at 662 keV (^{137}Cs γ-ray peak). The average energy resolution of the crystals is shown by the solid red line, R(E_γ=662 keV)$\sim$20%.

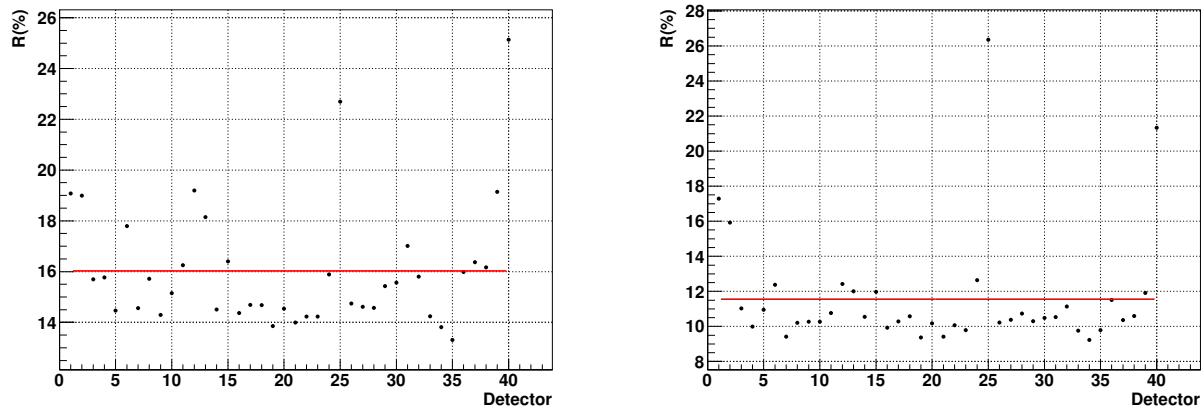

Figure 3.5: In the left hand panel is the energy resolution obtained for the individual BaF_2 crystals at the first γ-ray peak of the ^{88}Y standard calibration source, E_γ= 882 keV. The average energy resolution of the BaF_2 crystals at this deposited energy is R(E_γ= 882 keV)$\sim$16%. In the right hand panel is the energy resolution obtained for the individual BaF_2 crystals at the second γ-ray peak of ^{88}Y, E_γ=1880 keV. The average resolution of the BaF_2 crystals at this energy is R(E_γ=1880 keV)$\sim$11%.

3.1.3 Time calibration of the BaF_2 detectors

The TAC event reconstruction is based on the time coincidence between the signals detected by all the BaF_2 detectors. The detectors are connected to different flash-ADC cards with different chronometers. An offset is expected between the flash-ADC cards since the different digitizers commence the acquisition at slightly different times and the length of the cables from the detectors to the digitizers may be different. In addition, the finite accuracy of the flash-ADC chronometers produces slightly different time-cycles in the digitizers. Hence, the flash-ADC chronometers need to be synchronized by a linear function for the TAC event reconstruction. The synchronization is obtained by measuring a radioactive sample that simultaneously emits two γ-rays, such as the ^{88}Y calibration source. The time differences observed between events detected in two BaF_2 detectors with total deposited coincidence energy in the coincidence peak are stored along the entire flash-ADC buffer. These differences are used for the synchronization of the BaF_2 modules, as is shown in Fig. 3.6.

The time window used, forming the coincidences in the BaF_2 modules, is 20 ns. The process has been repeated for all the BaF_2 detectors using one detector as reference.

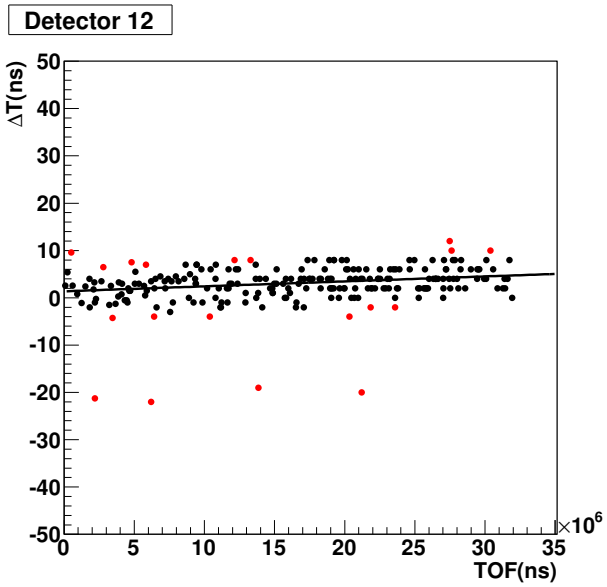

Figure 3.6: Time calibration performed to ADC channels of the BaF_2 detector number 12. The standard γ-ray calibration source used for the time calibration in the $^{235}U(n,\gamma)$ measurement was ^{88}Y.

In both panels of Fig. 3.7 one can see the counting rate detected by the TAC during a measurement with the ^{88}Y calibration source before (red line) and after (black line) the time synchronization, in the left hand panel for the non-coincidence deposited energy spectra 0 <E$_{sum}$ (MeV) < 2.0, and in the right hand panel for the coincidence peak, 2.4< E_{sum} (MeV)<3.5. The figure is used to cross-check the time correction since, for a calibration source, the counting rate along the digitalized buffer should be constant.

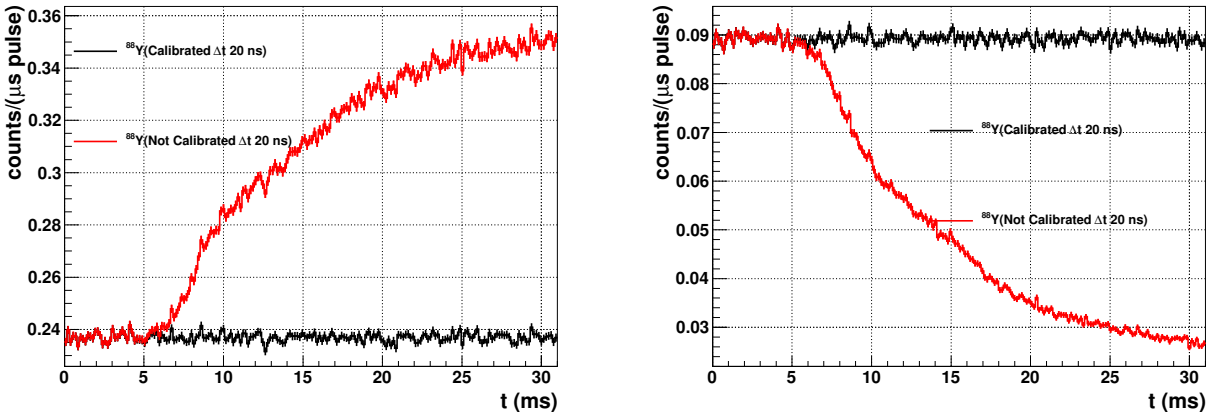

Figure 3.7: In the left hand panel is the counting rate detected by the TAC for events with $m_{cr} > 0$ and $0 < E_{sum}$ (MeV)< 2.0. In the right hand panel is the counting rate detected by the TAC for events with $m_{cr} > 1$ and deposited energy $2.4 < E_{sum}$ (MeV)< 3.5.

3.2 The fission tagging micromegas detectors

The analysis performed on the Fission Tagging Micromegas (FTMG) detectors is summarized as follows:

- Pulse height spectrum and fission amplitude threshold: the pulse height spectrum of the FTMG detectors is composed of the fission fragments from the neutron-induced fission reactions in the ^{235}U targets and the α-particles from the natural disintegration of the ^{235}U. The separation between α-particles and fission fragments has been obtained by applying a lower amplitude threshold to the amplitude spectra labelled as the fission amplitude threshold.
- Gain monitoring and correction: the gain of the FTMG detectors has been monitored and corrected throughout the measurement by comparison between the detected fission amplitude spectra. There are strong indications that the density of the gas inside the fission chamber changed with time, thus provoking a gain and detection time drift as a function of time, as will be explained in the sections 3.2.2 and 3.2.3.
- Time calibration: as was explained in the section 3.1.3 a synchronization between the different flas-ADC digitizers is needed for the coincidences. A similar procedure has been performed for the FTMG detectors.
- Monte Carlo simulation of these detectors: as will be explained in the section 3.5, the response of these detectors to the fission fragments is essential for understanding the prompt-fission γ-ray background. The response has been calculated by means of Monte Carlo simulations using the GEANT4 toolkit [90, 91].

3.2.1 Pulse height spectra and fission amplitude threshold for the FTMG

By the use of thin target samples, the scape probability of the reaction products is close to 100%. However, even for the thin layers one still has to take into account absorption in the target samples itself due to the reaction products emitted almost parallel to the sample [78, 79]. Fission reaction products lose a significant part of their kinetic energy before escaping from the sample and will show up as a low energy tail in the pulse height spectrum of the micromegas detectors. This low energy tail is very likely to overlap with the signals produced by the α-particles from the natural decay of the ^{235}U targets. The discrimination between the α-particles and fission fragments depends on the characteristics of the detector being used, the thickness of the samples and the kinetic energy of the α-particles.

The election of the fission amplitude threshold is based on the compromise between the exclusion of the α-particles and fission detection efficiency. It is chosen for the individual micromegas detectors attending to their α-background, measured during the dedicated no-beam measurements and the gain drift of these detectors (see the section 3.2.2).

In Fig. 3.8 can be seen the pulse height spectrum measured by one of the FTMG detectors during the 2FTMG experimental configuration. The solid blue line is the amplitude spectra measured in a run of the neutron beam impinging on the ^{235}U targets and the red curve is the background measured in a dedicated measurement without the neutron beam. Note that the background is the sum of α-particles and the electronic noise registered by the detector. The fission amplitude threshold is placed in the ADC channel 30 and it is shown as the solid red line.

The values of the fission amplitude threshold for the individual FTMG detectors in the 2FTMG experimental configuration are summarized in the table 3.1. The values of the fission thresholds given in the table correspond to a high fission amplitude threshold, situated in the upper part of the valley that separates the α-particles and fission fragments. The same calculation has been performed for the 10FTMG experimental configuration with similar values for the fission threshold.

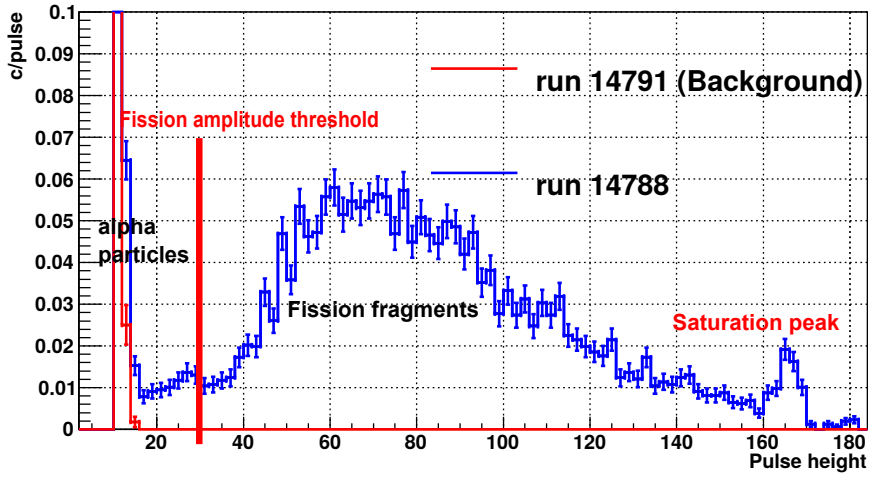

Figure 3.8: Pulse height spectrum obtained for one of the fission tagging micromegas detectors during a run of the 2FTMG experimental configuration.

Detector	Threshold ($ADCs$ channels)
1	30.0
2	40.0

Table 3.1: Fission amplitude threshold for the FTMG detectors in the 2FTMG experimental configuration.

3.2.2 Gain correction and motorization of the micromegas detectors

The gain of the FTMG detectors has been monitored during the measurement by comparing the amplitude spectra measured with one used as reference. Fig. 3.9 shows the comparison between the amplitude spectras measured at different moments of the measurement and the corrected one. The black histogram is the reference pulse height spectrum and the blue histogram is the pulse height registered in the detector at the end of the experimental configuration. Clearly, the gain of the FTMG detector has changed during the measurement. The red histogram is the blue histogram corrected by the gain shift. As is shown, a significant agreement is obtained between the reference histogram and the corrected one.

As with any gaseous detector, the gain of the FTMG detectors depends on two variables: the voltage applied to the detector and the gas density present in the fission chamber. The voltage applied to the detector is a magnitude which is well-known and is controlled from the high voltage power supply. However, the gas density in the micromegas chamber could change due to temperature drifts in the experimental area and other external sources such as the gas level of the bottles and the gas circuit. The differences in gas density are translated into gain shifts and different drift velocity (section 3.2.3).

The gain of the individual FTMG detectors has been corrected as a function of the run, minimizing the differences between the measured amplitude spectra and the reference histogram. The α factor, defined as the multiplicative constant needed for the gain correction, is shown in Fig. 3.10 and expresses the magnitude of this correction as a function of the run number. The blue points are the factors for the FTMG 1 and the red points indicate the FTMG 2 during the 2FTMG experimental configuration. The gain correction for the individual micromegas detectors is strongly correlated because the detectors are placed in the same fission chamber.

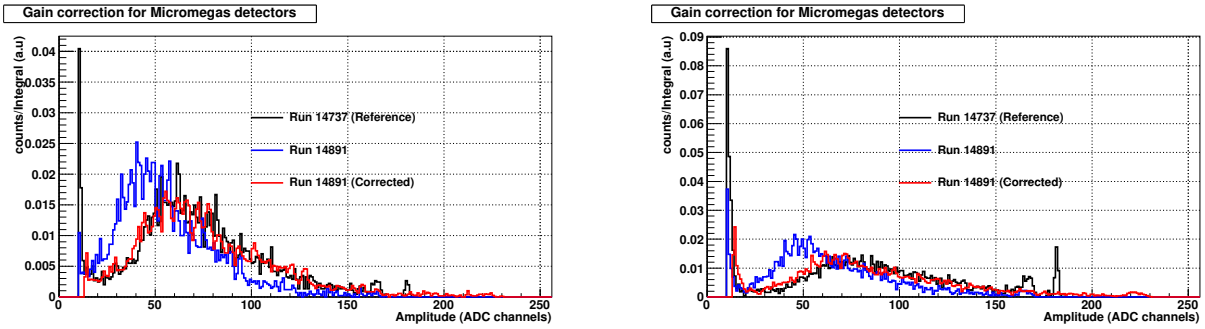

Figure 3.9: In the left hand panel are the fission pulse height spectra for the FTMG 1 at the end of the 2FTMG experimental configuration compared with the reference amplitude spectra at the beginning. In the right hand panel is the same data but for the FTMG 2.

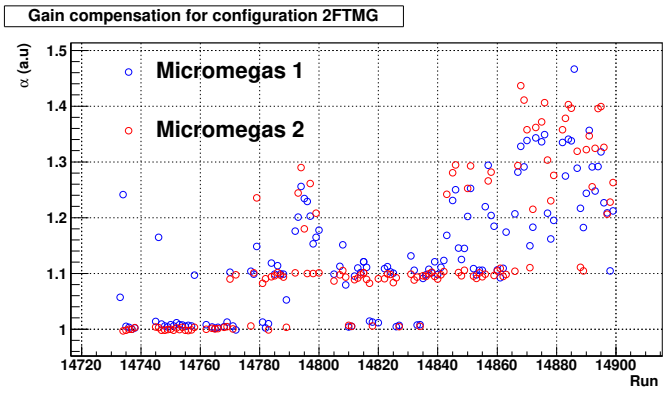

Figure 3.10: The Gain compensation factor α for the FTMG detectors as a function of the run number during the 2FTMG experimental configuration.

The correction applied produces constant fission detection efficiency during the measurement. In Fig. 3.11 can be seen the integral of the fission counts detected by the FTMG detectors in the neutron energy period from 0.3 to 10^4 eV divided by the number of protons imping on the spallation target throughout the measurement. The number of fissions occurring in the ^{235}U targets is proportional to the number of neutrons and this quantity is proportional to the number of protons, thus this ratio should be constant. For both panels of this figure, the red and blue points are these integrals before and after the gain correction respectively. In the same figure a linear fit can be seen (represented by the same color code), performed at the counting rate in order to check the performance of the correction. The difference observed between the beginning of the measurement and the end before the correction is ∼7-8% . However, after the gain correction the fit shows that the gain drift has been clearly reduced.

The coefficients of the linear fit performed are shown in the table 3.2. Despite the gain drift not being completely corrected, the gain drift effect on the detectors is clearly reduced for both detectors. Thus, the gain correction is well applied.

The same calculation has been performed on the FTMG detectors in the 10FTMG experimental configuration.

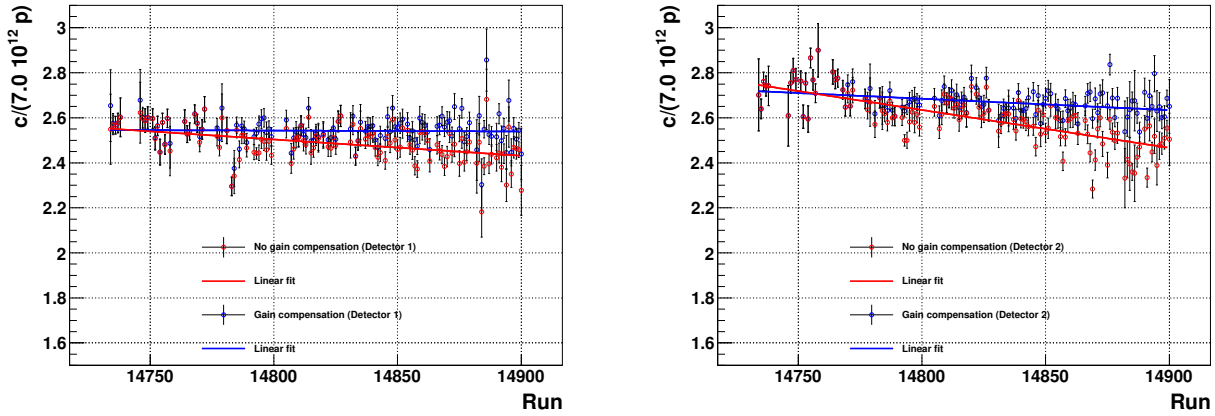

Figure 3.11: Integral of detected fission counts by the FTMG detectors during the measurement before and after the gain compensation, in the left hand panel for the FTMG detector 1 and in the right hand panel for the FTMG detector 2.

Detector	Gain Correction	p_0	$p_1 \cdot 10^{-5}$
1	Before	13±1	(-7.1±0.9)
1	After	3±1	(-4±9)
2	Before	27±1	(-16.7±9)
2	After	10±1	(-5±1)

Table 3.2: Results from the linear fit ($p_0+p_1 x$) performed on the detected fission counts as a function of the run number shown in Fig. 3.11.

3.2.3 Time calibration of the FTMG detectors

As was explained in the section 3.1.3, the Acquiris ADC chronometers of the different digitization cards must be synchronized. The time synchronization permits the reduction of the coincidence time window between the TAC and the FTMG, thus decreasing the probability of random coincidences. Since the FTMG detectors do not detect the γ-rays from the standard calibration sources, the procedure followed in section 3.1.3 cannot be used for the channels where the FTMG detectors are connected. Thus, the time calibration is performed using the possible fission events detected in coincidence between the TAC and the FTMG. For this purpose, the events used for the time calibration are likely fission events [32, 23]: events detected by the TAC with high crystal multiplicity (m_{cr} >4,5); and events detected by the FTMG with amplitude above the fission threshold.

Since the counting rate of the fission events detected by both detection systems strongly depends on the time of flight, the digitized buffer is divided into time periods of width $\Delta(t_{TAC})$. For each time period, the centroid of the time difference distribution between the TAC and the FTMG events (t_{TAC}-t_{FTMG}) is calculated, using a coincidence window from -200 to 200 ns. Then, the centroid of these distributions and the t_{TAC} are used for the time calibration of the ADC chronometers as is shown in Fig. 3.12.

The process has been repeated for different widths and crystal multiplicity conditions, finding compatible results as is shown in the tables 3.3 and 3.4. The first column of the tables are the crystal conditions applied to the TAC events, the second column is the time width of the $\Delta(t_{TAC})$ period used for the fit. The third column is the number of points used for the linear fit and the last two columns are the coefficients

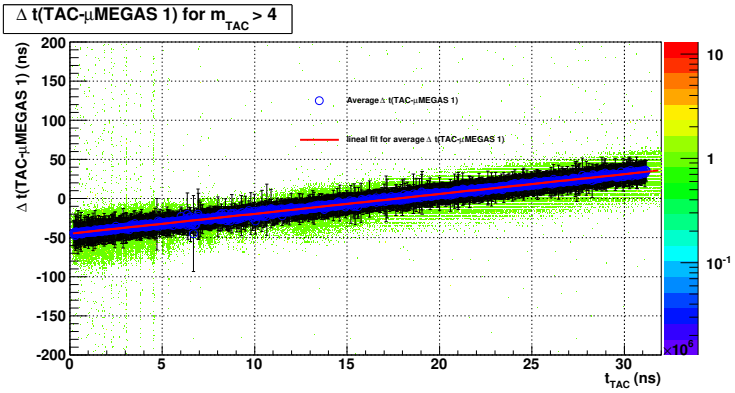

Figure 3.12: Time calibration performed to the FTMG 1 using TAC events with crystal multiplicity larger than 4 and $\Delta(t_{TAC})$=2500 ns.

values obtained from the fit.

m_{cr} >	$\Delta(t_{TAC})$ (ns)	Number of Points	a (ns)	b·10^{-6}
4	50000	620	-45±1	2.54±0.06
5	50000	620	-45±1	2.54±0.06
4	100000	310	-45±1	2.54±0.09
5	100000	310	-45±1	2.54±0.09
4	150000	206	-45±2	2.5±0.1
5	150000	206	-45±2	2.5±0.1
4	200000	155	-45±2	2.5±0.1
5	200000	155	-45±2	2.5±0.1
4	250000	124	-45±2	2.5±0.1
5	250000	124	-45±2	2.5±0.1

Table 3.3: Results from the linear fit applied to the FTMG detector 1 in the 2FTMG experimental configuration. The parameter a is the offset and the parameter b is the slope.

The time calibrations of these ADC channels have been checked performing a similar time calibration but using the BaF_2 detector used for the time calibration of all BaF_2 modules instead of the TAC events. For the calculation, all the BaF_2 signals detected have been used. The results are shown in the table 3.5.

The slope of this linear fit has similar results for the time synchronization of the ADC chronometers. The same procedure has been applied to the FTMG detectors in the 10FTMG experimental configuration.

As was explained in the section 3.2.2, the gas density shift in the fission chamber affects not only the gain of the FTMG detectors but also the drift velocity. In fact, when the gain decreases, the amplitude of the signals is affected, the charge recollection becomes slower and the maximum position of the signal is delayed. The pulse shape routine used to reconstruct the FTMG events determines the time of the signals from the maximum position, so the gain drift produces a delay in the signal detection and hence introduces a delay that scales with the gain drift of the micromegas detectors.

In order to quantify and correct this effect, for each run a new time synchronization TAC-FTMG has been performed, fixing the slope of the time synchronization. The offset calculated for each run is the effect of the gain drift to the time calibration of the FTMG detector due to the gain change. The results for the 2FTMG experimental configuration, as a function of the run, is shown in the left hand panel of

m_{cr} >	$\Delta(t_{TAC})$ (ns)	Number of Points	a (ns)	b·10^{-6}
4	50000	620	-44±1	2.53±0.06
5	50000	620	-45±1	2.54±0.06
4	100000	310	-44±1	2.53±0.09
5	100000	310	-45±1	2.54±0.09
4	150000	206	-44±2	2.5±0.1
5	150000	206	-45±2	2.5±0.1
4	200000	155	-45±3	2.5±0.2
5	200000	155	-45±2	2.5±0.1
4	250000	124	-45±3	2.5±0.1
5	250000	124	-45±3	2.5±0.1

Table 3.4: Results from the linear fit applied to the FTMG detector 1 in the 2FTMG experimental configuration. The parameter a is the offset and the parameter b is the slope.

Detector	a (ns)	b·10^{-6}
1	-35.87±0.09	2.465±0.005
2	-36.33±0.09	2.496±0.005

Table 3.5: Results from the time calibration performed to the FTMG detectors ADC chronometer with the reference BaF_2 crystal in the 2FTMG experimental configuration. The parameter a is the offset and the parameter b is the slope.

Fig. 3.13. In the right hand panel is shown the same calculation, but after the time synchronization of the runs to check the performance of the correction. As was expected, the effect of this delay is important for the 2FTMG configuration due to the large gain variation during the measurement. The effect of the gain drift in the time calibration has been completely removed and permits the reduction of the coincidence time window for the fission tagging procedure. Hence, decreasing the time window coincidence reduces the random coincidences.

The same calculation has been performed on the detectors of the 10FTMG configuration, but in this case the small gain drift observed in the detectors renders this effect negligible.

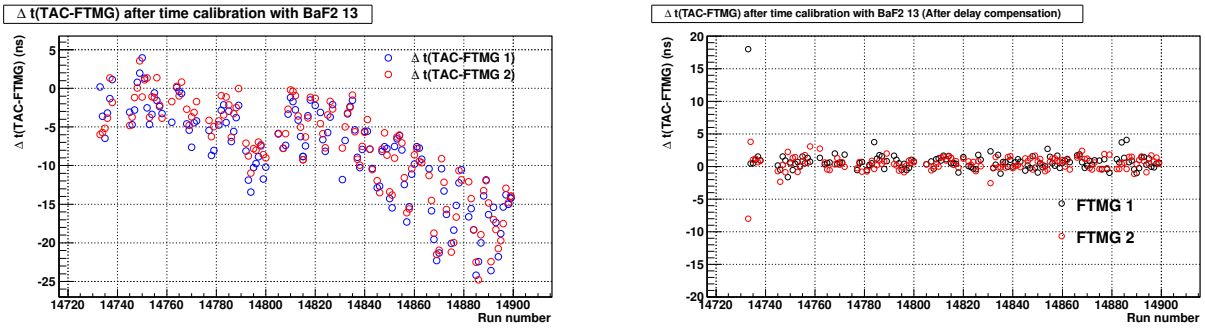

Figure 3.13: In the left hand panel is the time delay calculated as a function of the run number for the FTMG during the 2FTMG experimental configuration. In the right panel is the time delay calculated as a function of the run number after applying the delay to the time calibration of the FTMG detectors.

3.2.4 ^{235}U(n,f) Cross-section obtained with the FTMG data compared with the evaluated libraries

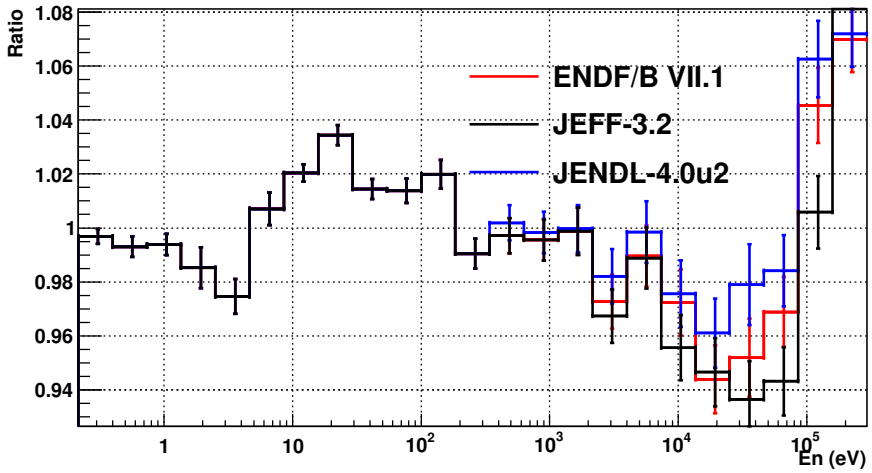

Figure 3.14: Ratio between the obtained experimental $^{235}U(n,f)$ cross-section and the evaluated libraries ENDF/B-VII.1, JEFF-3.2 and JENDL-4.0u2 in the neutron energy range from 0.2 to 10^5 eV. The uncertainty shown in the figure is only the statistical one.

The ^{235}U(n,f) cross-section has been obtained from the events detected by the fission tagging micromegas detectors in order to check the satisfactory behavior of these detectors. For this purpose, the experimental neutron-induced fission cross-sections obtained from the experimental data sets obtained in both experimental configurations have been normalized to the evaluated libraries at the neutron energy range from 7.8 to 11.0 eV.

The obtained experimental cross-section have been compared with the evaluated libraries ENDF/B-VII.1 [9], JEFF-3.2 [11] and JENDL-4.0u2 [10] as is shown in the figure 3.14. The comparison for different neutron energy periods is also shown in the table 3.6. The concordance of the experimental ^{235}U(n,f)

cross-section is within the 2% from 0.2 eV up to 10^4eV. From this point, the differences increase drastically due to dead time effects in the FTMG, reactions produced in the dead material that the detector consists of, and effects of the γ-flash.

E_n (eV)	ENDF/B-VII.1	JENDL-4.0u2	JEFF-3.2
0.2-1	0.992 ± 0.003	0.992 ± 0.003	0.992 ± 0.003
1-10	0.998 ± 0.003	0.998 ± 0.003	0.998 ± 0.003
10-10^2	1.019 ± 0.002	1.019 ± 0.002	1.019 ± 0.002
10^2-10^3	0.998 ± 0.004	0.998 ± 0.004	0.998 ± 0.004
10^3-10^4	0.989 ± 0.006	0.993 ± 0.006	0.982 ± 0.006
10^4-10^5	0.954 ± 0.008	0.973 ± 0.008	0.935 ± 0.008

Table 3.6: Ratio between the obtained experimental $^{235}U(n,f)$ cross-section and the evaluated libraries ENDF/B-VII.1 [9], JENDL-4.0u2 [10] and JEFF-3.2 [11] for different neutron energy range periods.

The conclusion extracted from this calculation is the satisfactory behavior of the fission-tagging micromegas detectors in the neutron energy range target of this measurement. This assures an accurate prompt-fission background subtraction for the calculation of the ^{235}U(n,γ) cross-section.

3.2.5 Monte Carlo simulation of the FTMG response to the ^{235}U fission fragments

The understanding of the FTMG response to the fission fragments plays an important role in many aspects of the ^{235}U(n,γ) analysis. Besides the neutron-induced fission cross-section calculated from the counting rate of the FTMG detectors (section 3.2.4), these are used in other critical manners such as the prompt-fission background subtraction (section 3.4.3) and the normalization of the measurement (section 3.8). Thus, the comprehensive understanding of the detector response to fission events is needed for the satisfactorily constructed ^{235}U(n,γ) analysis and the explanation of the correlation between fission fragments and prompt fission γ-ray cascades observed in the experimental data (section 3.5).

The detectors responses to such events have been calculated via Monte Carlo simulations. The simulation is divided into two different parts:

- The production of the fission observables used for the calculation: the ^{235}U neutron-induced fission observables such as the fission fragments mass, charge, total kinetic energies, excitation energies, prompt-neutrons and γ-rays cascades emitted from the fission fragments have been obtained event by event using the Monte Carlo GEF code [92]. It describes the observables for spontaneous fission, neutron-induced fission and, more generally, for fission of a compound nucleus from any other entrance channel, with given excitation energy and angular momentum. The GEF model is based on a general approach to nuclear fission that explains a great part of the complex appearance of fission observables on the basis of fundamental laws of physics and general properties of microscopic systems and mathematical objects. The description reproduces a number of somewhat peculiar observed features of the prompt-neutron multiplicities and of the even-odd effect in fission-fragment Z distributions.

- The Monte Carlo simulation of the FTMG response to the ions (fission fragments) generated by the GEF code in the step before: the ^{235}U fission fragments generated by the GEF code are used as input for the Monte Carlo simulation of the detector response with an application based on the GEANT4 toolkit [90, 91]. The simulation procedure followed in the simulations will be explained in the following sections.

The event generator

The event generator used for the GEANT4 application uses the output file from the Monte Carlo GEF code as input. In the Monte Carlo simulations we assume that the prompt-neutrons are quasi-instantaneously emitted after the scission process, i. e. at very prompt times. Following this, we have used the mass of the fission fragments and the total kinetic energy given after the prompt-neutron emission. The kinetic energy of each fission fragment is obtained by applying the conservation laws of the kinetic energy and momentum, assuming that the momentum carried out by the incident neutron is negligible. Then:

$$TKE^{a}_{Tot} = TKE^{a}_{A_1} + TKE^{a}_{A_2} \tag{3.3}$$

$$\overrightarrow{0} = \overrightarrow{P}_{A^{a}_{1}} + \overrightarrow{P}_{A^{a}_{2}} \tag{3.4}$$

where $A^{a}_{1,2}$ are the masses of the fission fragments after the emission of the prompt fission neutrons. Thus, solving the equations system given by Eq. 3.3 and 3.4, the kinetic energy of each individual fission fragments is:

$$TKE^{a}_{A^{a}_{1,2}} = TKE^{a}_{Tot}\frac{A^{a}_{2,1}}{A^{a}_{1} + A^{a}_{2}} \tag{3.5}$$

However, the direction of both fission fragments is fully determined by the conservation of the momentum, $\overrightarrow{P}_{A^{a}_{1}} = -\overrightarrow{P}_{A^{a}_{2}}$.

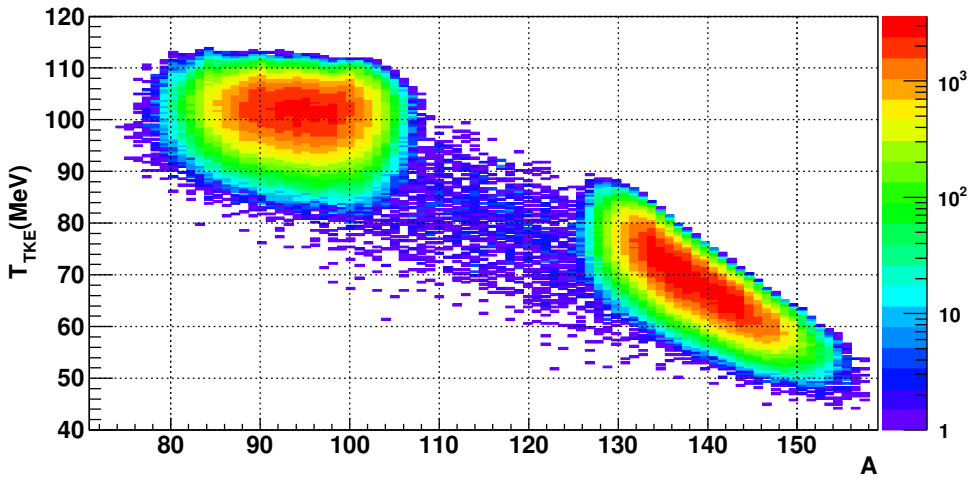

Figure 3.15: The two-dimensional distribution fission fragment mass, A, and fission fragment kinetic energy, TKE, used for the Monte Carlo simulation of the FTMG response to the fission fragments.

The two-dimensional distribution mass fission fragment (X axis) and their kinetic energies (Y axis) is shown in Fig. 3.15. The light fission fragments, in general, have large kinetic energies than the heavy fission fragments because of their smaller mass. The minimum and the maximum kinetic energy values of the light fission fragments goes from ∼90 MeV to ∼115 MeV. For the heaviest nuclei, the kinetic energies go from ∼45 MeV to ∼90 MeV as it shown in Fig. 3.15.

A schematic picture of the coordinate system used for the Monte Carlo simulation is shown in Fig. 3.16. The emission angles θ_{LAB}, ϕ_{LAB}, are defined as the angle with respect to the norm and the polar angle of the ^{235}U samples, respectively. This coordinate system (in the section 3.5) will be used later on as the TAC

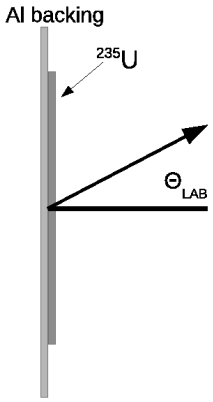

Figure 3.16: The angle θ_{LAB} is taken from the perpendicular plane of the ^{235}U sample. This angle coincides with the angle with respect to the direction of the neutron beam.

reference system. The θ_{LAB}=0 angle coincides with the direction of the neutron beam, while θ_{LAB}=$\pi/2$ is perpendicular to the direction of the neutron beam. The coordinate system is placed in the perpendicular plane of the ^{235}U sample, x and y being the ^{235}U sample plane coordinates and z the depth.

Fission fragments are emitted isotropically in the coordinate system, simulating only one of the fission fragments per event. The emission position is sorted randomly in the radius axis of the targets, using a gaussian function of σ=0.7 cm, that describes the neutron beam spatial profile. The depth of the emission is chosen randomly between 0 and the ^{235}U sample thickness. Once the direction and initial position are chosen, the fission fragment is emitted as a full striped ion with excitation energy given by the output of the GEF code.

Simplified geometry model of the fission tagging detectors

Since the simulation is intended for the understanding of the detector response, a simplified geometry has been used and is shown in Fig. 3.17. The geometry consists of a cylindrical aluminum tube which is 8.1 mm long and with a 2.5 cm radius, closed at one end by aluminum backing and the ^{235}U samples, and at the other end by the FTMG detector itself. The tube is filled with a gas mixture of 88% Ar, 10% CF_4 and 2% isobutane at 1 atm as was explained in the experimental setup (section 2.2). The thickness of each material is as follows: aluminum samples backing, ^{235}U samples and FTMG corresponds with the experimental ones: 20μm, 0.03μm and 0.035 mm, respectively. The PCB pieces that support the fission tagging micromegas detectors and the ^{235}U targets have not been included in the simplified geometrical model of the detector.

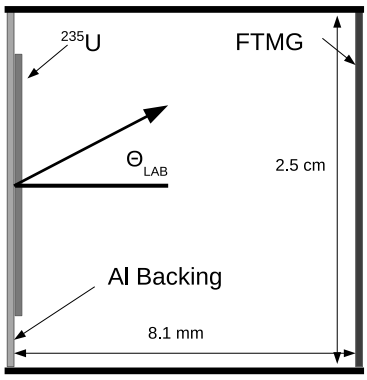

Figure 3.17: Simplified geometry implemented in the GEANT4 application for the simulation of the FTMG response to the fission fragments.

Reconstruction of the Monte Carlo events

The reconstruction process of the fission events from the Monte Carlo simulation of the fission fragments through the geometric model described before have been obtained as follows:

- The deposited energy in the active volume is converted to FTMG signal amplitude, Amp_{FTMG}, in ADC channels by a linear transformation. This is equivalent to assuming a proportionality between the deposited energy and the signal amplitude. Thus:

$$Amp_{FTMG} = m \cdot E_{dep} + b \tag{3.6}$$

  The parameters of this linear transformation, m and b, were obtained by a comparison between the Monte Carlo and the experimental data.

- The resolution broadening of the FTMG was produced by a Landau+gaussian function. The Landau function is used for the simulation of the avalanche process in the detector while the Gaussian function covers the remainder of the energy resolution of the detectors.

- If after the conversion and broadening, the signal amplitude simulated is larger than 165 ADC channels, the signal amplitude is kept in the 165 ADC channel, simulating the saturation effect observed in the amplitude spectra of the experimental data.

A reasonable reproduction of the experimental data, even with the simplified geometric model, is obtained as is shown in Fig. 3.18. The experimental amplitude spectra, shown as the blue solid line, has been taken from the 2FTMG configuration. The Monte Carlo amplitude spectra is shown in the same figure as the red curve. The parameters used for the reasonable reproduction of the experimental data and Monte Carlo simulation are shown in the table 3.7.

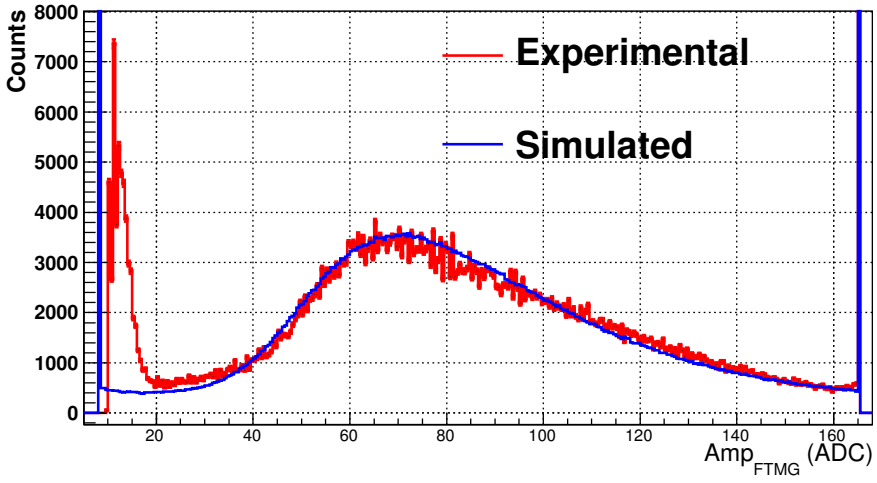

Figure 3.18: Experimental amplitude spectra of the FTMG (Red line) compared with the Monte Carlo reconstruction (Blue line).

m (ADC/MeV)	b (ADC)	σ
1.0	8.0	0.28

Table 3.7: Values of the parameters adjusted by the comparison of the Monte Carlo and the experimental data (Fig. 3.18). The parameters m and b are the slope and the offset used for the deposited energy conversion. The parameter σ is the parameter used in the Gaussian function for the broadening resolution.

FTMG response to the fission fragments

Two different aspects of the FTMG response to the fission fragments have been investigated through the Monte Carlo simulations:

- The total and angular fission detection efficiency as a function of the FTMG amplitude, Amp_{FTMG}.

  The total detection efficiency decreases rapidly with Amp_{FTMG} as is shown in the left hand panel of Fig. 3.19. From the Monte Carlo simulation, using low amplitude detection threshold ∼20 ADC channels, it can be deduced that the estimated fraction of lost fission fragments due to the absorption in the ^{235}U samples is close to ∼10%.

  The angular detection efficiency of the detector is similar to a $\cos(\theta_{LAB})$ as shown by the blue and red curves in the right hand panel of Fig. 3.19; only for emission angles near-parallel to the ^{235}U samples does the detection efficiency decrease rapidly. This is due to the self-absorption of fission fragments in the ^{235}U samples. For larger Amp_{FTMG} thresholds (dashed-red, dashed-blue, dashed-black and green curves) another experimental effect plays an important role. The gap chosen for the fission tagging micromegas detectors is not enough to stop the fission fragments emitted near-parallel to the neutron beam, thus the fission fragments with emission angles near-perpendicular to the ^{235}U samples are not detected because these fission fragments do not deposit all their kinetic energies in the active volume.

  To illustrate this angular effect, the simulated FTMG amplitude spectra, selecting different emission angles, are shown in Fig. 3.20. The blue curve represents the fission fragments emitted with the

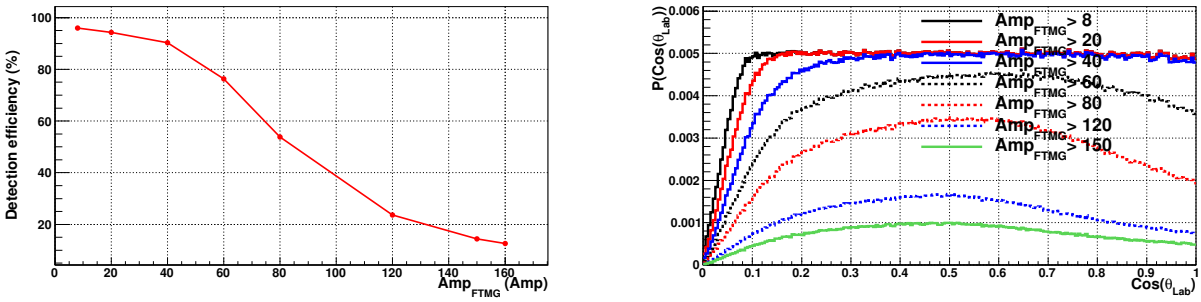

Figure 3.19: In the left hand panel, total FTMG detection efficiency as a function of Amp_{FTMG} is shown and in the right hand panel, angular detection efficiency as a function of $cos(\theta_{LAB})$ for different Amp_{FTMG} thresholds.

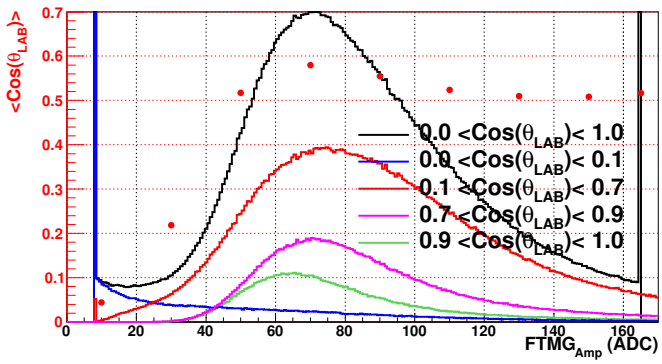

Figure 3.20: Monte Carlo reconstruction of the FTMG amplitude. The amplitude spectra are shown in different colors, selecting some emission angles.

largest emission angles, i. e. the fission fragments emitted near- parallel to the ^{235}U samples and lost due to self-absorption. These events are the main component of the low amplitude events detected by the FTMG. On the other hand, the fission fragments with the shortest emission angles (green curve) are not located in the upper part of the simulated Amp_{FTMG} spectra but near to the neck because of the gap effect mentioned previously. Thus, the fission fragments with the emission angles close to 45 degrees respecting the normal plane of the ^{235}U samples are the events with the largest deposition in the detectors.

- The detection efficiency of the different types of fission event. Since only one of the fission fragments can be detected per fission event, the question is rather not the detection efficiency change as a function of the fission fragment mass than: do the FTMG have a different detection efficiency, depending on the fission fragment mass?. This could provoke a different detection efficiency depending on the fission fragments with similar masses and fissions with very different masses. To answer this question, the detection efficiency has been calculated as a function of the heavy fission fragment mass A. If in the Monte Carlo calculation the light fission fragment is simulated, then the fission event detected/simulated is marked by the corresponding heavy fission fragment mass. The results of this calculation, for different amplitude FTMG thresholds, are shown in the left hand panel of Fig. 3.21.

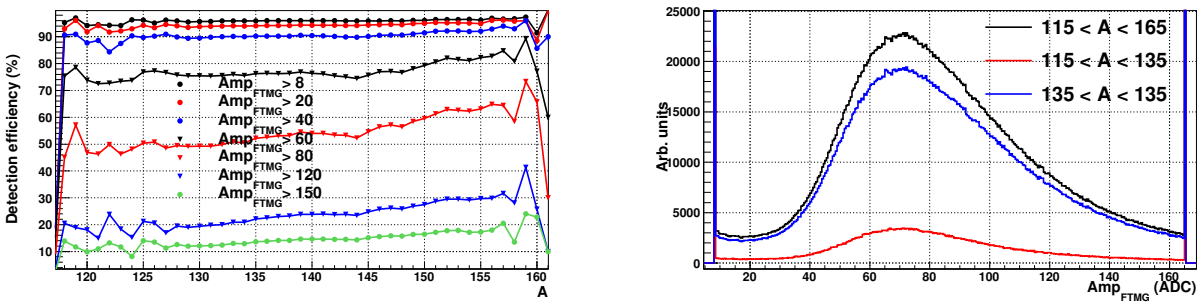

Figure 3.21: In the left hand panel is shown fission detection efficiency of the FTMG as a function of the mass of the heavy fission fragment A, for different FTMG amplitude. In the right hand panel, FTMG amplitude spectra selecting different fission fragments mass.

In the left hand panel of Fig. 3.21, the fission detection efficiency of the events with the smallest mass A corresponds with the more symmetric fission fragments while the events with the largest mass A correspond with the more asymmetric events. As the FTMG detection threshold is increased the detection efficiency of the symmetric and asymmetric fragments changes. Then, the masses of the fission fragments are not uniformly distributed along the FTMG amplitude spectra. Therefore, applying a cut in amplitude, we are selecting a specific kind of fission fragment. In the right hand panel of the same figure is shown the amplitude spectra for two different kinds of fission events, 115<A<135 and 135<A<165. As in the case of the angle emission, the fission fragments mass is non-uniformly distribute; thus, we have different fission events depending on the FTMG amplitude.

3.3 Coincidence analysis between the TAC and the FTMG

This sections describes the analysis carried out regarding the coincidences between the fissions detected by the FTMG and the events detected by the TAC. As was suggested in previous works [23, 32], the prompt fission events are characterized by high γ-ray multiplicity [92]. Thus, the prompt fission events will be detected by the TAC with high probability as high crystal multiplicity events.

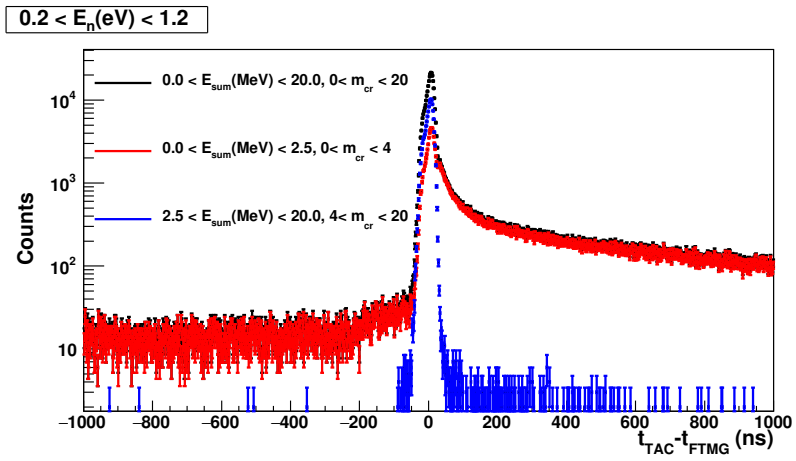

Figure 3.22: Time coincidence events distribution between the TAC and the FTMG detectors for different conditions applied to the TAC signals in the neutron energy range from 0.2 to 1.2 eV.

Fig. 3.22 shows coincidence time distribution between the TAC and the FTMG detectors. On the x-axis, the time difference t_{TAC}-t_{FTMG} is shown for different conditions applied to the TAC signals. The black histogram shows the distribution without any conditions applied. The distribution is explained as follows:

- For time differences t_{TAC}-t_{FTMG} <-300 ns, there is a flat distribution corresponding with random coincidences. It can be appreciated that all the events detected by the TAC in this time period have low m_{cr} and low E_{sum}, i.e non-fission events.
- For time differences in the range -300<t_{TAC}-t_{FTMG} <-50, there is an exponential distribution explained by the existence of (n,γ f) process (fission isomers) in the fissile nuclei [97]. This process will be discussed later in the section 3.3.1.
- For time differences in the range -50<t_{TAC}-t_{FTMG} <30, the events correspond with the prompt fission background as suggested by the characteristic of the events, large E_{sum} and m_{cr}.
- For time differences t_{TAC}-t_{FTMG} >30 ns, the exponential tail of the distribution corresponds with the detection of prompt fission neutrons, after being moderated by the neutron absorber, and the γ-rays from the decay of the fission products.

3.3.1 The coincidence time window and the event selection

Due to the time resolution of both detection systems, there is an optimum coincidence time window between the TAC and the FTMG detectors. This has been calculated based on TAC events with large multiplicity, m_{cr} >5, as shown in the left hand panel of Fig. 3.23. These events, called plausible fission events, follow the physical properties of the prompt fission γ-ray cascades suggested in other works [23, 32, 92]. The

optimum coincidence time window is chosen based on two opposite criteria: the maximization of prompt-fission γ-ray cascades tagged as fission events included in the coincidence time window, requirement for the correct determination of the fission detection efficiency (section 3.5), and the minimization of the random coincidences with other background sources and (n,γ) events.

The optimum has been calculated by the integration of the coincidence time distribution, shown in the right hand panel of Fig. 3.23 [1] For a time window of 80 ns, (-50,30) ns, it covers more than 99% of the distribution. Thus, it seems reasonable to use this time window for the coincidences between both detection systems.

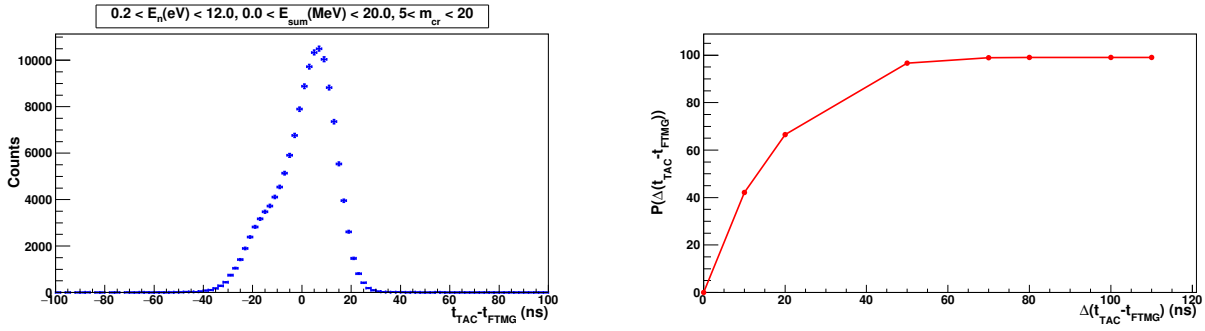

Figure 3.23: In the left hand panel is shown coincidence TAC-FTMG time distribution for events with crystal multiplicity larger than 5. In the right hand panel, the integral of the same distribution as a function of integration time.

Selecting more than one TAC event as prompt fission event per fission detected in the FTMG detectors leads inevitably to a mismatch in the subtraction of the background. For this reason, if two or more TAC events are detected within the time coincidence window, the TAC event with the largest crystal multiplicity is chosen as the prompt fission event. If both events have the same crystal multiplicity, then the fission event is selected as the TAC event with the shortest $\Delta(t_{FTMG}\text{-}t_{TAC})$. Fig. 3.24 shows the performance of this criteria. By the use of this criteria, the events from the neutron capture in the neutron absorber (470 keV signals) are avoided, giving a clean, prompt fission spectra.

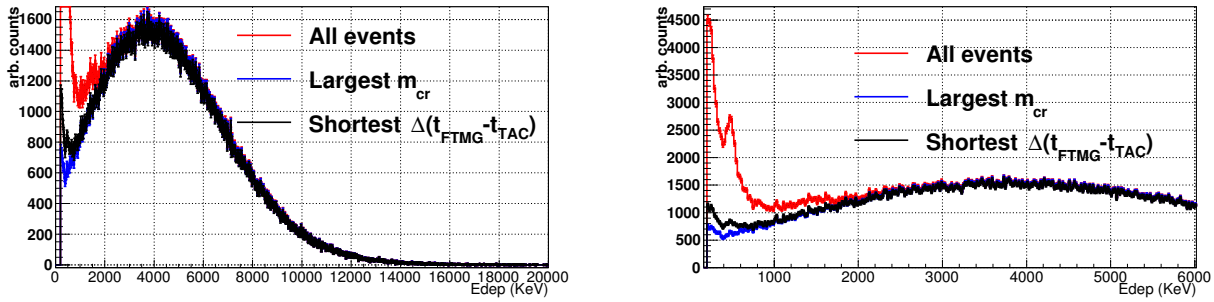

Figure 3.24: Tagged prompt fission deposited energy spectra taking into account all the events in the coincidence time window, the events with the large crystal multiplicity and with the shortest $\Delta(t_{FTMG}\text{-}t_{TAC})$.

[1] The limits of the time distribution are [5.0,-5.0], [10,-10], [+20,-30], [+30,-40], [+30,-50], [+30,-70], [+40,-70] (ns).

The (n,γ f) process and the random coincidences

As has been recently suggested by Patrick Talou *et al.* [96], the (n,γ f) process [97, 98] could be important in the Actinides region for low neutron energy resonances. This process corresponds with the decay of the fission isomers (see section 1.2.3). After the formation of the compound nucleus by the neutron-induced reaction, the configuration of the compound nucleus (deformation) can be situated either in the first, second or even third minimum of the fission barrier [99], thus fissioning or decaying to the first minimum by tunnel effect [49], emitting a γ-ray cascade in the decay path to the ground state (Fig. 1.6). Since the tunnel effect is not instantaneous, by construction this metastable state has a half-life that depends on the excitation energy of the minimum and height and width of the fission barrier. Fig. 3.22 and Fig. 3.25 show an exponential tail corresponding with γ-ray events detected before the fission is detected by the FTMG detectors. In 1965, V. Stavinsky *et als.* suggested in [97] that for the fissile isotopes, ^{233}U, ^{235}U and ^{239}Pu, the comparable average values of radiation width, $\bar{\Gamma}_\gamma$, fission width , $\bar{\Gamma}_f$, and the low $\bar{\Gamma}_n$ in the neutron resonances leads to an appreciable probability of fission after preliminary emission of a γ-ray. Therefore, it leads to an appreciable population of one or various fission isomers (section 1.2.3). The exponential tail observed in the coincidence distribution agree with the characteristics of this process.

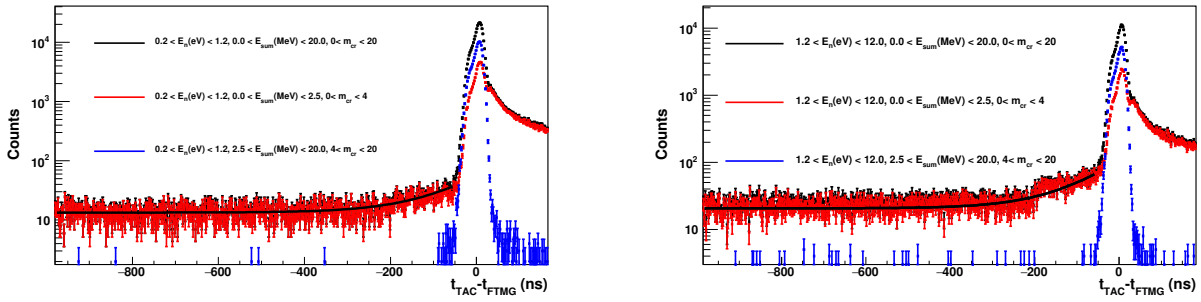

Figure 3.25: Fit performed on the coincidence distribution to the function described in Eq. 3.7. In the left hand panel, for the neutron energy period from 0.2 to 1.2 eV. In the right hand panel, for the neutron energy period from 0.2 to 1.2 eV.

The coincidence distribution has been fitted from -1μs to -50 ns, avoiding the prompt fission events, to the following functional form:

$$f(t) = a_0 + a_1 e^{a_2 t} \tag{3.7}$$

where a_0, a_1 and a_2 are the parameters that describe the random coincidences, the amount of (n,γf) counts present in the coincidence spectra and the half-life of the isomer respectively. The fit has been performed for two different neutron energy periods: from 0.2 to 1.2 eV where the first neutron resonance is located; and from 1.2 to 12 eV where the largest neutron resonances are placed. The fits are shown in both panels of Fig. 3.25. The results are shown in the table 3.8, where the uncertainties are only the statistical contribution.

The values obtained were used for the estimation of the isomer half-life $T_{1/2}$, the ratio between (n,γf), (n,f) events and the total number of random coincidences. Table 3.9 shows the values of the two first quantities.

The values of half-life obtained from this calculation in both neutron energy periods are compatible. The probability of the (n, γf) process is around 0.1% in respect to the (n,f) process. The (n,γf) ratio is different from one resonance to another. In particular, a lower value is expected in the first resonance due to the lower (n,γ)/(n,f) ratio [97].

E_n(eV)	a_0 (counts)	a_1 (counts)	$a_2(\cdot 10^{-2})$ (ns^{-1})
0.2 – 1.2	13.4±0.3	3.7±0.1	1.02±0.09
1.2 – 12.0	20.6±0.3	4.4±0.6	1.05±0.06

Table 3.8: Values of the fitted parameters for the different neutron energy periods. The uncertainties are only the statistical contribution.

E_n(eV)	$T_{1/2}$ (ns)	(n,γf)/(n,f) (%)
0.2 – 1.2	68±6	0.12±0.01
1.2 – 12.0	66±3	0.28±0.04

Table 3.9: Values calculated for the half life of the fission isomer and the ratio between (n,γf) and (n,f) counts in the TAC-FTMG coincidence time window. The uncertainty shown is only the statistical contribution.

The (n,γf) process will not present any problem for the analysis, taking into account that it represents 0.1% of the fission and the conditions applied to the TAC for (n,γ) as explained in the section 4.1. The values of the random coincidences obtained from this calculation, i.e, a_0, are in agreement with it as expected from the counting rate detected by the TAC in neutron energy range from 0.2 to 200 eV (0.1-0.3)c/μs as shown in Fig. 3.26.

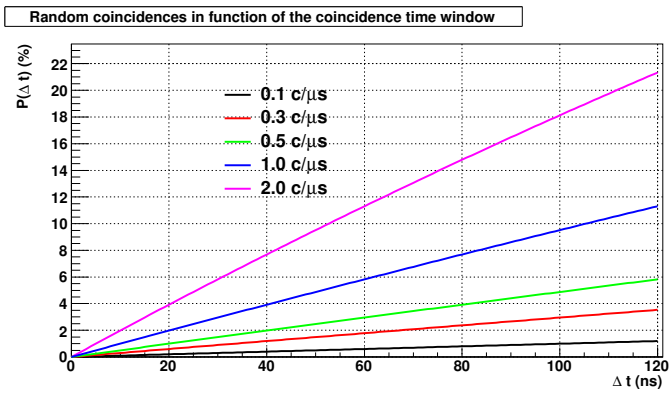

Figure 3.26: Probability of random coincidences for a given counting rate as a function of the coincidence time window.

3.4 Background subtraction in the ^{235}U(n,γ) cross-section measurement

The background, $c_{bkg}(E_n)$ present in the measurement is the sum of multiple contributions described as follows:

- No beam background (c_{Nobeam}): background related to the internal radioactive decay of the BaF_2 crystals, environmental background and natural radioactive decay from the ^{235}U samples. This component is obtained from dedicated measurements without neutron beam, retaining the same experimental setup.
- Beam background not related to the ^{235}U samples (c_{Beam}): the interaction of the neutron beam with the dead material layers of the fission chamber produces background events detected by the TAC. The component is obtained from the dedicated measurements replacing the ^{235}U targets with dummy samples with the same experimental setup.
- Prompt fission background (c_{Fiss}): during the neutron-induced fission process, prompt γ-ray cascades and neutrons are emitted from the highly excited fission fragments and detected by the TAC during the first nanoseconds. This component is obtained from the coincidences between the TAC and the FTMG detectors [23, 32].
- Other components related to the ^{235}U targets different to c_{Fiss} (c_{Others}): background induced by the interaction of the neutron beam with the targets, i. e., elastic scattering on the ^{235}U targets, delayed detection of the prompt fission neutrons and γ-ray decay from the fission fragments. These components, which are somewhat smaller than the previous components, have been calculated using Monte Carlo simulations.

Thus, the background is written as a function of the components described below:

$$c_{bkg}(E_n) = c_{Nobeam}(E_n) + c_{Beam}(E_n) + c_{Fiss}(E_n) + c_{Others}(E_n) \tag{3.8}$$

In the following sections the analysis performed of the individual components for the background estimation will be described.

3.4.1 The no-beam background component

The background related to the internal radioactive decay of the BaF_2 crystals, environmental background and natural radioactive decay of the ^{235}U samples is obtained from the dedicated measurements without the neutron beam. As explained in [34, 76] the detected internal decay of the BaF_2 detectors is produced by the radioactive decay chain of the Ra isotopes, radiochemical contaminants in the production of the BaF_2 crystals. The γ-ray emissions after the natural α decay of the ^{235}U samples produce a very low number of detected signals compared to the internal background of the BaF_2 detectors as shown in Fig. 3.27.

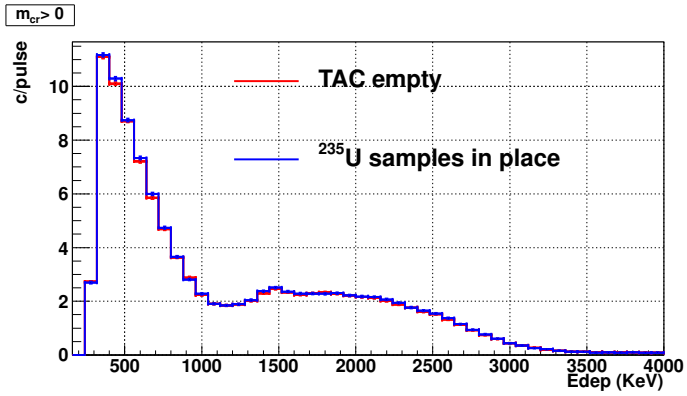

Figure 3.27: TAC deposited energy spectra measured during two dedicated configurations without the neutron beam, with the ^{235}U samples in place (blue line), and with the TAC empty (red line).

3.4.2 Beam background not related with the ^{235}U samples

The interaction of the neutron beam with the dead material that composes the fission chamber and the backing of the ^{235}U samples is measured directly by dedicated measurements, replacing the ^{235}U samples with dummy targets.

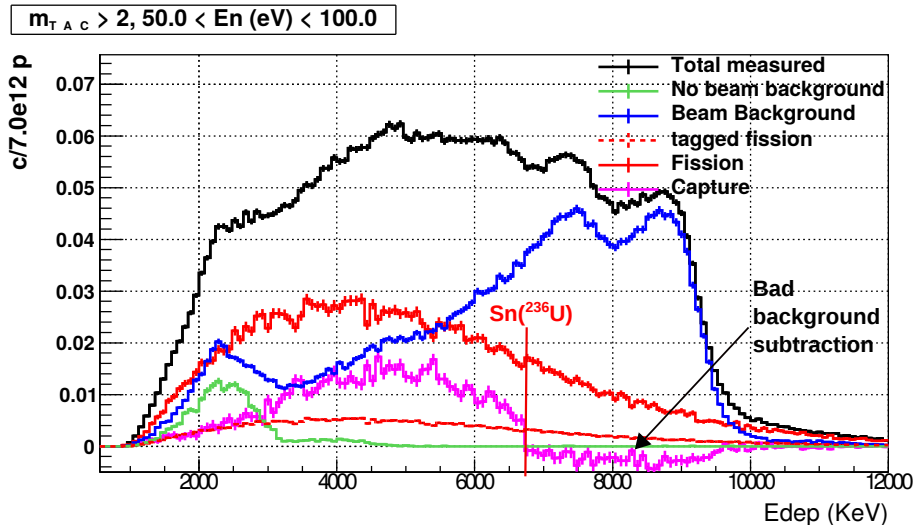

Figure 3.28: TAC Deposited energy spectra for m_{cr} >2 in the neutron energy range from 50 to 100 eV. The different components are shown by the different colored lines.

Despite the fact that, in principle, the calculation of this component is straightforward with the dedicated measurements, we noticed after the subtraction from the total spectrum of this component together with the fission background component, that negative counts appeared above the neutron separation energy of ^{236}U as shown in Fig. 3.28. Some hypotheses that could explain this effect are:

- The gas density inside the fission chamber fluctuates throughout the measurement as was shown by the effects observed in the FTMG detectors explained in the section 3.2. Therefore, a different

amount of material was present in the fission chamber at the time when the dedicated background configuration was measured.

- The neutron absorber was not entirely closed during the dedicated background configuration. Fig. 3.29 shows the counting rate of the individual BaF_2 detectors (E_γ >3 MeV) during the $^{235}U(n,\gamma)$ measurement (red) and during the dedicated background measurement (blue).

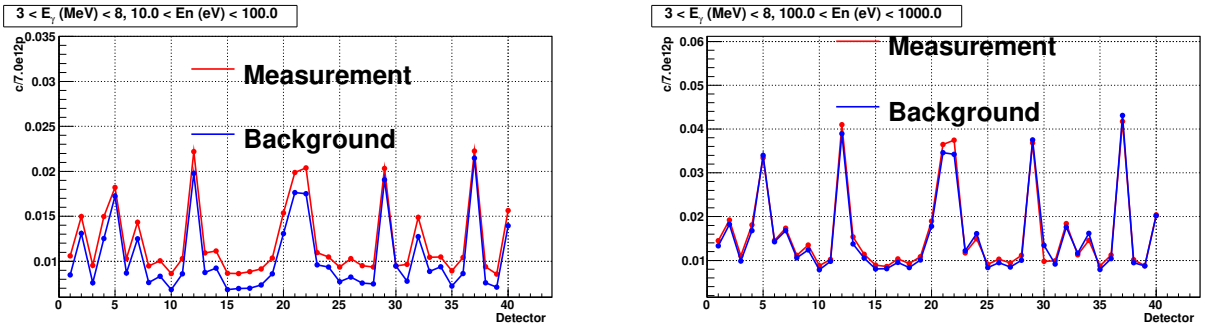

Figure 3.29: Counting rate of the BaF_2 detectors during different dedicated configurations. In the left hand panel, for 10<E_n(eV)<100 and in the right hand panel, for 100<E_n(eV)<1000.

As can be observed, the counting rate of some individual BaF_2 detectors was larger during the background measurement. These detectors are in the same geometrical plane, so one possibility could be that the neutron absorber, made of two semi-spheres, was not perfectly closed.

We have corrected the measured background using a factor which depends on the neutron energy and crystal multiplicity. This is based on the assumption that the deposited energy shape of the background with the ^{235}U targets in place is similar to the component obtained from the dedicated background measurement.

The scaling factor is calculated for a determined neutron energy period and crystal multiplicity condition by fitting the total deposited energy spectra with the ^{235}U samples in place, $C_t(E_n;E_{sum},m_{cr})$ above the ^{236}U neutron separation energy, E_{sum} >7 MeV, to two different components:

- The beam background $C_B(E_n;E_{sum},m_{cr})$: obtained from the background configuration measurement.
- The prompt fission component $C_f(E_n;E_{sum},m_{cr})$, that will be discussed in the section 3.4.3.

Thus, the fit performed on the total deposited energy is:

$$C_t(E_n;E_{sum},m_{cr}) = \alpha_B(E_n,m_{cr})C_B(E_n;E_{sum},m_{cr}) + \alpha_f C_f(E_n;E_{sum},m_{cr}) \quad (3.9)$$

where $\alpha_B(E_n,m_{cr})$ and α_f are the corresponding scaling factors for the beam background and prompt fission components. The prompt fission background will be examined in another section and no further correction is needed for this component. Thus, the value of α_f is fixed and the scaling factor $\alpha_B(E_n,m_{cr})$ calculated is the correction needed for this background component.

We have used three different methods for the determination of $\alpha_B(E_n,m_{cr})$: least squares (LS) [93], extended maximum likelihood (ELS) [94] and zero area method (ZA). The correction is then calculated as the average of the three fits and the uncertainty has been estimated as the difference between the maximum and minimum value obtained, divided by two. In the resultant background it has been ascertained that:

- The total deposited energy detected by the TAC is well reproduced as shown by the green line in the left hand panel of Fig. 3.30.

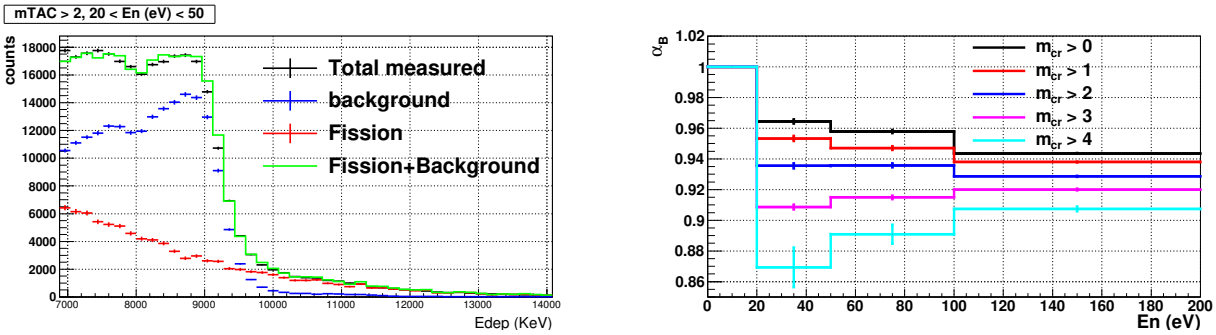

Figure 3.30: In the left hand panel is the fit performed on the total deposited energy for m_{cr} >2 in the neutron energy range from 20 to 50 eV. In the right hand panel are values obtained for $\alpha_B(E_n, m_{cr})$ as a function of the neutron energy and crystal multiplicity.

- The deposited energy shape of the capture signal is reasonably reproduced after the modification of the background, as shown in both panels of Fig. 3.31. The black solid line is the reference ^{236}U(n,γ) signature taken from the low energy resonances and the pink histogram the ^{235}U(n,γ) signature after the correction. The solid and dashed blue lines are the beam background components before and after the modification, respectively.

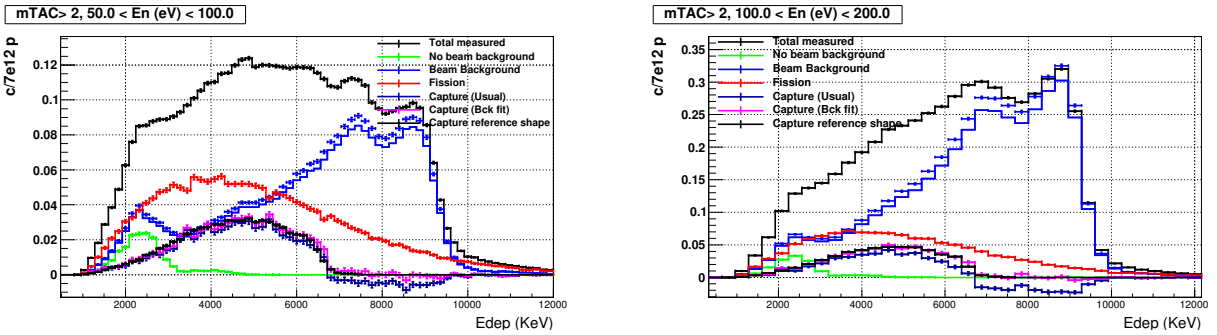

Figure 3.31: Examples of the fit performed on the total deposited above the $S_n(^{236}U)$ for m_{cr} >2. In the left hand panel, for 50<E_n(eV)<100. In the right hand panel, for 100<E_n(eV)<200.

The correction as a function of the neutron energy for different conditions applied to m_{cr} is shown in Fig 3.30. For neutron energies below 20 eV, non correction is needed. Therefore, the correction has been applied in the neutron energy range from 20 eV to 200 eV.

The corrected deposited energy spectras measured for the TAC for different conditions are shown in the appendix A.

The impact of this correction is considerable when the neutron capture cross-section is integrated in large neutron energy periods due to the valleys between resonances. However, it is very small when a resonance analysis of the experimental data is performed.

3.4.3 The prompt fission background component

The prompt fission background component, $c_{Fiss}(E_n;E_{sum},m_{cr})$, is determined as was explained 1.3 by the coincidences between the TAC and the FTMG detectors [23, 32], $c_{tagg}(E_n;E_{sum},m_{cr})$, divided by a factor labelled as fission tagging detection efficiency, ε_f^*. Thus:

$$c_{Fiss}(E_n;E_{sum},m_{cr}) = \frac{1}{\varepsilon_f^*} c_{tagg}(E_n;E_{sum},m_{cr}) \tag{3.10}$$

As was demonstrated by C. Guerrero *et als.* in [23], the fission tagging detection efficiency, ε_f^*, is the FTMG fission detection efficiency, ε_f, under the condition that the probability of detecting a fission reaction in one of the detectors does not depend on whether it has been detected in the other detector. However, for this experimental setup this is not entirely true, due to finding a small degree of correlation between the TAC and the FTMG detector systems as will be shown in section 3.5.

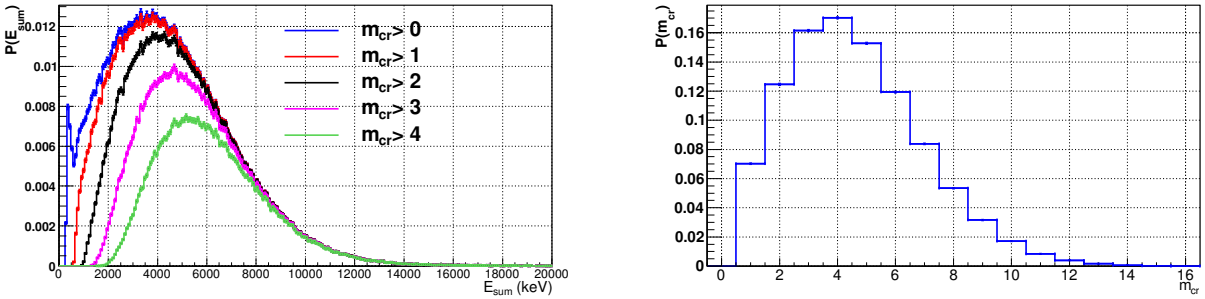

Figure 3.32: In the left hand panel is the deposited energy signature of the tagged prompt fission γ-ray cascades detected for different crystal multiplicity conditions. In the right hand panel is the crystal multiplicity distribution signature of the tagged prompt fission γ-ray cascades.

Fig 3.32 is the projections of the tagged prompt fission events in the TAC: In the left hand panel is shown the detected deposited energy signature, E_{sum}, as a function of the crystal multiplicity, m_{cr}. In the right hand panel of the same figure is shown the crystal multiplicity distribution. The average deposited energy of these cascades is shown in the table 3.10. As was expected, these events are characterized by large energy deposition on the TAC and large crystal multiplicity.

m_{cr} >	<E_{sum}(MeV)>	m_{cr} >	<E_{sum}(MeV)>
0	4.51	5	6.84
1	4.77	6	7.48
2	5.17	7	8.14
3	5.66	8	8.81
4	6.23	9	9.49

Table 3.10: Average deposited energy of the tagged prompt fission γ-rays cascades for different crystal multiplicity conditions.

3.4.4 Other background components related to the ^{235}U targets

The other small backgrounds related to the ^{235}U targets such as the prompt fission neutrons, the neutron elastic scattering and the γ-ray decay from the fission products has been calculated by Monte Carlo simulations using the GEANT4 toolkit with the thermal libraries for neutrons [90, 91], and the detailed model of the TAC [34, 76, 104], with the addition of the fission chamber and the FTMG detectors.

Neutron sensitivity and the background induced by the elastic scattering on the ^{235}U targets

The neutron sensitivity, ε_n, is defined as the probability of detecting a scattered neutron with kinetic energy E_n by the TAC. This quantity depends on the analysis conditions applied to the variables, E_{sum} and m_{cr}. For the TAC response, neutrons of different kinetic energies, emitted from the ^{235}U samples positions, were simulated[2]. The data reconstruction performed is analogous to the process carried out for the experimental data [34]. Fig. 3.33 shows the result as a function of m_{cr} for 2.5<E_{sum}(MeV)<6.5, conditions applied for the calculation of the ^{235}U(n,γ) cross section.

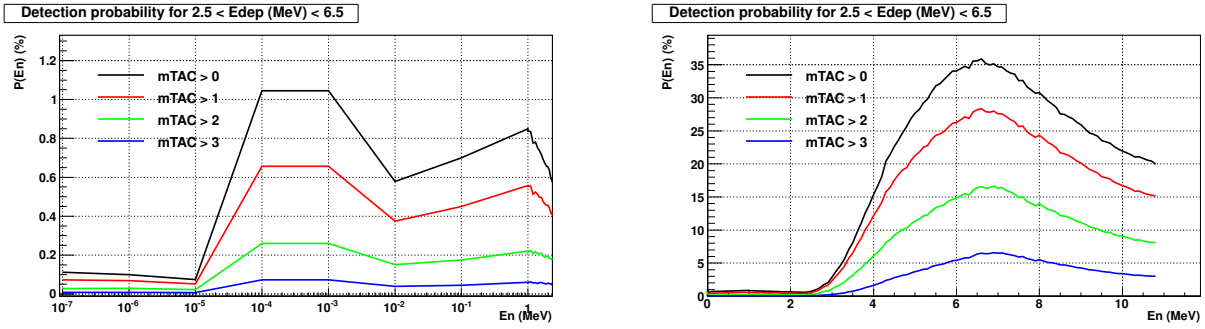

Figure 3.33: Neutron sensitivity,$\varepsilon_s(E_n;E_{sum},m_{cr})$, as a function of the neutron energy and crystal multiplicity for events with 2.5<E_{sum}(MeV)<6.5. In the left hand panel, for 0.1<E_n(eV)<10^6. In the right hand panel, for E_n >1 MeV.

To account for this background component, the following quantity has been determined:

$$R(E_n; E_{sum}, m_{cr}) = \frac{\varepsilon_n(E_n; E_{sum}, m_{cr})\sigma_n(E_n)}{\varepsilon_\gamma(E_n; E_{sum}, m_{cr})\sigma_\gamma(E_n)} \tag{3.11}$$

where σ_n(E$_n$), σ_γ(E$_n$), ε_n(E$_n$;E$_{sum}$,m$_{cr}$) and ε_γ(E$_n$;E$_{sum}$,m$_{cr}$) are the neutron elastic cross-section, (n,γ) cross-section, the TAC neutron sensitivity, and the (n,γ) TAC detection efficiency respectively. This ratio compares the background detected due to the neutron scattering in the samples with the expected number of (n,γ) reactions detected.

In Fig. 3.34 R(E$_n$;E$_{sum}$,m$_{cr}$) is shown, as a function of the neutron energy, for different conditions applied to the crystal multiplicity and for deposited energies in the range 2.5<E_{sum}(MeV)<6.5. The calculation has been performed in the neutron energy period of interest, from 0.2 to 200 eV. The peaks observed in the figure correspond with the valleys of the resonances as long as the region of low R with the neutron capture resonances regions.

The contribution of this background is strongly suppressed for m$_{cr}$ >2. It is larger (6% at most) for the valleys of the neutron resonances where the (n,γ) cross-section drops to close to zero. This component,

[2]The specific neutron kinetic energies are: 0.1 eV, 1 eV, 10 eV, 100 eV, 1000 eV, 100000 eV, and every 0.1 MeV for neutron energies from 1 MeV up to 10 MeV.

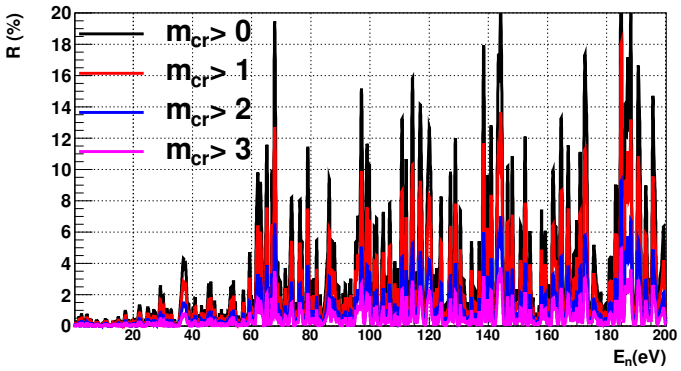

Figure 3.34: $R(E_n)$ as a function of the neutron energy and crystal multiplicity. The conditions applied to the E_{sum} for all the cases is 2.5< E_{sum}(MeV)<6.5

compared with the elastic scattering produced from the components of the fission chamber, is negligible. Thus, it will not be taken into account for the calculation.

Delayed background induced by the prompt-fission neutrons

As was explained in section 1.3 and shown in the section 3.3, the fission background is not entirely included in the fission tagging technique. The prompt fission neutrons can be detected even milliseconds after the fission occurs, thus producing the delayed fission background explained in the section 3.3.

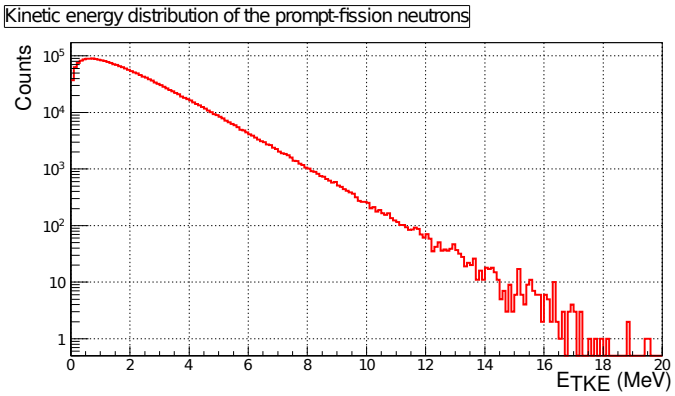

Figure 3.35: Kinetic energy distribution of the prompt fission neutrons released from the $^{235}U(n,f)$ at thermal energies. The distribution has been taken from ENDF/B-VII.1.

The average number of prompt fission neutrons released during the neutron-induced fission process, $\bar{\nu}$, and the kinetic energy distribution depends on the involved nuclei and slightly on the incident neutron kinetic energy. In the case of the ^{235}U and thermal kinetic neutron energies, the average number of neutrons released is $\bar{\nu}$=2.4 and their kinetic energy distribution is shown in Fig. 3.35.

The TAC response has been obtained by Monte Carlo simulations, performed as it was done in the previous section. The neutrons were emitted from the samples position randomly taking into account the spatial profile of the neutron beam, and their kinetic energies were selected following the kinetic energy

distribution of Fig. 3.35. The results reconstructed from the simulations are shown in both panels of Fig. 3.36. In the left hand panel is shown the deposited energy detected spectra for different detection times:

- For times below 20 ns (included in the prompt component), the signals detected by the TAC are mainly 470 KeV γ-rays emitted from the neutron capture reactions produced in the neutron absorber and 1435 KeV γ-rays emitted from the inelastic reactions produced in the BaF_2 crystals.
- In the long moderation tail, extended to hundreds of microseconds, the detected signals correspond with neutrons moderated and absorbed in the different parts of the TAC, mostly in the BaF_2 crystals deduced from the deposited energy distribution shown in the left hand panel of Fig. 3.36.

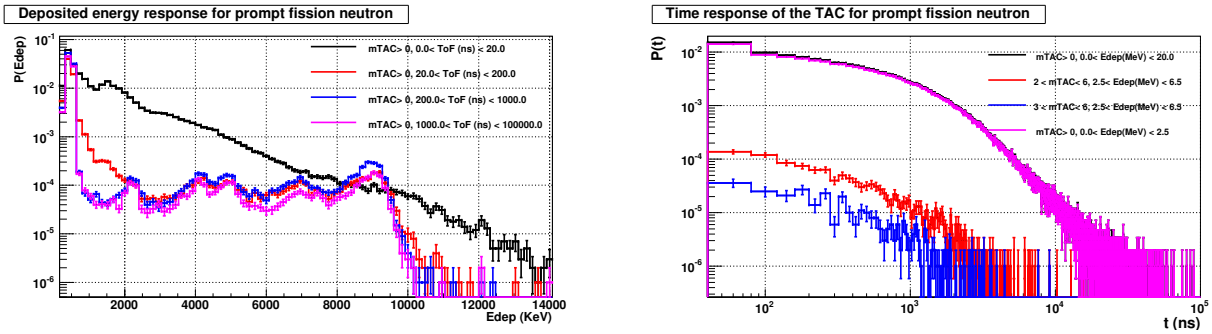

Figure 3.36: TAC response for the prompt fission neutrons obtained by Monte Carlo simulations. In the left hand panel is the TAC deposited energy response for different conditions applied to the detection time. In the right hand panel is the time response for different conditions applied to E_{sum} and m_{cr}.

The delayed fission background induced by the prompt fission neutrons for certain conditions applied to E_{sum} and m_{cr}, $C_{delayed}(E_n;E_{sum},m_{cr})$, is then calculated as a function of the neutron energy, by the convolution of the TAC time response shown in the right hand panel of Fig. 3.36, $P_{prompt-n}(t;E_{sum},m_{cr})$, with the total number of fissions occurring for a determined neutron energy E_n. The last quantity is calculated as the ratio between the fission detected by the FTMG detectors, $C_{FTMG}(E_n)$ and the fission detection efficiency, ε_f, calculated in the section 3.5. In the calculation we assume that coincident detection of two or more neutrons is extremely rare.

Therefore, the delayed fission is calculated as:

$$C_{delayed}(E_n;E_{sum},m_{cr}) = \frac{\bar{\nu}}{\varepsilon_f} C_{FTMG}(E_n) \circ P_{prompt-n}(m_{cr},E_{sum},t>20ns) \tag{3.12}$$

In the right hand panel of Fig. 3.36 the timing response for different crystal multiplicity and deposited energy conditions applied to the TAC is shown. This timing response goes up to miliseconds after the emission of the prompt-fission neutrons due to the large moderation times.

The delayed fission background is compared with the other background sources for the conditions applied to the (n,γ) cross-section calculation in Fig. 3.37 as the light green line. The correction due to this background source represent ~1-2 % of the prompt fission background.

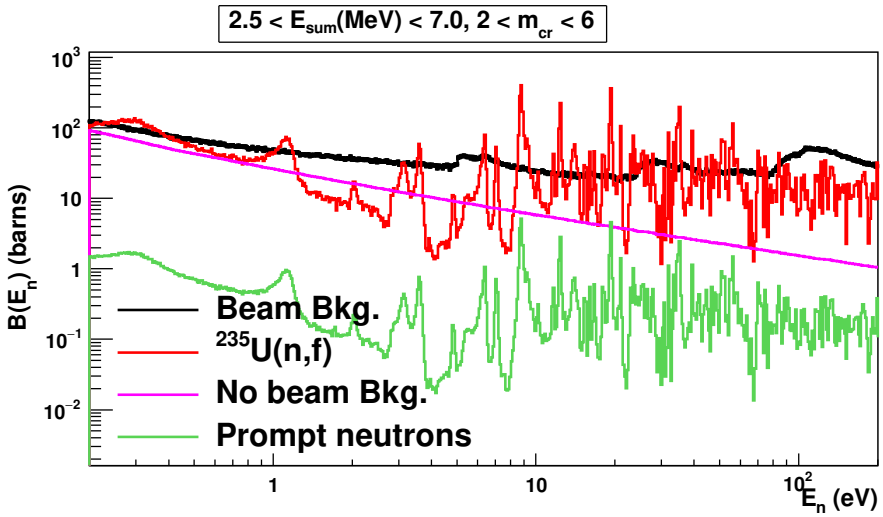

Figure 3.37: Delayed fission background for the (n,γ) analysis conditions compared with the other background sources in the neutron energy range from 0.2 to 200 eV.

Delay γ-rays emitted from the decay of the fission fragments

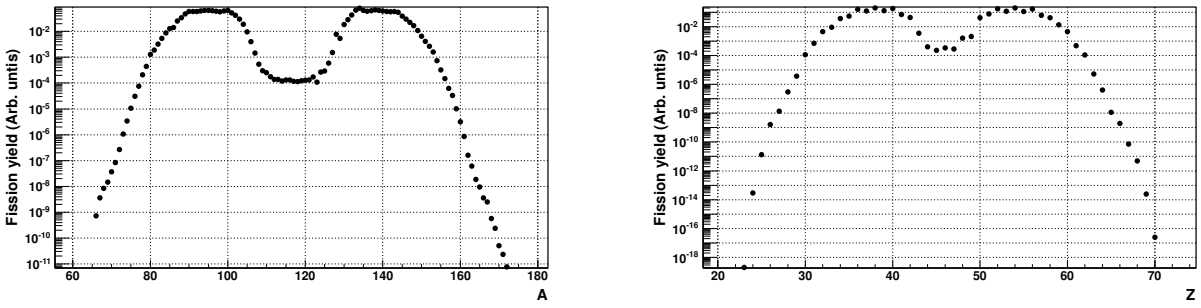

Figure 3.38: Projections of the 2D Mass/Charge distribution of the fission yields produced at thermal energies taken from ENDF/B-VII.1. In the left panel, mass distribution, A. In the right panel, atomic number distribution, Z.

The delayed γ-ray emitted from the decay of the fission fragments has been simulated using the GEANT4 toolkit [90, 91]. The fission products were produced randomly according to the two-dimensional distribution of mass and atomic number from the ENDF/B-VII.1 yields. The projections of this distribution are shown in both panels of Fig. 3.38. The decay of the fission products was simulated using the specific decay function of the GEANT4 toolkit. For the estimation of this component, only the events in the first 10 millisecond after the generation were taken into account. After the reconstruction of the events the conclusion was that this contribution can be neglected, due to the low amount of events registered in the first 10 milliseconds.

3.5 The fission detection efficiency and the fission tagging detection efficiency

The fission detection efficiency and the fission tagging detection efficiency are closed related quantities. We consider that both quantities do not depend on the neutron energy as was shown in the section 3.2.4. Their definitions are given by:

- **The fission detection efficiency**, $\varepsilon_f(\mathrm{A}_{th})$: this is the probability of detecting a fission reaction induced in any of the ten ^{235}U samples by the FTMG detectors. This quantity depends only on the amplitude threshold applied to the FTMG events, A_{th}.
- **The fission tagging detection efficiency**, $\varepsilon_f^*(\mathrm{A}_{th},\mathrm{E}_{sum},\mathrm{m}_{cr})$: this is the factor needed to rescale the tagged fissions for the prompt fission background subtraction. This factor, by definition, is the ratio between the tagged fission counts, $\mathrm{c}_{Tagg}(\mathrm{A}_{th},\mathrm{E}_{sum},\mathrm{m}_{cr})$, and the total fission counts detected by the TAC, $\mathrm{c}_{Fiss\_TAC}(\mathrm{E}_{sum},\mathrm{m}_{cr})$:

$$\varepsilon_f^*(A_{th},E_{sum},m_{cr}) = \frac{c_{Tagg}(A_{th},E_{sum},m_{cr})}{c_{Fiss\_TAC}(E_{sum},m_{cr})} \tag{3.13}$$

In the case that the probability of detecting a fission reaction in one of the detectors does not depend on whether it has been detected in the other detector [23], then:

1. The fission tagging detection efficiency, $\varepsilon_f^*(\mathrm{A}_{th})$, and the fission detection efficiency, $\varepsilon_f(\mathrm{A}_{th})$, are the same quantity. In addition, if the samples are well characterized, the individual FTMG detection efficiencies can be determined as is explained in the appendix B.
2. As a consequence of 1., the fission tagging detection efficiency depends only on A_{th}:

$$\varepsilon_f^*(A_{th},E_{sum},m_{cr}) = \varepsilon_f^*(A_{th}) \tag{3.14}$$

The condition 1 is easily proven: on the one hand, the fissions detected by the TAC, $\mathrm{c}_{Fiss\_TAC}(\mathrm{E}_{sum},\mathrm{m}_{cr})$, are expressed as a function of the TAC fission detection efficiency, $\varepsilon_{f\gamma}(\mathrm{E}_{sum},\mathrm{m}_{cr})$, and the total number of fission reactions occurring, N_{fiss}:

$$c_{Fiss\_TAC}(E_{sum},m_{cr}) = \varepsilon_{f\gamma}(E_{sum},m_{cr})N_{fiss} \tag{3.15}$$

On the other hand, the tagged fission counts, $\mathrm{c}_{Tagg}(\mathrm{A}_{th},\mathrm{E}_{sum},\mathrm{m}_{cr})$, are written as a function of the fission detection efficiency, $\varepsilon_f(\mathrm{A}_{th})$, the TAC fission detection efficiency $\varepsilon_{f\gamma}(\mathrm{E}_{sum},\mathrm{m}_{cr})$, and the total number of fission reactions occurring, N_{fiss},

$$c_{Tagg}(A_{th},E_{sum},m_{cr}) = \varepsilon_f(A_{th})\varepsilon_{f\gamma}(E_{sum},m_{cr})N_{fiss} \tag{3.16}$$

Thus, dividing both quantities the relationship is demonstrated:

$$\varepsilon_f^*(A_{th}) = \frac{c_{Tagg}(A_{th},E_{sum},m_{cr})}{c_{Fiss\_TAC}(E_{sum},m_{cr})} = \frac{\varepsilon_f(A_{th})\varepsilon_{f\gamma}(E_{sum},m_{cr})N_{fiss}}{\varepsilon_{f\gamma}(E_{sum},m_{cr})N_{fiss}} = \varepsilon_f(A_{th}) \tag{3.17}$$

If the probability of detecting a fission reaction in one of the detectors depends on whether it has been detected in the other detector, then the relation 3.16 is not fulfilled and thus, in general, $\varepsilon_f^* \neq \varepsilon_f$. In the case of this measurement, the assumption of independence detecting (n,f) events is almost fulfilled, but not strictly. We have calculated $\varepsilon_f^*(=\varepsilon_f)$ first ignoring any correlation between both detectors in the detection of (n,f) events, and then some corrections of the obtained results have been applied.

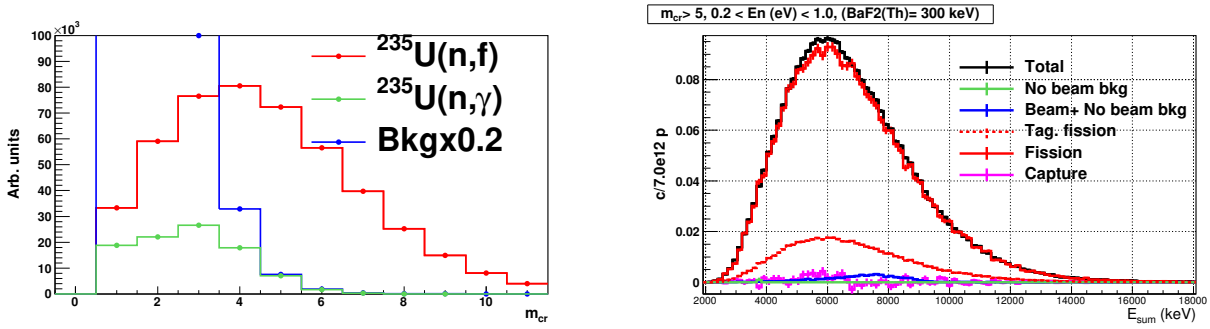

Figure 3.39: In the left hand panel, m_{cr} distribution for the different components detected by the TAC. In the right hand panel, deposited energy spectra detected by the TAC for m_{cr} >5 in the neutron energy range from 0.2 to 1.0 eV.

The methodology used for the calculation of these two quantities, which is more precise than the Monte Carlo simulations, has been applied to the first large neutron fission resonances, in the neutron energy period from 0.2 to 20 eV. It is based on the equation 5.3:

- The prompt tagged fission events are obtained by the coincidence of the TAC and FTMG as was explained in the section 3.3.
- The TAC detects many background components besides the ^{235}U(n,γ) reactions as was discussed in section 3.4. However, the number of components can be reduced to the prompt fission component and the background related to the dead material intercepting the neutron beam, selecting events with large crystal multiplicity, m_{cr} >5, and large total deposited energy, E_{sum} >S_n(^{236}U). For these conditions, the ^{235}U(n,γ) reactions and the background related to the no-beam background are removed from the analysis as is shown in both panels of Fig. 3.39. In addition, the contribution of the prompt fission neutrons is negligible as was shown in Fig. 3.36. Nevertheless, it has been experimantally checked that ε_f^* only changes as a function of A_{th} as is shown in Fig. 3.40 and tables 3.11 and 3.12.

  As more restrictions are applied to the TAC events, more sensitive is the calculation to systematic uncertainties such as the determination of the background as is shown in both panels of Fig. 3.40. However, the statistical uncertainty increases. Thus, the calculation must be performed with attention paid to the compromise between the systematic and statistical uncertainties.

For those conditions, the total fission events detected by the TAC are obtained by the difference between the total number of counts detected, $c_T(E_{sum},m_{cr})$, and the background related to the dead material intercepting the neutron beam obtained from the dedicated experimental measurement, $c_B(E_{sum},m_{cr})$. Then:

$$c_{Fiss\_TAC}(E_{sum},m_{cr}) = c_T(E_{sum},m_{cr}) - c_B(E_{sum},m_{cr}) \tag{3.18}$$

For the calculation of the ε_f^* statistical uncertainty, we have to take into account the correlation between $c_T(E_{sum},m_{cr})$ and $c_{Tagg}(A_{th},E_{sum},m_{cr})$: $c_T(E_{sum},m_{cr})$=$c_{Tagg}(A_{th},E_{sum},m_{cr})$+$c_{noTagg}(A_{th},E_{sum},m_{cr})$, where c_{noTagg} is the number of non-tagged events. Thus, the statistical uncertainty for ε_f^* parameter is given by:

$$\boxed{\Delta(\varepsilon_f^*) = \Delta(\varepsilon_f) = \frac{\sqrt{c_{tagg}}}{(c_T - c_B)^2}\sqrt{(c_T - c_{tagg} - c_B)^2 + c_{tagg}(c_T + c_{tagg} + c_B)}} \tag{3.19}$$

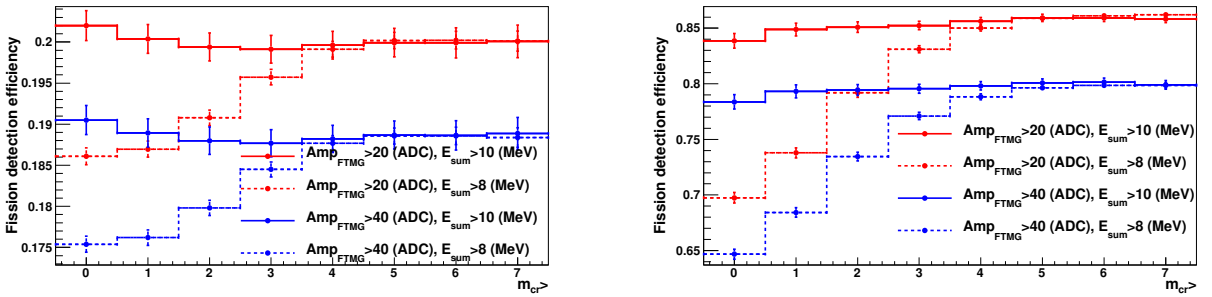

Figure 3.40: Fission detection efficiency as a function of m_{cr} and different amplitude thresholds applied to Amp_{FTMG}, in the left hand panel for the 2FTMG experimental configuration and in the right hand panel, for the 10FTMG experimental configuration.

3.5.1 Results for the 2FTMG experimental configuration

The fission tagging detection efficiency has been calculated for the 2FTMG experimental configuration as was explained in the previous section, in the first largest neutron fission resonances, from 0.2 to 20 eV. For the calculation, the TAC events were restricted to events with m_{cr} >5 and E_{sum} >10 MeV. For the FTMG detector, the threshold applied was A_{th}=40 ADC channels. The values obtained in the different neutron resonances are shown in the left hand panel of Fig. 3.41 by the black points. The value obtained for other conditions of the TAC and FTMG signals are shown in the table 3.11 and in the left hand panel of Fig. 3.40.

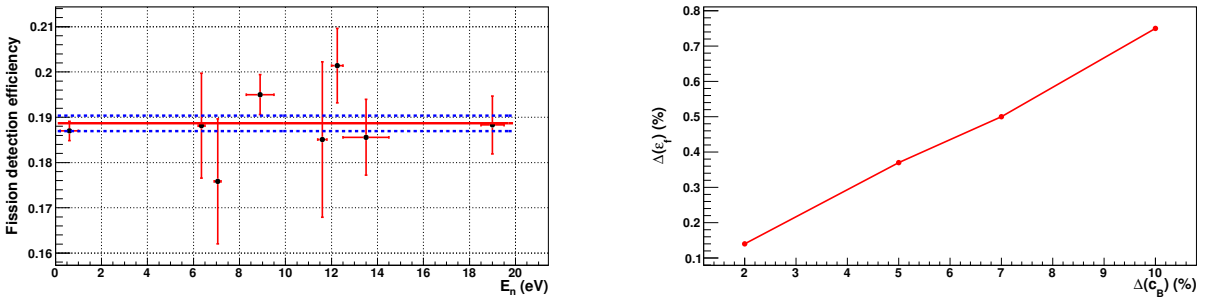

Figure 3.41: In the left hand panel, $\varepsilon_f^*(A_{th}=40)$ calculated in the different neutron resonances for the 2FTMG experimental configuration and in the right hand panel, variation of the fission detection efficiency as a function of the background variation.

The value of ε_f^* was calculated as the weighted average of the values obtained from the different neutron resonances. The value is shown in the left hand panel of Fig.3.41 by the solid red line and the statistical uncertainty by the dashed blue lines. The fission tagging detection efficiency for this experimental configuration is:

$$\varepsilon_f^*(A_{th}=40) = 0.1887(15)(3) \tag{3.20}$$

where the first uncertainty is the statistical component and the second one is the systematic uncertainty

due to the beam background subtraction. We estimated the latter by propagating a 2% uncertainty in the determination of the beam background.

Note that ε_f^* should vary only with Amp_{FTMG} as shown in the table 3.11.

E_n(eV)	$\varepsilon_f^*(1)$	$\varepsilon_f^*(2)$	$\varepsilon_f^*(3)$	$\varepsilon_f^*(4)$
0.2 – 1	0.1994(12)	0.1990(22)	0.1877(12)	0.1869(21)
6.2 – 6.5	0.206(7)	0.198(12)	0.197(7)	0.188(11)
6.9 – 7.2	0.190(8)	0.184(1)	0.181(8)	0.175(14)
8.3 – 9.5	0.2011(25)	0.205(5)	0.190(3)	0.195(4)
11.4 – 11.8	0.200(10)	0.192(17)	0.195(10)	0.185(17)
12.0 – 12.5	0.210(5)	0.209(8)	0.201(5)	0.201(8)
12.5 – 14.5	0.200(5)	0.196(9)	0.187(5)	0.185(8)
18.5 – 19.5	0.199(3)	0.198(6)	0.185(4)	0.188(6)

Table 3.11: ε_f^* calculated for for 2FTMG experimental configuration applying conditions applied to the TAC and FTMG signals: (1) Amp_{FTMG} >20,m_{cr} >5,E_{sum} >8MeV;(2) Amp_{FTMG} >20,m_{cr} >5,E_{sum} >10MeV;(3) Amp_{FTMG} >40,m_{cr} >5,E_{sum} >8MeV; (4) Amp_{FTMG} >40,m_{cr} >5,E_{sum} >10MeV.

3.5.2 Results for the 10FTMG experimental configuration

The fission tagging detection efficiency for the 10FTMG experimental configuration was calculated following the same procedure as in the case of the 2FTMG experimental configuration. The conditions applied to the TAC were the same; meanwhile, the amplitude threshold of the FTMG detectors in this configuration is A_{th} =20. In the left hand panel of Fig. 3.42 are shown the values obtained for the different neutron fission resonances in the neutron range from 0.2 to 20 eV for the specific conditions for the calculation of ε_f^*. The value for other conditions applied to the TAC and FTMG signals are shown in the table 3.12 and in the right hand panel of Fig. 3.40.

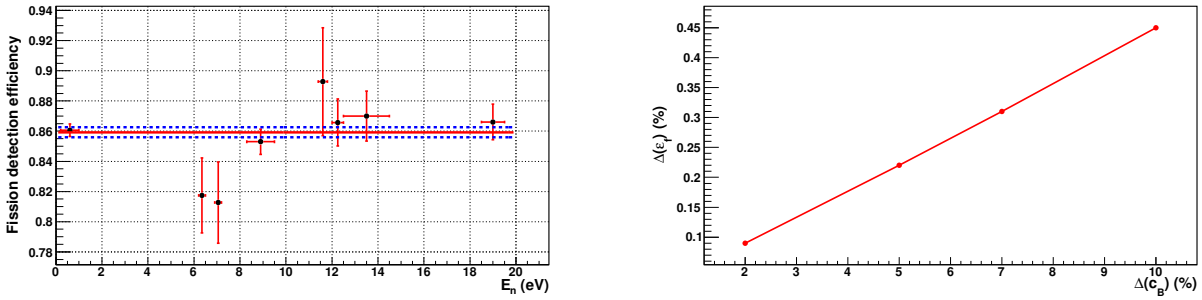

Figure 3.42: In the left hand panel, ε_f^* calculated in the different neutron resonances for the 10FTMG experimental configuration. In the right hand panel, variation of the fission detection efficiency as a function of the background variation.

The value of ε_f^* was calculated as the weighted average of the values obtained in the different resonances. It is shown in the left hand panel of Fig. 3.42 by the solid red line and the statistical uncertainty by the dashed blue lines. The value obtained for this experimental configuration is:

$$\varepsilon_f^*(A_{th} = 20) = 0.859(3)(1) \tag{3.21}$$

where the first uncertainty is the statistical component and the second one is the systematic uncertainty due to the beam background subtraction. We estimated the latter by propagating a 2% uncertainty in the determination of the beam background.

Note that ε_f^*, as in the case of the 2FTMG, should vary only with Amp_{FTMG} as is shown in the table 3.12.

E_n(eV)	$\varepsilon_f^*(1)$	$\varepsilon_f^*(2)$	$\varepsilon_f^*(3)$	$\varepsilon_f^*(4)$
0.2 – 1	0.854(3)	0.861(4)	0.798(3)	0.799(4)
6.2 – 6.5	0.829(15)	0.82(2)	0.7535(17)	0.75(2)
6.9 – 7.2	0.81(2)	0.81(3)	0.74(2)	0.74(3)
8.3 – 9.5	0.860(5)	0.853(8)	0.791(5)	0.796(9)
11.4 – 11.8	0.87(2)	0.89(4)	0.81(3)	0.85(4)
12.0 – 12.5	0.865(1)	0.865(1)	0.81(1)	0.82(2)
12.5 – 14.5	0.85(1)	0.870(17)	0.79(1)	0.81(2)
18.5 – 19.5	0.862(8)	0.86(11)	0.807(8)	0.82(1)

Table 3.12: ε_f^* calculated for 10FTMG experimental configuration applying conditions applied to the TAC and FTMG signals: (1) Amp_{FTMG} >20,m_{cr} >5,E_{sum} >8MeV;(2) Amp_{FTMG} >20,m_{cr} >5,E_{sum} >10MeV;(3) Amp_{FTMG} >40,m_{cr} >5,E_{sum} >8MeV; (4) Amp_{FTMG} >40,m_{cr} >5,E_{sum} >10MeV.

3.5.3 Correlation detecting the (n,f) events between the TAC and the FTMG detectors

In the previous sections (section 3.5.1 and section 3.5.2), ε_f^* and ε_f have been calculated under the hypothesis that the probability of detecting a fission reaction by one of the detectors does not depend on whether it has been detected by the other detector [23]. However, due to the complexity of this process, most of the observables are correlated. For instance, the average number of prompt fission neutrons and γ-rays emitted are closely related quantities with the pair of fission fragments produced and the primary nuclei involved [100].

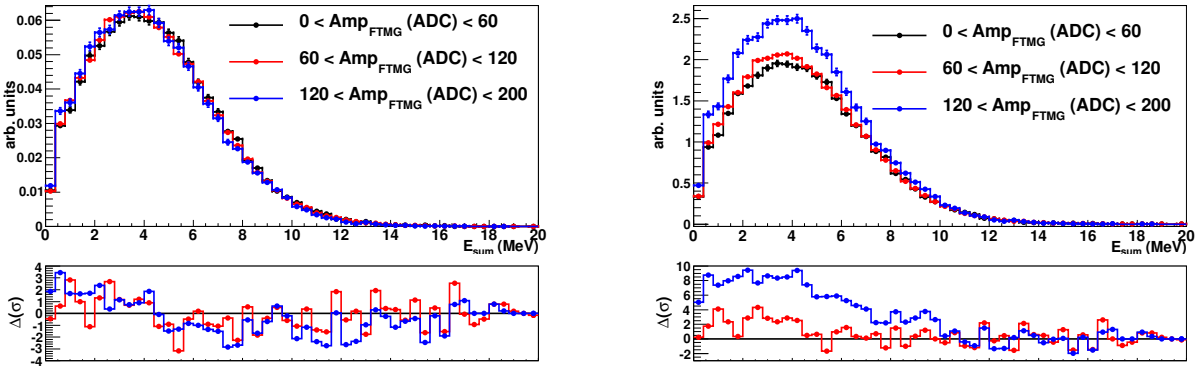

Figure 3.43: In the left hand panel, tagged prompt fission γ-ray cascades for different conditions applied to Amp_{FTMG} normalized in area. In the right hand panel, tagged prompt fission γ-ray cascades for different conditions applied to Amp_{FTMG} normalized in the large deposited energy tail (E_{sum} >10 MeV).

Thus, the correlation of the fission observables introduces small correlations in the simultaneous detection of fission events by the TAC and the FTMG detectors. That is, the fission reaction detected by one of the detectors depends slightly on whether it has been detected by the other detector as is shown in Fig. 3.43.

The left panel shows the tagged prompt fission γ-ray cascades for different conditions applied to the FTMG amplitude, Amp_{FTMG}, normalized in area. The differences observed, as a function of the deposited energy, are shown in the bottom section of the same panel. Despite the differences not being greater than 3σ, most of them are located in the large deposited energy tail.

To be precise, as was explained in the previous sections, this large deposited tail is used for the normalization and subtraction of the prompt fission component. Thus, this small correlation could introduce large differences in the background subtraction as is shown in the right hand panel of Fig. 3.43.

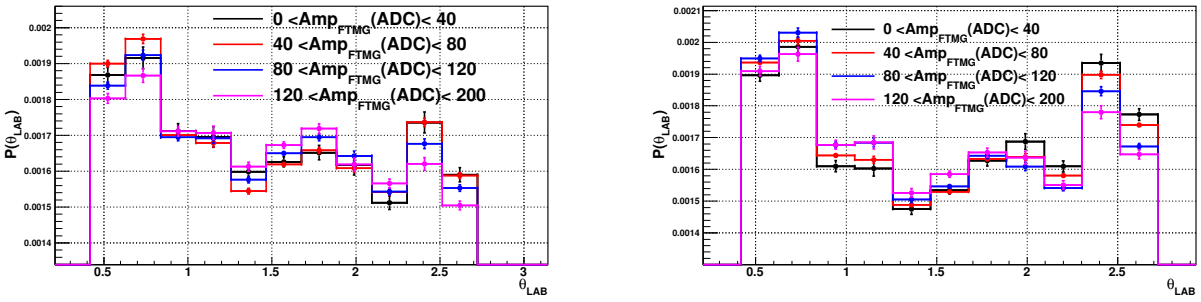

Figure 3.44: Angular distribution of the tagged prompt fission γ-ray cascades; in the left hand panel, for the 2FTMG experimental configuration and in the right hand panel, for the 10FTMG experimental configuration.

The correlation is not only observed in the deposited energy detected by the coincidence between the TAC and the FTMG, but is also measured in the angular distribution of the tagged prompt fission γ-rays. In Fig. 3.44 are shown the angular distribution of the tagged prompt fission γ-ray cascades for the 2FTMG (left panel) and for 10FTMG (right hand panel) experimental configurations, using as the z-axis the direction of the neutron beam: θ_{LAB}=0 and θ_{LAB}=π corresponding with the entrance and exit of the TAC, respectively. As is shown in this figure, the distribution of the tagged prompt fission γ-ray cascades changes as a function of the Amp_{FTMG} conditions applied for both experimental configurations.

Therefore, a small correlation exists in detecting the (n,f) events in coincidence between the TAC and the FTMG detectors. This experimental effect has been investigated by Monte Carlo simulations, using the fission observables provided by the GEF code [92], and detailed models of the TAC and the FTMG detectors using the GEANT4 toolkit. Three different types of causes were investigated:

- The kinematic boost of the prompt fission γ-ray cascades due to the high kinetic energy of the fission fragments: the effect of the kinematic boost is quite small. Therefore, this effect cannot explain the correlation observed in the experimental data.

- The directional correlation between the fission fragments and the prompt fission γ-ray cascades [101]: According to the simulations, it produces an appreciable effect in the simultaneous detection of the (n,f) events between the TAC and the FTMG detectors, thus correlating the simultaneous detection by both detectors. However, the Monte Carlo results do not reproduce the experimental data behavior.

- The FTMG fission detection efficiency depending on the mass of the heavy fission fragments: according to the simulations, the fission detection efficiency of the FTMG detectors is slightly different depending on whether the difference between the mass of the heavy and light fission fragments is lesser

or greater (∼1%). Since the γ-ray cascades emitted by fissions with lesser or greater differences in the fission fragment masses may be different, this could introduce correlations between both detectors in the detection of the fission events.

The correction of the correlation observed has been calculated experimentally in the section 3.5.4.

The kinematic boost of the prompt fission γ-ray cascades

The fission products are accelerated quasi-instantaneously after the scission of the primary nuclei (10^{-20}s) by the Coulomb forces. Then, the γ-rays cascades are emitted from fission fragments with large kinetic energies and detected by the TAC with slightly different directions and energies due to the Doppler effect.

To quantify this effect, the prompt fission γ-ray cascades correlated with the fission fragments were uniformly emitted from the fission fragment and transformed into the laboratory system using the Lorentz transformation, explained in appendix C. The β parameter needed for the transformation, defined as the speed of the fission fragments in terms of the light speed, c, is easily calculated from the kinetic energy T_{ff} and the fission fragment mass ,m_{ff}, by:

$$T = m_{ff}c^2(\gamma - 1) \tag{3.22}$$

where γ is a dimensionless parameter;

$$\gamma = \frac{1}{\sqrt{1+\beta^2}} \tag{3.23}$$

Therefore, combining Eq. 3.23 and Eq. 3.23, the β parameter is easily deduced:

$$\beta = \left(1 - \frac{1}{\left(\frac{T_{ff}}{m_{ff}c^2} + 1\right)^2}\right)^{1/2} \tag{3.24}$$

The transformed prompt fission γ-ray cascades in the laboratory system were simulated in the TAC+FTMG geometry using the GEANT4 toolkit and event reconstruction as was performed with the ^{235}U(n,γ) cascades and the prompt fission neutrons explained in the sections 3.6 and 3.4.4, respectively.

Three different cases were studied and compared with the simulation without the kinematic boost. The results are shown in Fig. 3.45:

- The fission fragments were emitted isotropically in the laboratory system (black line).
- The fission fragments were emitted only parallel to the neutron beam direction (blue line).
- The fission fragments were emitted only perpendicular to the neutron beam direction (pink line).

No substantial differences are observed between the deposited energy spectra of the different simulations. This is because the Doppler effect in the prompt fission γ-ray cascades induced by the kinematic boost is very low. Hence, this effect cannot be observed in the experimental data, and does not explain the experimental correlation observed between the fission fragments and the prompt fission γ-ray cascades.

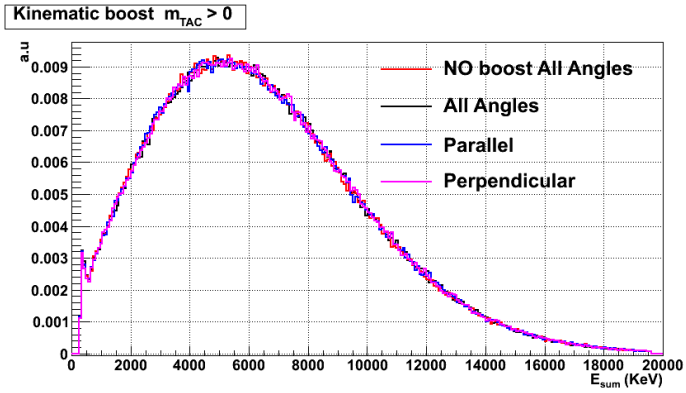

Figure 3.45: Prompt fission γ-rays cascades events reconstructed from the Monte Carlo simulated data.

Directional correlation between the fission fragments and the prompt fission γ-ray cascades

As was demonstrated by M. Marvin in [101], there is an angular anisotropy between the prompt fission γ-ray cascades and the motion direction of the fission fragments. The experimental angular distribution was described by two components with different angular spatial components: the first one, accounting for about 85% of the γ-rays, was isotropic. The remaining 15% had the angular distribution accounting quadrupole transitions from the fission fragments. The angular distribution is described in the fission fragment reference system by the following $W(\theta_{ff}, \phi_{ff})$ function [102]:

$$W(\theta_{ff}, \phi_{ff}) = a_0 + a_1 \cos^2(\theta_{ff}) + a_2 \cos^4(\theta_{ff}) \tag{3.25}$$

where a_0, a_1 and a_0 are the weighting factor for the isotropic, dipole and quadrupole components respectively. In the description given by M. Marvin, no dipole component is needed, thus a_1=0, and the ratio between the weighting factors a_0 and a_2 determine anisotropy of the prompt fission γ-ray cascades.

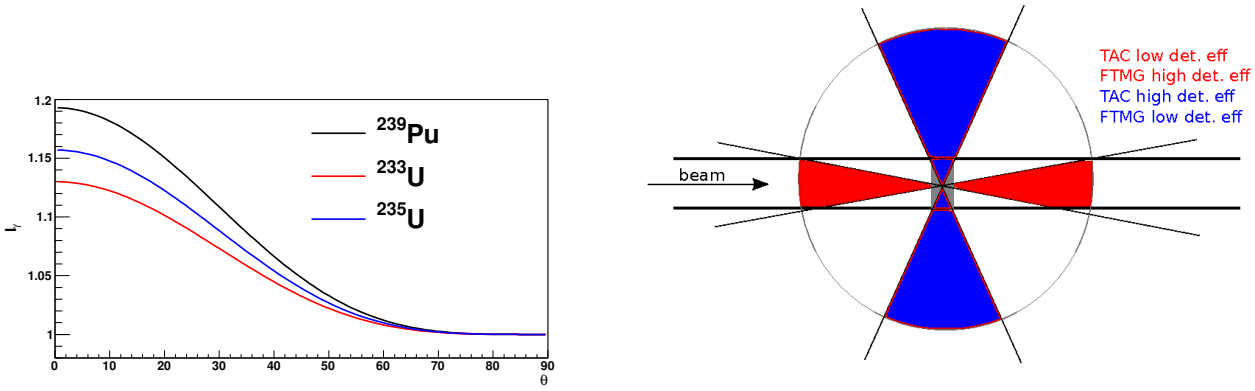

Figure 3.46: In the left hand panel, prompt fission γ-rays angular anisotropy in the fission fragment reference system for the ^{235}U, ^{233}U and ^{239}Pu isotopes taken from [101]. In the right hand panel, a schematic drawn of the TAC and the FTMG detection systems.

The left hand panel of Fig. 3.46 shows the angular distributions measured for three different isotopes,

^{233}U, ^{235}U and ^{239}Pu, with anisotropies between 12% and 19% [101]. The right hand panel of the same figure shows a schematic picture of the TAC and the FTMG detectors placed in the center of the TAC. In the plot there are different colored regions representing two different (n,f) simultaneous detection efficiencies regions due to the angular anisotropy [3]:

- The blue colored region corresponds with high detection efficiency for the TAC and low detection efficiency for the FTMG detectors. For this region, the fission fragments are emitted near parallel to the ^{235}U samples, where fission detection efficiency of the FTMG decreases rapidly due to the self-absorption of the fission fragments in the targets as was explained in the section 3.2.5. Hence, the fission fragments are barely detected by the FTMG but, at the same time, geometrically the prompt fission γ-ray cascades are almost entirely detected by the TAC.
- The red colored region corresponds to low detection efficiency for the TAC and high detection efficiency for the FTMG detectors. For this region, almost all the fission fragments deposit an appreciable energy in the active volume of the FTMG detectors. However, part of the prompt γ-rays cascades are not detected by the TAC due to the entrance and exit holes of the neutron beam.

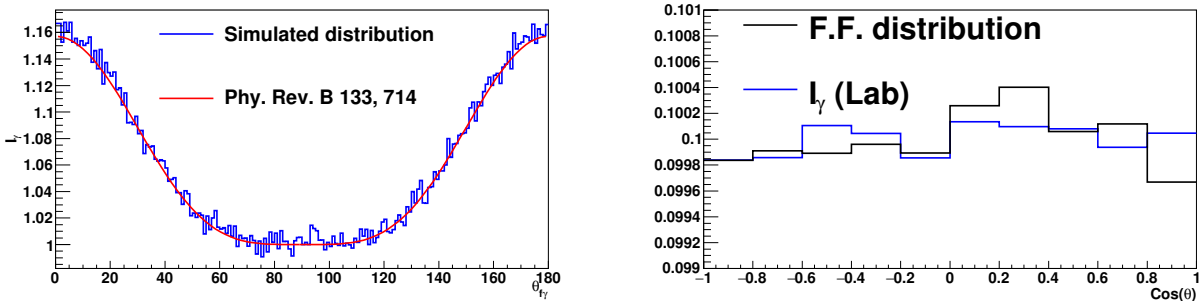

Figure 3.47: The left hand panel shows angular distribution of the prompt-fission γ-rays generated in the fission fragment reference system compared with the fitted curve taken from [101]. The right panel shows angular distributions of the fission fragments and prompt-fission γ-ray cascades simulated in the laboratory system.

The impact of the directional correlation was estimated using Monte Carlo simulations. As in the previous cases the output from the GEF code was used for the simulation of this effect.

Previous to the Monte Carlo simulation in the GEANT4 applications, the direction of the fission fragments was sampled isotropically, as shown by the black line in the right hand panel of Fig. 3.48. Then, each individual γ-ray cascade associated with the individual fission fragment was sampled in this coordinate system following the angular anisotropy described by the equation 3.25. The angular γ-ray distribution obtained is compared with the model used in the left hand panel of Fig. 3.48. Then, the correlated γ-ray cascades were transformed in the laboratory system following the procedure explained in the appendix D. The γ-ray distribution in the laboratory system is shown by the blue line in the right hand panel of Fig. 3.48. At this point the simulation was divided in two:

- The fission fragments were simulated in the FTMG model as was described in the section 3.2.5.
- The correlated prompt fission γ-ray cascades were simulated in the TAC+FTMG geometry as was performed with the ^{235}U(n,γ) cascades, explained in the section 3.6.

[3] In any of these cases, the detection efficiencies of both detectors are high. Note that 'low' and 'high' mean here 'slightly lower' and 'slightly higher'

The Monte Carlo data from the simulation is then reconstructed correlating the FTMG events with TAC events. From the the reconstruction of correlated data only, a general behavior is expected for two reasons:

- The FTMG geometry has been simplified and other experimental effects such as deformations of the electric field, the charge recollection and the electronic of the FTMG detectors need to be included for an accurate simulation.
- The results of the Monte Carlo simulations using the fission γ-rays from the GEF code do not reproduce the experimental results.

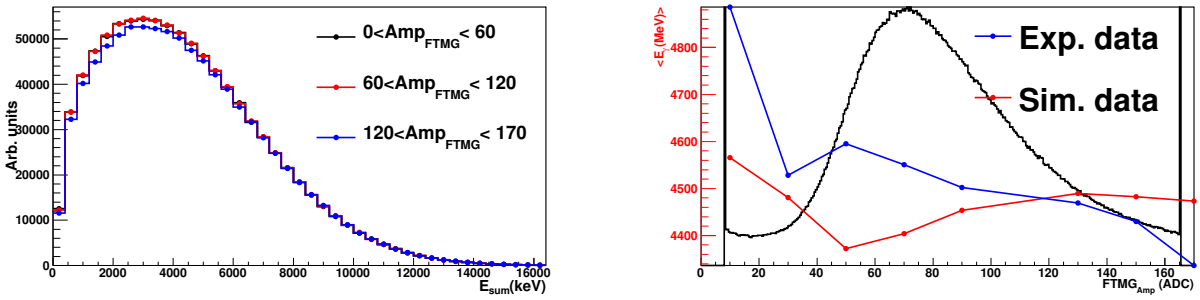

Figure 3.48: In the left hand panel is shown the deposited energy signature of the prompt fission γ-ray cascades obtained from the Monte Carlo reconstruction for different FTMG amplitude cuts. In the right hand panel is the average deposited energy of the prompt fission γ-ray cascades as a function of the FTMG amplitude.

The left hand panel of Fig. 3.48 shows the prompt fission γ-ray deposited energy spectra reconstructed from the Monte Carlo data for three different amplitude conditions applied to the FTMG events. The deposited energy distributions were normalized in the high deposited energy tail for the comparison. As for the experimental data, shown in Fig. 3.43, the distributions reconstructed for $0<\text{Amp}_{FTMG}<40$ and $40<\text{Amp}_{FTMG}<120$ cannot be distinguished. However, for $\text{Amp}_{FTMG}>120$, the simulated data does not reproduce the experimental behavior, while for the experimental data the ratio between the belly and the long deposited energy tail of the deposited energy distribution decreases, in the case of the reconstructed Monte Carlo data increase.

The right hand panel of Fig. 3.48 shows the average deposited energy of the simulated prompt fission γ-ray cascades (red line) and the experimental one (blue line) as a function of the simulated FTMG amplitude. Despite the fact that the Monte Carlo data does not reproduce the experimental data, there is an appreciable effect as a function of the FTMG amplitude. Therefore, it is expected that in the experimental data the anisotropy emission of the prompt fission γ-ray cascades will produce an appreciable effect. Thus, as was explained previously, a fraction of the prompt fission γ-rays of the prompt cascades are not detected by the TAC due to the angular anisotropy, hence reducing the number of γ-ray detected and lowering the total deposited energy in the TAC.

In conclusion, the anisotropy of the prompt fission γ-rays cascades could be part of the cause of the correlation between the detectors, but we were not able to reproduce the effect with simulations.

The fission detection efficiency of the fission fragment mass as a function of the FTMG amplitude

As was shown in the section 3.2.5, the fission detection efficiency of the fission fragments as a function of the mass depends on the FTMG amplitude conditions applied to the detector. Fig. 3.21 shows the detection

probability as a function of the heaviest fission fragment mass for different amplitude detection conditions applied to the FTMG detectors.

For the conditions applied to the FTMG in this analysis (Amp_{FTMG} >40 ADC channels), there is a difference of 1.2% detecting fission events in which the fission fragments masses are smaller and larger. In terms of the heavy fission fragment masses, the difference in the detection efficiency corresponds with fissions with heavy fission fragment mass of 120<A<130 and 150<A<150. Therefore, since the number of γ-rays and prompt fission neutrons are closely related to the pair of fission fragments produced, it is expected that the prompt fission γ-ray cascades detected only by the TAC and by the coincidences between the TAC and the fission fragments will be slightly different. This detection efficiency effect, added to the angular anisotropy explained in the previous section, could be a reasonable explanation of the correlation observed detecting simultaneously the (n,f) events between the TAC and the FTMG.

3.5.4 Experimental correction of the fission tagging detection efficiency and the fission detection efficiency

As was explained at the beginning of this section, the fission tagging detection efficiency is calculated using the equation 5.3:

$$\varepsilon_f^*(A_{th}, E_{sum}, m_{cr}) = \frac{c_{Tagg}(A_{th}, E_{sum}, m_{cr})}{c_{Fiss\_TAC}(E_{sum}, m_{cr})} \tag{3.26}$$

In the specific case of (n,f) reactions being independently detected by the TAC and the FTMG detectors [23], ε_f^* only depends on the threshold applied to the FTMG events:

$$\varepsilon_f^*(A_{th}, E_{sum}, m_{cr}) = \varepsilon_f^*(A_{th}) \tag{3.27}$$

Thus, $\varepsilon_f^*(A_{th})$ can be obtained from the equation 3.26 using certain restrictive conditions in E_{sum} and m_{cr} (sections 3.5.1 and 3.5.2), and the obtained value used for the less restrictive conditions in E_{sum} m_{cr} used to obtain the capture cross section. However, due to the small correlation observed in the experimental data (section 3.5.3):

1. The fission tagging detection efficiency depends slightly on the conditions applied to the TAC. Therefore, this quantity must be determined for the conditions of the ^{235}U(n,γ) cross-section: 2.5<E_{sum}(MeV)<7.0 2<m_{cr} <6.

2. The fission detection efficiency has to be calculated, since in general, $\varepsilon_f \neq \varepsilon_f^*$.

For this purpose, the ratio between the ε_f^* for *restrictive conditions* applied to the TAC, i.e. conditions such as the conditions applied in the sections 3.5.1 and 3.5.2 (superscript 1), and ε_f^* for *relaxed conditions* applied to the TAC (superscript 2), i.e. conditions used for the ^{235}U(n,γ) cross-section, is computed using the equation 3.26:

$$\frac{\varepsilon_f^*(A_{th}, E^1_{sum}, m^1_{cr})}{\varepsilon_f^*(A_{th}, E^2_{sum}, m^2_{cr})} = \frac{c_{Tagg}(A_{th}, E^1_{sum}, m^1_{cr})}{c_{Tagg}(A_{th}, E^2_{sum}, m^2_{cr})} \cdot \frac{c_{Fiss\_TAC}(E^2_{sum}, m^2_{cr})}{c_{Fiss\_TAC}(E^1_{sum}, m^1_{cr})};$$

$$\frac{\varepsilon_f^*(A_{th}, E^1_{sum}, m^1_{cr})}{\varepsilon_f^*(A_{th}, E^2_{sum}, m^2_{cr})} = f(A_{th}) \cdot \frac{c_{Fiss\_TAC}(E^2_{sum}, m^2_{cr})}{c_{Fiss\_TAC}(E^1_{sum}, m^1_{cr})} \tag{3.28}$$

where $f(A_{th})$ is defined as the ratio between the tagged fission counts for *restrictive conditions* and the tagged fission counts for *relaxed conditions*:

$$f(A_{th}) = \frac{c_{Tagg}(A_{th}, E^1_{sum}, m^1_{cr})}{c_{Tagg}(A_{th}, E^2_{sum}, m^2_{cr})} \tag{3.29}$$

and for simplicity, the dependence of $f(\mathrm{A}_{th})$ with the E_{sum} and m_{cr} variables is implicit.

The fission tagging detection efficiency for the *relaxed conditions*, $\varepsilon_f^*(\mathrm{A}_{th},\mathrm{E}^2_{sum},\mathrm{m}^2_{cr})$, can be calculated using the equation 3.28 since:

- $\varepsilon_f^*(\mathrm{A}_{th},\mathrm{E}^1_{sum},\mathrm{m}^1_{cr})$ and $\mathrm{c}_{Fiss\_TAC}(\mathrm{E}^1_{sum},\mathrm{m}^1_{cr})$ can be calculated using restrictive conditions such as was calculated in the sections 3.5.1 and 3.5.2.
- $f(\mathrm{A}_{th})$ is easily computed for any condition applied to the TAC events restricted to A_{th} above the detection threshold.

The only value that must be estimated is the number of fissions for the *Relaxed conditions*: $\mathrm{c}_{Fiss\_TAC}(\mathrm{E}^2_{sum},\mathrm{m}^2_{cr})$. For the estimation, let us assume that the detection efficiency of the FTMG detectors is 100%, corresponding to A_{th}=0. Here we include the fission reactions which induce a signal in the FTMG below the detection threshold and also those (n,f) reactions in which the fission fragments are absorbed in the sample. In this special case, the (n,f) events are detected independently by both detection systems. Thus, $\varepsilon_f^*(\mathrm{A}_{th}{=}0,\mathrm{E}^1_{sum},\mathrm{m}^1_{cr}){=}\varepsilon_f^*(\mathrm{A}_{th}{=}0,\mathrm{E}^2_{sum},\mathrm{m}^2_{cr})$ and the equation 3.28 can be solved for $\mathrm{c}_{Fiss\_TAC}(\mathrm{E}^2_{sum},\mathrm{m}^2_{cr})$,

$$c_{Fiss\_TAC}(E^2_{sum},m^2_{cr}) = \frac{1}{f(A_{th}=0)} c_{Fiss\_TAC}(E^1_{sum},m^1_{cr}) \tag{3.30}$$

Inserting the equation 3.30 in equation 3.28 we obtain:

$$\frac{\varepsilon_f^*(A_{th},E^1_{sum},m^1_{cr})}{\varepsilon_f^*(A_{th},E^2_{sum},m^2_{cr})} = \frac{f(A_{th})}{f(A_{th}=0)} \cdot \frac{c_{Fiss\_TAC}(E^1_{sum},m^1_{cr})}{c_{Fiss\_TAC}(E^1_{sum},m^1_{cr})} \tag{3.31}$$

Rewriting the last equation, we obtain the relationship between fission tagging detection efficiencies for any amplitude threshold applied to the FTMG, A_{th}.

$$\boxed{\varepsilon_f^*(A_{th},E^2_{sum},m^2_{cr}) = \frac{f(A_{th})}{f(A_{th}=0)} \varepsilon_f^*(A_{th},E^1_{sum},m^1_{cr})} \tag{3.32}$$

In order to calculate $f(\mathrm{A}_{th}{=}0)$, some assumptions need to be taken into account:

1. From the study presented in the sections 3.5.1 and 3.5.2 we know that the FTMG detectors have individual efficiencies close to 90%.
2. The ratio between the ∼10% of non-tagged fission counts for *restrictive conditions* and for *relaxed conditions* has a similar value to that of the same ratio but obtained with tagged counts with low A_{th}.

The ratio between these two quantities for different FTMG amplitude regions is shown in Fig. 3.49. Each region represents ∼10% of the fission reactions detected by the TAC, under the conditions in E_{sum} and m_{cr}. $f(\mathrm{A}_{th})$ is then calculated for any threshold as the average of all the amplitude periods. In order to get $f(\mathrm{A}_{th}{=}0)$, we compute this average including the 10% of artificial tagged events shown in the figure by the shadowed region.

For the conditions used in the sections 3.5.1 and 3.5.2 and the conditions used for ^{235}U(n,γ) cross section:

$$\frac{f(A_{th}=40)}{f(A_{th}=0)} = 0.98 \tag{3.33}$$

Thus, the fission tagging detection efficiency for both the 2FTMG and 10FTMG obtained in the sections 3.5.1 and 3.5.2 have to be lowered to 2%. We estimate that the systematic uncertainty of this correction is 15%. Thus, propagating it to the value of ε_f^*, the uncertainty is:

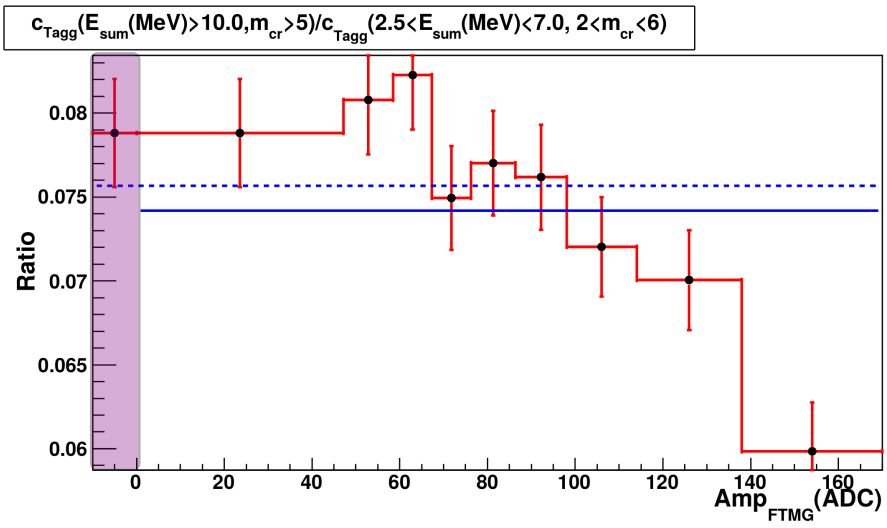

Figure 3.49: Ratio between the number of fission counts detected in coincidence by the TAC and the FTMG for restrictive conditions (E_{sum} >10 MeV, $m_{cr} > 5$ and relaxed conditions (2.5<E_{sum}(MeV)<7 MeV, 2<m_{cr}¿6) conditions in the detected TAC events, as a function of Amp_{FTMG}.

$$\Delta(\varepsilon_f^*) \sim 0.25\%. \tag{3.34}$$

Due to the high (n,f) detection efficiency of the TAC for the capture conditions we can consider that for these conditions in the detected events, the (n,f) reactions are detected (practically) independently in both detectors. Note that the ratio of efficiencies under the *restrictive conditions* and the *relaxed conditions* is ~ 0.08 (Figure 3.49), and the ratio between their corresponding fission tagging efficiencies is 1.02. Thus, we can assume that:

$$\varepsilon_f(A_{th}) = \varepsilon_f^*(A_{th}, E_{sum}^2, m_{cr}^2) \tag{3.35}$$

including an additional systematic uncertainty equal to the uncertainty calculated for ε_f^*.

3.5.5 Final results

The results of the fission tagging detection efficiency, ε_f^*, and the fission detection efficiency, ε_f, are summarized as follow:

- **Fission tagging efficiency** ε_f^*: This quantity has been determined for the ^{235}U(n,γ) conditions for both experimental configurations as was explained in the section 3.5 and corrected in the section 3.5.4. We include the following uncertainties:
  - **Statistical uncertainty**: The statistical uncertainty for the 2FTMG experimental configuration is 0.8%, and for the 10FTMG experimental configuration 0.4%.
  - **The background subtraction and the prompt fission neutrons**: 0.14% for the 2FTMG experimental configuration and 0.1% for the 10FTMG experimental configuration.
  - **The correction applied due to the correlation**: In this case, for both experimental configurations, the systematic uncertainty due to the correction is 0.25%.

Thus, the value of ε_f^* in the ^{235}U(n,γ) conditions for the 2FTMG experimental configuration is:

$$\varepsilon_f^* = 0.1847(22) \tag{3.36}$$

and for the 10FTMG experimental configuration is:

$$\varepsilon_f^* = 0.842(5) \tag{3.37}$$

The uncertainty given for both configurations is the linear sum of the statistical and systematic uncertainty.

- **Fission detection efficiency** ε_f: As was explained before, we consider that for the *relaxed conditions*, i.e., ^{235}U(n,γ) conditions, the fission detection efficiency and the fission tagging detection efficiency have the same value due to the large TAC efficiency for the (n,f) events in such conditions. Thus, the ε_f value for the 2FTMG experimental configuration is:

$$\varepsilon_f = 0.1847(22) \tag{3.38}$$

and for the 10FTMG experimental configuration:

$$\varepsilon_f = 0.842(5) \tag{3.39}$$

3.6 The TAC detection efficiency of the ^{235}U(n,γ) events

The neutron capture detection efficiency, ε_γ, is defined as the probability of detecting a (n,γ) reaction in a certain nucleus by the TAC. It depends on the BaF_2 deposited energy thresholds, the conditions applied to the TAC events in E_{sum} and m_{cr}, and the counting rate of the detectors due to pile-up effects. In our case, the pile-up effects for the calculation of ε_γ are negligible. We assume that the detection efficiency does not depend on the neutron energy of interest. This is because:

- The energies of the incident neutrons are much smaller than the neutron separation energy (S_n), thus the total energy of the cascade is almost always the same ($E_{tot} \cong S_n + E_n$).
- The nuclear level density is large below S_n, thus the possible decay paths of the compound nucleus are large enough, and the signature of the capture cascades registered by the TAC is independent of the resonance (nuclear level of the compound nucleus) where the neutron capture occurs.

When both conditions are fulfilled, then the neutron capture signature registered by the TAC will be almost identical, independent of the neutron energy as it has been checked.

The efficiency has been calculated by Monte Carlo simulations as was performed for previous measurements with the TAC [34, 76]. It is obtained by the comparison between the experimental signature and the Monte Carlo deposited energy spectra of the γ-ray cascades. For the comparison the following is necessary:

- Neutron capture cascades generator: the (n,γ) cascades are generated by Monte Carlo codes, such as the DICEBOX code [47] or the DECAYGEN code [48], attending to the nuclear structure and decay models as was explained in the section 1.2.2.
- Geometry for the simulation of the (n,γ) cascades: the cascades generated must be simulated in an accurate geometric implementation of the experimental setup with a realistic description of its interactions. For this purpose, the TAC-FTMG geometry has been implemented using the GEANT4 toolkit [90, 91].
- Event reconstruction from the Monte Carlo data [34, 76]: the data obtained from the simulation of the (n,γ) cascades in the geometry are reconstructed taking into account experimental effects such as the energy resolution of the BaF_2 crystals or the pile-up effects.

3.6.1 The event generator used for the ^{235}U(n,γ) reaction

The event generator used for the ^{235}U(n,γ) cascades is the Monte Carlo DICEBOX code [47]. The (n,γ) cascades can generally proceed via many intermediate levels. In the particular case of the decay of neutron capturing levels in heavy nuclei, the overall number of encountered intermediate levels is 10^5—$\cdot 10^6$. The proposed method used in the DICEBOX code is based on the following:

- Below a certain energy E_{cr} a full set of experimentally determined nuclear levels are known, including the level energies E, spins J, parities π and all branching ratios for the transitions between levels.
- The nuclear levels above E_{cr} are generated randomly according to a level density formula, $\rho(E,J^\pi)$.
- The probability transitions between a nuclear level a, above E_{cr}, and nuclear level b are given by the radiation widths, $\Gamma_{a\gamma b}$, which are obtained from:

$$\Gamma_{a\gamma b} = \sum_{X,L} y_{XL}^2 (E_a - E_b)^{2L+1} \frac{S_\gamma^{(XL)}(E_a - E_b)}{\rho(E_a, J_a^{\pi_a})} \tag{3.40}$$

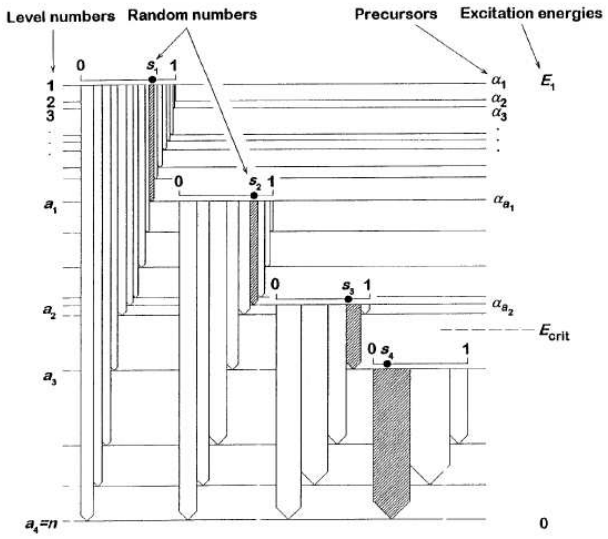

Figure 3.50: Simplified schematic decay of the DICEBOX code. The figure has been taken from [47].

Here, $S_\gamma^{(XL)}(E_\gamma)$ is the photon strength function for a given type X (electric or magnetic) and multipolarity L. The summation is assumed over all allowed values XL. The Porter-Thomas fluctuations of the nuclear densities are included by the random value y_{XL}, sampled from a normal distribution with zero mean and unit variance.

- Each cascade starts from a single, well-defined initial level with a known excitation energy, spin and parity E_1,J_1 and π_1, respectively.

The algorithm for the de-excitation of the nuclear level can be summarized as follows:

1. The level density $\rho(E, J^\pi)$ is discretized to yield energies E_a, spins J_a and parities π_a of individual level a above the critical energy E_{cr}. For the sake of simplicity, the levels are labeled by integer numbers (a=1,2,...,n), assuming that the energy E_a decreases with increasing a. Levels a=1 and a=n correspond, respectively, to the initial level, where all cascades starts, and the ground state where they stop.

2. To each level a with energy $E_a > E_{cr}$ a generator seed α_a is ascribed, including the level a=1;

3. The partial widths $\Gamma_{a\gamma a'}$ for a full set of transitions $1 \rightarrow a'$, leading from the initial level to all possible final levels a′ with $E_{a'} < E_{cr}$ are generated.

4. A total radiation width $\Gamma_{a\gamma}$ is calculated from the initial level a=1:

$$\Gamma_{1\gamma} = \sum_{a'>1} \Gamma_{1\gamma a'} \tag{3.41}$$

A set of intensities $I_{1a'}$ for all the transitions initiating at the same level are then determined following a simple expression:

$$I_{1a'} = \Gamma_{1\gamma a'}/\Gamma_{1\gamma} \tag{3.42}$$

These intensities are in fact 'branching intensities'

5. It is assumed that the level a=1 is populated. A level, a_1, to which it decays is determined from a random number, s_1, yielded by another random number generator. The choice of a_1 follows from the requirement:

$$\sum_{a'=2}^{a_1-1} I_{1a'} \leq s_1 \leq \sum_{a'=2}^{a_1} I_{1a'} \tag{3.43}$$

   As a result, the level a_1, reached by the first cascade step, is known.

6. If the energy E_{a_1} of level the a_1 is greater than E_{cr}, a full set of partial widths $\Gamma_{a_1\gamma a'}$ for a full set of transitions $a_1 \rightarrow a'$, leading from the fixed level a_1 are generated. Then, the branching intensities $I_{a_1a'}$ are calculated for the same level. If E_{a_1} falls below E_{cr}, the branching intensities $I_{a_1a'}$ are deduced exclusively from the evaluated data. Using these intensities, a second intermediate level, a_2, to which the level a_1 decays, is chosen at random following the requirement:

$$\sum_{a'=2}^{a_2-1} I_{a_1a'} \leq s_2 \leq \sum_{a'=a_1+1}^{a_2} I_{a_1a'} \tag{3.44}$$

7. The part of the simulation procedure outlined before is repeated until the excited nuclei reach the ground state or metastable state.

The cascades are then characterized by the γ-ray energies E_γ, multiplicity m_γ, and the intermediate levels described by J_{a_i}, π_{a_i} and E_{a_i}. A simplified schema of the decay process followed by the algorithm is shown in Fig. 3.50.

As was explained in the section 1.2.2, the nuclear density $\rho(E, J^\pi)$ and the photon strength function S^n_γ are obtained from physical models depending on some adjustable parameters. These parameters are adjusted to reproduce the experimental data obtained from the deposited energy registered by the TAC for different conditions applied to the crystal multiplicity m_{cr}.

3.6.2 The simulation of the (n,γ) cascades in the GEANT4 geometry

The detailed geometry of the TAC already implemented [34, 76, 104] in the GEANT4 [90, 91] application includes the BaF_2 crystals with their capsules, the photomultipliers and the whole structure that supports the array detector as is shown in the left hand panel of Fig. 3.51. To this geometry, we have added the fission chamber with the required detail level: it includes the FTMG detectors, with all the PCB structural pieces, the gas and the kapton windows. Also included are the aluminum beam pipes and the geometry of the borated neutron absorber used during the ^{235}U(n,γ) cross-section measurement. The new geometry added to the model is shown in the right hand panel of the Fig. 3.51.

The γ-ray cascades generated by the DICEBOX Monte Carlo code were simulated in this GEANT4 geometry taking into account the particle interaction physics and recording in a binary file the time, deposited energy and the BaF_2 crystal number where the energy deposition occurs.

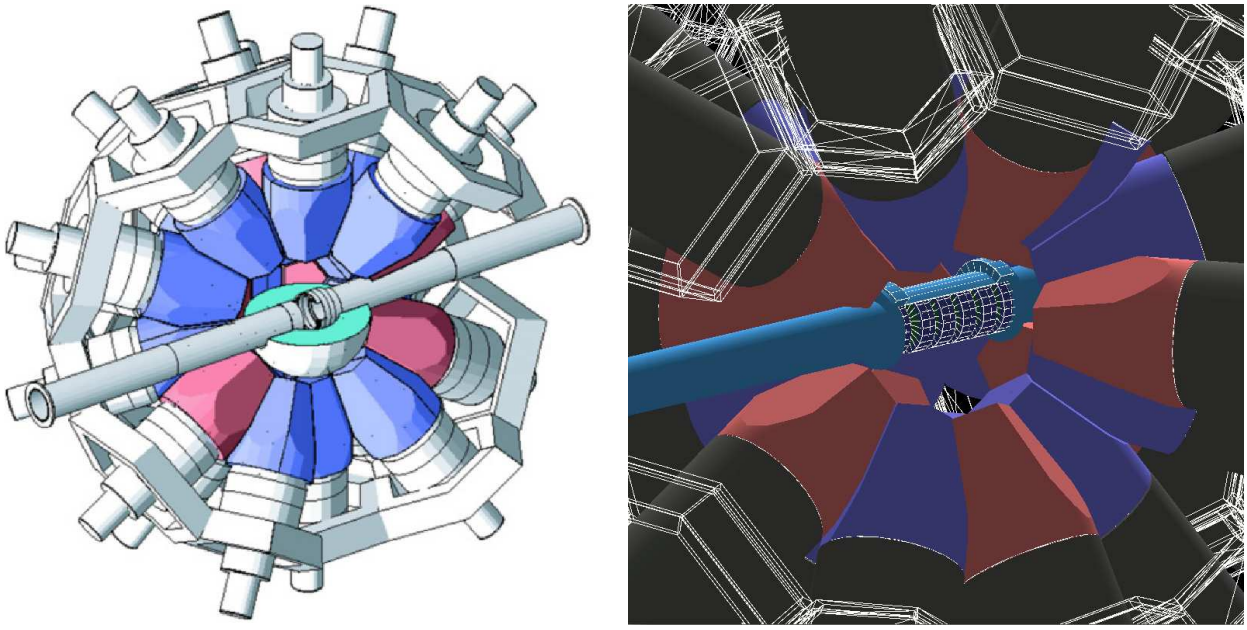

Figure 3.51: In the left hand panel, TAC geometry used in the previous measurements; in the right hand panel, the geometry of the FTMG fission chamber with the aluminum beam pipes implemented in the center of the TAC geometry.

3.6.3 The event reconstruction software

The results obtained from the GEANT4 simulations are processed by an event reconstruction software [34, 76], analogous to the reconstruction process performed on the experimental data:

1. All the hits (signals) registered in the BaF_2 crystals are read from the binary file. The deposited energy in each crystal is sampled according to the energy resolution of the detector (section 3.1.2). The uncertainty in the experimental energy calibration is taken into account including an artificial error in the Monte Carlo energy calibration sampled at the beginning of the simulation according to a Gaussian distribution with standard deviation of 3%, obtained from the comparison with the experimental data. All the Monte Carlo energies are then multiplied by their corresponding factor, thus simulating the error committed in the experimental energy calibration process. The starting time of each simulated cascade is sampled according to a certain predefined reaction rate, and the time between the origin of the cascade and the detection of the γ-rays, which is very small, is given by the Monte Carlo simulation.

2. In the case of the $^{235}U(n,\gamma)$ measurement, it is not necessary to apply the pile-up effects for the neutron energies where ε_γ is calculated since the counting rates detected due to the capture reactions are very low. Therefore, pile-up corrections are not applied to the reconstruction process.

3. Then, the coincidences of the BaF_2 are made with a coincidence time window of 20 ns, in the same way as is done with the experimental data. The result is a list of events with a total deposited energy, detected multiplicity and detection time.

3.6.4 Validation of the simulation process

The whole simulation process was validated by the comparison of the experimental data from known γ-ray calibration sources, ^{137}Cs and ^{88}Y, with the simulated deposited energy spectra applying different conditions to the TAC events in m_{cr}.

The validation for ^{137}Cs is shown in Fig. 3.52, and for ^{88}Y in 3.53. For both figures, the solid lines are the experimental data for different m_{cr} conditions and the dashed lines the Monte Carlo results.

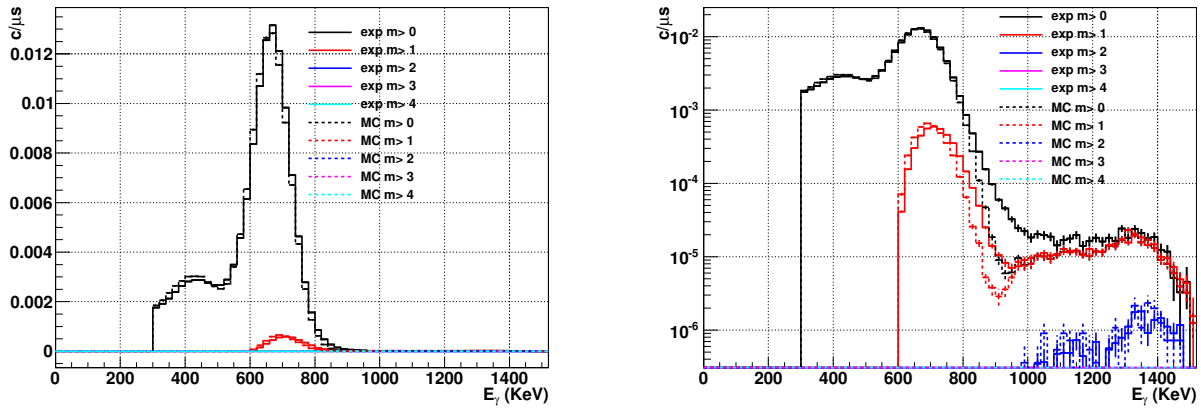

Figure 3.52: Comparison between the experimental data and the Monte Carlo results for the standard γ-ray ^{137}Cs calibration source. In the left hand panel the y-axis is in linear scale and in the right hand panel in logarithmic scale.

The close agreement between the experimental and Monte Carlo results shown for both calibration sources permits the determination of the two essential parameters for the simulations:

- The experimental BaF_2 detection threshold (E_{th}): by the comparison of the experimental data and the Monte Carlo results it is possible to detect the limit of the BaF_2 analysis routine, identifying the low energy limit for the γ-ray detection.
- The inner radius of the TAC (R_{TAC}): this parameter was modified in $\pm$2 mm until the experimental data was reproduced by the Monte Carlo results.

The values determined for those parameters are shown in the table 3.13.

E_{th}=300 keV	R_{TAC}=11.40 mm

Table 3.13: Detection energy threshold determined for BaF_2 detectors and TAC Monte Carlo inner radius obtained from the comparison of the simulations with the experimental data.

In addition, the detection efficiency for monoenergetic γ-rays has been determined as a function of the incident particle energy as is shown in Fig 3.54. The black line is the TAC detection efficiency for BaF_2=300 keV. The blue and the red lines are the TAC detection efficiency for E_{th}=400 keV and E_{th}=500 keV, respectively. The TAC detection efficiency increases with the energy reaching a maximum which depends on the BaF_2 threshold.

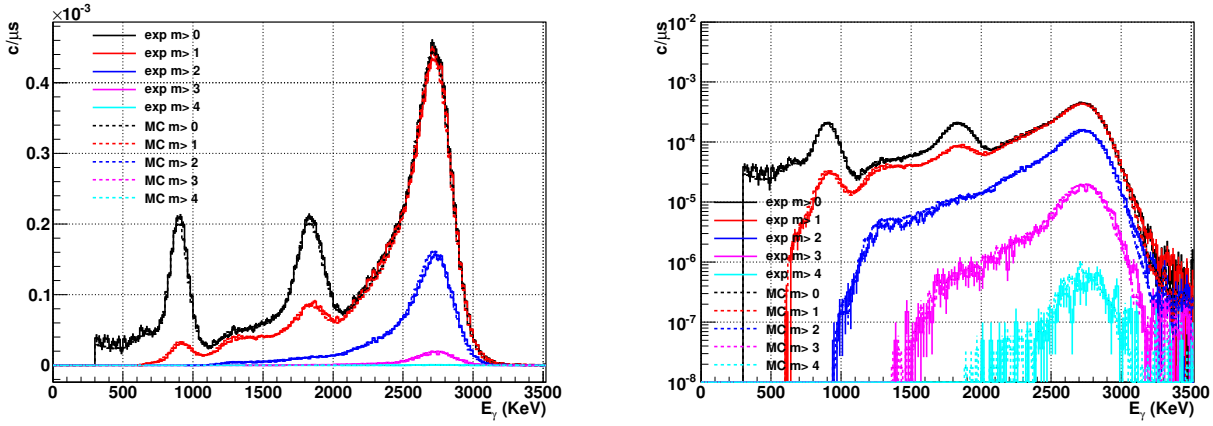

Figure 3.53: Comparison between the experimental data and the Monte Carlo results for the standard γ-ray ^{88}Y calibration source. In the left hand panel the y-axis is in linear scale and in the right hand panel in logarithmic scale.

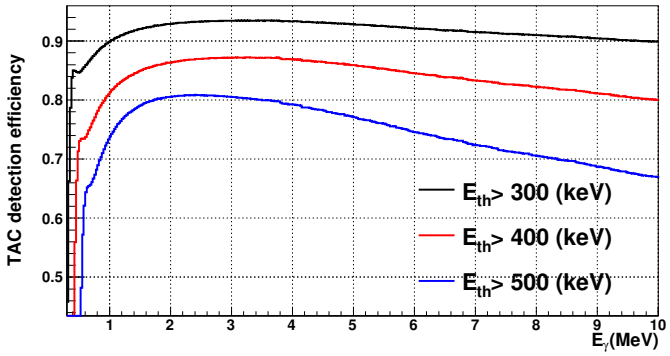

Figure 3.54: TAC detection efficiency for monoenergetic γ-rays a function of the incident particle energy and for different BaF_2 thresholds.

3.6.5 The generation of the ^{235}U(n,γ) cascades

The γ-ray cascades used for the determination of ε_γ were adjusted from other experiments performed at DANCE at Los Alamos [32] by Milan Krtička using the DICEBOX code [47]. The parameters of the photon strength functions were adjusted based on the previous works from the Oslo nuclear physics group [108, 109, 110]. The results from this group show the evidence of large M1 resonances in the photon strength functions with energies about 2.5 MeV for the actinide region as is shown in the right hand panel of Fig. 3.55. In this figure is plotted the E1 component, M1 component and the photon total as blue, red and black lines respectively. Larger Electromagnetic multipolarity was neglected for this calculation.

The ^{235}U is an special nucleus compared with others measured before at the n_TOF facility due to fissile character and the presence of the fission isomers, as was explained in the section 1.2.3. This fact complicates the description of the γ-decay for the fissile nuclei such as the ^{235}U and ^{239}Pu.

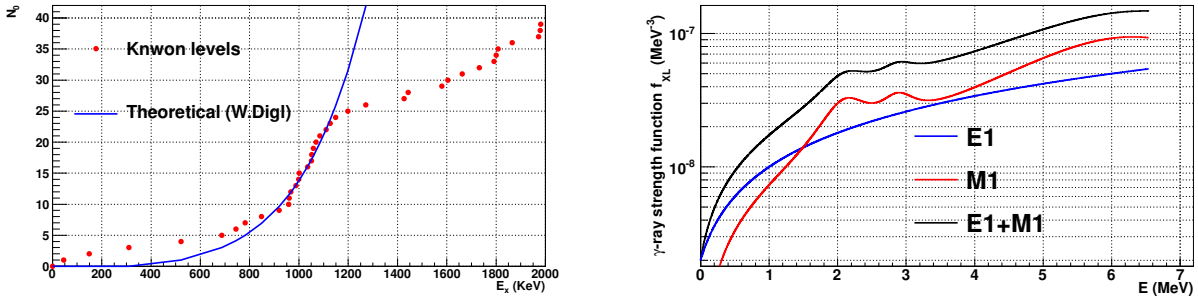

Figure 3.55: In the left hand panel, theoretical cumulative nuclear levels density [46] of ^{236}U compared with the experimental nuclear states accessible in the ENDSF library [103]. In the right hand panel, the Photon Strength Function adjusted to reproduce the ^{236}U γ-ray decay measured at DANCE in Los Alamos.

In the particular case of ^{236}U, the population of isomers was reported for the first time by Lars in 1969 [105] through (d,p) reactions. Studies using these surrogated reactions performed in 1972 [106] lead to a half-life for this fission isomer of $T_{1/2}$ ~100 ns. Later on, in 1976, studies with thermal neutron reactions [107] suggest that the isomeric state mainly decays by the γ de-excitation channel instead of the isomeric fission channel, since experimentally delayed fission events were not observed. The effect of this delayed isomeric γ-ray decay, present in our experimental ^{235}U(n,γ) data, has to be taken into account for the determination of the ^{235}U(n,γ) detection efficiency because the population of this nuclear state via nuclear reactions is 10-20% of the total (n,γ) reactions [56].

The DANCE experimental data also reports the presence of another fission isomer: the deposited energy shape of the γ-ray cascade depends on the coincidence time window used. This fact strongly supports the presence of long isomeric states present in the decay: specifically, one state at about 687 keV with a very short half-live $T_{1/2}$ ~4 ns and another one at about 1154 keV with a relative long half-live $T_{1/2}$ ~100 ns.

From the DANCE experimental data, it is deduced that the population of this long-lived isomeric state via the γ-ray decay is estimated to be very likely more than 10%. In order to obtain a reasonable reproduction of the experimental data, several completely artificial long-lived isomeric 3^- and 4^- levels were added to the ^{236}U level scheme near to 1155 keV. In the calculation, the level scheme used has been taken from the ENDSF library [103] below 1160 keV, where the number of known nuclear levels starts to deviate from the expected numbers of nuclear states given by the nuclear state density model integral [51, 52]. That is the limit of the applicability of the experimental measured nuclear level scheme. From this point, the experimental nuclear scheme has been replaced by a statistical model up to the neutron separation energy of the ^{236}U. The comparative between the experimental number of levels (dotted points) and the integral

of the statistical model (blue line) is shown in the left hand panel of Fig. 3.55. As is shown, the number of missing nuclear levels for excitation energies above 1160 keV deviates from the expected values.

3.6.6 The TAC efficiency to ^{235}U(n,γ) reactions

The DICEBOX γ-ray cascades were simulated in the n_TOF experimental setup for the three different measurement configurations: 2FTMG with the borated neutron absorber; 2FTMG without the borated neutron absorber and 10FTMG with the neutron absorber. No significant differences were observed between the deposited energy spectra for the configurations 2FTMG and 10FTMG with neutron absorber as is shown in Fig. 3.57. For this reason, in the following the 10FTMG and 2FTMG configurations will be labelled as FTMG configuration with absorber in terms of ε_γ.

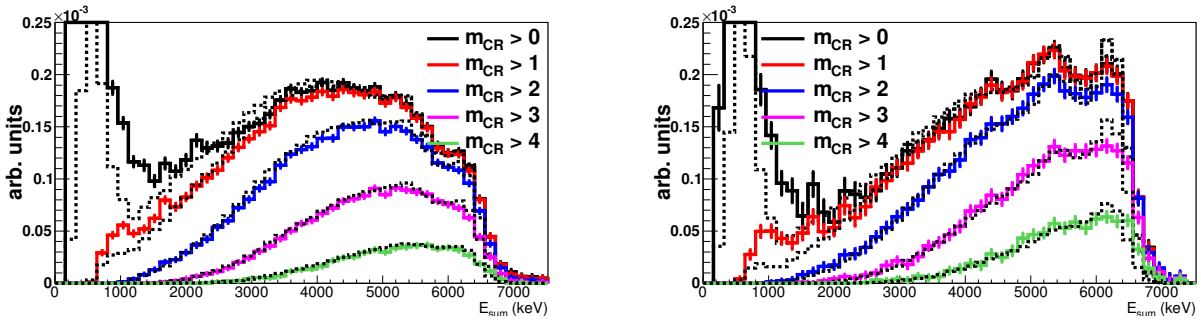

Figure 3.56: Monte Carlo simulated $^{235}U(n,\gamma)$ deposited energy spectra compared with the experimental data for different m_{cr} conditions. In the left hand panel are the results for the experimental FTMG configuration with the borated neutron absorber. In the right hand panel are the results for the FTMG experimental configuration without the borated neutron absorber.

In Fig. 3.56 is shown the simulated and experimental deposited energy spectra detected by the TAC for both configurations and conditions applied in m_{cr}: in the left hand panel, for the configuration with the neutron absorber and in the right handpanel, for the configuration without the neutron absorber. The experimental data is shown as colored solid lines and the simulated data as dashed lines. A significant agreement has been obtained between the simulated and experimental data in all the deposited energy spectra for the different m_{cr} conditions.

The TAC efficiency obtained for ^{235}U(n,γ) events in both configurations applying different conditions in m_{cr} are shown in the table. 3.14.

m_{cr} >	<E_{sum}(MeV)<	ε_γ(Abs) (%)	ε_γ(No Abs) (%)
0	2.5 - 7.0	78.4	85.8
1	2.5 - 7.0	75.8	83.5
2	2.5 - 7.0	58.8	67.3
3	2.5 - 7.0	30.9	38.4
4	2.5 - 7.0	10.6	14.7
5	2.5 - 7.0	2.3	3.8
6	2.5 - 7.0	0.3	0.6

Table 3.14: TAC efficiency calculated for the $^{235}U(n,\gamma)$ reactions using different conditions applied to the TAC events.

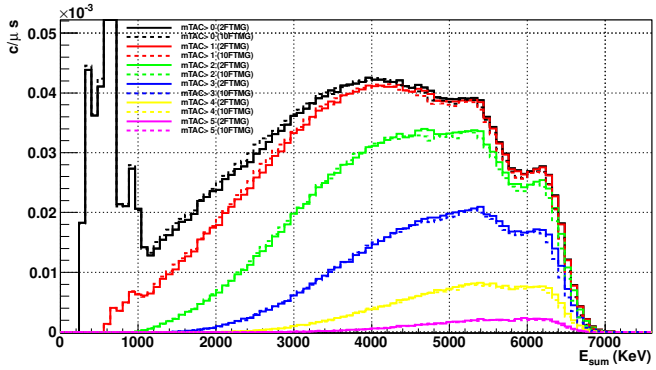

Figure 3.57: $^{235}U(n,\gamma)$ signature reconstructed from the Monte Carlo simulations for the 2FTMG and 10FTMG configurations with the neutron absorber.

3.6.7 Uncertainty in the determination of the TAC efficiency

The larger sources of uncertainty for the TAC efficiency to the ^{235}U(n,γ) events have been identified:

- The uncertainty due to the geometry modeled: in previous works [34, 76, 104] it was determined that the parameter with the greatest impact on the ε_γ was the TAC inner radius. We have assumed that an uncertainty in the determination of this parameter is $\Delta(R_{TAC})=\pm 1$ mm. For larger variations, the deposited energy spectra from the calibration sources shown in Fig. 3.52 and Fig. 3.53 were not accurately reproduced by the Monte Carlo simulations.

  The uncertainty of this parameter has been propagated in the result, thus obtaining the uncertainty in the neutron capture efficiency due to this parameter. It is estimated as the difference between the maximum and minimum efficiencies divided by two. The values obtained for the different conditions applied to the TAC are shown in table 3.15.

$< m_{cr} <$	$< E_{sum}$(MeV) $<$	$\Delta_{Geom}(\varepsilon_\gamma^{Geom}$(Abs)) (%)
2 - 6	2.5 - 7.0	1.2
2 - 6	2.5 - 6.5	1.5
2 - 6	3.0 - 6.5	1.6
3 - 6	2.5 - 6.5	2.0
3 - 6	3.0 - 6.5	2.2

Table 3.15: TAC detection efficiency uncertainty due to the TAC inner radius parameter.

  In the worst scenario, using very restrictive analysis conditions, the systematic uncertainty associated with the model implemented in the GEANT4 application is 2.2%. For the conditions that will be used for the calculation of the neutron capture cross section, the systematic uncertainty is 1.2%.

- The uncertainty due to the ^{235}U(n,γ) cascades model used: it has been estimated from the dispersion of the ratio between the integral of the experimental deposited energy spectra, I_{exp}, and the Monte Carlo reconstruction, I_{MC} for different crystal multiplicities conditions as is shown in the table 3.16.

  The excellent reproduction of the experimental data by the Monte Carlo reconstruction permits the estimation of the uncertainty due to the model of ^{235}U(n,γ) cascades model for the configuration with the neutron absorber:

m_{cr} >	<E_{sum}(MeV)<	I_{MC}/I_{exp}
0	2.5 - 6.5	1
1	2.5 - 6.5	1.00
2	2.5 - 6.5	1.01
3	2.5 - 6.5	1.01
4	2.5 - 6.5	1.03

Table 3.16: Ratio between the experimental and the Monte Carlo deposited energy spectra integral for 2.5<E_{sum}(MeV)<7.0 and different m_{cr}. The normalization of the deposited energy spectras was carried out for m_{cr} >0.

$$\Delta_{Model}(\varepsilon_\gamma) = 1\% \tag{3.45}$$

Therefore, the uncertainty in the determination of ε_γ for the analysis conditions used for the calculation of neutron capture cross section (2< m_{cr} <6 2.5<E_{sum}(MeV)<7.0) is:

$$\Delta(\varepsilon_\gamma) = \sqrt{(\Delta_{Geom}(\varepsilon_\gamma))^2 + (\Delta_{Model}(\varepsilon_\gamma))^2} \approx 1.7\% \tag{3.46}$$

3.7 The neutron fluence

During the 2012 campaign, the neutron fluence was monitored with the SiMons [72]. In previous campaigns, the neutron fluence was determined by dedicated measurements together with other detectors such as the PPACS or the absolute calibrated PTB chamber [62, 63, 64]. Since the concentration of ^{10}B dissolved in the spallation target moderator changes from one year to another, small differences in the neutron fluence shape for low neutron energies could appear. Three different aspects of the neutron fluence have been checked:

- The shape of the neutron fluence, as a function of the neutron energy, explained in section 3.7.1.
- Correction of the neutron fluence due to the dead material layers intercepting the neutron beam, explained in section 3.7.2.
- The effect of the different samples positions in the neutron capture cross-section is discussed in section 3.7.3.

3.7.1 The neutron fluence shape as a function of the neutron energy

The shape of the neutron fluence during the 2012 campaign has been determined using the Silicon Monitors from the counting rate of the Silicon Monitors as a function of the neutron energy, the well-known ^{6}Li(n,t)^{4}He cross-section, and taking into account that the detection efficiency does not vary for neutron energies below 1 keV [72]. For neutron energies above this limit, no valued or dependable correction can be applied without the explicit knowledge of the SiMon detection efficiency as a function of the neutron energy.

The calculated 2012 neutron fluence is compared with the values in the campaigns of 2009, 2010 and 2011 in Fig 3.58. The neutron fluence at low neutron energies is smaller compared with the previous years, suggesting an increment of amount of boron present in the moderator during the 2012 campaign.

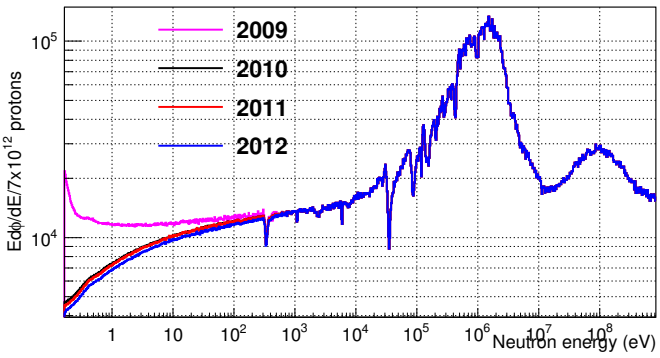

Figure 3.58: The Neutron fluence as a function of the neutron energy for the n_TOF facility measured at EAR1 in 2009, 2010 and 2011 campaigns. The 2009, 2010 and 2011 campaigns are shown by the pink, black and red lines, respectively. The 2012 neutron fluence is shown by the blue line.

3.7.2 The dead material intercepting neutron fluence

The neutron fluence calculated in the previous section is the neutron fluence at the entrance of the experimental area. The fission chamber used in the experimental setup is composed of a large amount of material

intercepting the neutron beam: the kapton windows, aluminum backings of the ^{235}U targets, the gas for the operation of the FTMG detectors, the FTMG detectors themselves, etcetera. Thus, a small correction of the neutron fluence is necessary. The correction has been obtained analytically, as is explained in the appendix E, and verified by Monte Carlo simulations.

The correction calculated for both experimental configurations in the neutron energy period from 0.1 to 10^4 eV is shown in the left hand panel of Fig. 3.59: the 2FTMG and 10FTMG experimental configurations are shown by the blue and red lines respectively.

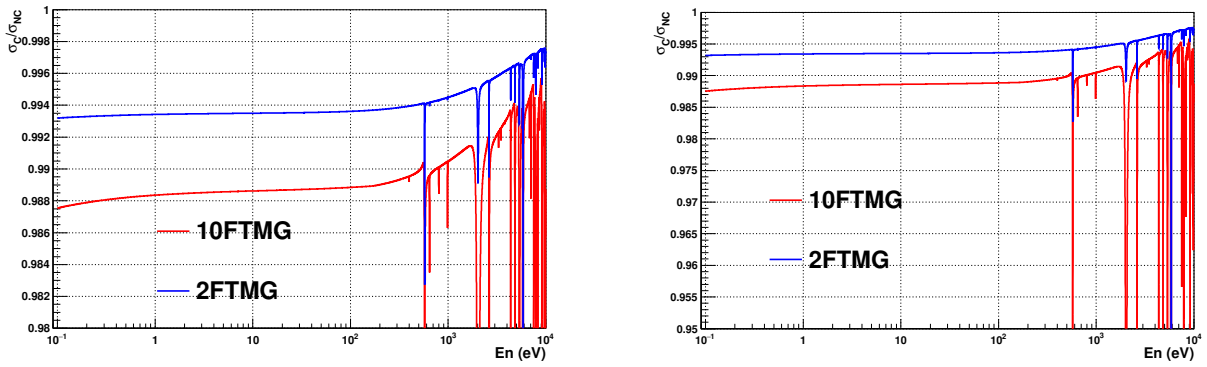

Figure 3.59: In the left hand panel, neutron fluence attenuation due to the dead material present during the measurement for the 2FTMG and 10FTMG experimental configurations, shown by blue and red line. In the right hand panel, the same calculation increasing the ^{235}U total neutron cross section ten times.

For the neutron energy period of interest, from 0.2 to 200 eV there is no neutron resonance from the the dead materials. The results from the experimental configurations are summarized as:

- 2FTMG configuration: The net effect for this experimental configuration is a global attenuation of the ∼0.6% in the neutron energy range of interest. Non-appreciable differences in the neutron fluence shape are observed, thus non-correction in the neutron energy shape is needed.
- 10FTMG configuration: The attenuation in this case is large, a factor of ∼1.2%, due to the large amount of dead material present. In addition, it appreciably changes the shape of the incoming neutron fluence. Therefore, for this configuration the correction due to the material must be applied.

In order to check the impact of total neutron cross section of the ^{235}U in this calculation, the correction factor for the neutron fluence has been recalculated by multiplying the ^{235}U total cross-section by a factor of ten. The results are shown in the right hand panel of Fig. 3.59. As can be observed, the ^{235}U neutron cross-section does not play a significant role in the correction of the neutron fluence.

3.7.3 Effect of the samples position

During the measurement, the ^{235}U targets were situated at slightly different flight times positions. Thus, it could broaden the measured neutron capture cross-section, since an event measured at the same time of flight in two different samples (i and j), could correspond with different neutron energies:

$$E_n^i(d_{TOF}(i), t_{TOF}) \neq E_n^j(d_{TOF}(j), t_{TOF}) \tag{3.47}$$

The effect on the ^{235}U(n,γ) cross-section has been calculated by comparing the cross-section and shifting the time of flight distance from the nominal position to first and last sample positions.

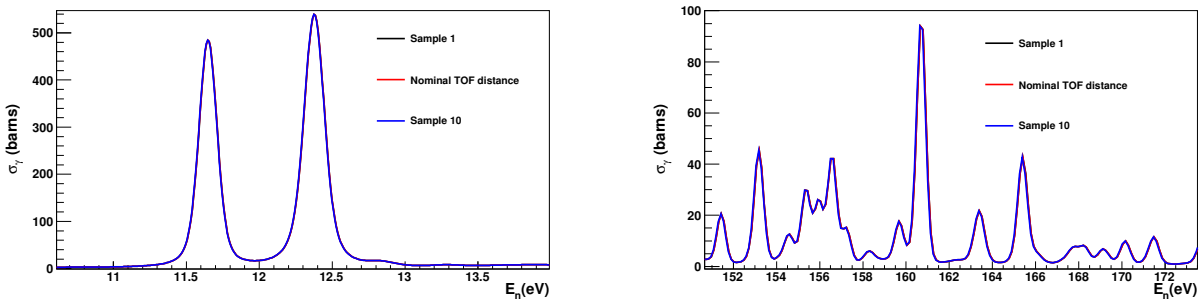

Figure 3.60: Apparent $^{235}U(n,\gamma)$ cross-section at different flight time distances: in the left hand panel, from 11 eV to 13 eV. and in the right hand panel from 150 to 175 eV.

As is shown in both panels of Fig. 3.60, this effect on the neutron energy period of interest is negligible, from 0.2 eV to 200 eV. For higher neutron energies, the effect should be taken into account.

3.8 The normalization

As was shown in the section 1.3, two different quantities can be determined from the simultaneous measurement of the neutron capture and neutron induced fission cross-section. Depending on the quantity, different normalization is performed to the experimental data. Thus, different uncertainties due to the normalization are obtained.

- **The $\alpha(E_n)$ ratio**: This quantity is determined experimentally as:

$$\alpha(E_n) = N_\alpha \frac{c_\gamma(E_n)}{c_f(E_n)} \tag{3.48}$$

where $c_\gamma(E_n)$ and $c_f(E_n)$ are the number of capture and fission counts detected by both detection systems. This is an absolute measurement of the ratio between the neutron capture and fission cross-section and no additional external normalization is required. The normalization, N_α, is the ratio between the detection efficiencies:

$$N_\alpha = \frac{\varepsilon_f}{\varepsilon_\gamma} \tag{3.49}$$

Therefore, the uncertainty in the normalization of this quantity is the sum of the uncertainty of these two parameters:

$$\Delta(N_\alpha) = 2.95\% \tag{3.50}$$

where 1.7% is the uncertainty due to the TAC efficiency, ε_γ, and 1.25% the uncertainty due to the fission detection efficiency, ε_f.

- **The neutron capture cross-section, $\sigma_\gamma(E_n)$**: the normalization of the experimental neutron capture cross-section data has been carried out to the well-known ^{235}U(n,f) cross-section in the neutron energy range which is almost a standard value. Thus, the neutron capture cross-section is given, as was explained in the section 1.3, by:

$$\sigma_\gamma(E_n) = \frac{c_{tot}(E_n - c_{bkg}(E_n)}{N_\gamma \phi_N(E_n)} \tag{3.51}$$

where N_γ includes the normalization due to sample thickness, the detection efficiency and the absolute value of the neutron fluence. The methodology applied almost removes any systematic uncertainty such as the target thickness and the absolute value of the neutron fluence. As was explained in the section 1.3, the experimental neutron reaction yield for any reaction channel x is experimentally determined as:

$$Y_{x,exp}(E_n) = \frac{C_T(E_n) - C_B(E_n)}{\varepsilon_x(E_n)\phi_N(E_n)} \tag{3.52}$$

Theoretically, the same quantity is determined, excluding multiple scattering effects, as:

$$Y_{x,th}(E_n) = \frac{\sigma_x(E_n)}{\sigma_T(E_n)} \left(1 - e^{-n_s \sigma_T(E_n)}\right) \tag{3.53}$$

Therefore:

$$\frac{\int_{E_1}^{E_2} Y_{\gamma,th} dE_n}{\int_{E_1}^{E_2} Y_{f,th} dE_n} = \frac{\int_{E_1}^{E_2} \frac{\sigma_\gamma(E_n)}{\sigma_T(E_n)} \left(1 - e^{-n_s \sigma_T(E_n)}\right) dE_n}{\int_{E_1}^{E_2} \frac{\sigma_f(E_n)}{\sigma_T(E_n)} \left(1 - e^{-n_s \sigma_T(E_n)}\right) dE_n} \tag{3.54}$$

The only difference between the numerator and the denominator of Eq. 3.54 are the capture and the neutron-induced fission cross-sections, $\sigma_\gamma(\mathrm{E}_n)$ and $\sigma_f(\mathrm{E}_n)$. Therefore, this ratio has a small dependency with the total neutron cross-section $\sigma_T(\mathrm{E}_n)$ and the target thickness, n_s since both quantities appear in the same way in the numerator and denominator. In the thin target approximation, which is a very good approximation for this measurement, this quantity yields to:

$$\frac{\int_{E_1}^{E_2} Y_{\gamma,th} dE_n}{\int_{E_1}^{E_2} Y_{f,th} dE_n} \approx \frac{\int_{E_1}^{E_2} n_s \sigma_\gamma(E_n) dE_n}{\int_{E_1}^{E_2} n_s \sigma_f(E_n) dE_n} = \frac{\int_{E_1}^{E_2} \sigma_\gamma(E_n) dE_n}{\int_{E_1}^{E_2} \sigma_f(E_n) dE_n} \tag{3.55}$$

In Eq. 3.55, the dependency with $\sigma_T(\mathrm{E}_n)$ and n_s disappears. On the other hand:

$$\frac{\int_{E_1}^{E_2} Y_{\gamma,exp} dE_n}{\int_{E_1}^{E_2} Y_{f,exp} dE_n} = \frac{\int_{E_1}^{E_2} \frac{C_T(E_n) - C_B(E_n)}{\varepsilon_\gamma(E_n)\phi_N(E_n)} dE_n}{\int_{E_1}^{E_2} \frac{C_f(E_n)}{\varepsilon_f(E_n)\phi_N(E_n)} dE_n} \tag{3.56}$$

In the Eq. 3.56 it is assumed that the background for the fission reaction channel is completely removed. We consider that ε_f and ε_γ do not vary in the neutron energy range from E_1 to E_2. Hence, these quantities are removed from the integral and Eq. 3.56 amounts to:

$$\frac{\int_{E_1}^{E_2} Y_{\gamma,exp} dE_n}{\int_{E_1}^{E_2} Y_{f,exp} dE_n} \approx \frac{\varepsilon_f}{\varepsilon_\gamma} \frac{\int_{E_1}^{E_2} \frac{C_T(E_n) - C_B(E_n)}{\phi_N(E_n)} dE_n}{\int_{E_1}^{E_2} \frac{C_f(E_n)}{\phi_N(E_n)} dE_n} \tag{3.57}$$

Eq. 3.57 explicitly shows that the reaction yields ratio does not depend on the absolute value of the neutron fluence. The dependency with the neutron fluence shape is also very small if E_1 and E_2 are close because it appears in the numerator and denominator as a weighting function. Combining the Eq. 3.55 and 3.57 we obtain the normalization of the neutron capture cross section:

$$\boxed{N_\gamma = \int_{E_1}^{E_2} \sigma_\gamma(E_n) dE_n = \int_{E_1}^{E_2} \sigma_f(E_n) dE_n \frac{\varepsilon_f}{\varepsilon_\gamma} \frac{\int_{E_1}^{E_2} \frac{C_T(E_n) - C_B(E_n)}{\phi_N(E_n)} dE_n}{\int_{E_1}^{E_2} \frac{C_f(E_n)}{\phi_N(E_n)} dE_n}} \tag{3.58}$$

The integral value of the ^{235}U neutron-induced fission cross-section is a well-known reference value of the OCDE Nuclear Energy Agency (NEA) in the neutron energy range from E_1=7.8 to E_2=11.0 eV [9]. This integral value is known with an accuracy below 0.5%:

$$\int_{E_2=11.0eV}^{E_1=7.8eV} \sigma_f(E_n) dE_n = (246.4 \pm 1.2) barns \cdot eV \tag{3.59}$$

Then, the normalization of the neutron capture cross-section is performed to this well-known ^{235}U(n,f) integral value. The uncertainty only depends on the the accuracy of the detection efficiencies and the statistic achieved by the FTMG detectors. The methodology is equivalent to normalizing our neutron-induced fission data to the well-known integral value. Therefore, the systematic uncertainty associated with the normalization is:

$$\Delta(N_\gamma) = 3.35\% \tag{3.60}$$

where 1.7% is due to the uncertainty of ε_γ, 1.25% due to the uncertainty of ε_f and 0.4% due to the statistic achieved by the FTMG detectors.

Note that ε_f and ε_f^* are correlated, therefore producing larger systematic uncertainties. The systematic uncertainty due to the determination of ε_f^* will be treated in the section 4.2.

3.9 The dead time corrections

One of the corrections which has to be applied to the experimental data in the procurement of the experimental neutron capture cross-ction is related to the dead time in the TAC detection system, which begins to be non-negligible for counting rates larger than several hundred events per ms. Notice that the entire response of each BaF_2 detector is digitized every 2 or 4 ns, and thus the detection system does not have a dead time as it is usually defined. The dead time is defined here as the difficulty of resolving a signal pile-up. Hence, the dead time on the detectors depends on the counting rate, the signal amplitude and the dedicated pulse shape routine used for the reconstruction of the events from the digitized signals [34, 76, 88, 111]. In the case of a pile-up event, the dedicated pulse shape routine has three possible outcomes:

- The signal pile-up is not resolved: The second signal is lost and the parameters of the first signal determined by the pulse shape routine cannot be well estimated; i.e., wrong particle identification, poor determination of the signal area (deposited energy),etcetera.
- The signal pile-up is not well-resolved: the individual signals are detected, but their parameters are not determined: i.e., incorrect particle identification, poor determination of the signal area, etcetera.
- The signal pile-up is well-resolved: the individual signals are detected and the parameters obtained from the dedicated pulse shape routine are well-determined.

In two of the three possible outcome cases, the parameters reconstructed from the digitized signals are distorted by the dead time effects, thereby distorting the detected deposited energy spectra and the detected counting rate, complicating the background subtraction and the determination of the neutron capture cross-section [34, 76, 88]. If the global reaction rate during the measurement is large enough, the TAC can suffer from an additional problem - the summing effect: two or more γ-ray cascades could be detected within the time window used for the BaF_2 detector coincidence. Therefore the γ-ray signals of all the detectors are detected as the same cascade, hence summing-up the deposited energy of the cascades and the crystal multiplicity of all the detected cascades.

Hence, the dead time effects distort the total deposited energy and the crystal multiplicity detected by the TAC. Fortunately, in the case of the ^{235}U(n,γ) measurement, the counting rate of the individual BaF_2 detectors were large enough to have pile effects, but small enough to avoid the summing effects in the TAC. For the analysis performed, the FTMG are considered free from dead time effects in the neutron energy region of interest, since the average time between the next two signals was much greater when compared with the typical signal width.

For a detailed discussion of the dead time effects in the TAC use the references [34, 76, 88, 111].

3.9.1 The dead time correction model

The dead time model used for the ^{235}U(n,γ) measurement is based on the methodology described in [34, 88] to correct the dead time effects on the TAC. The model maps the performance of the dedicated pulse shape routine, reconstructing the parameters from the BaF_2 signals at different counting rates. The model uses digitized signals of different amplitude (deposited energy), E_γ, and the experimental raw digitized buffers to provide two related probability distributions needed for the correction of the dead time effects as a function of the neutron energy: the total detection probability, $P_{E_\gamma}(E_n)$, defined as the probability to detect a γ-ray with energy E_γ; and the detected energy probability, $P_{E_\gamma,E'_\gamma}(E_n)$, defined as the probability of detecting the incident γ-ray with a different energy E'_n.

For the calculation of these probability distributions, the BaF_2 signals were grouped in different deposited energy intervals and amplitude intervals. The detection probability depends on the BaF_2 signal amplitude: this is lower for the small digitized signals and increases with the signal amplitude. Hence, the width of these intervals was not regular, being narrow for the low amplitude signal intervals and large for the intervals that enclose higher BaF_2 signals amplitude.

More than 90% of the counting rate registered in the BaF_2 detectors during the measurement of the $^{235}U(n,\gamma)$ is the large background induced by the dead material intercepting the neutron beam, and not from the (n,f) and (n,γ) reactions. Therefore, the dead time effects as a function of the neutron energy were characterized using the experimental BaF_2 digitized buffers from the dedicated 2FTMG background experimental configuration. The procedure followed for the determination of the probability distributions is summarized as follow:

- The BaF_2 digitized buffers from the dedicated background measurement of the 2FTMG configuration were read individually.
- These digitized raw buffers were analyzed by the dedicated pulse routine at low neutron energies, from 0.2 to 1 eV. If the pulse shape routine detects a γ-ray signal with the amplitude in the deposited energy interval of interest, then the signal is saved for the study of the routine performance. If there is no signal in the amplitude region of interest, then the next pulse is analyzed.
- The digitized signal is copied in the digitized buffers at times corresponding to higher neutron energies for its reconstruction by the dedicated pulse shape routine as shown in Fig. 3.61. In this figure, the original buffer is shown as the solid blue-grey color, whereas the original digitized buffer plus signal under study is shown as the solid red line.
- The composed signal buffers, original buffer + signal under analysis, were then analyzed by the dedicated pulse shape routine. In Fig. 3.61, the black solid lines correspond to BaF_2 signals identified by the pulse shape routine,while the dotted green lines are the signals not detected by the pulse shape routine. The correspondence of time-of-flight energies to each buffer and the signal energies obtained by the routine are indicated on top of each panel.
- The detection probability functions $P_{E_\gamma}(E_n)$ and $P_{E_\gamma,E'_\gamma}(E_n)$ were calculated from the analysis of these composed digitized buffers. An example of the probability functions obtained for different conditions is shown in Fig. 3.62.

  The left panel shows the $P_{E_\gamma,E'_\gamma}(E_n)$ obtained for signals of different amplitude at different positions of the digitized buffer. In this, the ξ variable is defined by the relationship $E'_\gamma=(1+\xi)E_\gamma$ and provides information about the difference in deposited energy reconstructed for different neutron energies. The right hand panel shows the total detection probability $P_{E_\gamma}(E_n)$ for different deposited energy signal intervals at different neutron energies.
- The procedure is repeated for all the BaF_2 detectors, thus obtaining the probability distributions as a function of the neutron energy for all the deposited energy intervals and individual detectors.

As the counting rate increases, the detection probability decreases due to the signal pile-up as is shown in the right panel of Fig. 3.62. Moreover, the deposited energy reconstructed from the detected signals tends to be larger due to the pile-up as shown in the left hand panel of Fig. 3.62. This behavior changes slightly, depending on the signal amplitude, as was explained previously For a further discussion of the dead time effect as a function of the signal amplitude see references [34, 76].

Once the probability functions that map the performance of the routine are built, the dead time model reconstructs the efficiency as follows:

- Given a distribution of γ-ray cascades which is not affected by the dead time effects, i.e. the Monte Carlo $^{235}U(n,\gamma)$ cascades or the tagged prompt fission γ-rays cascades at low neutron energy, these are translated to high neutron energies by applying the dead time effects.
- The dead time effects are applied to the individual γ-rays of the cascades, distorting them by Monte Carlo methods following the probability distributions $P_{E_\gamma}(E_n)$ and $P_{E_\gamma,E'_\gamma}(E_n)$.

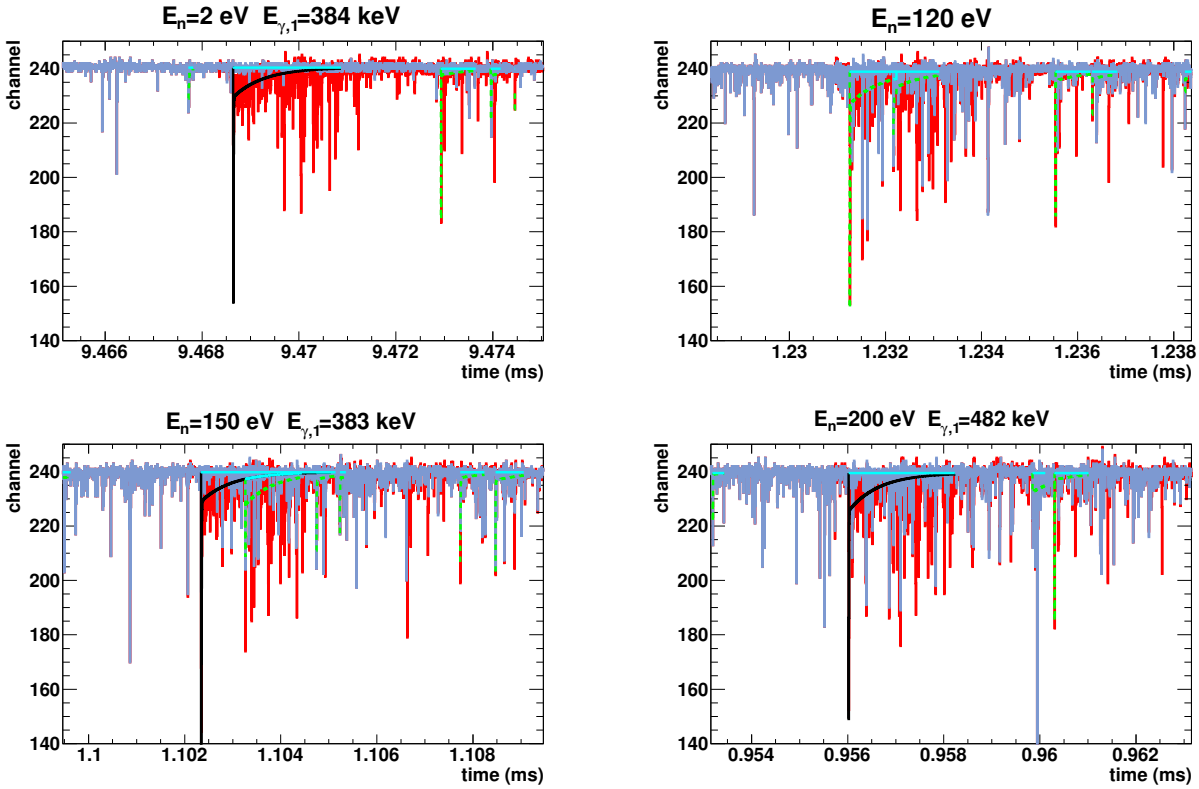

Figure 3.61: Detection of the same BaF_2 digitized signal at four different places on the digitized buffers. The original signal buffers are shown as the solid blue-grey color, whereas the original digitized buffer plus signal under study is shown as the solid red line. The signals identified by the pulse shape analysis routine are shown with solid lines; otherwise, the original pulse shape is indicated by a dotted green line. The correspondence of time-of-flight energies and the signal energies obtained by the routine are indicated at the top of each panel.

- The TAC events events are then reconstructed from these built distorted γ-ray distributions, producing a distorting signature in the TAC.
- Applying the desired analysis conditions to the TAC, E_{sum} and m_{cr}, the dead time correction is obtained by the comparison of the efficiency calculated at low neutron energies, where the dead time corrections are not needed, and the distorted one.

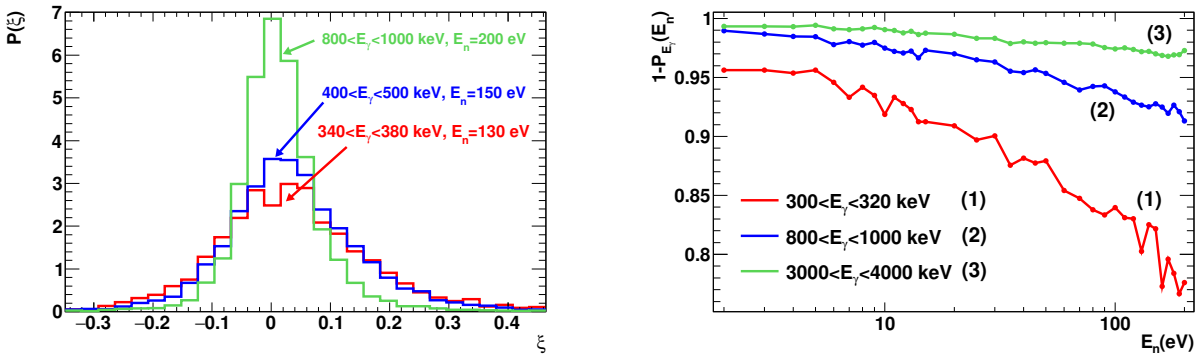

Figure 3.62: In the left hand panel,$P_{E_\gamma,E'_\gamma}(E_n)$ obtained for different deposited energies in the BaF_2 crystals at different neutron energies. The ξ variable is defined from the relationship $E'_\gamma=(1+\xi)E_\gamma$, where E_γ is the real energy of the γ-ray and E'_γ the energy reconstructed from the routine. In the right hand panel, $P_{E_\gamma}(E_n)$ for different deposited energy signal intervals at different neutron energies.

3.9.2 Validation of the dead time model with the prompt-fission γ-ray cascades

The validation of the dead time model applied to the BaF_2 signals has been performed using the tagged prompt fission γ-ray cascades. Since these cascades do not change for any physical reason in the neutron energy period of interest, the distortion observed in them as a function of the neutron energy is due to the dead time effects in the TAC. For this reason, these γ-ray cascades are a perfect candidate for testing the dead time corrections. The validation has focused on three different aspects of these γ-ray distributions: the individual energy deposition of the γ-rays in the BaF_2 crystals; the summed signature of the prompt fission γ-rays in the TAC; and the ratio between the tagged fission counts and the total fission counts detected in the FTMG as a function of neutron energy.

Prompt fission γ-ray deposited energy for the BaF_2detectors

The individual prompt fission γ-ray distribution for different neutron energy periods is shown in Fig. 3.63. The solid black line shows the distribution for low neutron energies, from 0.2 to 1 eV, where the counting rate is low. The solid red line is the tagged prompt fission γ-ray distribution for higher neutron energies, from 100 to 150 eV. From the low neutron energy distribution, a distorted one has been reconstructed applying the dead time probability functions mapped for the neutron energy from 100 to 150 eV. This is shown as the solid blue line. A high level of agreement is obtained by comparing the distorted with the experimental distribution obtained by the fission tagging procedure for neutron energies from 100 to 150 eV.

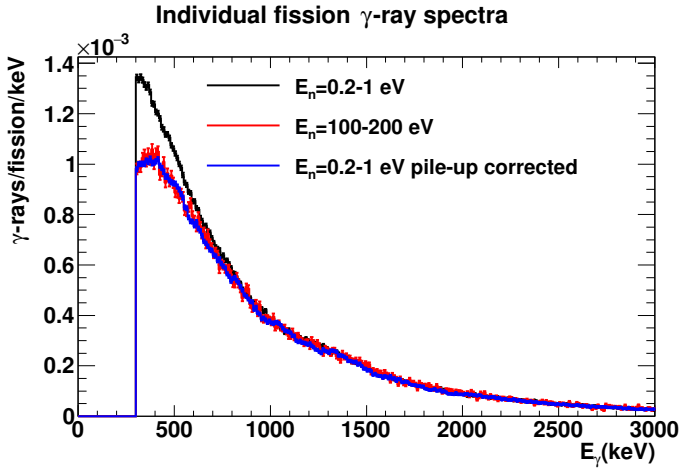

Figure 3.63: Comparison between the deposited energy of the individual tagged prompt fission γ-rays for different neutron energy ranges and the corrected one. The distribution measured at the low neutron energies, from 0.2 to 1.0 eV, is shown as a black solid line. The distribution measured at high neutron energies, from 100 eV to 200 eV, is shown as a solid red line and a blue solid line plots the reconstructed γ-ray distribution applying the dead time corrections to the low neutron energy distribution.

Prompt fission γ-ray deposited energy signature detected by the TAC

The dead time corrections have been validated for the TAC events using the prompt fission γ-ray deposited energy signature for different crystal multiplicity as is shown in Fig. 3.64. In the left hand panel is shown the prompt fission signature for different crystal multiplicities in two different situations: at low neutron energies, from 0.2 to 1 eV, where the dead time effects are negligible, shown as colored solid lines, and at high neutron energies, from 100 to 200 eV, where the dead time effects have an appreciable impact on the γ-ray cascades, shown as dashed black lines. In the right hand panel of the same figure is shown the high level of agreement obtained between the experimental and the corrected γ-ray distributions at high neutron energy.

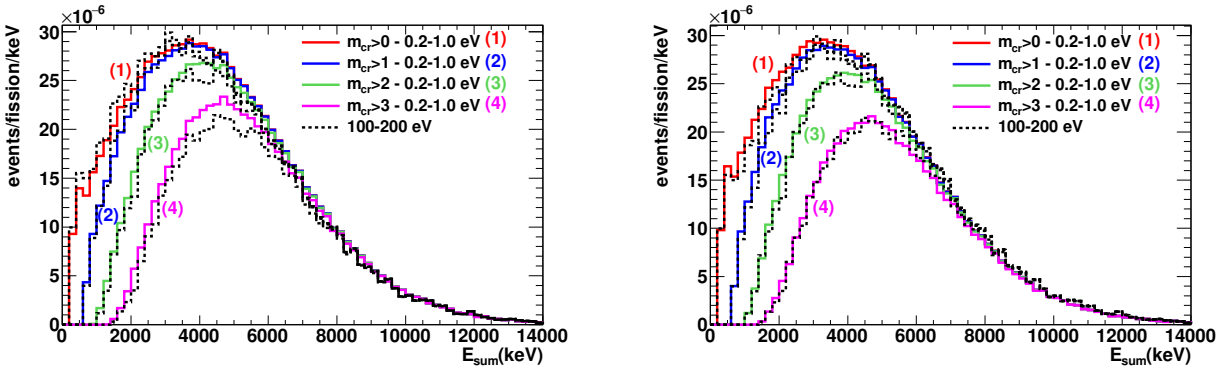

Figure 3.64: In the left hand panel, prompt fission γ-ray tagged deposited energy signatures for different crystals multiplicity measured at low neutron energies (solid colored lines) and high neutron energies (dashed black lines). In the right hand panel are the same deposited energy signatures but applying the dead time effects to the experimental data at low neutron energies.

Ratio between the TAC-FTMG and the FTMG the total fission events detected by the FTMG

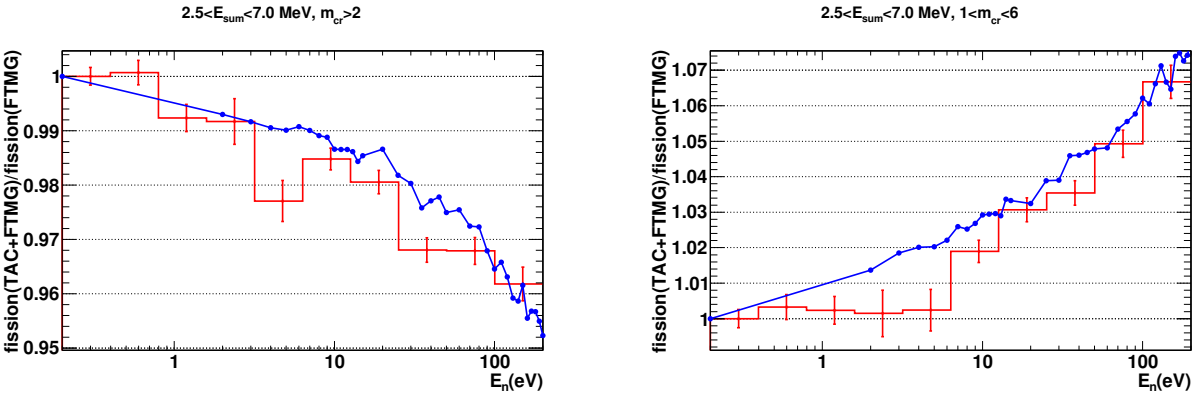

Figure 3.65: Ratio between the tagged counts detected in the TAC and the fission counts detected in the FTMG as a function of the neutron energy for different analysis conditions in the TAC. The red line is the experimental data and the blue line is the expected one from the dead time model.

Another aspect of the dead time corrections that have been validated is the ratio between the tagged fission counts detected by the TAC and the total number of fission events detected by the FTMG. Since the FTMG are considered free of dead time effects, the ratio between these two quantities offers information about the dead time effects for different cuts applied to the TAC as a function of the neutron energy.

Two examples are shown in both panels of Fig. 3.66. The red lines are the experimental ratio between the number of tagged prompt fission γ-ray cascades for a given analysis cut and the total fission detected by the FTMG as a function of the neutron energy. The blue line is the same ratio, calculated using the prompt fission γ-ray distribution obtained at low neutron energy range, and applying the dead time effects. As is shown, a high level of agreement is obtained for both cases in the figure 3.66.

Through these three checks, the conclusion drawn is that the dead time model developed corrects in a very precise way the three different fundamental aspects:

- The individual deposited energy detected by the individual BaF_2 crystals.
- The deposited energy detected by the TAC for different crystal multiplicity and deposited energy.
- The behavior of the dead time effects as a function of neutron energy.

3.9.3 Dead time corrections for the ^{235}U(n,γ) cascades

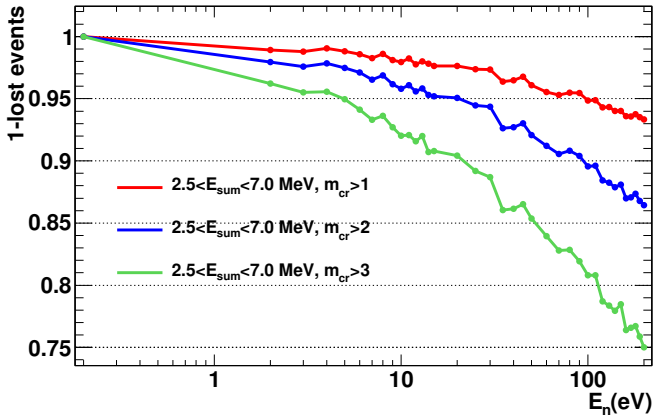

Figure 3.66: Lost detection probability for the ^{235}U(n,γ) cascades as a function of the neutron energy, from 0.2 to 200 eV.

The dead time corrections for the ^{235}U(n,γ) cascades, as a function of the neutron energy, are then calculated by the methodology before being explained. Hence, the efficiency in detecting the ^{235}U(n,γ) cascade has been calculated for a specific analysis conitions applied to the TAC.

In Fig. 3.66 is shown the dead time correction as a function of the neutron energy for three different conditions applied to the TAC events. The more restrictive are the conditions applied to the TAC, the greater are the dead time corrections, reaching more than 20% at 200 eV.

The dead time correction applied to the ^{235}U(n,γ) data introduces a systematic uncertainty that must be considered. In order to estimate the systematic uncertainty due to this correction, the experimental ^{235}U neutron capture cross-section has been obtained for different conditions applied to the TAC events in m_{cr} and E_{sum} finding compatible results in the neutron resonances. For this reason we estimate that the systematic uncertainty due to the dead time corrections, calculated as the standard deviation observed in the neutron resonances between the neutron capture cross-section calculated for different conditions, is 0.8% in the whole neutron energy range of the measurement, from 0.2 to 200 eV. This systematic uncertainty source is, compared with other, small enough not to be taking into account for the determination of the neutron capture cross-section.

Chapter 4

The experimental ^{235}U(n,γ) cross-section

This chapter is devoted to presenting the results of the experimental ^{235}U(n,γ) cross-section obtained from the analysis shown in chapter 3. The chapter is organized as follows:

- In the section 4.1 the choice of the analysis conditions for the calculation of ^{235}U(n,γ) cross-section is described.
- In the section 4.2 the estimated systematic uncertainties are presented.
- The section 4.3 shows the comparison of the obtained experimental ^{235}U(n,γ) cross-section obtained in the different experimental configurations.
- The section 4.4 gives the results obtained from this work, including the comparison with evaluated libraries and previous measurements.
- The section 4.5 presents the ENDF/B-VIII.0 (Beta-II) neutron library for the ^{235}U isotope released from the CIELO pilot project [12] after the incorporation this work with the new available experimental measurements.

4.1 Analysis conditions for the ^{235}U(n,γ) cross-section

In order to improve the ^{235}U(n,γ) signal-to-background ratio, specific conditions were applied to the TAC events. The more restrictive are the conditions, the better is the ratio, but the TAC detection efficiency is lower, thus compromising the statistics achieved and increasing the sensitivity of the ^{235}U(n,γ) cross-section to the background subtraction and corrections applied.

In Fig. 4.1 the signature of the different components detected by the TAC is shown. In the left hand panel the m_{cr} distributions are shown: the background events related to the dead material intercepting the neutron beam and the no-beam background is indicated by the blue line; the tagged prompt fission background is indicated by the red line; and the ^{235}U(n,γ) events obtained from the Monte Carlo simulations are shown as the green line. In the right hand panel the deposited energy signature for these components is given: the experimental deposited energy shape of the ^{235}U(n,γ) reactions is shown by the pink line; the tagged prompt fission is indicated by the red line; the background due to the dead material intercepting the neutron beam is shown by the blue line; and the no-beam background is indicated by the green line. Therefore, paying attention to the different component distributions, the conditions that improve the signal to background ratio are chosen as follows:

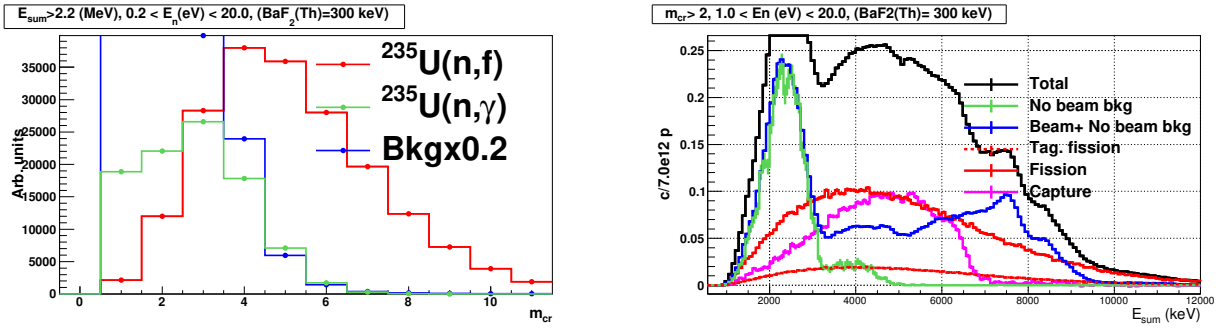

Figure 4.1: In the left hand panel, m_{cr} distribution for E_{sum} >2.2 MeV of the different components detected by the TAC. In the right hand panel, E_{sum} distribution is shown for the deposited energy signature of these components for m_{cr} >2 at low neutron energies.

- **Conditions applied to m_{cr}**: The non-related background events of the prompt fission component are strongly suppressed for m_{cr} >2-3. In addition, due to the m_{cr} signature of the (n,γ) and (n,f) events, the prompt fission background is strongly suppressed, removing the events with m_{cr} >5. Thus, the best conditions in crystal multiplicity are: 2<m_{cr} <6 and/or 3<m_{cr} <6.
- **Conditions applied to E_{sum}**: Background events non-related to the prompt fission component are strongly suppressed for E_{sum} >2.5 MeV. In addition, as is shown in the right hand panel of Fig. 4.1 the deposited energy of the ^{235}U(n,γ) reactions is not detected above 7.0 MeV. Thus, the signal-to-background ratio is improved, excluding the events with E_{sum} >6.5-7.0 MeV. Therefore, the best conditions for the signal to background ratio in E_{sum} are 2.5<E_{sum} <6.5 MeV and/or 2.5<E_{sum} <7.0.

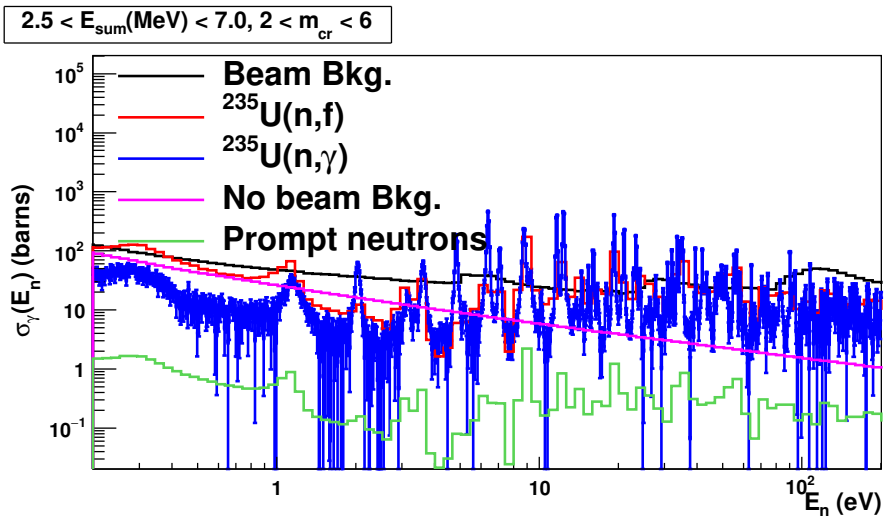

Figure 4.2: $^{235}U(n,\gamma)$ cross-section from 0.2 to 200 eV for the specific conditions: 2.5<E_{sum} <7.0 and 2<m_{cr} <6. In addition, all the background components subtracted are shown.

We have finally selected the following conditions of the TAC events: 2.5<E_{sum} <7.0 and 2<m_{cr} <6, because they are a satisfactory compromise between the TAC detection efficiency and the improvement of

the signal-to-background ratio. Fig. 4.2 shows the experimental ^{235}U neutron capture cross-section obtained by applying the best conditions, including all the components subtracted.

4.2 Systematic uncertainties

Fig. 4.3 shows the different systematic uncertainty sources considered for the ^{235}U(n,γ), integrated in the neutron resonances for the different neutron energy periods.

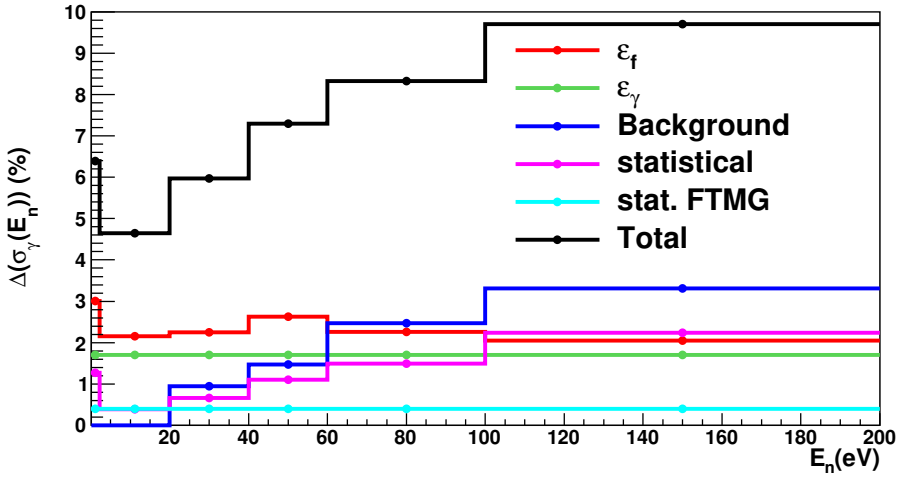

Figure 4.3: Systematic uncertainty sources for the different neutron energy periods. The black line represents the total uncertainty for each period, calculated as the linear sum of statistical and systematic sources.

The uncertainty sources are separated as follow:

- **The TAC detection efficiency,** ε_γ: as was explained in the section 3.6, the systematic uncertainty in this parameter is:

$$\Delta(\varepsilon_\gamma) = 1.7\% \tag{4.1}$$

  Thus, propagated in the ^{235}U(n,γ) cross-section this produces an uncertainty of 1.7% for the entire neutron energy range as is shown by the green line in Fig.4.3.

- **The Fission detection efficiency and the fission tagging detection efficiency,** ε_f **and** ε_f^*: The systematic uncertainty in both parameters has been propagated in the neutron capture cross-section. Integration along the different neutron energy periods is shown by the line in Fig. 4.3. The uncertainty for the individual resonances is shown by the red lines in the bottom panels of Fig. 4.5, 4.6, 4.7, 4.8, 4.9 and 4.10.

- **The correction applied to the beam background**: The uncertainty of this correction, explained in the section 3.4.2, was propagated in the neutron cross-section and is shown for the different neutron energy periods by the blue line in Fig. 4.3. The uncertainty for the individual resonances is shown by the blue lines in the bottom panels of Fig. 4.5, 4.6, 4.7, 4.8, 4.9 and 4.10.

- **Additional uncertainty due to the normalization**: Due to the normalization performed on the experimental cross-section, as explained in the section 3.8, an additional 0.4% of systematic uncertainty must be added along the entire neutron energy range due to the statistics achieved by the FTMG detectors as shown by the light blue line in Fig. 4.3.
- **The pile-up corrections**: The uncertainty due to pile-up corrections, for the conditions used for the calculation of the ^{235}U(n,γ) cross-section, has been considered low enough, when compared with the rest of systematic uncertainties, not to be taken into account for the calculation.
- **The subtraction of the prompt fission neutrons**. The uncertainty in the determination of the background induced by the prompt fission neutrons has been considered low enough to be excluded from the calculation. Even if we consider an uncertainty of 20% in the determination of this component, the contribution to the total systematic uncertainty is very low (1.0%).

In addition, Fig. 4.3 shows the statistical and systematic uncertainties integrated in the cross-section resonances for the different neutron energy periods (pink line) and the total uncertainty (black line), calculated as the linear sum of the systematic and statistical components.

4.3 Comparison between the results obtained with the 2FTMG and the 10FTMG configurations

The ^{235}U(n,γ) cross-section obtained for the different experimental configurations has been compared at low neutron energies, in the first largest neutron resonances. The background due to dead material intercepting the neutron beam for the 10FTMG experimental configuration is much larger when compared to the 2FTMG configuration. For this reason, the data of the 2FTMG experimental configuration was used for the calculation of the ^{235}U(n,γ) cross-section. However, the comparison is necessary for two reasons:

- **Validation of the prompt fission background subtraction**: For the 10FTMG experimental configuration, ε_f is much larger when compared to the 2FTMG. Thus, for the 10FTMG configuration the prompt fission background subtraction is more accurate. The comparison permits us to validate the reliable subtraction of the prompt fission background for the 2FTMG experimental configuration.
- **Validation of the normalization performed**: The compatibility of the experimental ^{235}U(n,γ) cross-section for both configurations also validates the normalization of the experimental data to the well-known ^{235}U(n,f) cross-section.

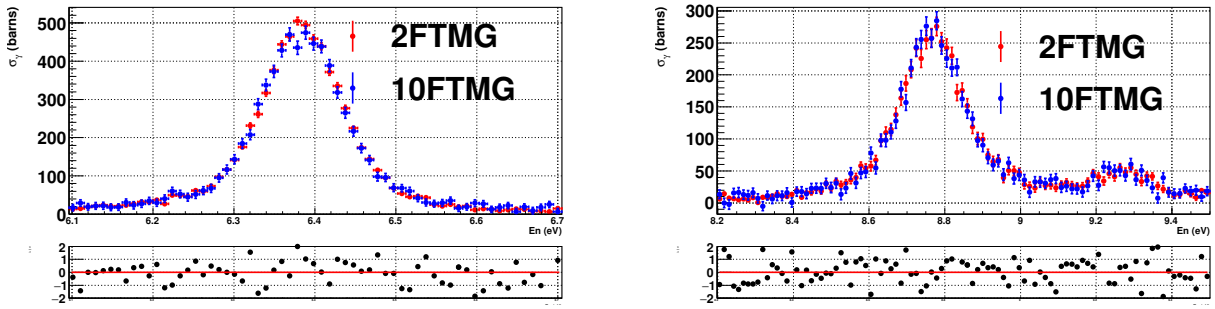

Figure 4.4: Comparison between the ^{235}U(n,γ) cross-section obtained from 2FTMG and the 10FTMG experimental configuration in the largest neutron resonances at low neutron energy: in the left hand panel, for the neutron energy range from 6.1 and 6.6 eV; in the right hand panel for the neutron energy range from 8.2 eV to 9.5 eV.

The ^{235}U(n,γ) cross-sections obtained for both experimental configurations are shown in both panels of Fig. 4.4: the 2FTMG configuration data are shown by the red points and the 10FTMG configuration data are shown by the blue points. The left hand panel shows the results for the neutron energy period from 6.1 to 6.6 eV and the right hand panel for the neutron energy range from 8.2 eV to 9.5 eV. The residuals between the two configurations, computed as y_1-$y_2/\sqrt{\sigma_1^2+\sigma_2^2}$, are shown in the bottom panels of the same figure. In terms of absolute value, the ^{235}U(n,γ) cross-sections obtained for both experimental configurations are compatible within 2%. Thus, compatible results are obtained, taking into account the systematic uncertainties and validating the prompt fission background subtraction.

Therefore, this calculation validates the prompt fission background subtraction and the normalization performed to the experimental ^{235}U(n,γ) cross-section calculated with the 2FTMG experimental configuration.

4.4 Results and comparison with evaluations and other experimental data

As was explained in the section 3.4.2, the correction applied to the beam background introduces large systematic uncertainties in the experimental ^{235}U(n,γ) cross-section integrated in large neutron energy ranges, specifically due to the valleys of the neutron resonances. For this reason, the comparison of the obtained experimental ^{235}U(n,γ) cross-section with the evaluations and other measurements has been performed in the neutron resonances. This section is organized as follows:

- The section 4.4.2 shows the comparison with the evaluated libraries ENDF/B-VII.1 [9], JENDL-4.0a [10], JEFF-3.2 [11] and the ENDF/B-VIII.0 (Beta-I) [12].
- The section 4.4.1 shows the comparison with other experimental data sets.

4.4.1 Comparison with the evaluated libraries

The obtained ^{235}U(n,γ) cross-section has been compared with the evaluations ENDF/B-VII.1 [1] and the ENDF/B-VIII.0 (Beta-I) released by the IAEA CIELO pilot project [12, 31]. For the comparison, the resonance parameters of the different evaluations were processed with SAMMY8 code [112] to take into account in the cross-section the Doppler broadening and resolution function of the n_TOF facility [62, 63, 64].

The comparison, for the different neutron energy periods is shown in Fig. 4.5, 4.6, 4.7, 4.8, 4.9 and 4.10. The top panel shows the point-wise ^{235}U(n,γ) cross-section as a function of the neutron energy: the data obtained from this work is shown by the blue points; ENDF/B-VII.1 is shown by the red line; and ENDF/B-VIII.0 (Beta-I) is shown by the green line. In the bottom panels of the same figures are shown the ratio between the experimental ^{235}U(n,γ) resonance integrals and the ENDF/B-VII.1, including the largest sources of systematic uncertainties: the uncertainty due to ε_f and ε_f^* is shown by the red line, and the uncertainty due to background correction is shown by the blue line. The statistical uncertainty is shown by the black points.

Figure	Neutron energy period	I(σ_γ(E$_n$))/I(ENDF/B-VII.1)	Sys. uncertainty (%)
4.5	0.2 – 2.2	1.03±0.01	5.1
4.6	2.2 – 20.0	1.088±0.004	4.2
4.7	20.0 – 40.0	1.072±0.007	5.3
4.8	40.0 – 60.0	1.10±0.01	6.1
4.9	60.0 – 100.0	1.09±0.02	6.8
4.10	100.0 – 200.0	1.06±0.02	7.4

Table 4.1: Ratio between the integral of the resonances from this work and ENDF/B-VII.1 for the different neutron energy periods. The final column shows the systematic uncertainty (in percent) for each neutron energy period.

The integral of the neutron resonances has been computed and compared with the ENDF/B-VII.1 for the different neutron energy periods as shown in the table. 4.1. The last column shows the systematic uncertainty (in percent) calculated for each neutron energy period.

The data obtained from this work is, in general, greater than the ENDF/B-VII.1. However, taking into account the uncertainties calculated, the ^{235}U(n,γ) cross-section obtained from this analysis is compatible with the evaluations.

[1] The evaluated libraries ENDF/B-VII.1, JEFF-3.2 and JENDL-4.0a have the same resonance parameters for the resolved resonance region. Hence, the ^{235}U(n,γ) cross-section is equally described by all the evaluated libraries.

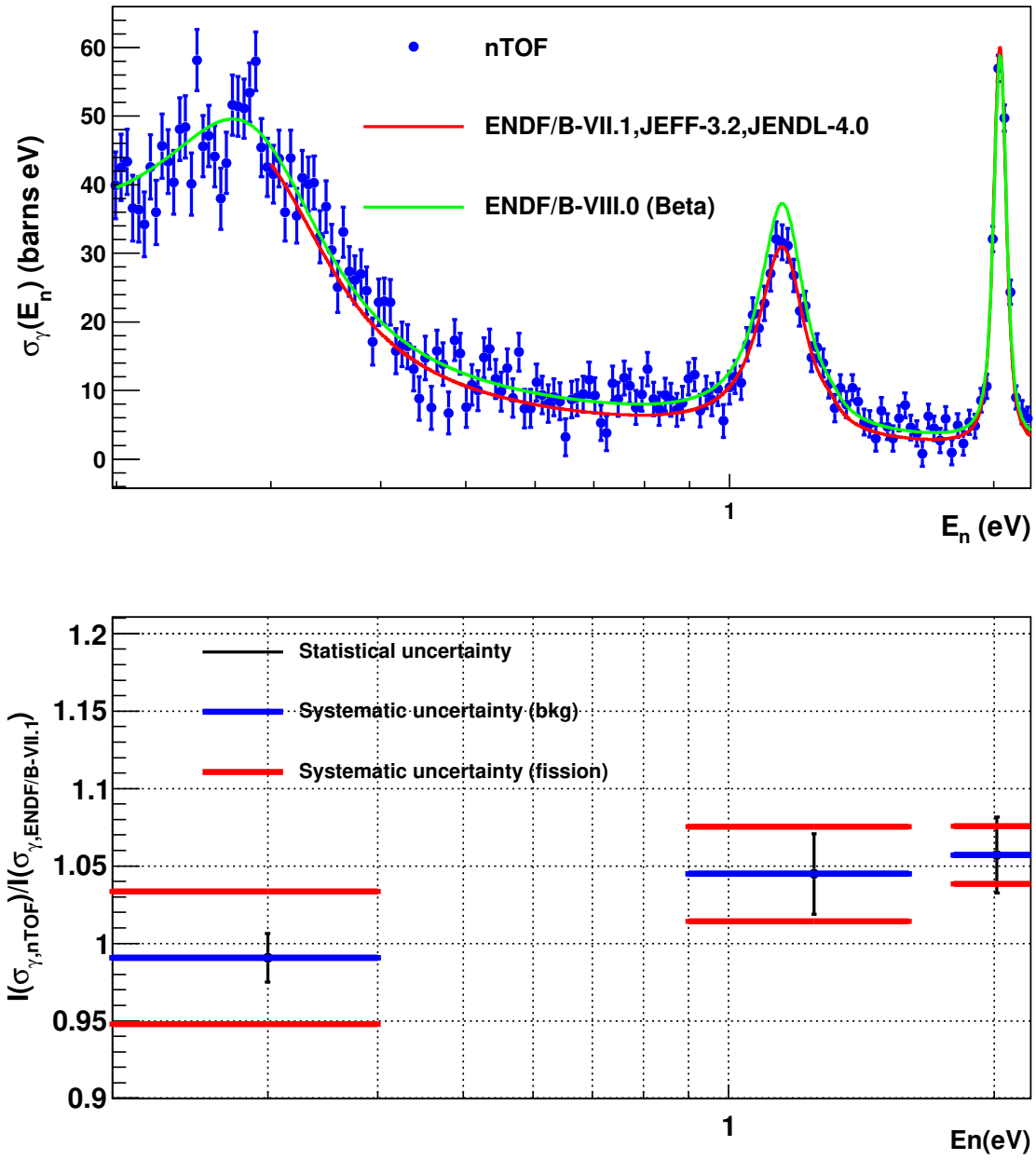

Figure 4.5: In the upper panel, the experimental $^{235}U(n,\gamma)$ cross-section compared with ENDF/B-VII.1, JEFF-3.2, JENDL-4.0a and the ENDF/B-VIII.0 (Beta) in the neutron energy range from 0.2 to 2.2 eV. In the lower panel, ratio of the experimental cross-ection resonance integrals compared to the evaluated data.

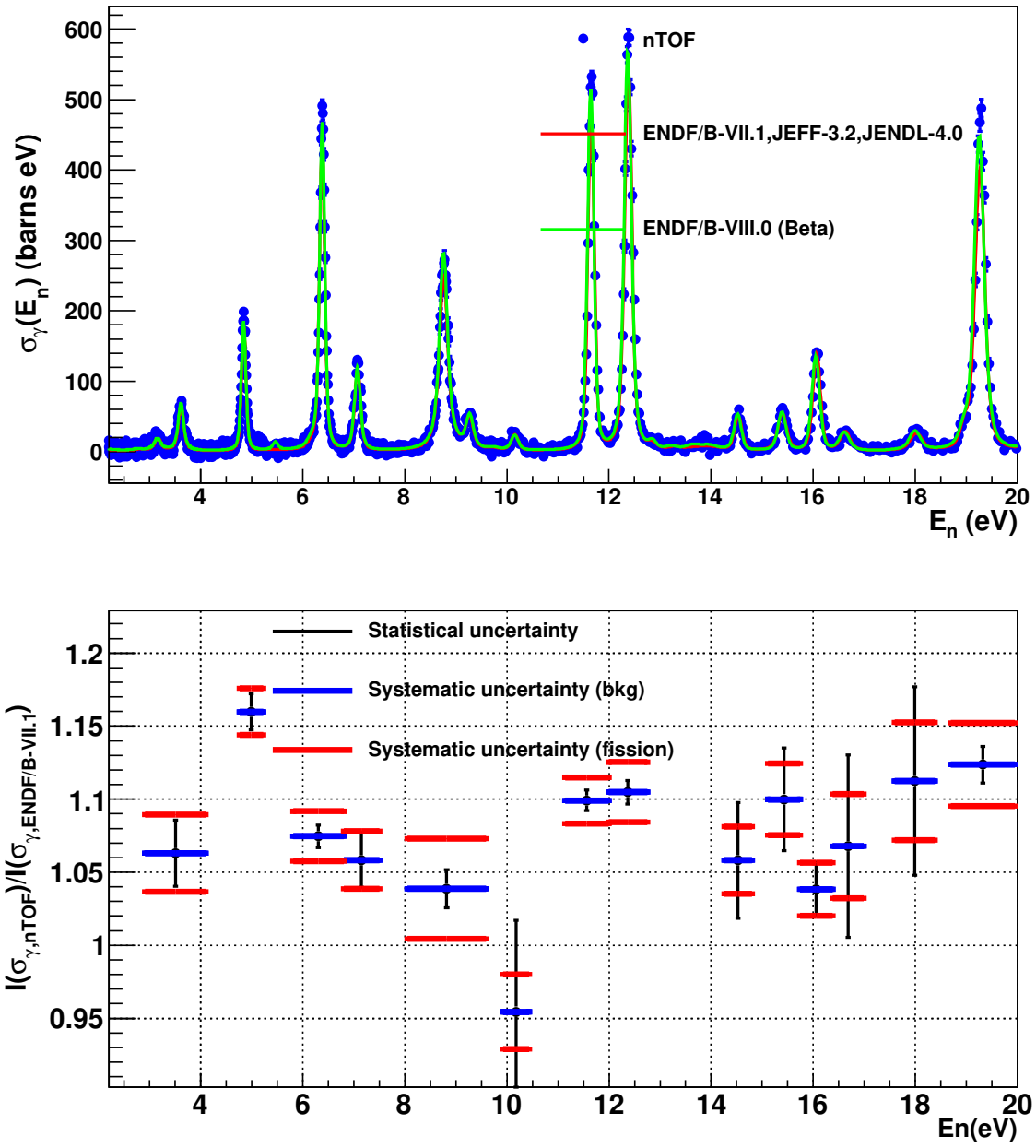

Figure 4.6: In the upper panel, the experimental $^{235}U(n,\gamma)$ cross-section compared with ENDF/B-VII.1, JEFF-3.2, JENDL-4.0a and the ENDF/B-VIII.0 (Beta) in the neutron energy range from 2.2 to 20.0 eV. In the lower panel, ratio of the experimental cross-section resonance integrals compared to the evaluated data.

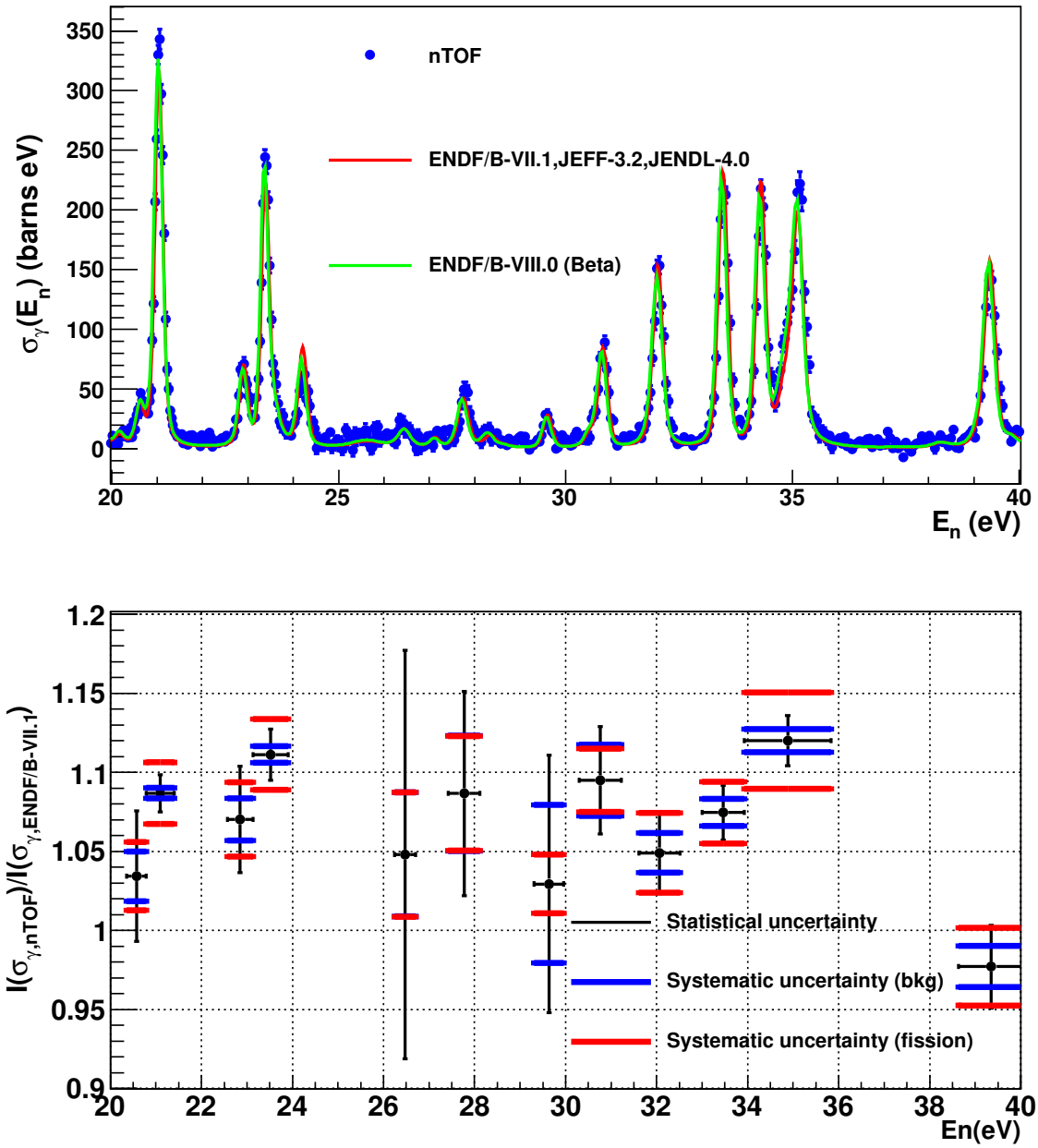

Figure 4.7: In the upper panel, the experimental $^{235}U(n,\gamma)$ cross-section compared with ENDF/B-VII.1, JEFF-3.2, JENDL-4.0a and the ENDF/B-VIII.0 (Beta) in the neutron energy range from 20.0 to 40.0 eV. In the lower panel, ratio of the experimental cross-section resonance integrals compared to the evaluated data.

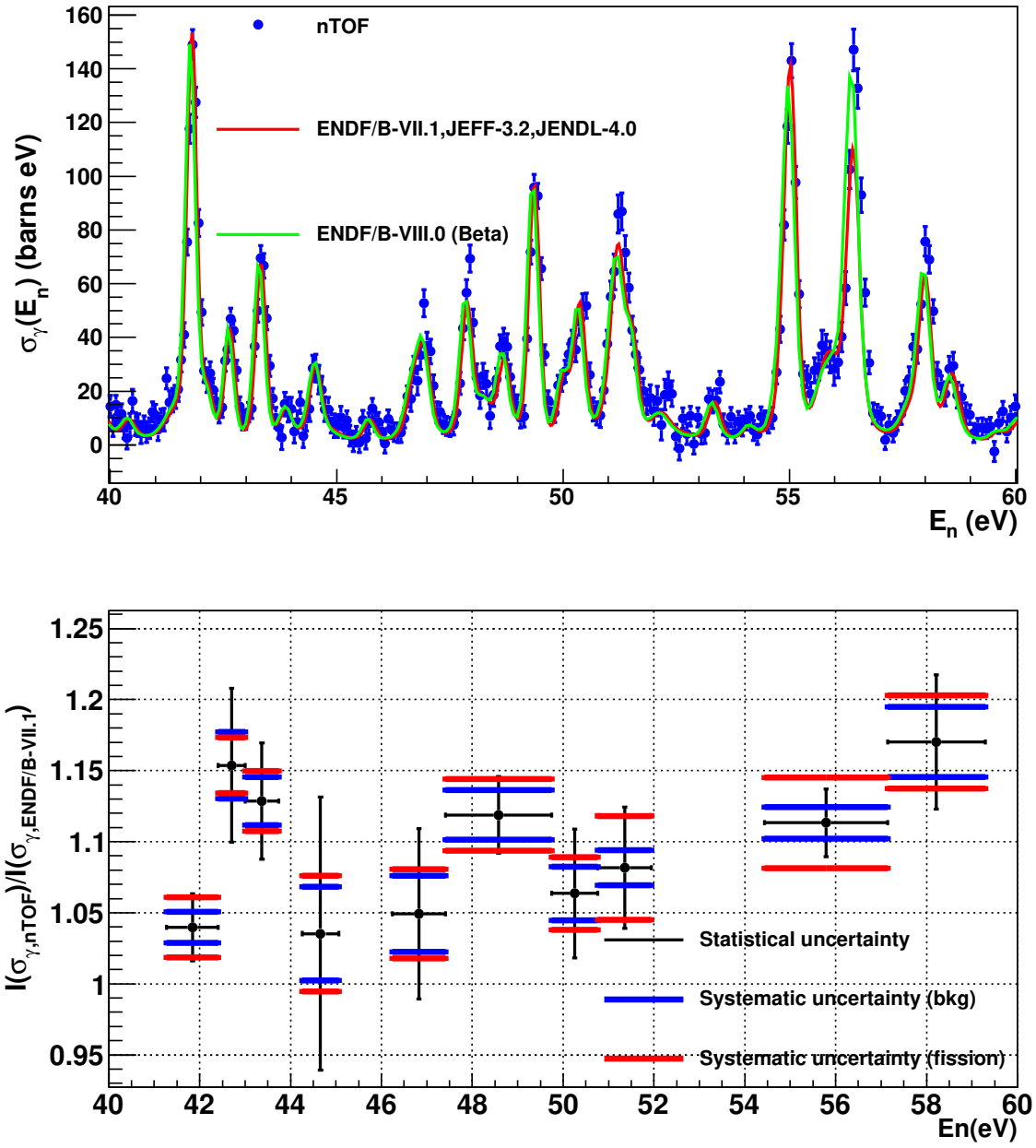

Figure 4.8: In the upper panel, the experimental $^{235}U(n,\gamma)$ cross-section compared with ENDF/B-VII.1, JEFF-3.2, JENDL-4.0a and the ENDF/B-VIII.0 (Beta) in the neutron energy range from 40.0 to 60.0 eV. In the lower panel, ratio of the experimental cross-section resonance integrals compared to the evaluated data.

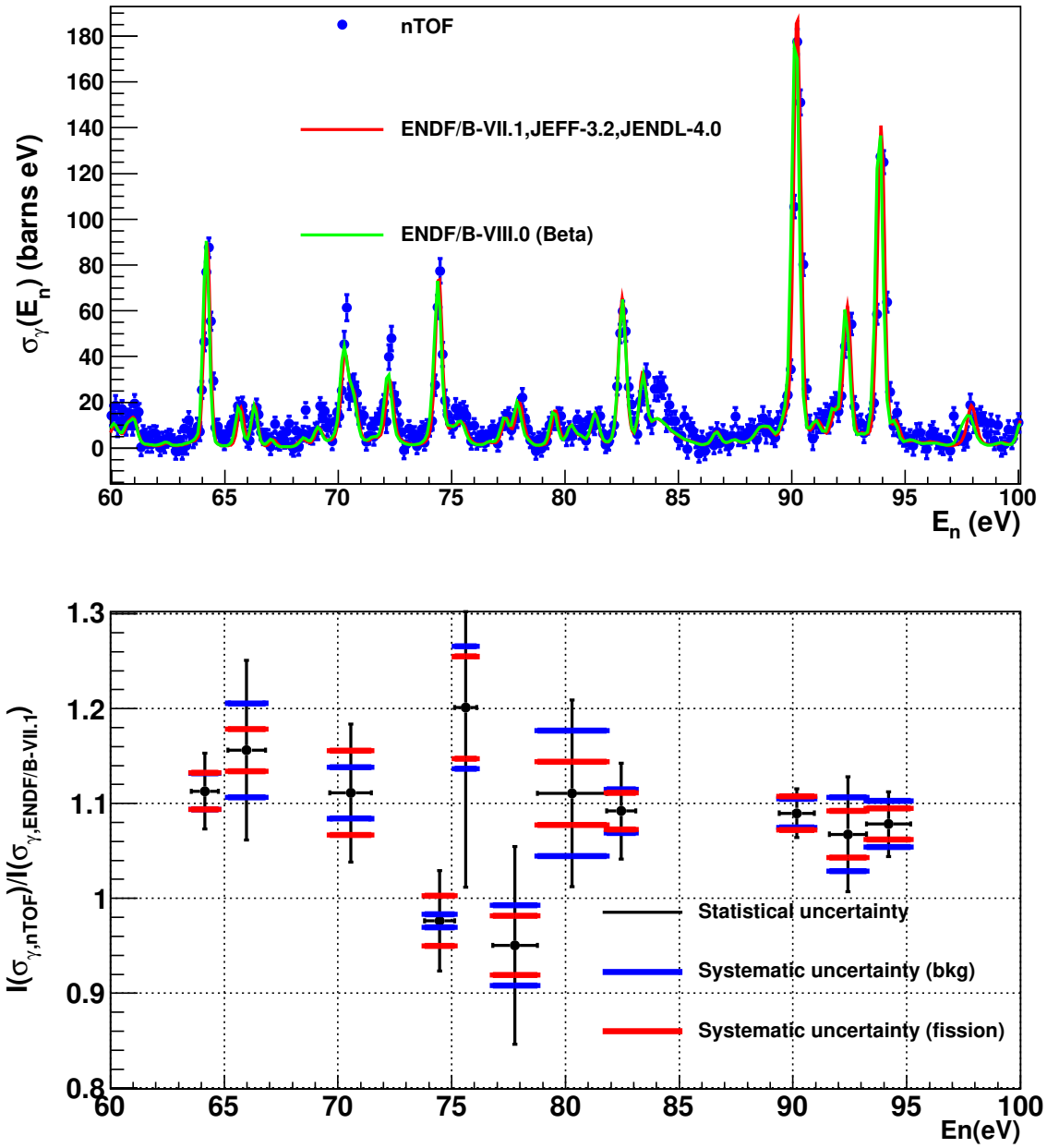

Figure 4.9: In the upper panel, the experimental $^{235}U(n,\gamma)$ cross-section compared with ENDF/B-VII.1, JEFF-3.2, JENDL-4.0a and the ENDF/B-VIII.0 (Beta) in the neutron energy range from 60.0 to 100.0 eV. In the lower panel, ratio of the experimental cross-section resonance integrals compared to the evaluated data.

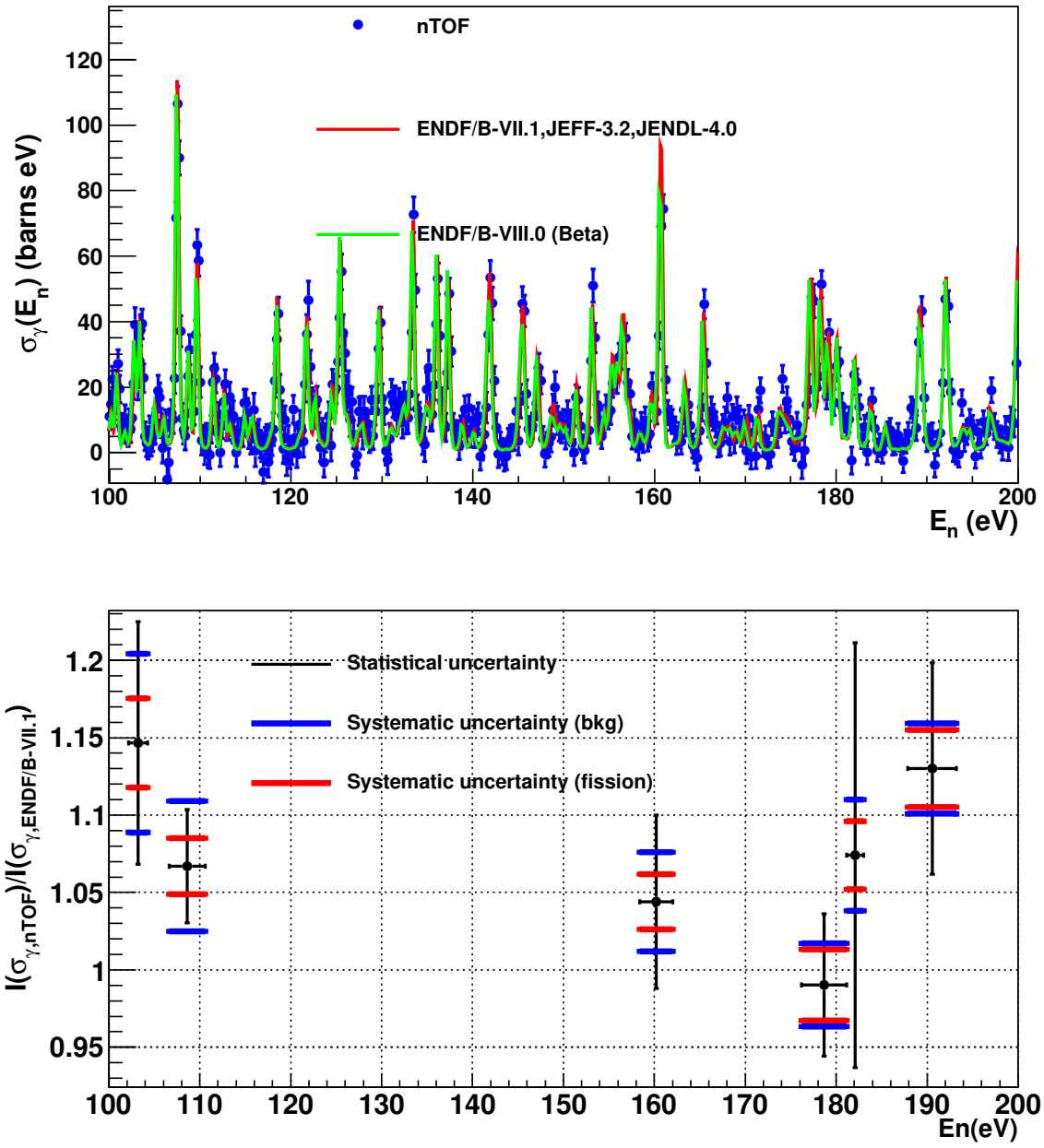

Figure 4.10: In the upper panel, the experimental $^{235}U(n,\gamma)$ cross-section compared with ENDF/B-VII.1, JEFF-3.2, JENDL-4.0a and the ENDF/B-VIII.0 (Beta) in the neutron energy range from 100.0 to 200.0 eV. In the lower panel, ratio of the experimental cross-section resonance integrals compared to the evaluated data.

4.4.2 Comparison with previous measurements

The obtained experimental ^{235}U(n,γ) and α-ratio has been compared with all the previous measurements overlapping within the neutron energy range. These experimental data sets, retrieved from the EXFOR database [24], are listed in the table 4.2.

Quantity measured	Author	Year	Neutron energy range (eV)	Reference
$\eta(E_n)$	H. Palevsky *et al.*	1956	0.01 - 0.9	[13]
$\eta(E_n)$	J. R. Smith *et al.*	1957	0.1 - 9.0	[14]
$\sigma_\gamma(E_n)$	G. de Saussure *et al.*	1966	0.4 - 62.0	[15]
$\int \sigma_\gamma(E_n)$	G. de Saussure *et al.*	1966	10.0- 1800.0	[15]
$\eta(E_n$	F.D. Brooks *et al.*	1966	0.9 - 200	[16]
$\int \sigma_\gamma(E_n)$	F.D. Brooks *et al.*	1966	10 - 200	[16]
$\sigma_\gamma(E_n)$	R.B. Perez *et al.*	1973	8.0 - 200.0	[17]
$\int \sigma_\gamma(E_n)$	G.V. Muradyan *et al.*	1977	100 - 20000	[18]
$\alpha_R(E_n)$	G.V. Muradyan *et al.*	1985	2.0 - 32.0	[19]
$\eta(E_n)$	H. Weigmann *et al.*	1990	0.001 0.4	[20]
$\sigma_\gamma(E_n)$	M. Jandel *et al.*	2012	4.0 - $8{\cdot}10^6$	[32]
$\sigma_\gamma(E_n)$	C. Guerrero *et al.*	2012	-	[23]

Table 4.2: List of ^{235}U(n,γ) cross-section measurements retrieved from the EXFOR database [24] overlapping within the neutron energy period in this work.

There are three different techniques for the determination of the ^{235}U(n,γ) cross-section, directly or by derived data, available in the database:

- The reactivity measurements (H.Palevsky [13], J. R. Smith [14], F.D.Brooks [16] and H.Weigmann [20]): The quantity measured is the reproduction factor, $\eta(E_n)$, defined as the ratio between the number of neutrons produced by the fission reactions divided by the total number of neutrons absorbed by the target sample. That is:

$$\eta(E_n) = \frac{\bar{\nu}\sigma_f(E_n)}{\sigma_f(E_n) + \sigma_\gamma(E_n)} \tag{4.2}$$

  where $\bar{\nu}$ is the average neutrons emitted per fission and $\sigma_f(E_n)$, $\sigma_\gamma(E_n)$ are the neutron-induced fission cross-section and the neutron capture cross-section respectively. The alpha ratio, $\alpha(E_n)$, is easily derived from this parameter:

$$\alpha(E_n) = \frac{\sigma_\gamma(E_n)}{\sigma_f(E_n)} = \frac{\bar{\nu}}{\eta(E_n)} - 1 \tag{4.3}$$

- The simultaneous measurement of the neutron capture and neutron-induced fission cross-section (G. de Saussure [15], R.B. Perez [17], M. Jandel [32], C. Guerrero [23] and this work): Despite the wide variety of scintillator detectors and fission chambers used for this technique, all the measurements are based on an accurate subtraction of the prompt fission background using the coincidences between the fission detection system and the γ-ray detection system.

- The multiplicity spectrometry technique, developed by G. V. Muradyan [19, 21]: This technique is based on the physical properties from the γ-ray cascades of the (n,f) and (n,γ) reactions. Due to the high efficiency and the different γ-ray multiplicity signature of the (n,f) and (n,γ) events observed by a high efficiency segmented detector, the neutron capture events are cascades efficiently discriminated

from the fission events and other background events [19]. Hence, the $\alpha(E_n)$ is determined observing the ratio between the (n,γ) and (n,f) events registered by the same detector.

The experimental ^{235}U(n,γ) cross-section obtained is compared with the results of measurements using the same technique [15, 17, 32] in Fig. 4.14 and Fig. 4.12. The left hand panel shows the point-wise experimental ^{235}U(n,γ) cross-section with the rest of the measurements and ENDF/B-VII.1 and the right hand panel presents the resonance integral for the different neutron energy periods.

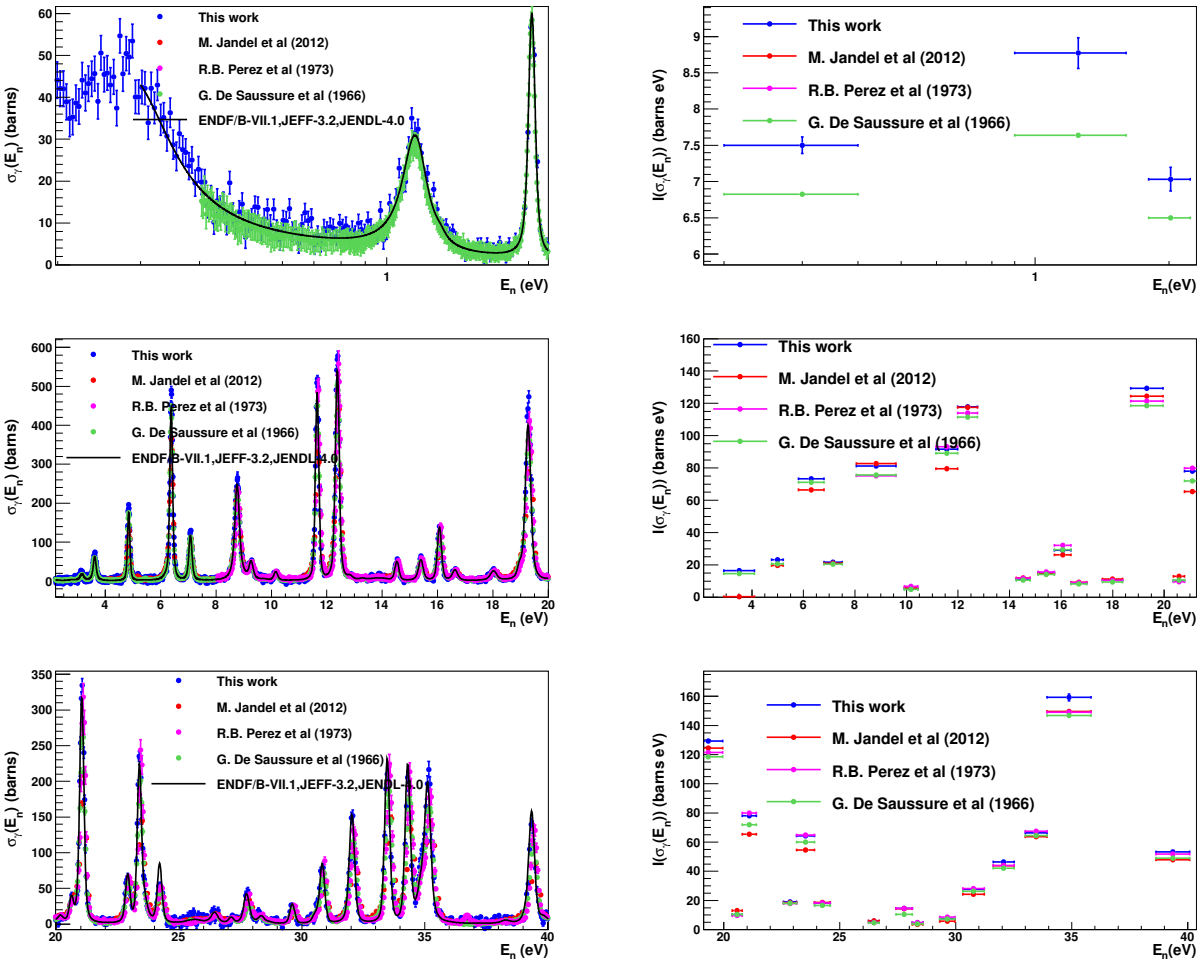

Figure 4.11: The left hand panel shows the n_TOF $^{235}U(n,\gamma)$ cross-section compared with the experimental data from G. De Saussure [15], R. B. Perez [17] and M. Jandel [32] for the neutron energy periods 0.2–2.2, 2.2–20 and 20.0–40.0 . The right hand panel shows the integral value of the resonances obtained for the same neutron energy periods.

The integral values for the different resonances were computed in the overlapping neutron energy periods as shown in the table 4.4 and table 4.5. The left hand panel of Fig. 4.13 shows the differences between resonance integrals for these measurements and this work where possible. On average, the data M. Jandel *et al.* and G. de Saussure *et al.* data sets are 6% lower than the experimental ^{235}U(n,γ) cross- section from

this work. The R.B.Perez *et al.* data is a 2% larger. The right hand panel of Fig. 4.13 shows the differences as functions of neutron energy.

Despite the different data sets being measured independently, they were not normalized. The G. de Saussure [15] experimental data was normalized to the ^{235}U(n,γ) cross-section estimated by F.J Shore and V.L Sailor (1958) [22] at low neutron energies, from 0.45 eV to 1.0 eV. This normalization was preferred to the normalization calculated by themselves to the ^{235}U(n,f) cross-section in order to reduce the systematic uncertainty associated [15]. In the case of the R.B. Perez *et al.* data set [17], the neutron capture cross-section was normalized to the neutron evaluated ENDF/B-V data in the neutron energy range from 100 to 200 eV, derived from the G. de Saussure [15] experimental data. The M. Jandel *et al.* experimental data set [32] was normalized to the integral value of the ENDF/B-VII.1 ^{235}U(n,γ) cross-section in the neutron energy range from 45 to 100 eV. The values used for the normalization of each individual experimental data set are shown in the table 4.3.

Exp. data set	Normalization (barns·eV)
G.de Saussure *et al.* [15]	$\int_{0.4eV}^{1eV} \sigma_\gamma(E_n)dE_n$=53.02
R.B.Perez *et al.* [17]	$\int_{100eV}^{200eV} \sigma_\gamma(E_n)dE_n$=1145
M.Jandel *et al.* [32]	$\int_{45eV}^{100eV} \sigma_\gamma(E_n)dE_n$=837.8
This work	$\int_{7.4eV}^{11.0eV} \sigma_f(E_n)dE_n$=246±1

Table 4.3: Normalization for the different experimental data set used for the comparison with the ^{235}U(n,γ) cross-section obtained from this work.

In Fig. 4.14 is shown the α-ratio obtained from this work compared with the experimental data from Brooks [16], Muradyan [19, 21], Weigmann [20] and the α-ratio for the ENDF/B-VVI.1 library. As is shown, the α-ratio obtained in this work is compatible with these measurements.

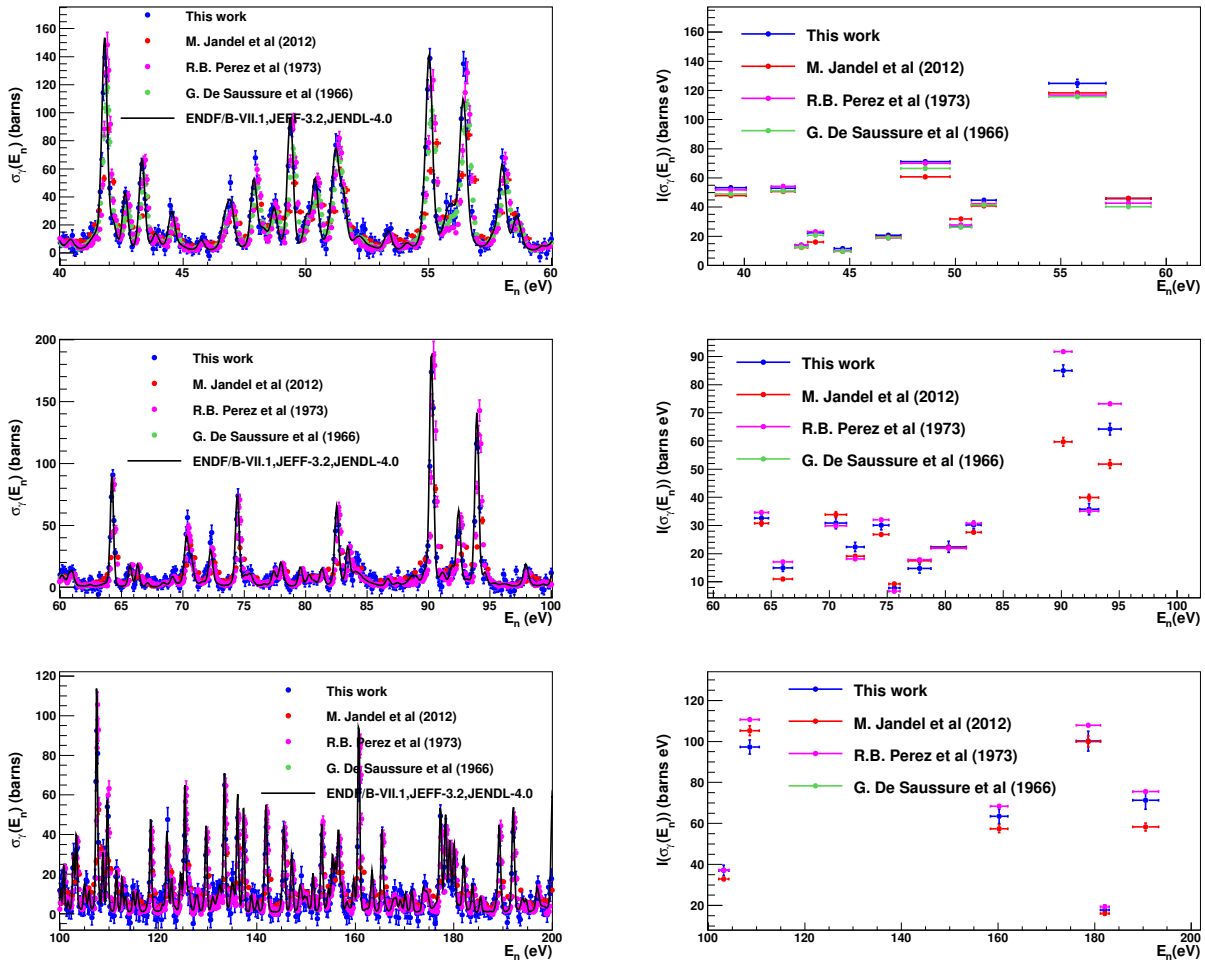

Figure 4.12: The left hand panel shows the n_TOF $^{235}U(n,\gamma)$ cross-section compared with the experimental data from G. De Saussure [15], R. B. Perez [17] and M. Jandel [32] for the neutron energy periods 40.0–60.0, 60.0–100.0 and 100.0–200.0 . The right panel shows the integral value of the resonances obtained for the same neutron energy periods.

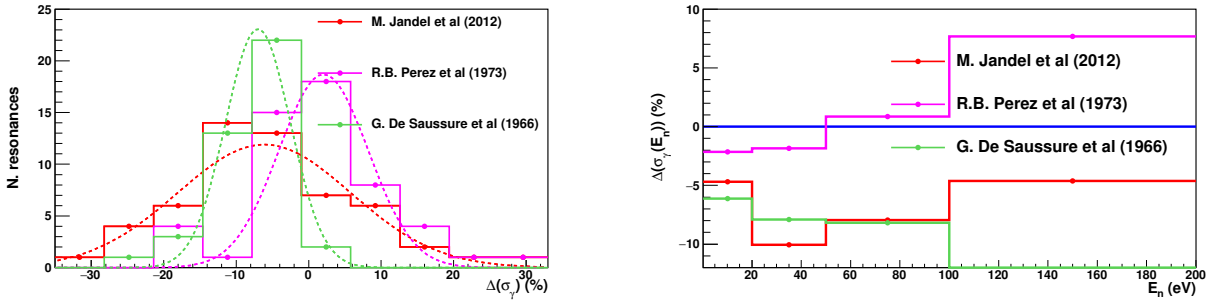

Figure 4.13: The left panel presents differences obtained in the neutron resonance integrals between this work and the different experimental data set as indicated. For G. de Saussure et al. [15] data, the differences are shown by the green line. For the R.B.Perez et al. [17] the data is shown by the pink lines and the differences obtained for M.Jandel et al. [32]
are shown by the red line.

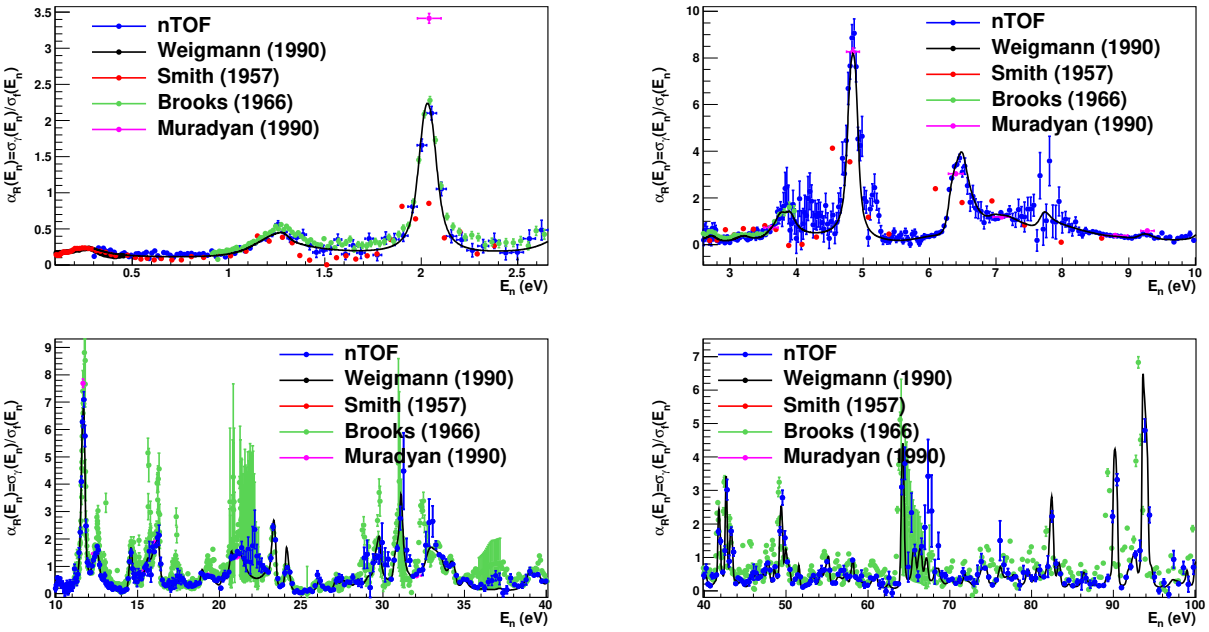

Figure 4.14: α_R obtained as a function of the neutron energy, compared with the data retrieved from [16, 19, 20, 21] for different neutron energy periods.

E_n (eV)	This work	M. Jandel (2012)	R.B. Perez (1973)	G. de Saussure (1966)
0.2–0.4	7.54±0.11	-	-	-
0.9–1.6	8.79±0.21	-	-	7.63
1.8–2.23	7.03±0.16	-	-	6.4
2.91–4.1	16.4±0.3	-	-	14.5
4.76–5.22	23.18±0.25	19.7±0.5	-	20.6
5.81–6.8	73.3±0.5	66.5±0.9	-	71.1
6.8–7.5	21.7±0.4	21.0±0.5	-	20.4
8.05–9.59	81±1	82.7±0.7	75.1	75.7
9.92–10.43	5.2±0.3	5.80±0.17	6.6	4.8
11.14–11.99	91.6±0.6	79.5±0.9	93.1	89.1
11.99–12.75	117.9±0.9	117±1	114.0	111.5
14.26–14.8	11.1±0.4	12±0.3	11.7	10.5
15.11–15.74	14.9±0.5	14.5±0.3	15.5	14.1
15.74–16.38	29.1±0.5	26.2±0.5	32.0	29.5
16.38–16.99	8.8±0.5	9.2±0.3	9.00	8.3
17.6–18.38	10.6±0.6	11.3±0.3	10.5	9.4
18.7–19.95	129±1	124±1	121	118
20.36–20.79	10.3±0.4	13.3±0.3	9.6	10.5
20.79–21.4	78.0±0.9	65.3±0.9	79.9	72.0
22.57–23.13	19.0±0.6	18.5±0.4	17.9	18.0
23.13–23.91	64±1	54.6±0.8	64	60
23.912–24.59	18.4±0.7	18.6±0.5	18.2	16.5
26.24–26.7	5.77±0.7	5.9±0.3	4.8	4.6
27.42–28.12	14.7±0.9	14.4±0.5	14.5	10.5
28.12–28.58	4.8±0.5	3.62±0.22	4.8	3.8
29.31–29.96	7.5±0.6	5.69±0.27	8.6	7.2
30.3–31.23	27.5±0.9	24.2±0.6	28.0	26.2
31.61–32.515	46±1	43.9±0.9	43	42.1
33–33.93	66±1	64±1	67	64
33.93–35.83	159±2	150±2	149	146
38.63–40.08	53±1	47.9±0.8	51	49
41.27–42.41	53±1	50.6±0.9	54	51
42.41–43	13.9±0.6	12.2±0.4	14.0	12.4
43–43.74	22.3±0.8	16.1±0.5	23.1	20.7
44.26–45.06	11±1	9.6±0.4	9.8	9.6
46.24–47.41	21±1	19.4±0.6	18	19.0
47.41–49.75	71±2	61±1	70	66.5
49.75–50.767	27±1	31.8±0.7	27	26.2
50.767–51.94	45±2	41±1	42	41.6
54.435–57.14	125±3	118±2	116	115
57.14–59.29	46±2	46±1	42	40

Table 4.4: Integral resonance value for the different experimental data sets. Only the statistical uncertainty is shown.

E_n (eV)	This work	M. Jandel (2012)	R.B. Perez (1973)	G. de Saussure (1966)
63.55–64.75	33±1	31±1	34	-
65.17–66.81	15±1	11.0±0.5	17	-
69.65–71.47	31±2	33±1.0	29	-
71.47–73	22±2	19.1±0.8	18	-
73.8–75.14	30±2	26.9±0.9	32	-
75.14–76.09	8±1	9.23±0.6	6	-
76.8–78.76	15±2	17.4±0.7	17	-
78.76–81.82	22±2	22.1±0.8	21	-
81.82–83.09	30±1	27.6±0.9	30	-
89.4–90.93	85±2	60±2	91	-
91.598–93.223	36±2	40±1	351	-
93.223–95.17	64±2	52±1	73	-
102.176–104.26	37±3	33±1	37	-
106.647–110.573	97±3	105±2	110	-
158.4–162.046	63±3	57±2	68	-
176.2–181.176	100±5	100±3	107	-
181.176–183.02	17±2	16±1	19	-
187.9–193.21	71±4	58±2	75	-

Table 4.5: Integral resonance value for the different experimental data sets. Only the statistical uncertainty is shown.

4.5 The ENDF/B-VIII.0 evaluated library

The obtained experimental ^{235}U(n,γ) cross-section was deployed to the IAEA CIELO project [12, 31] for evaluation together with all the experimental datasets available up to this moment. From this new evaluation, the ENDF/B-VIII.0, a new neutron data library for the ^{235}U isotope was produced. The library includes a new set of standard values for the ^{235}U at the thermal point shown in the table 4.6.

Quantity	ENDF/B-VII.1	ENDF/B-VIII.0 (Beta-II)	Δ (%)
σ_{el} (E_n=0.025 eV)	15.46±1.06 (barns)	14.09±0.22 (barns)	- 8.0
σ_f (E_n=0.025 eV)	584.25±1.11 (barns)	587.2±1.4 (barns)	+ 0.5
σ_γ (E_n=0.025 eV)	98.96±0.74 (barns)	99.3±2.0 (barns)	+ 0.3
ν (E_n=0.025 eV)	2.4355±0.0023	2.4250±.0045	+ 0.4

Table 4.6: Values of the elastic, fission and capture cross-sections and $\bar{\nu}$ at the thermal point taken from the ENDF/B-VII.1 and ENDF/B-VIII.0 (Beta-II) evaluated libraries.

All the updated standard values are statistically compatible (within 1 or 2 σ) with the values from the previous ENDF/B-VII.1 library. The elastic cross-section has been decreased 8%, and the neutron induced fission and capture cross-sections have been increased 0.5% and 0.3%, respectively. In addition, the $\bar{\nu}$ value has been increased to 0.4%.

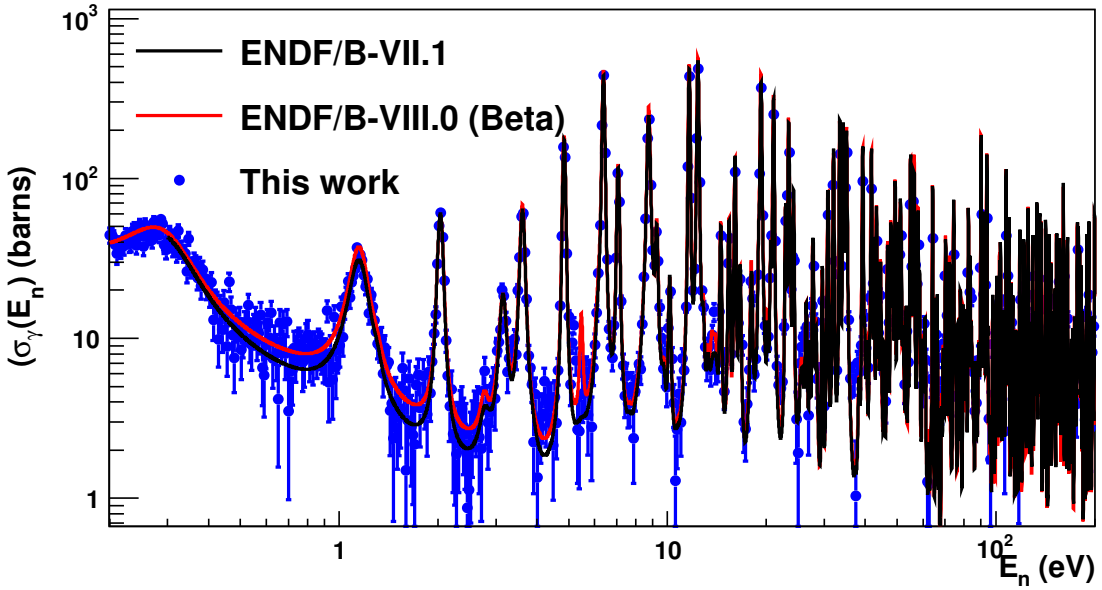

Figure 4.15: $^{235}U(n,\gamma)$ cross-section from ENDF/B-VII.1 and ENDF/B-VIII.0 (Beta-II) and the n_TOF data for the neutron energy range from 0.2 to 200 eV.

Concerning the resolved resonance region, which in the case of the ^{235}U isotope covers the neutron energy range from the thermal point up to 2.2 keV, we separate the results into two regions:

- **Neutron energy region from 0.2 to 200 eV**: In the neutron energy range from 0.2 up to 100 eV, the evaluated ^{235}U(n,γ) cross-section has been increased, on average, ∼5% as is shown in the left hand

panel of Fig. 4.16 in agreement with our experimental cross-section. In the neutron energy period covering 100 to 200 eV, despite the evaluation having lowered the neutron capture cross-section to 2%, our data is fully compatible for this period. The evaluations and the experimental data for this neutron energy range is shown in Fig. 4.15.

- **Neutron energy region from 200 eV to 2.2 keV**: For neutron energies above 200 eV, the new library decreased the ^{235}U(n,γ) cross-section in a factor -30% in the keV region, in agreement with the fast criticality experiments performed by the Japanese Nuclear Agency [29] and the experimental data from the DANCE experiment at Los Alamos [32]. The difference between evaluated libraries is shown in the right hand panel of Fig. 4.16.

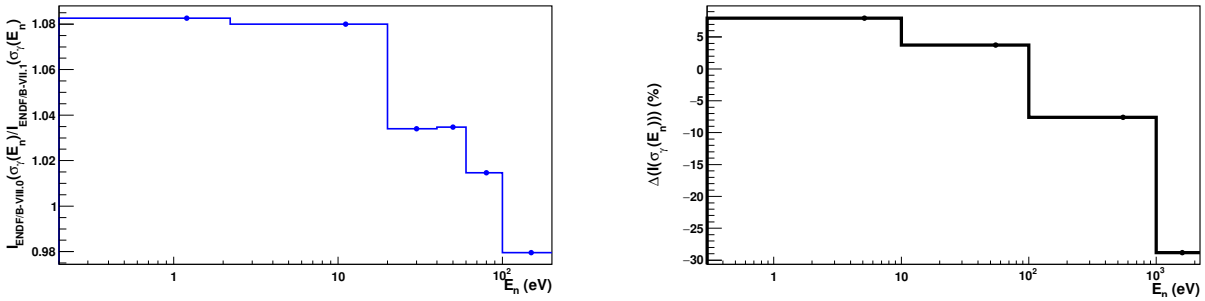

Figure 4.16: In the left hand panel is the ratio between the ENDF/B-VIII.0 (Beta-II) and ENDF/B-VII.1 for different neutron energy periods from 0.2 to 200 eV. In the right hand panel are the differences (in percent) of both libraries in the neutron energy range where the ^{235}U is described by the resonance parameters, from 0.2 up to 2.2 keV.

The contribution of the n_TOF data to this evaluation fulfills the main goal of this measurement: the dataset has been included in the evaluation of this important isotope, producing new resonance parameters that described the neutron capture cross-section in agreement with our experimental data, thus contributing to the design of new nuclear power reactor plants with improved levels of performance and efficiency.

Chapter 5

Summary, conclusions and future work

This manuscript describe the analysis performed to the measurement of the ^{235}U(n,γ) cross section at the CERN n_TOF facility in 2012. The aim of this measurement was the validation of the fission tagging technique using the n_TOF experimental setup as task 8.2 of CHANDA project [113] and provide to the nuclear data community a set of accurate experimental data with a good control and realistic values of the systematic uncertainties associated to the technique. This last issue is crucial for the work of the evaluators that combine the available measurements by weighting each of them by their reliability and accuracy.

The work presented in this manuscript is restricted to the analysis and data reduction performed to the experimental data, focused in the complementary methodology developed for the fission tagging technique [15, 17, 23, 32].

5.1 Analysis and data reduction

The neutron capture cross-section, $\sigma_\gamma(E_n)$, is usually measured by detecting γ-ray cascades after the formation of the compound nucleus. For the fissile nucleus the probability of a neutron producing a fission reaction is, on average, greater than that of producing a neutron capture reaction. Moreover, since the resonances are the excited levels of the compound nucleus, both cross-sections have the same resonant structure as a function of the neutron energy. In addition, the amount of γ-ray emitted in a fission reaction is larger than in a (n,γ) reaction. Thus, measuring (n,γ) reactions in fissile isotopes is challenging due to the fact that it competes with the fission reaction channel.

To accomplish the subtraction of the prompt fission background for the measurement of the ^{235}U(n,γ) cross-section, the fission tagging technique [15, 17, 23, 32] has been used. The main idea of the technique is to measure simultaneously the fission and capture reaction channels by means of fission and electromagnetic detectors respectively. By evaluating the time coincidence between both detection systems, the fission γ-ray cascades can be tagged. There are some difficulties inherent to the technique:

- The large amount of dead material intercepting the neutron beam: the fission tagging detectors, together with all the components of the fission chamber, must intercept the neutron beam, thus producing a large amount of background material which is detected by the γ-ray detector.

- The systematic uncertainties associated with the detection efficiencies: these parameters, critical for the determination of the ^{235}U(n,γ) cross-section, must be carefully determined.

- The low count statistics: for high efficiency in detecting fission fragments via fission detectors, the use of very thin targets with low mass is required. Therefore, the capture to background ratio will be lower compared to thicker samples, and longer periods of measurement are required.

The methodology requires:(i) high detection efficiency γ-ray detectors for (n,γ) cascades such as the segmented n_TOF Total Absorption Calorimeter (TAC) [58]; (i) high detection efficiency fission detectors for the (n,f) events, of low mass and sufficiently compact to fit inside the small fission chamber used in the experimental setup, such as Fission Tagging Micromegas detectors [59]. In the thin target approximation, the neutron capture cross-section is obtained as (see section 1.3)

$$\sigma_\gamma(E_n) = \frac{c_{tot}(E_n; E_{sum}, m_{cr}) - c_{Fiss}(E_n; E_{sum}, m_{cr}) - c_{Other}(E_n; E_{sum}, m_{cr})}{N_{norm}\varepsilon_\gamma(E_n, E_{sum}, m_{cr})\phi_N(E_n)} \tag{5.1}$$

where $c_{tot}(E_n;E_{sum},m_{cr})$ is the total counting rate of the Total Absorption Calorimeter, $c_{Fiss}(E_n;E_{sum},m_{cr})$ is the prompt fission background, $c_{Other}(E_n;E_{sum},m_{cr})$ is the rest of background components, $\phi_N(E_n)$ is the neutron fluence, $\varepsilon_\gamma(E_n,E_{sum},m_{cr})$ is the detection efficiency and N_{norm} is the normalization factor for the neutron capture cross-section.

The prompt fission background is determined by the fission tagging technique [23, 32], obtained from the number of coincidences between the fission and γ-ray detection systems, $c_{tagg}(E_n)$, divided by a factor labelled here as fission tagging detection efficiency, ε_f^*, which takes into account that not all fission events are tagged by the fission detection system. Then:

$$c_{Fiss}(E_n) = \frac{1}{\varepsilon_f^*} c_{tagg}(E_n) \tag{5.2}$$

The neutron capture cross section strongly depend on the ε_f^* parameter. In the particular case of the ^{235}U, $\sigma_f(E_n)/\sigma_\gamma(E_n)$ the ratio depends on the resonance but it is, on average, a factor of 2-3. Thus, for an uncertainty of 1% in the fission tagging detection efficiency parameter, this introduces to the neutron capture cross section a systematic uncertainty of 3-4%. Therefore, the determination of this parameter is critical for the accurate calculation of the neutron capture cross-section.

The data analysis involve the data reduction of a complex experimental setups including a large number of detectors and their correlations. In this section, we summarize the critical parts of the analysis during the ^{235}U(n,γ) cross section measurement:

- Coincidence analysis between the TAC and the FTMG detectors.
- Fission tagging detection efficiency and fission detection efficiency
- The TAC detection efficiency for the ^{235}U(n,γ) reactions.
- The dead time corrections applied to the neutron cross-section.

5.1.1 Coincidence analysis and the (n,γ f) process

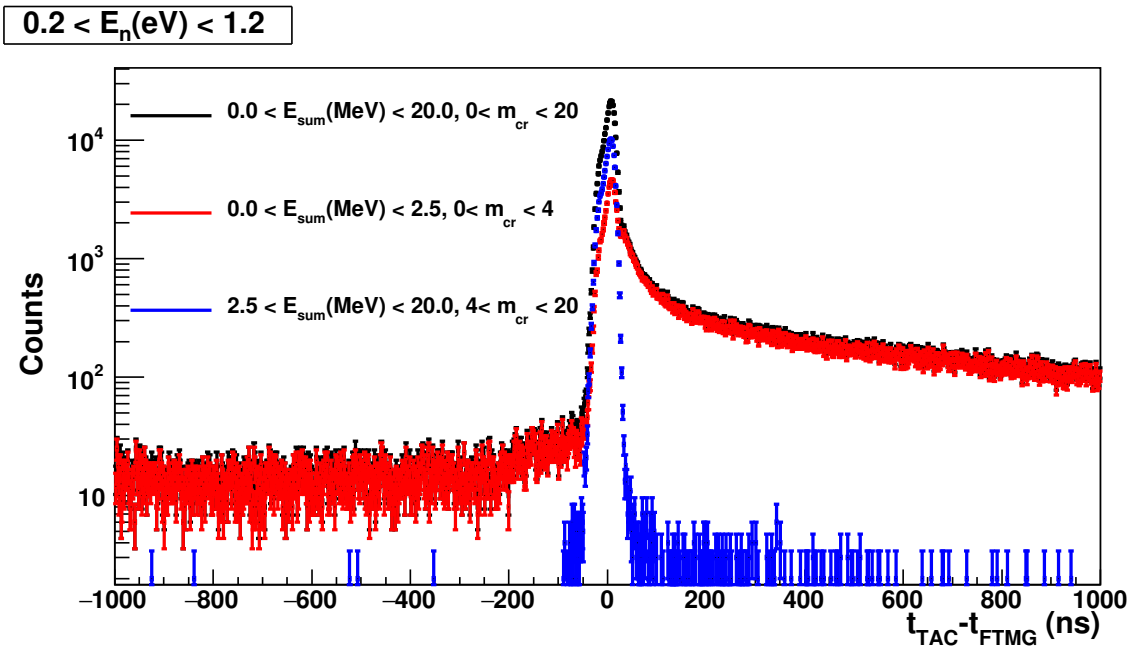

Figure 5.1: Time coincidence events distribution between the TAC and the FTMG detectors for different conditions applied to the TAC signals in the neutron energy range from 0.2 to 1.2 eV.

Fig. 5.1 shows coincidence time distribution between the TAC and the FTMG detectors. On the x-axis, the time difference t_{TAC}-t_{FTMG} is shown for different conditions applied to the TAC signals. The optimum coincidence-time window was selected attending to two opposite criteria: the maximization of prompt-fission γ-ray cascades tagged as fission events included in the coincidence time window, requirement for the correct determination of the fission detection efficiency, and the minimization of the random coincidences with other background sources and (n,γ) events. Thus, the coincidence-time window selected attending to the high crystal multiplicity events (m_{cr} >5) with a total width of 80 ns, (-50,30) ns, covering more than 99% of the event distribution.

In the coincidence analysis was observed also a process compatible with the physics characteristic of the (n,γ f) event [97] from the coincidence analysis performed to the events detected in coincidence between the TAC and the FTMG detectors. The analysis leads a fission isomer with the characteristics described in the table 5.1.

E_n(eV)	$T_{1/2}$ (ns)	(n,γf)/(n,f) (%)
0.2 – 1.2	68(6)	0.12(1)
1.2 – 12.0	66(3)	0.28(4)

Table 5.1: Values obtained for fission isomer the half life and ratio between (n,γf) and prompt (n,f) events for different neutron energy periods. The uncertainty given is only statistical.

5.1.2 Fission tagging detection efficiency and fission detection efficiency

The fission detection efficiency and the fission tagging detection efficiency are closed related quantities. We consider that both quantities do not depend on the neutron energy. Their definitions are given by:

- **The fission detection efficiency**, $\varepsilon_f(\mathrm{A}_{th})$: this is the probability of detecting a fission reaction induced in any of the ten ^{235}U samples by the FTMG detectors. This quantity depends only on the amplitude threshold applied to the FTMG events, A_{th}.
- **The fission tagging detection efficiency**, $\varepsilon_f^*(\mathrm{A}_{th},\mathrm{E}_{sum},\mathrm{m}_{cr})$: this is the factor needed to rescale the tagged fissions for the prompt fission background subtraction. This factor, by definition, is the ratio between the tagged fission counts, $\mathrm{c}_{Tagg}(\mathrm{A}_{th},\mathrm{E}_{sum},\mathrm{m}_{cr})$, and the total fission counts detected by the TAC, $\mathrm{c}_{Fiss\_TAC}(\mathrm{E}_{sum},\mathrm{m}_{cr})$:

$$\varepsilon_f^*(A_{th},E_{sum},m_{cr}) = \frac{c_{Tagg}(A_{th},E_{sum},m_{cr})}{c_{Fiss\_TAC}(E_{sum},m_{cr})} \tag{5.3}$$

In the case that the probability of detecting a fission reaction in one of the detectors does not depend on whether it has been detected in the other detector [23], then: (i) the fission tagging detection efficiency, $\varepsilon_f^*(\mathrm{A}_{th})$, and the fission detection efficiency, $\varepsilon_f(\mathrm{A}_{th})$, are the same quantity; (ii) as a consequence of (i), the fission tagging detection efficiency depends only on A_{th}:

$$\varepsilon_f^*(A_{th},E_{sum},m_{cr}) = \varepsilon_f^*(A_{th}) \tag{5.4}$$

As it was explained in the analysis, the inherent correlation of the prompt fission γ-ray cascades with the primary fission fragments produced in the scission process introduce undesired correlations in the simultaneous detection of the (n,f) events by the FTMG and the TAC. This correlation wasn't reported in the previous works with similar setups [23, 32] and constitute one of the larger source of systematic uncertainty. This correlation introduces heavy consequences in the analysis:

1. The fission tagging detection efficiency, ε_f^*, depend slightly on the conditions applied to the TAC and the FTMG as it shown in Fig. 5.2. Thus, this quantity can not determined for the (n,γ) conditions using restrictive conditions applied to the TAC events.
2. The fission tagging detection efficiency and the fission detection efficiency are not the same quantity.

Since the experimental correlation is small, both quantities were calculated in first approximation neglecting the correlation. Then, an experimental correction was applied accounting for the (n,f) events detected by the TAC but not by the FTMG detectors (i.e. fission fragments with large emission angle and self-absorbed in the ^{235}U targets). The results obtained for both experimental configurations are shown in the table 5.2.

Configuration	ε_f	ε_f^*
2FTMG	0.1847(22)	0.1847(22)
10FTMG	0.842(5)	0.842(5)

Table 5.2: Values of the fission detection efficiency and fission tagging detection efficiency for the different experimental configurations. The uncertainty includes the statistical and the systematic components.

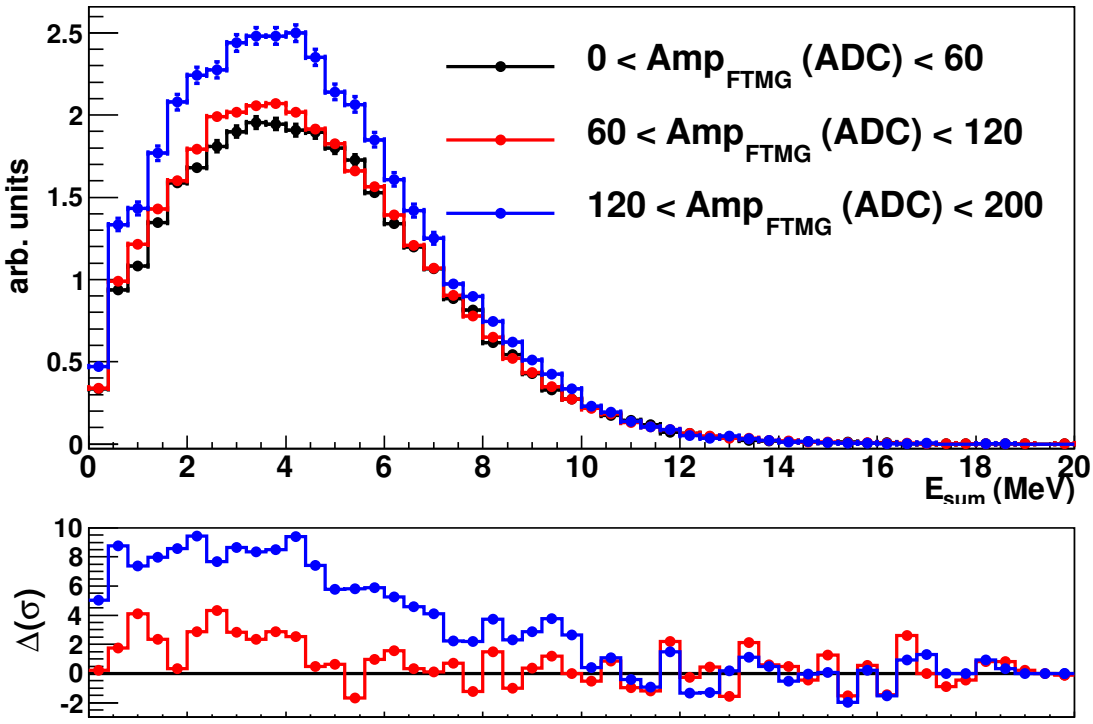

Figure 5.2: Prompt fission γ-ray spectra obtained by the coincidence between the FTMG and TAC for different conditions applied to the FTMG events and normalized to the high deposited energy tail, $E_{sum} > 10$ MeV.

5.1.3 The TAC detection efficiency and the validation of the ^{235}U(n,γ) cascades

The neutron capture detection efficiency, ε_γ, is defined as the probability of detecting a (n,γ) reaction in a certain nucleus by the TAC. It depends on the BaF_2 deposited energy thresholds, the conditions applied to the TAC events in E_{sum} and m_{cr}, and the counting rate of the detectors due to pile-up effects.

The efficiency has been calculated by Monte Carlo simulations as was performed for previous measurements with the TAC [34, 76]. It is obtained by the comparison between the experimental signature and the Monte Carlo deposited energy spectra of the γ-ray cascades.

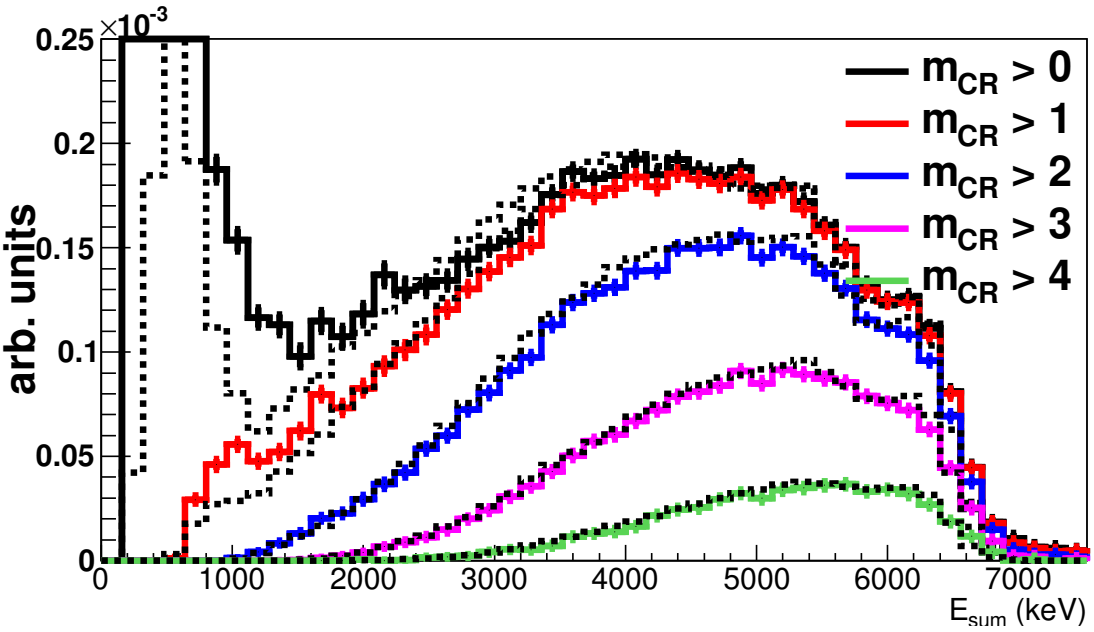

Figure 5.3: Experimental ^{235}U(n,γ) signature detected by the TAC compared with the Monte Carlo simulation for different conditions applied to m_{cr}.

The ^{235}U(n,γ) cascades, adjusted from other experiment carried out at DANCE in Los Alamos [32], were simulated into the experimental setup by a specific GEANT4 application [34, 76]. The cascades includes a long lived isomeric state that distort the γ-ray signature detected by the TAC. The experimental signature together with the Monte Carlo simulations for the experimental configuration with the neutron absorber is shown in Fig 5.3. The validation of the γ-ray cascades allow the determination of several physical parameters of the ^{236}U such as:

- The photon strength functions of the ^{236}U nuclei.
- The population of the long lived isomer throw the neutron capture reaction channel.

Besides, the good agreement permit the determination of the TAC detection efficiency with an uncertainty of 1.7%, including the modeling of (n,γ) reactions and the geometry implemented.

5.1.4 The dead time corrections

The large counting rate registered in the BaF_2 detectors induced by the dead material intercepting the neutron beam introduces dead time effects in the γ-ray cascades detected as a function of the time-of-flight. To correct this effect, a new dead time model as a function of the neutron energy was developed based on the previous works [34, 76, 88, 111] for the calculation of the $^{235}U(n,\gamma)$ cross-section.

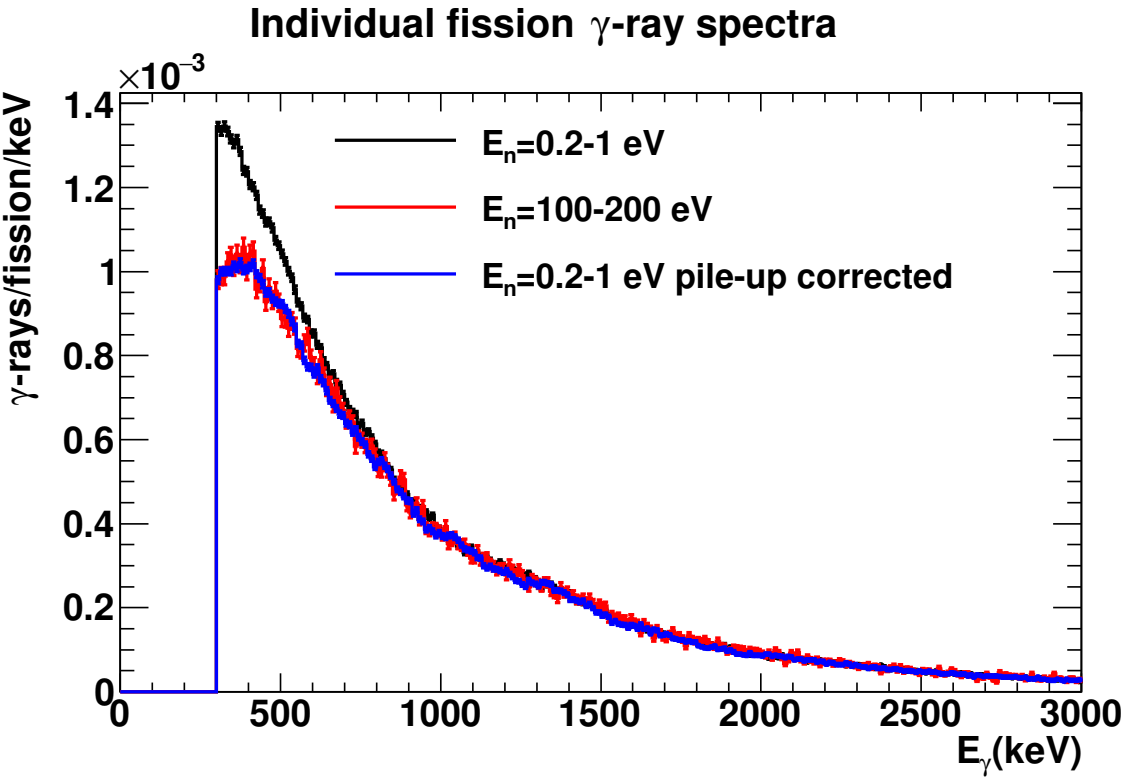

Figure 5.4: Individual γ-ray distribution of the tagged prompt fission cascades for different neutron energy periods: 0.2-1 eV, black line; 100-200 eV red line; and the γ-ray with the dead time applied, blue line.

The dead time model was validated using the tagged prompt fission γ-ray cascades as it shown in Fig. 5.4. The good agreement obtained in the individual γ-ray distributions and coincidence distributions permit a realistic correction of the dead time effects in the whole neutron energy range. The correction was applied, as a function of the neutron energy, to the neutron capture cross-section for different conditions applied to the TAC obtaining compatible results.

5.2 The neutron capture cross-section

The main result from this analysis is the neutron capture cross section of the ^{235}U in the neutron energy range from 0.2 to 200 eV with a careful identification of the systematic uncertainties associated to the technique as it was shown in the chapter 4.

The ^{235}U(n,γ) data obtained from this work, which is the absolute ratio between the fission and the capture cross sections as it was explained in the section 1.3, was normalized to the neutron-induced fission cross section in the neutron energy range from 7.8 to 11 eV. Our data, in the whole neutron energy range, is shown in Fig. 5.5 by the blue dot points. The evaluated libraries are shown for comparison in the same figure by the black and red lines.

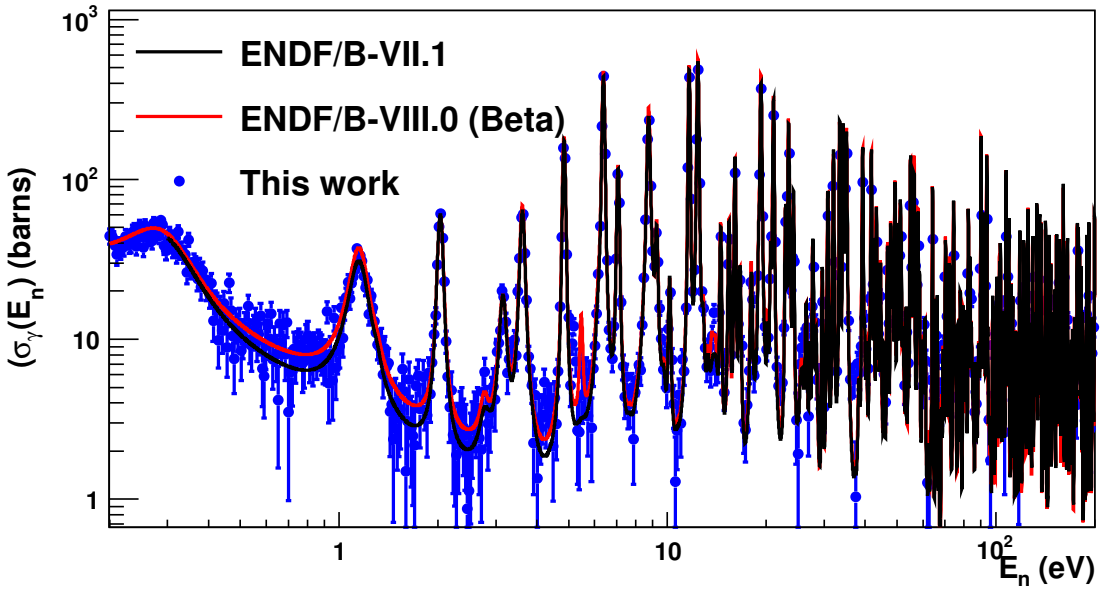

Figure 5.5: ^{235}U(n,γ) cross section from ENDF/B-VII.1 and ENDF/B-VIII.0 (Beta-II) and the n_TOF data for the neutron energy range from 0.2 to 200 eV.

In this section we summarize the identified systematic uncertainty sources and the calculated experimental neutron capture cross section.

5.2.1 Systematic uncertainties in the measurement

Fig. 5.6 shows the statistical and systematic uncertainties integrated in the cross-section resonances for the different neutron energy periods (pink line) and the total uncertainty (black line), calculated as the linear sum of the systematic and statistical components.

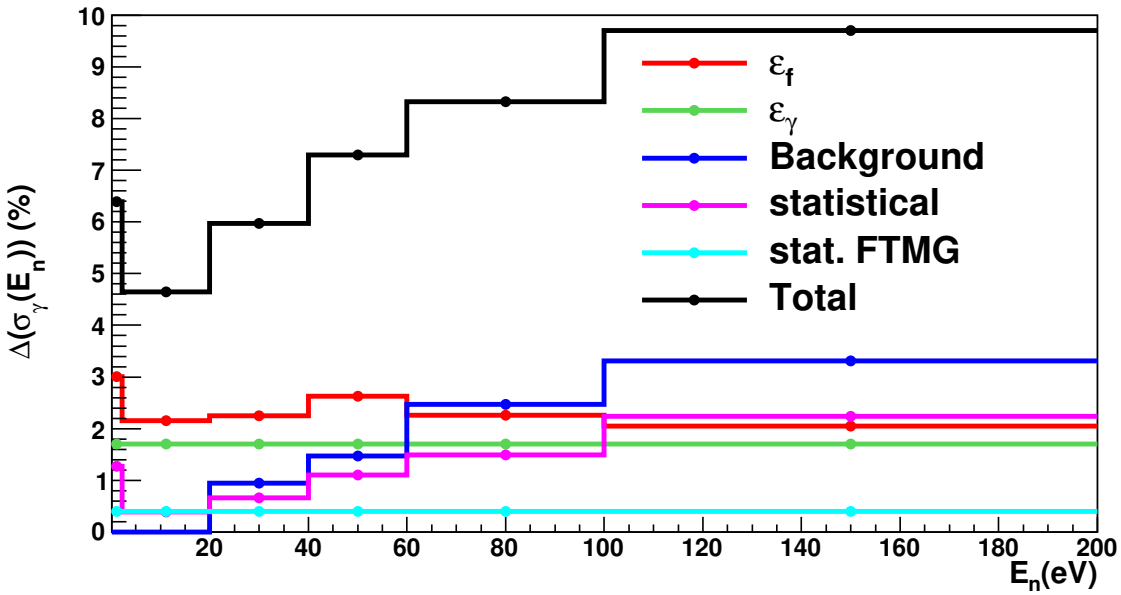

Figure 5.6: Systematic uncertainty sources for the different neutron energy periods. The black line represents the total uncertainty for each period, calculated as the linear sum of statistical and systematic sources.

The systematic uncertainty sources identifies are summarized as follow:

- **The TAC detection efficiency,** ε_γ: The systematic uncertainty in this parameter, $\Delta(\varepsilon_\gamma)$=1.7%, was propagated in the ^{235}U(n,γ) cross-section producing an uncertainty of 1.7% for the entire neutron energy range as is shown by the green line in Fig.5.6.
- **The Fission detection efficiency and the fission tagging detection efficiency,** ε_f **and** ε_f^*: The systematic uncertainty in both parameters were propagated in the neutron capture cross-section. Integration along the different neutron energy periods is shown by the line in Fig. 5.6.
- **The correction applied to the beam background**: The uncertainty of this correction was propagated in the neutron cross-section and is shown for the different neutron energy periods by the blue line in Fig. 5.6.
- **Additional uncertainty due to the normalization**: Due to the normalization performed on the experimental cross-section an additional 0.4% of systematic uncertainty must be added along the entire neutron energy range due to the statistics achieved by the FTMG detectors as shown by the light blue line in Fig. 5.6.
- **The pile-up corrections**: The uncertainty due to pile-up corrections, for the conditions used for the calculation of the ^{235}U(n,γ) cross-section, has been considered low enough, when compared with the rest of systematic uncertainties, not to be taken into account for the calculation.

- **The subtraction of the prompt fission neutrons**. The uncertainty in the determination of the background induced by the prompt fission neutrons has been considered low enough to be excluded from the calculation. Even if we consider an uncertainty of 20% in the determination of this component, the contribution to the total systematic uncertainty is very low (1.0%).

5.2.2 Comparison with the evaluated libraries and the CIELO project

Our experimental data, integrated in the largest neutron resonances, is compared with the ENDF/B-VII.1 evaluated library in the second column of the table 5.3. This work is systematically above this evaluation in all the neutron energy range but compatible taking into account the systematic uncertainties for the different neutron energy ranges.

Energy period (eV)	I(This work)/I(ENDF/B-VII.1)	I(This work)/I(ENDF/B-VIII.0)	Sys. Unc. (%)
0.2 – 2.2	1.03(1)	0.93(1)	5.1
2.2 – 20.0	1.088(4)	1.0148(4)	4.2
20.0 – 40.0	1.072(7)	1.040(7)	5.3
40.0 – 60.0	1.10(1)	1.06(1)	6.1
60.0 – 100.0	1.09(2)	1.07(2)	6.8
100.0 – 200.0	1.06(2)	1.08(2)	7.4

Table 5.3: Ratio between the integral of the resonances from this work and the different evaluations, ENDF/B-VII.1 and ENDF/B-VIII.0 (Beta-II), for the different neutron energy periods. In the last column is shown the systematic uncertainty (in percent) for each neutron energy period.

The systematic increment of the ^{235}U neutron capture cross section is in agreement with other strong suggestions from integral and differential experiments carried out in the last years. Our experimental data, together with all the systematic uncertainties was disposed to the IAEA CIELO project [12, 31], which its principal goal is the reevaluation of the neutron cross section in the main isotopes important for the nuclear applications: ^{1}H, ^{16}O, ^{235}U, ^{238}U and ^{239}Pu.

Including this experimental data among the other measurements and benchmark available, this reevaluation released a new evaluated neutron library for the ^{235}U isotope, the ENDF/B-VIII.0 (Beta-II) increasing the ^{235}U(n,γ) cross section in the first neutron resonances as it show in the third column of the table 5.3. The ratio of the integral resonance value of this work and both evaluations is shown in Fig. 5.8 and Fig. 5.9, where the uncertainty was omitted for simplicity.

Our experimental dataset, together with all the available data set have contribute to the production of new resonance parameters in the neutron energy range from 0.2 to 200 eV. In this neutron energy range, the new library have increased the neutron capture cross section an 8% in the first neutron resonances according with our experimental data (see Fig. 5.7). Thus improving the existing neutron library of this important nuclei for the actual and future nuclear power plants in matter of efficiency, safety and nuclear waste.

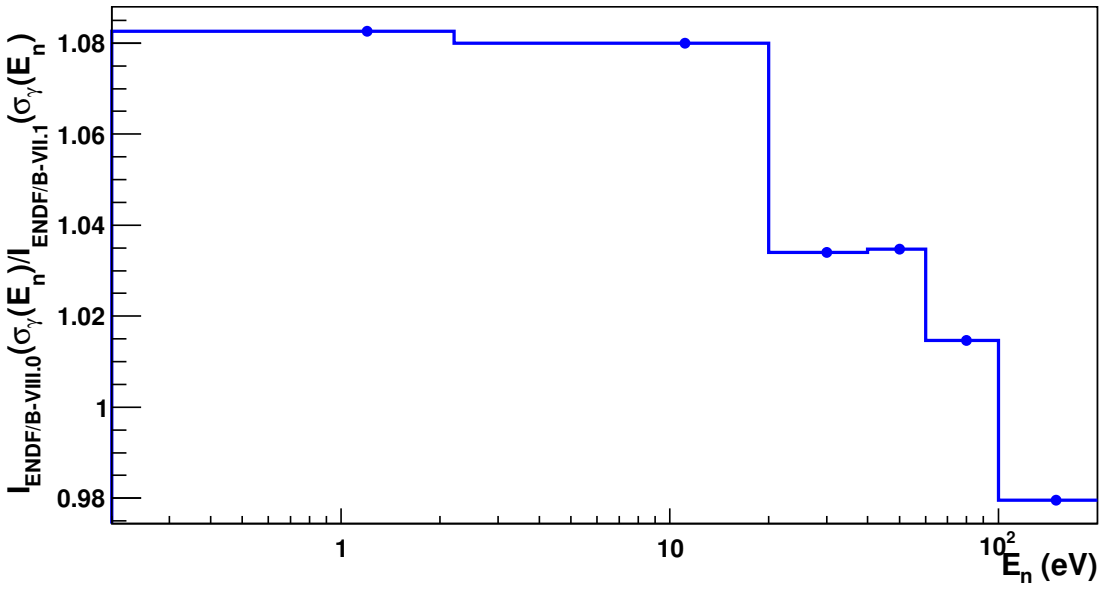

Figure 5.7: Ratio between the ENDF/B-VIII.0 (Beta-II) and ENDF/B-VII.1 for different neutron energy periods from 0.2 to 200 eV.

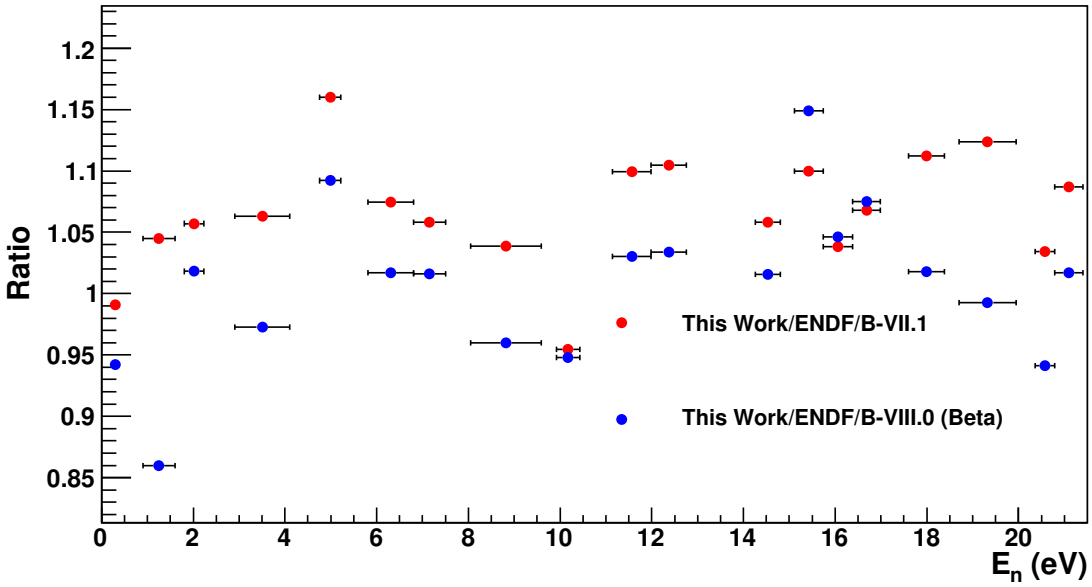

Figure 5.8: In the top panel, ratio between the experimental resonance integral from this work and ENDF/B-VII.1. In the bottom panel, , ratio between the experimental resonance integral from this work and ENDF/B-VIII.0. The uncertainties were deliberated omitted for simplicity.

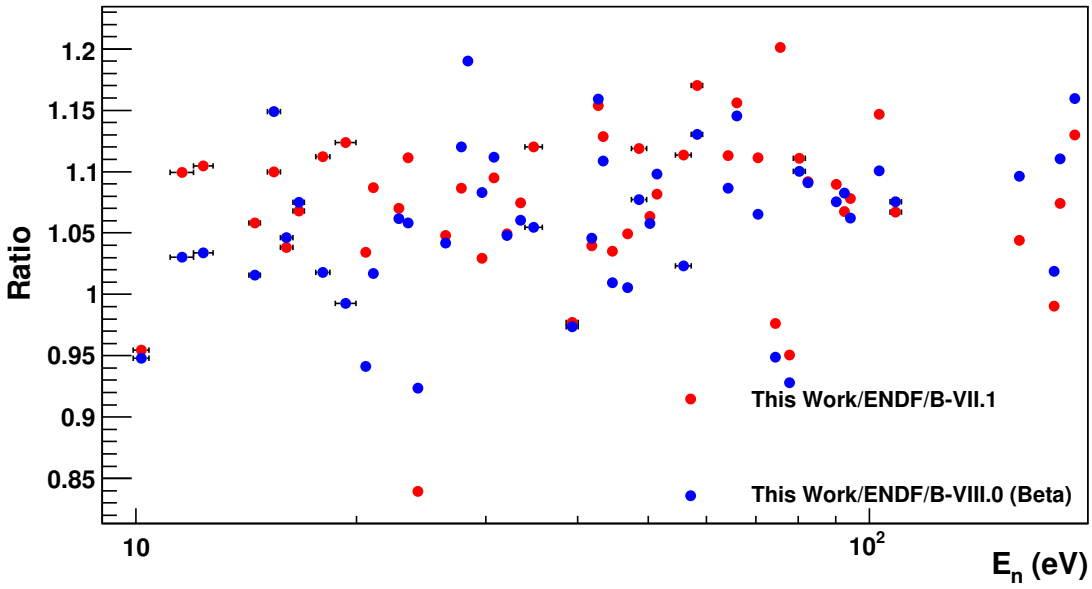

Figure 5.9: In the top panel, ratio between the experimental resonance integral from this work and ENDF/B-VII.1. In the bottom panel, , ratio between the experimental resonance integral from this work and ENDF/B-VIII.0. The uncertainties were deliberated omitted for simplicity.

5.3 Improvements and future work

Many efforts have been made since 2012 at n_TOF in order to improve the front-end electronic of the data acquisition system, upgrading the TAC and building new detectors. There are two main lines in the improvement of the fission tagging technique:

- **Extend the neutron energy period of measurement**: In this way, the n_TOF data acquisition system has been upgraded, replacing the old digitization cards by new ones, which its large buffer permit save 100 ms with a high sampling rate (1 Gs/s). Therefore, reaching thermal neutron energies with a better quality of the digitized signals.

  New detectors are being developed to improve the fission tagging experimental setup. In this matter, a new fission chamber [114] based on aluminum detectors and fast electronic that permit the measurement of high radioactive sample and high counting rates. This fission detectors are planned to replace the actual fission tagging micromegas detectors since the aluminum doesn't have resonances in the neutron energy of interest, i.e. from the thermal point up to tens of keV. In addition, the study and design of a new total absorption calorimeter with the new generation of inorganic scintillators is under study for the experimental area 2 at the n_TOF facility. The good deposited energy resolution, time resolution, low neutron sensitivity and fast γ-flash recovery are the characteristic desired from this study. That task is being fund by the CHANDA project [113] and plans to replace the actual TAC.

- **Reduction of the uncertainties**: There are two critical points for the reduction of the systematic uncertainties:

  1. **Improvement of the signal to background ratio**: The experimental setup used in this measurement confirms the accurate prompt fission background subtraction using less fission tagging detectors than targets under study. Thus, the setup could be improved by the use of thin targets included in the fission detectors and thicker targets for the rest of samples.
  2. **Reduce the correlation effect observed between the TAC and the FTMG**: The correlation observed, despite the origin is not clear, could be reduced by the use of other geometrical fission detectors. For instance, since the principal suspect of the cause is the directional correlation of the prompt fission γ-ray cascades, the angular effect could be reduced turning the fission samples 45 degrees as it used in other experimental setups used by the PPACS for the neutron-induced fission cross section measurements.

Part of these efforts are already applied for the measurement of the ^{233}U(n,γ) in 2016, including the new fission tagging detectors and an upgrading of the TAC electronics. The results from this measurement will clarified the improvement achieved by these upgrading.

Appendices

Appendix A

The deposited energy spectra in the TAC ^{235}U(n,γ) measurement

In Fig. A.1 A.2 A.3 A.4 A.5 are presented the deposited energy spectra of the different dedicated backgrounds and ^{235}U capture measurements. Each plot corresponds to a certain neutron energy range and to certain conditions applied to the multiplicity of the detected events, given in the upper part of the different panels.

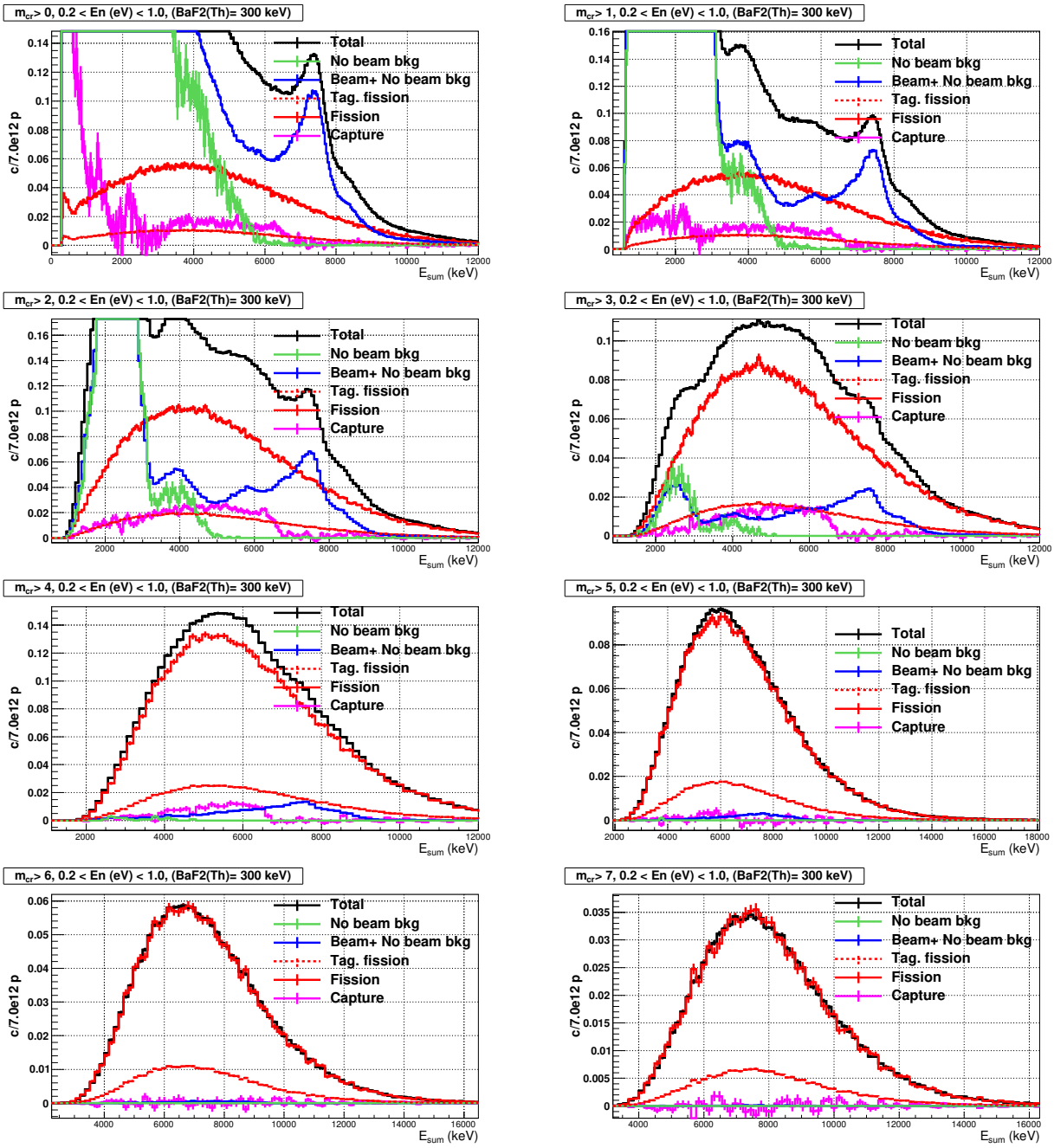

Figure A.1: Deposited energy spectra detected by the TAC for different multiplicity conditions in the neutron energy range from 0.2 to 1 eV.

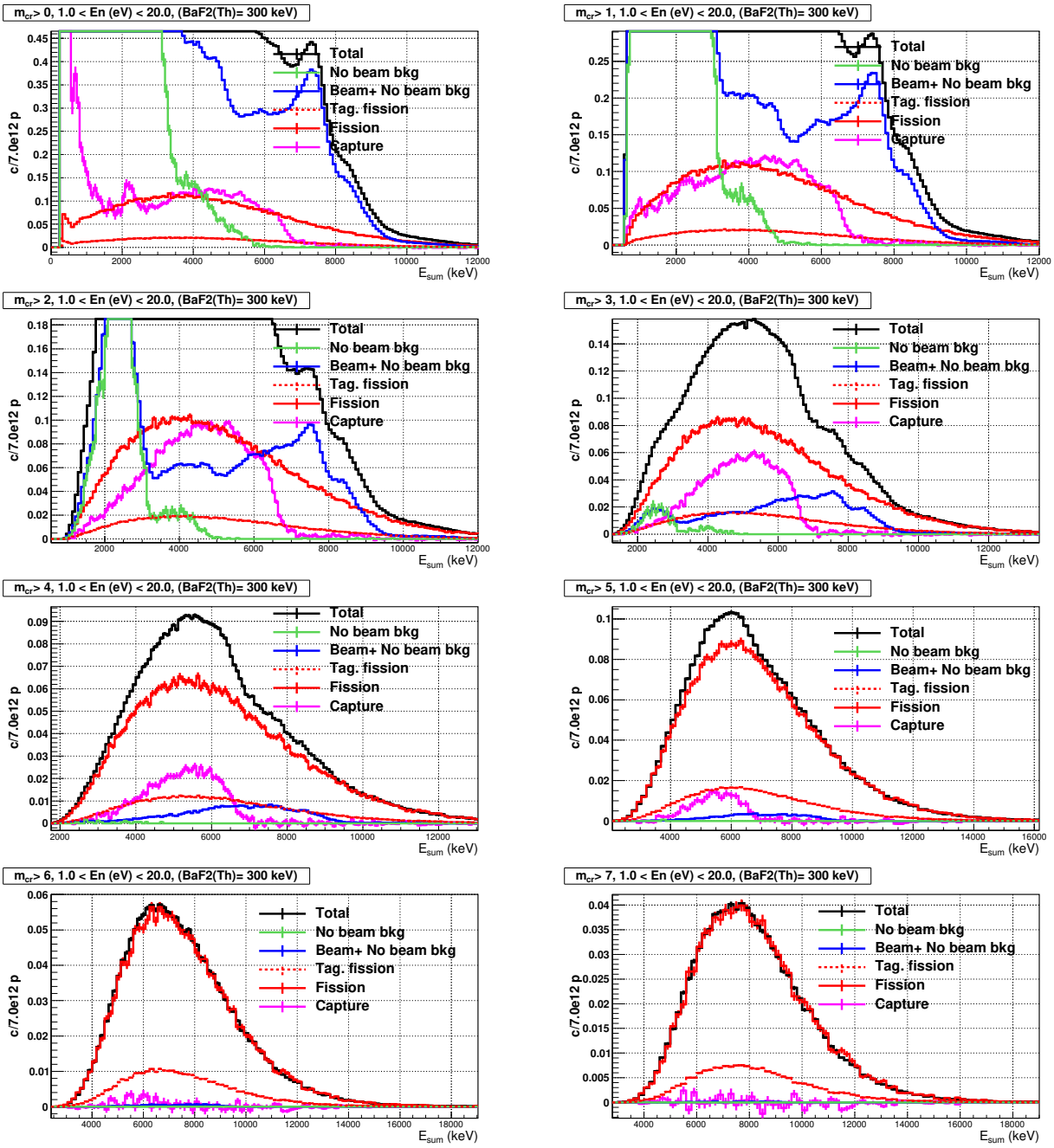

Figure A.2: Deposited energy spectra detected by the TAC for different multiplicity conditions in the neutron energy range from 1 to 20 eV.

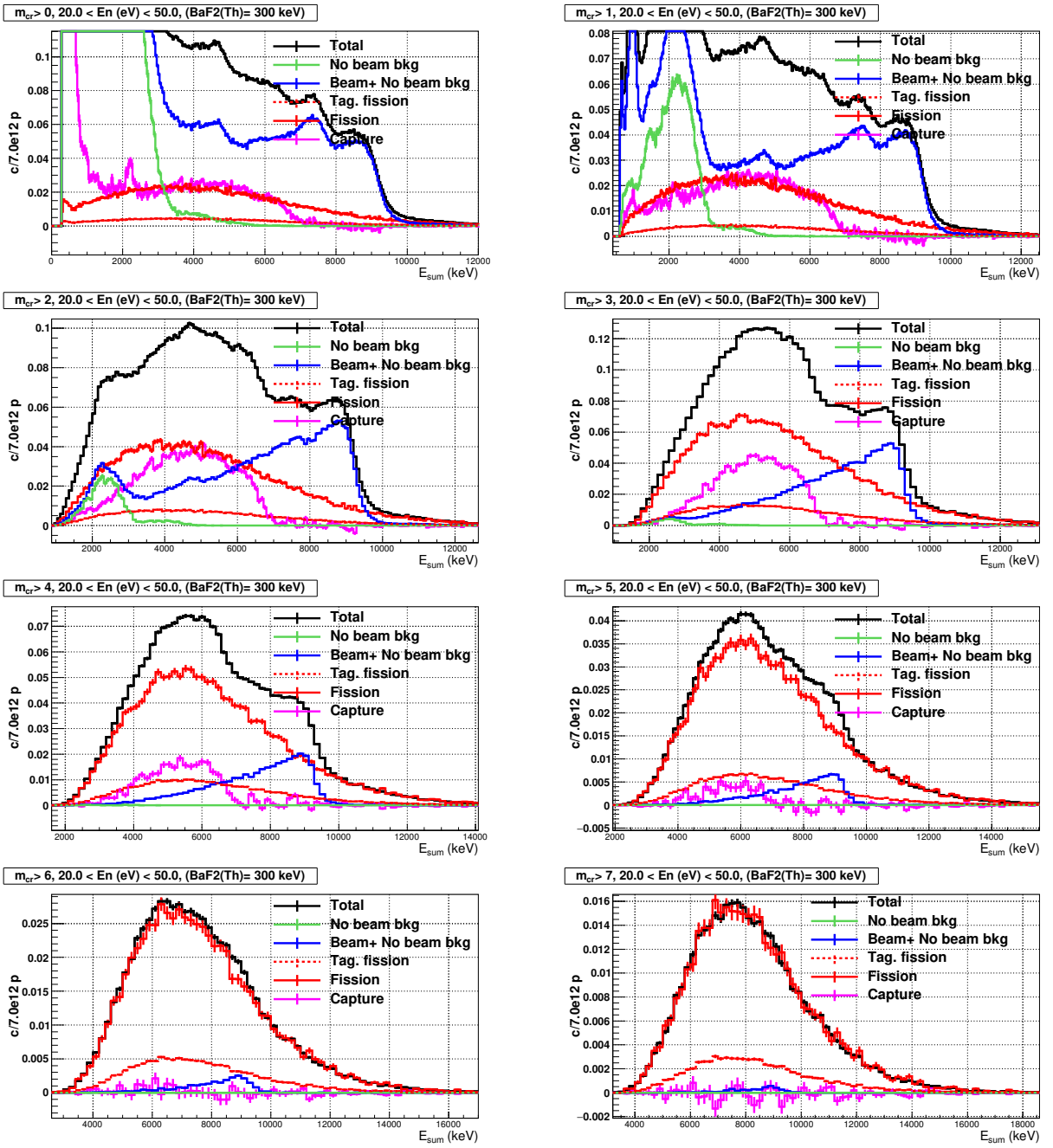

Figure A.3: Deposited energy spectra detected by the TAC for different multiplicity conditions in the neutron energy range from 20 to 50 eV.

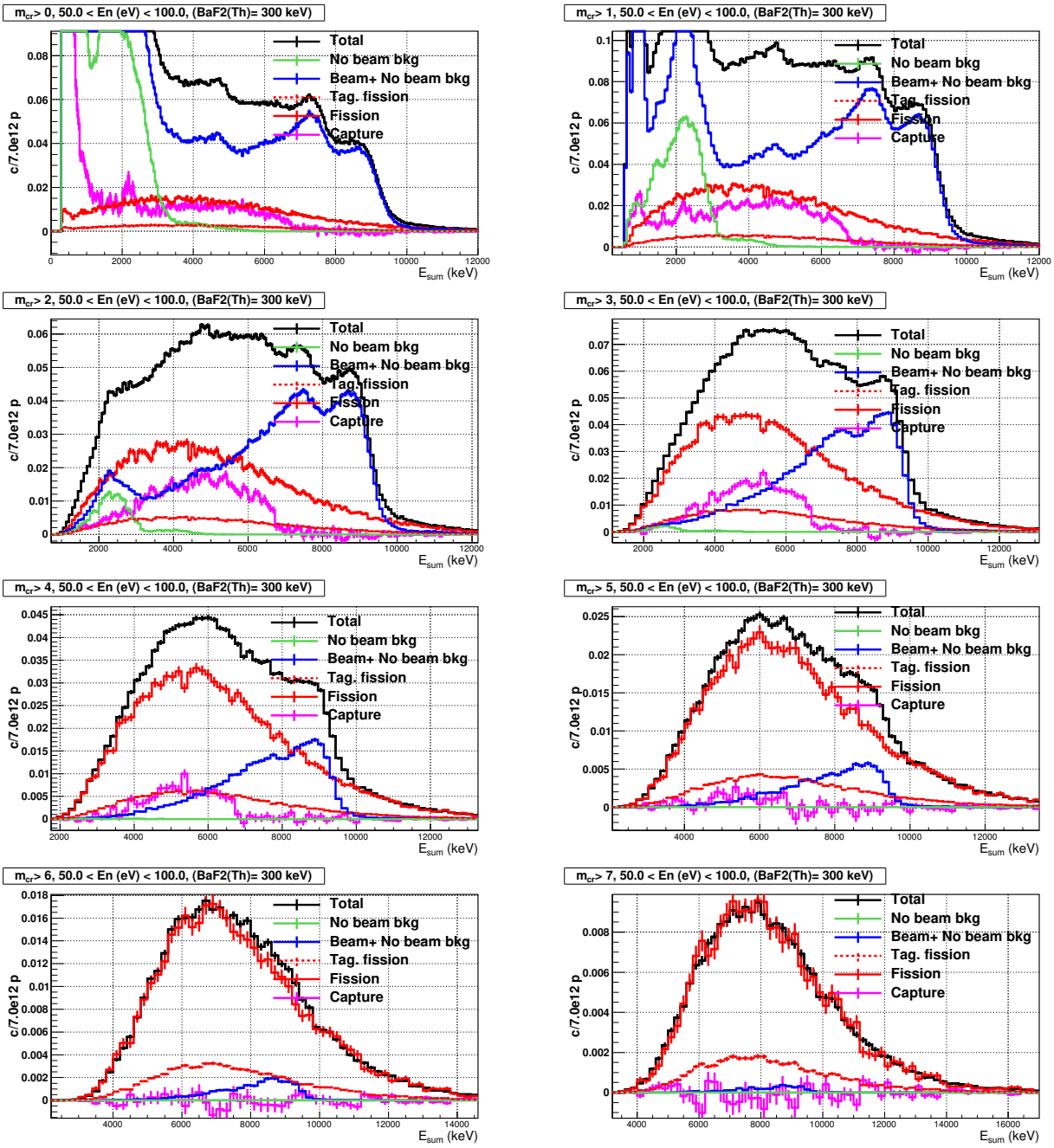

Figure A.4: Deposited energy spectra detected by the TAC for different multiplicity conditions in the neutron energy range from 50 to 100 eV.

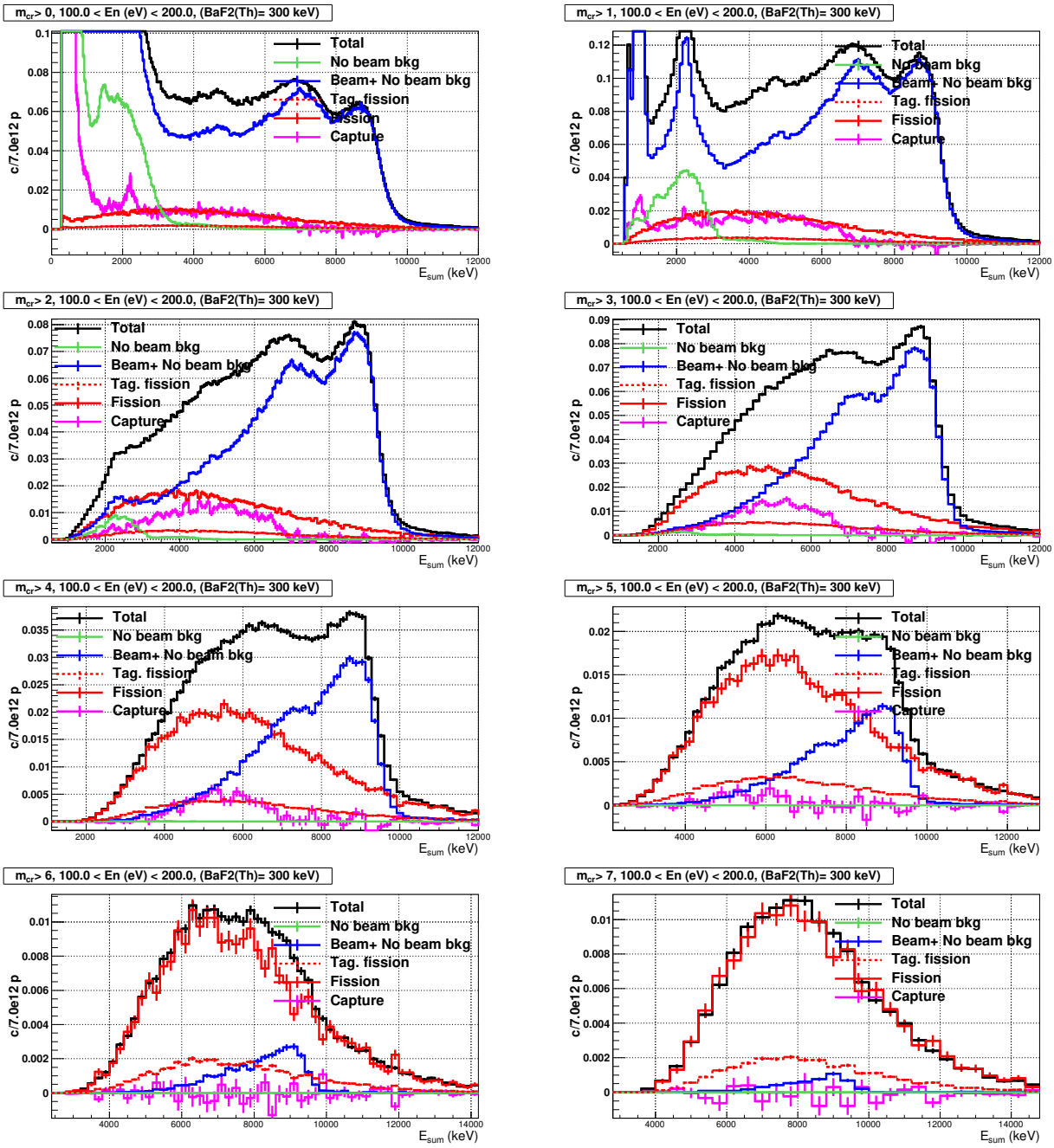

Figure A.5: Deposited energy spectra detected by the TAC for different multiplicity conditions in the neutron energy range from 100 to 200 eV.

Appendix B

The fission detection efficiency and the FTMG detection efficiency

If the mass of the fission targets is well known, the fission detection efficiency of the individual FTMG can be accurately calculated experimentally, as was also calculated the total fission detection efficiency.

For an individual ^{235}U target with superficial density n_s, the number of fissions occurring in the target, $N(E_n)$, is calculated in the thin target approximation and as a function of the neutron energy as:

$$N(E_n) = n_s \phi(E_n) \sigma_f(E_n) \tag{B.1}$$

where $\phi(E_n)$ is the incident neutron flux and $\sigma_f(E_n)$ is the neutron-induced fission cross-section.

The number of fissions detected by the TAC, $N_{detf\gamma}$, or by the fission detectors, N_{det_f}, is easily calculated as the number of fission occurring times the fission detection efficiency of each detection system, $\varepsilon_{f\gamma}$, ε_f. Thus:

$$N_{det_{f\gamma,f}}(E_n) = \varepsilon_{f\gamma,f} N(E_n) = \varepsilon_{f\gamma,f} n_s \phi(E_n) \sigma_f(E_n) \tag{B.2}$$

If both detection system are independent, the number of fission events detected in conjunction between the TAC and FTMG detectors, $N_{tagg}(E_n)$, is expressed as:

$$N_{tagg}(E_n) = \varepsilon_{f\gamma} \varepsilon_f N(E_n) = \varepsilon_{f\gamma} \varepsilon_f n_s \phi(E_n) \sigma_f(E_n) \tag{B.3}$$

B.1 Simplest case: one fission detector and one fission sample

In the simplest case where there is only one FTMG and only one ^{235}U target, the fission detection efficiency (ε'_f), calculated as was explained in the section 3.5, corresponds with the detection efficiency of the fission tagging micromegas detector. This is easily checked by calculating the fission detection efficiency as was explained. Therefore:

$$\varepsilon'_f = \frac{N_{tagg}(E_n)}{N_{det_{f\gamma}}} = \frac{\varepsilon_{f\gamma} \varepsilon_f n_s \phi(E_n) \sigma_f(E_n)}{\varepsilon_{f\gamma,f} n_s \phi(E_n) \sigma_f(E_n)} = \varepsilon_f \tag{B.4}$$

The result is that both detection efficiencies are equal, as was expected.

B.2 General case: N_{det} FTMG and N_s fission samples

In the general case with N_{det} FTMG and N_s fission samples ($N_s \geq N_{det}$), the fission detection efficiency and the FTMG detection efficiency of the FTMG are slightly different. For each individual ^{235}U target, the number of fissions occurring in the TAC-FTMG system are:

$$N_i(E_n) = n_{s_i}\phi(E_n)\sigma_f(E_n) \tag{B.5}$$

Thus, the fission events detected by the TAC are:

$$N_{det_{f\gamma}}(E_n) = \sum_{j=1}^{j=N_s} n_{s_j}\phi(E_n)\sigma_f(E_n)\varepsilon_{f\gamma} = \varepsilon_{f\gamma}\sum_{j=1}^{j=N_s} n_{s_j}\phi(E_n)\sigma_f(E_n) \tag{B.6}$$

and the number of fission detected in coincidence by the TAC and FTMG:

$$N_{tagg}(E_n) = \sum_{i=1}^{i=N_{det}} n_{s_i}\phi(E_n)\sigma_f(E_n)\varepsilon_{f\gamma}\varepsilon_{f_i} = \varepsilon_{f\gamma}\sum_{i=1}^{i=N_{det}} \varepsilon_{f_i} n_{s_i}\phi(E_n)\sigma_f(E_n) \tag{B.7}$$

Thus, the fission detection efficiency ε'_f and the individual fission detection efficiency of the FTMG are related as:

$$\varepsilon'_f = \frac{N_{tagg}(E_n)}{N_{det_{f\gamma}}} = \frac{\varepsilon_{f\gamma}\sum_{i=1}^{i=N_{det}} \varepsilon_{f_i} n_{s_i}\phi(E_n)\sigma_f(E_n)}{\varepsilon_{f\gamma}\sum_{j=1}^{j=N_s} n_{s_j}\phi(E_n)\sigma_f(E_n)} = \frac{\sum_{i=1}^{i=N_{det}} \varepsilon_{f_i} n_{s_i}}{\sum_{j=1}^{j=N_s} n_{s_j}} \tag{B.8}$$

Thus, the fission detection efficiency is the weighted sum of the detection efficiency of the individual fission tagging micromegas detectors.

Appendix C

The Lorentz transformation for the prompt fission γ-rays

Since the prompt fission γ-rays are emitted from the fission fragments with high kinematic energy (section 3.5.3), the direction and the energies of the γ-rays in the fission fragments and the laboratory systems are slightly different.

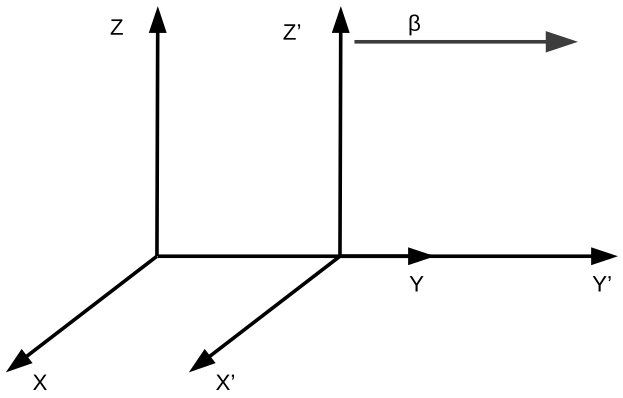

Figure C.1: Inertial reference systems that move away in respect to the other at a velocity β in terms of light speed c.

The cuadrumomentum of the γ-rays of the cascade in the laboratory system, $\widetilde{x}$, and fission fragment

reference system, $\widetilde{x}'$, are defined as:

$$\widetilde{x} = \begin{pmatrix} E/c \\ p_x \\ p_y \\ p_z \end{pmatrix} \tag{C.1}$$

$$\widetilde{x}' = \begin{pmatrix} E'/c \\ p'_x \\ p'_y \\ p'_z \end{pmatrix} \tag{C.2}$$

where E is the energy and $\vec{p}$ the momentum of the γ-ray in the respective reference systems.

The laboratory and fission fragment reference systems are shown in Fig. C.1. Both reference systems are considered inertial reference systems with a relative velocity $\vec{v} = v\vec{n}$ in the direction $\vec{n} = (n_x, n_y, n_z)$, with the restriction $n_x^2+n_y^2+n_z^2=1$.

Therefore, the quantities $\widetilde{x}$ and $\widetilde{x}'$ are connected by the Lorentz transformation [115], $B(\vec{v})$, defined as:

$$B(\vec{v}) = \begin{pmatrix} \gamma & -\gamma\beta n_x & -\gamma\beta n_y & -\gamma\beta n_z \\ -\gamma\beta n_x & 1+(\gamma-1)n_x^2 & (\gamma-1)n_x n_y & (\gamma-1)n_x n_z \\ -\gamma\beta n_y & (\gamma-1)n_x n_y & 1+(\gamma-1)n_y^2 & (\gamma-1)n_y n_z \\ -\gamma\beta n_z & (\gamma-1)n_x n_z & (\gamma-1)n_y n_z & 1+(\gamma-1)n_z^2 \end{pmatrix} \tag{C.3}$$

where the β and γ quantities are expressed in terms of the speed of light, c, by:

$$\beta = \frac{|\vec{v}|}{c} \tag{C.4}$$

$$\gamma = \frac{1}{\sqrt{1-\beta^2}} \tag{C.5}$$

Therefore, both γ-ray quadrumomentum from the fission fragment reference system to the laboratory system is obtained by the transformation:

$$\widetilde{x} = B(\vec{v})\widetilde{x}' \tag{C.6}$$

where $B(\vec{v})$ is defined by the equation C.3.

Appendix D

Rotation of the coordinates system

The directional correlation between the prompt fission γ-ray and fission fragments described in the section 3.5.3 is given by the fission fragment coordinate system. In general, this coordinate system does not correspond to the laboratory system. Only in the particular case of fission fragments emitted in the direction of the neutron beam are both coordinate systems equivalent. In order to simulate correctly the directional correlation, the prompt fission γ-ray cascades correlated in the fission fragment coordinate system must be transformed in the laboratory system.

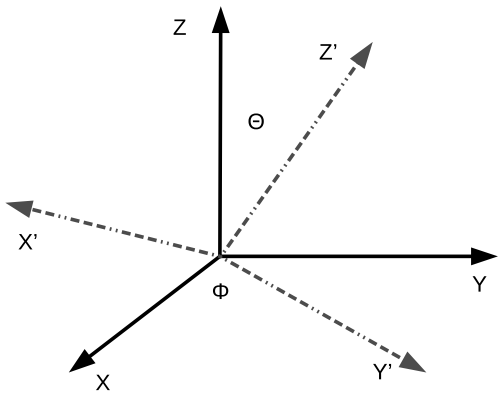

Figure D.1: Laboratory and fission fragment coordinate systems defined by the axis $\{x, y, z\}$ and $\{x', y', z'\}$, respectively.

Both coordinates systems, the laboratory and the fission fragment, are shown in Fig. D.1:

- The laboratory coordinate system: This is defined by the $\{x, y, z\}$ axis, where the z axis is the direction of the neutron beam.
- The fission fragment coordinate system: This is defined by the $\{x', y', z'\}$ axis, where the z$'$ axis corresponds to the direction of the emission of the fission fragment, defined by the angles θ_{ff} and ϕ_{ff} as shown in Fig. D.1.

Therefore, given the direction of the fission fragments defined by the angles θ_{ff} and ϕ_{ff}, and the direction of the γ-ray in the fission fragment coordinate system defined by the vector $\vec{u}_{ff} = (u_x, u_y, u_z)$ ($u_x^2+u_y^2+u_z^2=1$), the direction in the laboratory system, $\vec{u}_{lab}$, is obtained by the transformation defined as:

$$\vec{u}_{lab} = R_x(-\theta_{ff})R_z(-\phi_{ff})\vec{u}_{ff} \tag{D.1}$$

where $R_x(\theta)$ and $R_z(\theta)$ are the rotation matrix in the x and z axis, defined by:

$$R_x(\theta) = \begin{pmatrix} 1 & 0 & 0 \\ 0 & cos(\theta) & -sin(\theta) \\ 0 & sin(\theta) & cos(\theta) \end{pmatrix} \tag{D.2}$$

$$R_z(\theta) = \begin{pmatrix} cos(\theta) & -sin(\theta) & 0 \\ sin(\theta) & cos(\theta) & 0 \\ 0 & 0 & 1 \end{pmatrix} \tag{D.3}$$

Appendix E

Neutron fluence correction due to the dead material layers

As was explained in section 1.2, the experimental reaction yield ($Y_{exp,x}(E_n)$) is calculated as a function of the neutron energy by:

$$Y_{exp,x}(E_n) = \frac{C_x(E_n)}{\varepsilon_x(E_n)\phi(E_n)} \tag{E.1}$$

where $C_x(E_n)$ is the detected counting rate for the reaction x, $\varepsilon_x(E_n)$ is the detection efficiency and $\phi(E_n)$ the neutron fluence. Eq. E.1 is true under the assumption that there is no other dead material layer intercepting the neutron beam before the target sample under study. In another case, the neutron fluence that interacts with the target sample is distorted by the interaction of the neutrons with the previous dead material layers that are present along the neutron beam. Thus, the neutron flux needs to be corrected in accordance with these dead material layers. The correction of the neutron fluence as a function of the neutron energy has been calculated under the following assumptions:

- The total neutron cross-section for all the materials, including the target samples, present in the calculation, are well-known.
- The neutrons can only interact once: the neutrons that have an interaction with one material are assumed lost even if the reaction produced by a is an elastic scattering.
- Other neutron sources such as the production of neutrons via nuclear reactions (i.e prompt fission neutrons) are neglected.

In the following sections the calculation performed will be explained, first for the simplest case of one dead material layer before the target sample and then, for N target samples with dead material layers that intercept the beam between them.

E.1 One target sample and one dead material layer

The simplest system under study is shown in Fig. E.1. It is composed of one layer of dead material (blue layer) and one target sample (green layer). It is assumed that this system, dead material layer + samples, is indivisible from the detection point of view and the incident direction of the neutron beam is from left to right as shown by the purple arrow.

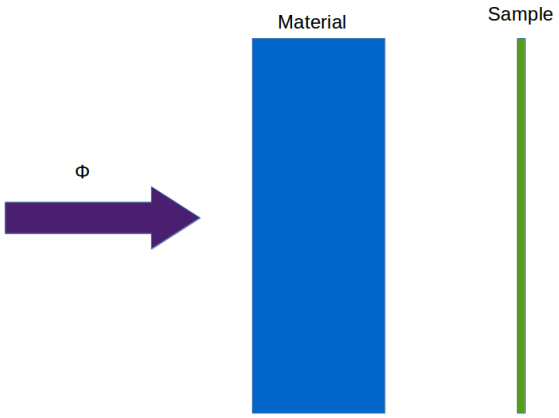

Figure E.1: The simplest system under study. The dead material layer is shown as the blue colored region and the target sample is shown as the green layer.

In this case, the experimental reaction yield of the system dead material+samples is defined as the probability a single neutron has of producing the reaction in the target sample, $Y_{x,sample}(E_n)$, times the probability of the neutron of not interacting with the dead material that intercepts the neutron beam, 1-$P_{D.M.}(E_n)$. Then:

$$Y_{exp,x}(E_n) = (1 - P_{D.M.}(E_n)) \cdot Y_{x,sample}(E_n) \tag{E.2}$$

The transmission factor for the dead material is defined by:

$$T_{D.M}(E_n) = 1 - P_{D.M.}(E_n) = e^{-n_{at}\sigma_T^{mat}(E_n)} \tag{E.3}$$

where n_{at} is the superficial density in atoms per barn and $\sigma_T^{mat}(E_n)$ is the microscopic neutron total cross-section of the dead material. The reaction yield of the target sample is obtained by the use of the definition of the experimental reaction yield, Eq. E.2 and the definition of the transmission factor Eq. E.3. Therefore:

$$Y_{sample,x}(E_n) = \frac{Y_{exp,x}(E_n)}{T_{D.M}(E_n)} = \frac{C_x(E_n)}{\varepsilon_x T_{D.M}(E_n)\phi(E_n)} = \frac{C_x(E_n)}{\varepsilon_x \phi'(E_n)} \tag{E.4}$$

Where $\phi'(E_n)$ is defined as the effective neutron fluence, defined as:

$$\phi'(E_n) = T_{D.M}(E_n)\phi(E_n) \tag{E.5}$$

The partial cross-ection of the target sample $\sigma_x^{sample}(E_n)$ can be easily obtained from the definition of the partial reaction yield in terms of the superficial density of the target sample, n_{sample}, the neutron total cross-section of the target sample, $\sigma_t^{sample}(E_n)$, and the partial cross-section of the reaction x, $\sigma_x^{sample}(E_n)$:

$$Y_{sample,x}(E_n) = \left(1 - e^{-n_{sample}\sigma_t^{sample}(E_n)}\right) \frac{\sigma_x^{sample}(E_n)}{\sigma_t^{sample}(E_n)} \tag{E.6}$$

Hence, the partial cross-section is obtained using Eq. E.4 and Eq. E.6

$$\sigma_x^{sample}(E_n) = \frac{\sigma_t^{sample}(E_n)}{\left(1 - e^{-n_{sample}\sigma_t^{sample}(E_n)}\right)} \frac{C_x(E_n)}{\varepsilon_x \phi'(E_n)} \tag{E.7}$$

E.2 N samples and N dead material layers

The calculation performed for the simplest system composed of one target sample and one dead material layer has been generalized in the case where the system is formed by N dead material layers plus N target samples, one between each two dead material layers. The experimental reaction yield for this system is defined as the probability that the neutrons will not interact with the first dead material layer times the reaction yield of the first sample plus the probability of the neutrons of not interacting with the first dead material layer nor with the second one times the probability of not interacting with the first sample times the reaction yield of the second sample, etcetera. Thus, the experimental reaction yield is written as:

$$Y_{exp,x}(E_n) = (1-P_1(E_n))Y_{1,x}(E_n)+(1-P_2(E_n))Y_{2,x}(E_n)+...+(1-P_N(E_n))Y_{N,x}(E_n) = \sum_{i=1}^{N} T_i(E_n)Y_{i,x}(E_n) \tag{E.8}$$

The transmission factor for the sample i used in the last equation ($T_i(E_n)$) takes into account all the materials, including other target samples, placed before the sample i. The reaction cross-section of the N target samples is obtained using the definition of the sample reaction yield defined in Eq. E.4 and the relationship between the sample reaction yield and the partial reaction cross-section given in Eq. E.6. Then:

$$\sigma_x(E_n) = \frac{Y_{exp}(E_n)}{\sum \left[1 - e^{-n_i\sigma_T(E_n)}\right] T_i(E_n)/\sigma_T(E_n)} = \frac{C_x(E_n)}{\varepsilon(E_n)\phi'(E_n)} \tag{E.9}$$

The effective neutron fluence, $\phi'(E_n)$, is expressed in terms of the incoming neutron fluence, the total neutron cross-section and the individual transmission factors as:

$$\phi'(E_n) = \frac{\sum \left[1 - e^{-n_i\sigma_T(E_n)}\right] T_i(E_n)}{\sigma_T(E_n)} \phi(E_n) \tag{E.10}$$

The effective neutron fluence take into account all the materials present in the system, including the effect of the other target samples that intercept the neutron beam.

Appendix F

Summary in English

The aim of this manuscript is to present the analysis and results of the ^{235}U neutron capture cross- section measurement performed at the CERN n_TOF facility in the neutron energy range from 0.2 to 200 eV.

F.1 Introduction

Current and future energy demands require the development of new energy sources as well as the improvement of existing ones (Fig. F.1).

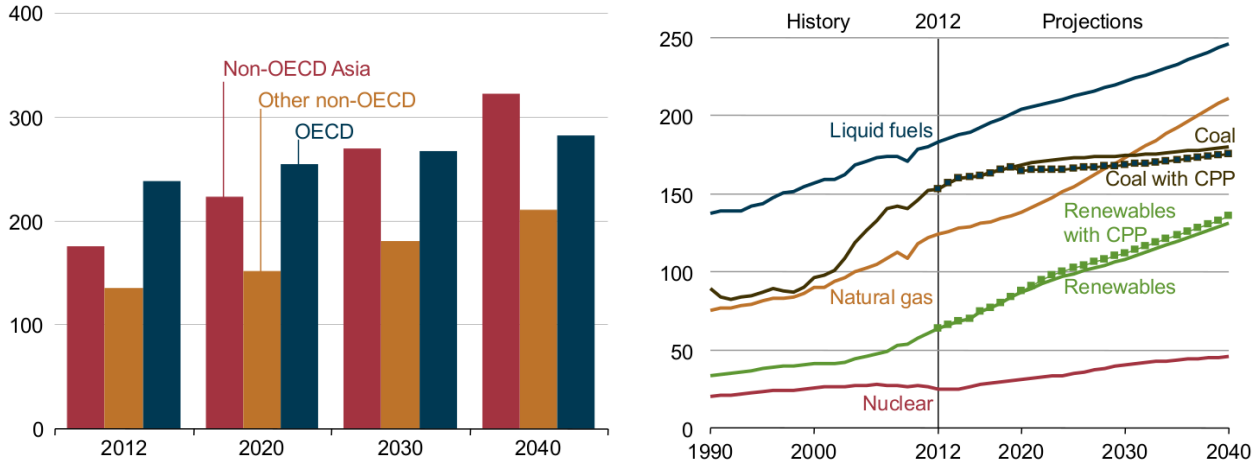

Figure F.1: In the left hand panel is the projection of energy consumption, in Btu, for the period from 2012 to 2040. In the right hand panel is the projection of energy consumption by energy source in Btu from 1990 to 2040 [5].

The first crucial ingredient of reactor and fuel cycle analysis is nuclear data. When designing or assessing the safety of a reactor system, nuclear data for a wide range of reactions and materials has to be known. Designers and physicists must address many variants of nuclear plants and undertake extensive calculations to estimate the performance of critical nuclear system. For accurate and reliable estimates, these studies should incorporate the most accurate and reliable nuclear data and neutron cross-sections, compiled in evaluated libraries such as ENDF/B-VII.1 [9], JENDL-4.0a [10] or JEFF-3.2 [11]. These evaluated libraries are tested against relevant benchmark experimental data, thus validating the current knowledge of nuclear

cross- sections and nuclear data. These major evaluated libraries predict the measured criticality of nuclear systems extremely well (for many assemblies, although not for all). However, such good performance in integral testing creates a false sense of optimism [12] due to compensating errors, calibration of some critical parameters and discrepancies between libraries.

Quantity measured	Author	Year	Neutron energy period (eV)	Reference
$\eta(E_n)$	H. Palevsky *et al.*	1956	0.01 - 0.9	[13]
$\eta(E_n)$	J. R. Smith *et al.*	1957	0.1 - 9.0	[14]
$\sigma_\gamma(E_n)$	G. de Saussure *et al.*	1966	0.4 - 62.0	[15]
$\int \sigma_\gamma(E_n)$	G. de Saussure *et al.*	1966	10.0- 1800.0	[15]
$\eta(E_n$	F.D. Brooks *et al.*	1966	0.9 - 200	[16]
$\int \sigma_\gamma(E_n)$	F.D. Brooks *et al.*	1966	10 - 200	[16]
$\sigma_\gamma(E_n)$	R.B. Perez *et al.*	1973	8.0 - 200.0	[17]
$\int \sigma_\gamma(E_n)$	G.V. Muradyan *et al.*	1977	100 - 20000	[18]
$\alpha_R(E_n)$	G.V. Muradyan *et al.*	1985	2.0 - 32.0	[19]
$\eta(E_n)$	H. Weigmann *et al.*	1990	0.001 0.4	[20]
$\sigma_\gamma(E_n)$	M. Jandel *et al.*	2012	4.0 - $8{\cdot}10^6$	[32]
$\sigma_\gamma(E_n)$	C. Guerrero *et al.*	2012	-	[23]

Table F.1: List of $^{235}U(n,\gamma)$ cross-section measurements retrieved from the EXFOR database [24] overlapping in some regions with the neutron energy range of this work.

Over the years, great efforts have been made to obtain reliable neutron-induced cross-sections of the ^{235}U, which are the most important physical constants in nuclear energy applications. In particular, for the neutron capture cross-section there are several measurements in the neutron resonance region as is shown in the table F.1. The neutron-induced cross-sections for this isotope are very important, not only for major nuclear thermal reactors but for Fast Breeder Reactors (FBRs) because many critical experiments for FBRs have been performed at critical assemblies where UO_2 fuels were used as driver fuels. The experimental data obtained at such critical assemblies has a great impact on design work for FBRs. Recent studies show that calculated sodium void reactivity values for BFS experiments underestimate the experimental results by 30-50% [25]. These significant discrepancies not only exceed the target accuracy of 20% for a FBR design but also undermine the design accuracy estimated with the cross-section adjustment and bias factor techniques.

Therefore, there is a requested accuracy of the ^{235}U neutron capture cross-section reflected in the High Priority Request List [26] of the International Atomic Energy Agency (IAEA). The accuracy as a function of the neutron energy range is included in the table F.2.

Neutron energy interval	Accuracy target (%)
100 eV - 1 keV	5
1keV -30 keV	8
30 keV - 1 MeV	3

Table F.2: Required accuracy of the ^{235}U neutron capture cross-section requested in the High Priority Request List of the Nuclear Energy Agency [26].

To tackle the discrepancies in the neutron cross-section data of the major nuclides, the IAEA CIELO pilot project [12, 31] is re-evaluating the major nuclides important for the nuclear applications: ^{1}H, ^{16}U, ^{235}U, ^{238}U and ^{239}Pu. The main goal of this project is the production of improved and validated evaluated nuclear data files. The work presented in this manuscript focuses on the framework for improving the

neutron capture cross-section at low neutron energy and improving current knowledge of the resonance parameters in the ^{235}U isotope.

F.2 Experimental configuration

The experiment was carried out at the n_TOF facility at CERN. The n_TOF facility at CERN [60] is a pulsed neutron beam time-of-flight facility with a high instantaneous flux and low repetition rate and two neutron beam lines ending in two separated experimental areas [68]. The ^{235}U(n,γ) cross-section measurement was performed at the horizontal 185 m long beam line. The facility was designed to measure low mass samples and high radioactivity in the neutron energy period from meV to GeV.

The neutron beam is produced by CERN's PS proton beam impinging on the spallation target formed by a lead block surrounded by a thin layer of water acting as moderator and refrigerant. In addition, for the horizontal beam line, there is another layer of borated water to reduce the amount of thermal neutrons and γ-ray background measured in the experimental area. The neutrons travel from the spallation target to the experimental areas and their energy is determined by the time-of-flight technique. In the neutron beam line are placed two collimators and magnets to deflect the neutrons produced outside the neutron beam and the charged particles created in the spallation reactions such as π^+ and π^- particles.

The facility, whose main purpose is to provide neutron-induced reaction data for astrophysics ans nuclear technology applications, has been used to measure neutron-induced fission and capture reactions in different isotopes. A list of the measurements performed at the facility since the beginning of the operation is found in the reference [68].

During the measurement of the ^{235}U(n,γ) cross-section, five different detectors were used for different purposes:

- Three different neutron beam monitors: *Wall current monitor* [81], *wall current transformer* [81] and the *silicon monitor* [72] used for the motorization of the neutron beam and for normalization purposes.
- Two independent detection systems for the determination of the reaction rate in the ^{235}U samples:
  - The Total Absorption Calorimeter (TAC) [58], formed by 40 BaF_2 crystals used for the detection of the ^{235}U(n,γ) cascades. A schematic view of the detector is shown in the figure F.2.
  - The Fission Tagging Micromegas detectors(FTMG) [59], gaseous detectors used for the detection of fission fragments produced in the ^{235}U(n,f) reactions. A schematic plot of these detectors is shown in the figure F.3.

Between the fission chamber, where the FTMG and ^{235}U samples were placed, and the TAC were placed a borated neutron absorber ∼5 cm thicker in order to reduce the amount of neutrons detected by the TAC.

The signals from the detectors were recorded by the n_TOF Digital Acquisition System [74] based on Acquiris-DC270 digitization cards with 8 bits of resolution operated with the specific requirement of each detector. The data registered was saved for its posterior analysis by the dedicated pulse shape routines [77, 83]. For the measurement of the neutron capture cross-section, 41 mg of U_3O_8 distributed in ten non-encapsulated samples with high purity of ^{235}U (>99%) were used. Two different experimental configurations were used:

- 2FTMG: With a low simultaneous TAC-FTMG detection efficiency for fission events, this was used for the calculation of the neutron cross-section of the ^{235}U due to the low amount of material intercepting the neutron beam, therefore improving the signal-to-background ratio.
- 10 FTMG: The experimental configuration with ten FTMG, one per sample, had a high TAC-FTMG detection efficiency for the fission events. However, the large amount of dead material that intercepted

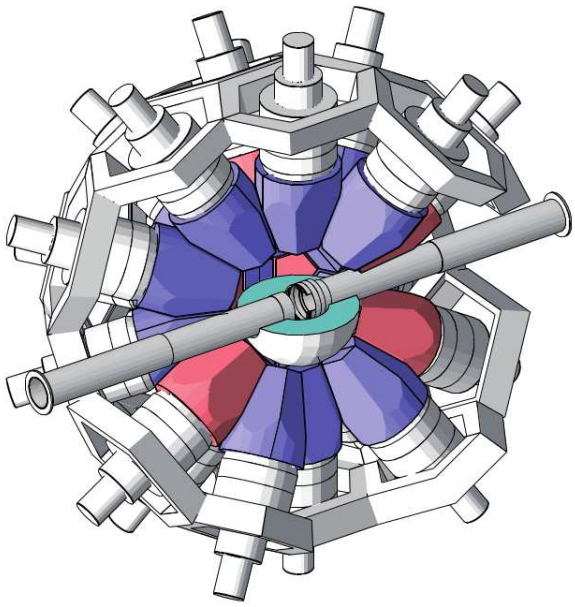

Figure F.2: Geometry of the TAC already implemented for the GEANT4 application.

the neutron beam resulted in a worse signal-to-background ratio. This configuration was used to cross-check the experimental data obtained in the 2FTMG configuration.

In total, more than $4{\cdot}10^{18}$ was used for the measurement. The protons were used in different measurements with different experimental configurations as shown in Fig. F.4. However, due to experimental problems, only $\sim 2.5{\cdot}10^{18}$ was useful for the determination of the ^{235}U(n,γ) cross-section.

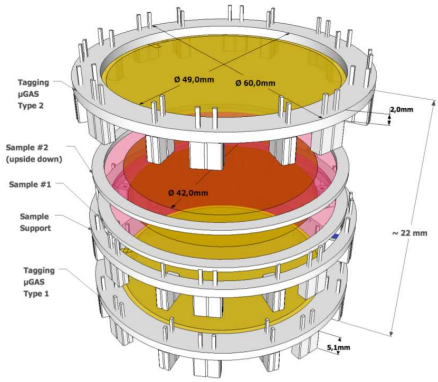

Figure F.3: Schematic drawn of the FTMG used during the measurement of the $^{235}U(n,\gamma)$ cross section [59].

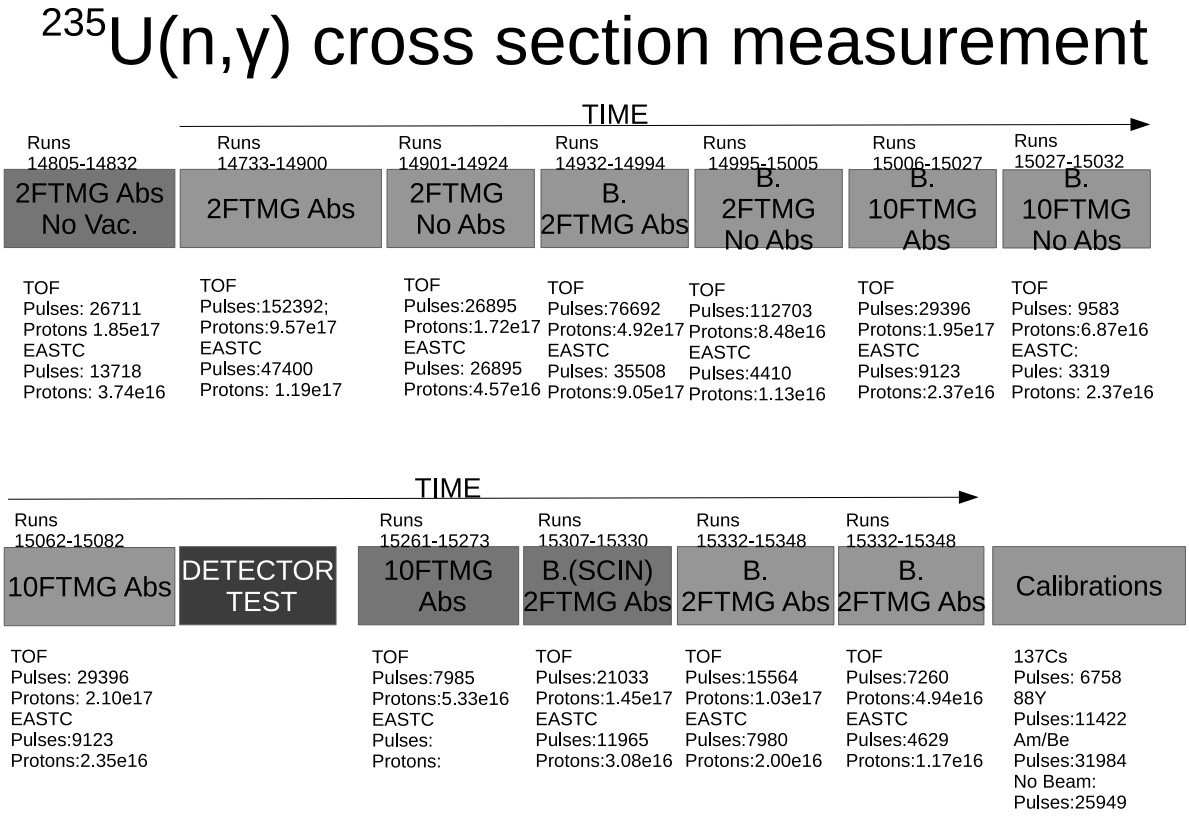

Figure F.4: Detailed time calendar of the $^{235}U(n,\gamma)$ cross-section. The dedicated total number of protons and the number of pules is shown for each period detailed in the calendar.

F.3 Data reduction

The neutron capture cross-section is experimentally calculated in the thin target approximation by:

$$\sigma_\gamma(E_n) = \frac{C_{tot}(E_n) - C_{bkg}(E_n)}{N_{norm}\varepsilon_\gamma\phi(E_n)} \tag{F.1}$$

where $C_{tot}(E_n)$ are $C_{bkg}(E_n)$ the total number of counts detected and background counts respectively: under the analysis conditions E_{sum} and m_{cr}; ε_γ is the detection efficiency for the ^{235}U(n,γ) events; $\phi(E_n)$ is the neutron fluence; and N_{norm} is the normalization factor that encloses the target masses and the fraction of the neutron beam intercept.

The analysis performed in this work is very similar to the previous analysis performed with the TAC [34, 76]. However, for the analysis performed in coincidence with the FTMG, new tools have been developed. The background, $C_{bkg}(E_n)$, is the sum of the different contributions:

- No-beam background (C_{NB}): The background related to the internal radioactive decay of the BaF_2 crystals [34, 76], environmental background and natural radioactive decay of the ^{235}U samples. This component has been obtained from the dedicated measurements without neutron beam, keeping the same experimental setup.

- Beam background (C_B): The interaction of the neutron beam with the dead material that intercepts the neutron beam profile produces background events that are detected by the TAC. This background component is obtained from the dedicated measurements replacing the ^{235}U targets by the dummy samples and keeping the same experimental setup.

- Prompt fission background (C_F): During the fission process, prompt γ-ray cascades and neutrons are emitted from the highly excited fission fragments that are detected by the TAC [23, 32]. This background component is difficult to subtract due to the resonant character of the neutron-induced fission cross-section, coincident with the neutron capture cross-section. It is accurately obtained by the fission tagging procedure.

- Other components related to the ^{235}U targets (C_{Other}): Background induced by the neutron beam with the targets, i. e., background induced by the elastic scattering of the neutron beam with the ^{235}U targets, prompt-neutron emission that is detected and delayed γ-ray emitted during the β-decay of the the fission fragments. The magnitude of these background components cannot be directly measured; thus, these components have been calculated by means of Monte Carlo simulations.

Therefore:

$$C_{bkg}(E_n) = C_{noBeam}(E_n) + C_{Beam}(E_n) + \frac{1}{\varepsilon_f^*}C_{tagg}(E_n) + C_{Other}(E_n) \tag{F.2}$$

where ε_f^* is the fission tagging detection efficiency. Figure F.5 shows an example of the different components measured by the TAC and the background subtractions.

The fission detection efficiency and the fission tagging detection efficiency are closely related quantities. We consider that neither quantities depend on neutron energy. Their definitions are given by:

- **The fission detection efficiency**, $\varepsilon_f(A_{th})$: This is the probability of detecting a fission reaction induced in any of the ten ^{235}U samples by the FTMG detectors. This quantity depends only on the amplitude threshold applied to the FTMG events, A_{th}.

- **The fission tagging detection efficiency**, $\varepsilon_f^*(A_{th},E_{sum},m_{cr})$: This is the factor needed to rescale the tagged fissions for the prompt fission background subtraction. This factor, by definition, is the

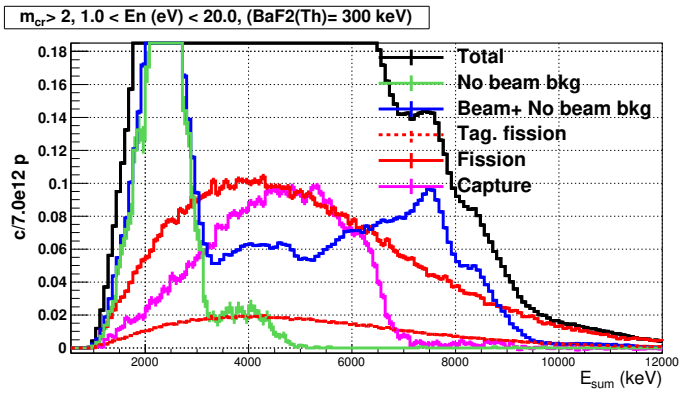

Figure F.5: Deposited energy spectra detected by the TAC for m_{cr} >2 in the neutron energy period from 1.0 to 20 eV.

ratio between the tagged fission counts, $c_{Tagg}(A_{th},E_{sum},m_{cr})$, and the total fission counts detected by the TAC, $c_{Fiss\_TAC}(E_{sum},m_{cr})$:

$$\varepsilon_f^*(A_{th},E_{sum},m_{cr}) = \frac{c_{Tagg}(A_{th},E_{sum},m_{cr})}{c_{Fiss\_TAC}(E_{sum},m_{cr})} \tag{F.3}$$

In the case that the probability of detecting a fission reaction in one of the detectors does not depend on whether it has been detected in the other detector [23], then:

1. The fission tagging detection efficiency, $\varepsilon_f^*(A_{th})$, and the fission detection efficiency, $\varepsilon_f(A_{th})$, are the same quantity.

2. As a consequence of 1., the fission tagging detection efficiency depends only on A_{th}:

$$\varepsilon_f^*(A_{th},E_{sum},m_{cr}) = \varepsilon_f^*(A_{th}) \tag{F.4}$$

The methodology used for the calculation of these two quantities, which is more precise than the Monte Carlo simulations, has been applied in the first large neutron fission resonances, in the neutron energy period from 0.2 to 20 eV. It is based on the equation F.3:

- The prompt tagged fission events are obtained by the coincidence of the TAC and FTMG as was explained in the section 3.3.

- The TAC detects many background components besides the $^{235}U(n,\gamma)$ reactions as was discussed in section 3.4. However, the number of components can be reduced to the prompt fission component and the background related to the dead material intercepting the neutron beam, selecting events with large crystal multiplicity, m_{cr} >5, and large total deposited energy, E_{sum} >$S_n(^{236}U)$. For these conditions, the $^{235}U(n,\gamma)$ reactions and the background related to the no-beam background are removed from the analysis as is shown in both panels of Fig. 3.39. In addition, the contribution of the prompt fission neutrons is negligible as was shown in Fig. 3.36. Nevertheless, it has been ascertained experimentally that ε_f^* only changes as a function of A_{th} as is shown in Fig. 3.40 and tables 3.11 and 3.12.

  As more restrictions are applied to the TAC events, the calculation is less sensitive to systematic uncertainty sources such as the determination of the background as shown in both panels of Fig. 3.40.

However, the statistical uncertainty increases. Thus, the calculation must be performed taking into consideration the compromise between the systematic and statistical uncertainties.

For those conditions, the total fission events detected by the TAC are obtained by the difference between the total number of counts detected, $c_T(E_{sum},m_{cr})$, and the background related to the dead material intercepting the neutron beam obtained from the dedicated experimental measurement; $c_B(E_{sum},m_{cr})$.

The fission tagging detection efficiency has been calculated for both experimental configurations in the first largest neutron fission resonances, from 0.2 to 20 eV. For the calculation, the TAC events were restricted to events with m_{cr} >5 and E_{sum} >10 MeV. For the FTMG detector, the threshold applied was A_{th}=40 ADC channels.

However, due to the complexity of this process, most of the observables are correlated. For instance, the average number of prompt fission neutrons and γ-rays emitted are closely related quantities with the pair of fission fragments produced and the primary nuclei involved [100]. Thus, the correlation of the fission observables introduces small correlations in the simultaneous detection of fission events by the TAC and FTMG detectors.

Therefore, a experimental correction was applied as explained in the section 3.5.4 and the final results obtained for both experimental configurations are shown in the table F.3. The uncertainty shown is the sum of the statistical and systematic components.

Quantity	2FTMG	10FTMG
ε_f	0.1847(22)	0.842(5)
ε_f^*	0.1847(22)	0.842(5)

Table F.3: Fission detection efficiency and fission tagging detection efficiency calculated for both experimental configurations.

The TAC detection efficiency was determined by Monte Carlo simulation as was obtained in previous works [104, 34, 76]. The γ-ray cascades were generated by the DICEBOX [47] including a long-lived isomeric state $T_{1/2}$ ~100 ns that distorts the neutron capture signal detected by the TAC. The γ-ray cascades were simulated in the detailed model of the TAC including the fission chamber with the ^{235}U samples.

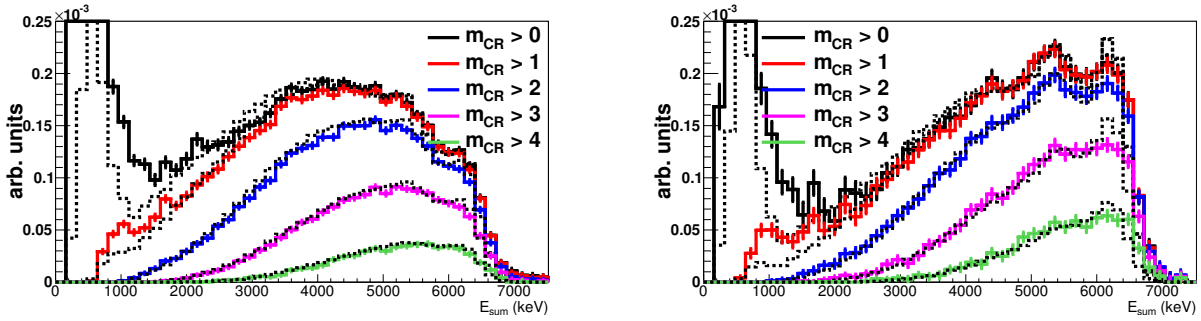

Figure F.6: Monte Carlo simulated $^{235}U(n,\gamma)$ deposited energy spectra compared with the experimental data for different m_{cr} conditions. In the left hand panel are the results for the experimental FTMG configuration with the borated neutron absorber. In the right hand panel are the results for the FTMG experimental configuration without the borated neutron absorber.

The excellent reproduction of the experimental data by the Monte Carlo cascades permits the determination of this parameter with an accuracy of 1.7%.

The normalization of the ^{235}U(n,γ) cross-section was performed to the well-known integral value of the ^{235}U(n,f) cross-section in the neutron energy range from 7.8 to 11.0 eV, thus reducing systematic uncertainties. The uncertainty in the normalization is $\Delta(N_{norm})$=2.1%

The high count rate registered in the BaF_2 detectors induced by the large amount of material that intercepts the neutron beam introduces pile-up effects distorting the γ-ray cascades, thus the detection efficiency changes as a function of the neutron energy. To correct these effects, a new dead time model has been developed, based on previous works [76, 34, 88, 111]. The dead time model was tested in the prompt γ-ray cascades detected in conjunction between the TAC and FTMG. The excellent results are shown in the left hand panel of Fig.F.7. In the right hand panel of the same figure is shown the dead time corrections needed for the ^{235}U(n,γ) cross- section.

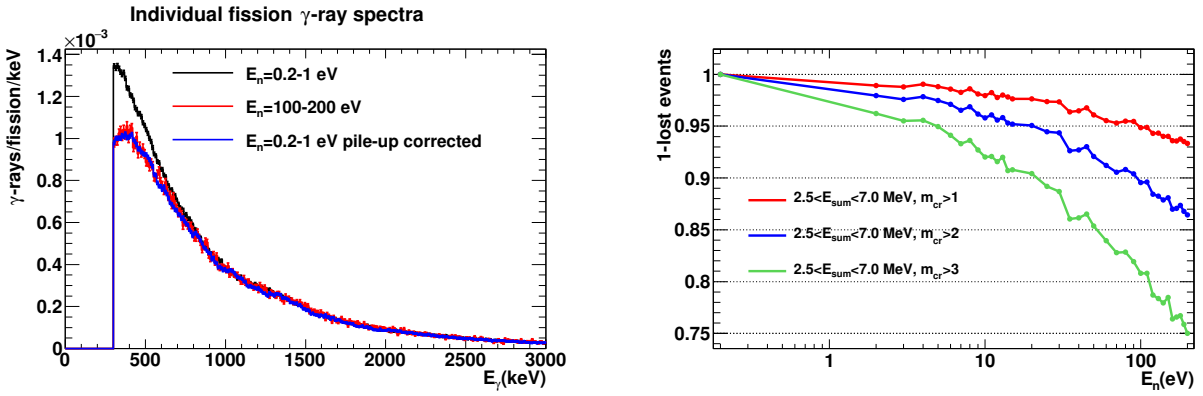

Figure F.7: The left hand panel gives a comparison between the deposited energy of the tagged prompt fission individual γ-rays for different neutron energy ranges and the corrected one. The distribution measured at low neutron energies, from 0.2 to 1.0 eV, is shown as a black solid line. The distribution measured at high neutron energies, from 100 eV to 200 eV, is shown as a solid red line and as blue solid line plots the reconstructed γ-ray distribution applying the dead time corrections to the low neutron energy distribution. In the right hand panel are the dead time corrections for the ^{235}U(n,γ) cross section.

F.4 Results

The integral of the neutron resonances has been computed and compared with the ENDF/B-VII.1 for the different neutron energy periods as shown in the table. F.4. In the final column is shown the systematic uncertainty (in percent) calculated for each neutron energy period.

The data obtained from this work is, in general, greater than the ENDF/B-VII.1. However, taking into account the uncertainties calculated, the ^{235}U(n,γ) cross-section obtained from this analysis is compatible with the evaluations. The experimental neutron capture cross-section was deployed to the CIELO collaboration [31, 12] for its analysis. As result, an update of the evaluated libraries will be released (ENDF/B-VIII.0), improving current knowledge of the neutron induced cross-section of the ^{235}U.

Figure	Neutron energy period	I(σ_γ(E$_n$))/I(ENDF/B-VII.1)	Sys. uncertainty (%)
4.5	0.2 – 2.2	1.03±0.01	5.1
4.6	2.2 – 20.0	1.088±0.004	4.2
4.7	20.0 – 40.0	1.072±0.007	5.3
4.8	40.0 – 60.0	1.10±0.01	6.1
4.9	60.0 – 100.0	1.09±0.02	6.8
4.10	100.0 – 200.0	1.06±0.02	7.4

Table F.4: Ratio between the integral of the resonances from this work and ENDF/B-VII.1 for the different neutron energy periods. In the last column is shown the systematic uncertainty (in percent) for each neutron energy period.

F.5 Conclusions

The neutron capture cross-section of the ^{235}U has been measured in the n_TOF facility at CERN in the neutron energy range from 0.2 to 200 eV.

In the measurement, two different and independent detection systems have been used; the Total Absorption Calorimeter and the Fission Tagging Micromegas detectors.

Due to the high resolution power of the n_TOF facility, the results obtained improve current knowledge of the resolved resonance region. However, due to systematic uncertainties, the data from this work is compatible with current evaluated neutron libraries.

The data has been used by the CIELO collaboration, contributing to the creation of a new evaluated library for use in the design of new and more efficient nuclear power plants.

Appendix G

Resumen en español

El objetivo de este manuscrito es presentar el análisis y resultados de la medida de la sección eficaz de captura del ^{235}U llevado a cabo en la instalación n_TOF del CERN en el rango de energías del neutrón desde 0.2 a 200 eV.

G.1 Introducción

Las actuales y futuras demandas de energía requieren el desarrollo de nuevas fuentes de producción así como la mejora de las ya existentes (Fig. G.1).

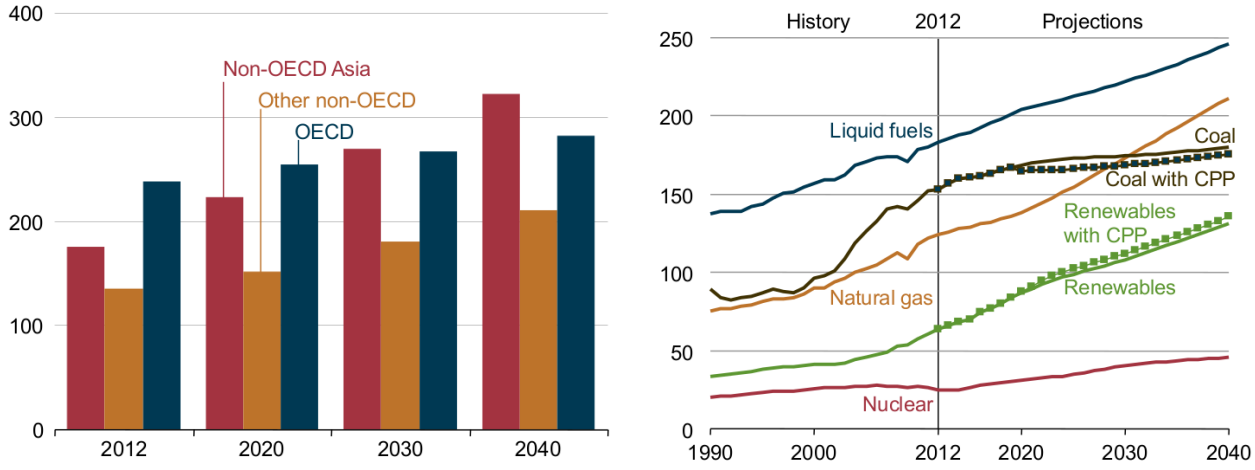

Figure G.1: En el panel izquierdo, proyección de consumo de energía en los proximos años (2012-2040) en Btu. En el panel derecho, proyección de consumo de energía en el periodo desde 1990 hasta 2040 [5].

El primer y crucial ingrediente para el diseño de los reactores nucleares y el ciclo de combustible son los datos nucleares. A la hora de diseñar y evaluar la seguridad de los reactores nucleares es necesario una gran cantidad de datos nucleares para distintos materiales. Los ingenieros y físicos deben afrontar diferentes variantes de los reactores nucleares y realizar grandes cálculos para estimar el rendimiento de los sistemas nucleares críticos. Para tener estimaciones fiables, estos estudios deben incoporar las secciones eficaces más precisas que se conocen, habitualmente incluidas en las librarias evualadas tales como ENDF/B-VII.1 [9],

JENDL-4.0a [10] o JEFF-3.2 [11]. Estas librerías evaluadas son probadas con experimentos integrales y de esta manera se valida los actuales datos y secciones eficaces nucleares. Estas librerías predicen de manera muy precisa para la mayoria de sistemas nucleares críticos su comportamiento. Sin embargo, la buena estimación en estos experimentos integrales crea la falsa sensación de optimismo debido a la compensación de errores, calibraciones de los datos y discrepancias entre librerías [12].

Quantity measured	Author	Year	Neutron energy period (eV)	Reference
$\eta(E_n)$	H. Palevsky *et al.*	1956	0.01 - 0.9	[13]
$\eta(E_n)$	J. R. Smith *et al.*	1957	0.1 - 9.0	[14]
$\sigma_\gamma(E_n)$	G. de Saussure *et al.*	1966	0.4 - 62.0	[15]
$\int \sigma_\gamma(E_n)$	G. de Saussure *et al.*	1966	10.0- 1800.0	[15]
$\eta(E_n$	F.D. Brooks *et al.*	1966	0.9 - 200	[16]
$\int \sigma_\gamma(E_n)$	F.D. Brooks *et al.*	1966	10 - 200	[16]
$\sigma_\gamma(E_n)$	R.B. Perez *et al.*	1973	8.0 - 200.0	[17]
$\int \sigma_\gamma(E_n)$	G.V. Muradyan *et al.*	1977	100 - 20000	[18]
$\alpha_R(E_n)$	G.V. Muradyan *et al.*	1985	2.0 - 32.0	[19]
$\eta(E_n)$	H. Weigmann *et al.*	1990	0.001 0.4	[20]
$\sigma_\gamma(E_n)$	M. Jandel *et al.*	2012	4.0 - $8{\cdot}10^6$	[32]
$\sigma_\gamma(E_n)$	C. Guerrero *et al.*	2012	-	[23]

Table G.1: Lista de medidas de la sección eficaz de captura del ^{235}U extraida de la base de datos EXFOR [24] solapando en alguna región con los datos de este trabajo.

A lo largo de los años, se han hecho gran esfuerzos para obtener datos fiables de las secciones eficaces del ^{235}U inducidas por neutrones, uno de las constantes físicas más importantes en apliaciones nucleares relacionadas con la energía. En particular, para la región de resonancias del canal de captura, existen diveras medidas así como se muestra en la tabla G.1. Estas medidas no son solo importantes para los reactores térmicos sino que también lo son para los reactores rápidos ya que los experimentos de criticidad se realizan con combustibles de UO_2. Recientes experimentos han concluido que la reactividad en los reactores de sodio se subestiman entre un 30-50% [25]. Estas discrepancias significativas no solo exceden la precisión deseada para el diseño de los reactores rápidos sino que también devaluan el diseño de estos reactores debido al ajuste de las secciones eficaces para los reactores térmicos.

Por lo tanto, para acabar con estas discrepancias existe una necesidad de mejorar la precisón de esta importante sección eficaz así como se refleja en la High Priority Request List [26] de la Agencia Internacional de la Energía Atómica (IEAA). La precisión requerida en función de la energía del neutrón está reflejada en la tabla G.2.

Neutron energy interval	Accuracy target (%)
100 eV - 1 keV	5
1keV -30 keV	8
30 keV - 1 MeV	3

Table G.2: Precisión requerida en la High Priority Request List of the Nuclear Energy Agency [26] para la sección eficaz de captura del ^{235}.

Para afrontar las discrepancias de los isótopos de mayor relevancia en las aplicaciones nucleares energéticas, ^{1}H, ^{16}U, ^{235}U, ^{238}U y ^{239}Pu, el proyecto CIELO de la IAEA [12, 31] está reevaluando las secciones eficaces inducida por neutrones para dichos elementos. La principal meta de este proyecto es la producción de una mejorada y validada librería evaluada. El trabajo presentado en este manuscrito está centrado en

el marco de la mejora de la sección eficaz de captura del ^{235}U así como en la mejora de parámetros de las resonancias actuales.

G.2 Configuración experimental

El experimento fué llevado a cabo en la instalación n_TOF del CERN [60]. Esta, es una instalación de tiempo de vuelo con un haz de neutrones pulsado con gran flujo instantaneo y baja repetición [68]. La medida fue realizada en la línea horizontal con una longitud de 185 m. La instalación fúe diseñada para medir muestras de baja masa y/o alta radioactividad en un rango de energías desde los meV hasta los GeV.

El haz de neutrones es producido por los pulsos dedicados del PS que impactan sobre un bloque de espalación formado por un bloque de plomo rodeado de agua que actúa como moderador y refrigerante. Además, para la línea horizontal, existe una capa de agua borada adicional para reducir el número de neutrones térmicos y fondo γ en el área experimental. Los neutrones viajan desde el bloque de espalación hasta el área experimental y su energía es determinada por la técnica de tiempo de vuelo. En la línea del haz existen dos colimadores y un imán para desviar los neutrones fuera del haz y las partículas cargadas producidas en la reacción de espalación.

Esta instalación, cuyo principal proposito es proveer de datos nucleares inducidos por neutrones para astrofísica y aplicaciones nucleares, ha sido usada para medir la captura y fisión en diferentes isótopos tal y como se muestra en la referencia [68].

Durante la medida de ^{235}U(n,γ), se han usado 5 detectores para diferentes propositos:

- Tres de ellos como monitorización del haz de neutrones: *Wall current monitor* [81], *wall current transformer* [81] y los *silicon monitor* [72].
- Dos sistemas independientes para la determinación de la tasa de reacción en las muestras de ^{235}U:
  - El Total Absorption Calorimeter (TAC) [58], está formado por 40 BaF_2 usados para la detección de las cascadas electromagnéticas del proceso ^{235}U(n,γ). Una visión esquemática de este detector se encuentra en la figura G.2.
  - Los Fission Tagging Micromegas detectors(FTMG) [59], detectores gaseosos usados para la detección de los fragmentos de fisión producidos en la reacción ^{235}U(n,f). Un dibujo esquemático de este detector está en la figura G.3.

Entre la cámara de fisión y el TAC se colocó un absorbente neutrónico de 5cm de radio para reducir la cantidad de neutrones detectados por el TAC.

Las señales de los detecotes fueron digitalizadas por el n_TOF Digital Acquisition System [74] basado en tarjetas Acquiris-DC270 operadas para las necesidades de cada detector. Los datos registados fueron guardados para su posterior análisis con las rutinas de análisis [77, 83]. Para la medida se han usuado 41 mg de U_3O_8 distribuidas en 10 muestras sin encapsular de gran pureza en ^{235}U (>99%). Se usaron dos configuraciones experimentales:

- 2FTMG: Con una baja eficiencia de detección simultanea de las reacciones (n,f) por TAC-FTMG, Esta configuración fué usada para la determinación de la sección eficaz de captura debido a su mejor señal/fondo.
- 10 FTMG: En esta configuración, con 10 detectores FTMG, se obtiene una gran eficiencia para la detección simultanea de los eventos (n,f). Sin embargo, esta configuración se usó para confirmar los datos experimentales obtenidos a bajas energías del neutrón en la configuración 2FTMG debido a su peor señal/fondo.

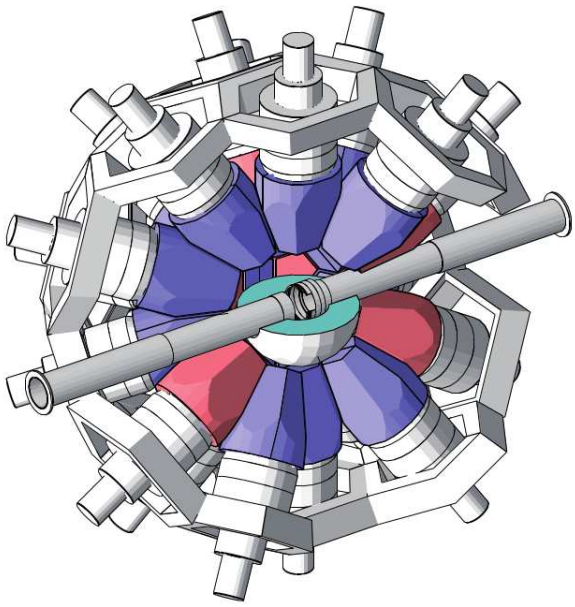

Figure G.2: Geometria del TAC implementada en la aplicación GEANT4.

En total, se han usado mas de $4{\cdot}10^{18}$ protones. Estos, fueron distribuidos en diferentes medidas y configuraciones experimentales tal y como se muestra en Fig. G.4. Sin embargo, debido a problemas experimentales, solo $\sim 2.5{\cdot}10^{18}$ fueron útiles.

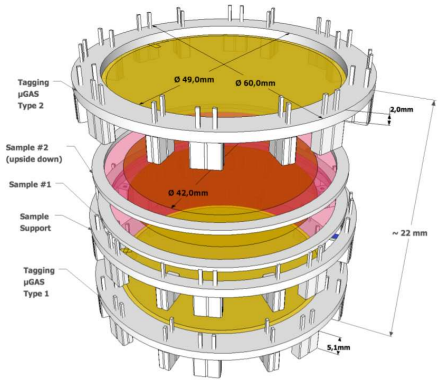

Figure G.3: Dibujo esquemático de los detectores FTMG usados durante la medida de la sección eficaz $^{235}U(n,\gamma)$ [59].

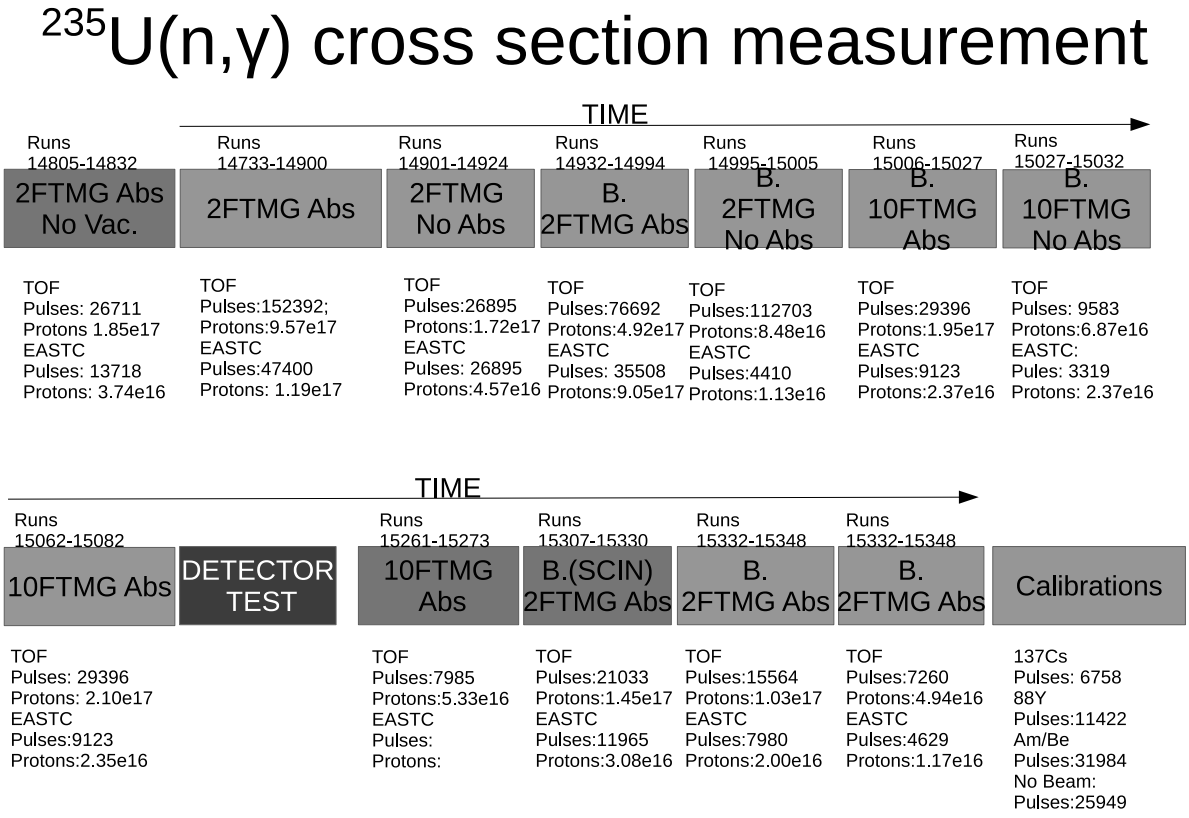

Figure G.4: Calendario detallado de la medida. El número total de protones y pulsos para cada periodo está indicado.

G.3 Análisis de los datos

La sección eficaz es determinada experimentalmente en la aproximación del blanco delgado como:

$$\sigma_\gamma(E_n) = \frac{C_{tot}(E_n) - C_{bkg}(E_n)}{N_{norm}\varepsilon_\gamma\phi(E_n)} \tag{G.1}$$

Donde $C_{tot}(E_n)$ y $C_{bkg}(E_n)$ son el número total de cuentas detectadas y fondo con las condiciones E_{sum} y m_{cr}; ε_γ es la eficiencia de detección para los eventos ^{235}U(n,γ); $\phi(E_n)$ es el flujo de neutrones; y N_{norm} es el factor de normalización que engloba la masa de las muestras y la fracción de haz interceptado por las muestras.

El análsis realizado en este trabajo es similar a los análisis de medidas previas realizadas con el TAC [34, 76]. Sin embargo, para el análisis de las coincidencias entre distintos detectores se han desarrollado nuevas herramientas. El fondo es suma de diferentes contribuciones:

- Fondo no relacionado con el haz de neutrones (C_{NB}): Fondo ambiental, fondo debido a la desintegración de las muestras de ^{235}U y desintegración de de los contaminantes de los BaF_2 [34, 76]. Esta componente ha sido obtenida de las medidas dedicadas sin haz, dejando la misma configuración experimental.

- Fondo relacionado con el haz (C_B): Fondo debido a la interacción de los neutrones con los diferentes materiales. Esta componente se ha obtenido en medidas dedicadas reemplazando las muestras por backings de aluminio y manteniendo la misma configuración experimental.

- Fondo de fisión prompt (C_F): Durante el proceso de fisión son emitidas, cascadas de γs y neutrones de los altamente excitados fragmentos de fisión y detectados por el TAC [23, 32]. Esta componente es dificil de sustraer debido al carácter resonante de las secciones eficaces. Esta componente es obtenida por la coincidencia del TAC y los FTMG

- Otras componentes relacionadas con las muestras de ^{235}U (C_{Other}): Componente inducida por los neutrones en las muestras que no es el proceso de fisión, por ejemplo, elastic scattering. Esta componente ha sido determinada por simulaciones Monte Carlo.

Por lo tanto:

$$C_{bkg}(E_n) = C_{noBeam}(E_n) + C_{Beam}(E_n) + \frac{1}{\varepsilon_f^*}C_{tagg}(E_n) + C_{Other}(E_n) \tag{G.2}$$

Donde ε_f^* es la eficiencia de tagging. La figura G.5 muestra un ejemplo de las diferentes componentes durante la medida.

La eficiencia de fisión y la eficiencia de tagging son cantidades íntimamente relacionadas. Consideramos que ambas no dependen de la energía del neutrón. Su definición viene dada por:

- **Eficiencia de fisión**, $\varepsilon_f(A_{th})$: Es la probabilidad de detectar una fisión en cualquiera de las 10 muestras de ^{235}U por los FTMG. Esta magnitud depende solamente del corte en amplitudes aplicado, A_{th}.

- **Eficiencia de tagging**, $\varepsilon_f^*(A_{th},E_{sum},m_{cr})$: Este es el factor necesario para realizar la subtracción del fondo de fisión. Por defínción, es el cociente entre las reacciones (n,f) detectadas en coincidencia, $c_{Tagg}(A_{th},E_{sum},m_{cr})$, y el número total de reacciones de fisión detectadas por el TAC $c_{Fiss\_TAC}(E_{sum},m_{cr})$:

$$\varepsilon_f^*(A_{th}, E_{sum}, m_{cr}) = \frac{c_{Tagg}(A_{th}, E_{sum}, m_{cr})}{c_{Fiss\_TAC}(E_{sum}, m_{cr})} \tag{G.3}$$

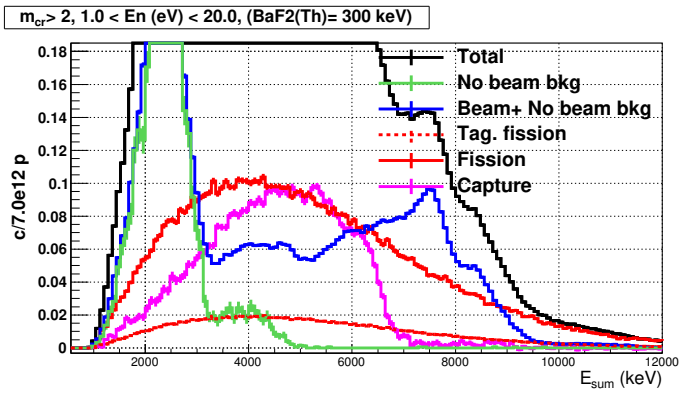

Figure G.5: Energía depositada en el TAC para m_{cr} >2 en el periodo de enegías del neutrón desde 1.0 a 20 eV.

En el caso de que la probabilidad de detectar una fisión en uno de los detectores no dependa de lo que ha sido detectado en el otro [23], entonces:

1. La eficiencia de fisión y la eficiencia de tagging son la misma cantidad, $\varepsilon_f^*(A_{th})=\varepsilon_f(A_{th})$.
2. Como consecuencia de 1, la eficiencia de tagging solo depende de A_{th}:

$$\varepsilon_f^*(A_{th}, E_{sum}, m_{cr}) = \varepsilon_f^*(A_{th}) \tag{G.4}$$

La metodología usada para el cálculo de estas dos magnitudes, la cual es más precisa que las simulaciones montecarlo, ha sido aplicada en las primeras resonancias desde 0.2 a 20 eV. Este está basado en la ecuación G.3:

- Las cuentas de fisión taggeadas son obtenidas por la coincidencia de los detectores TAC y FTMG.
- El TAC detecta muchas componentes además de las reacciones ^{235}U(n,γ). Sin embargo, el número de componentes puede ser reducida a la componente instantanea de fisión y al fondo inducido por material que intercepta el haz applicando restricciones a los eventos detectados por el TAC, m_{cr} >5, y E_{sum} >$S_n(^{236}U)$.

  Cuanto más restrictivas sean las condiciones aplicadas al TAC, menos sensible es el cálculo a incertidumbres sistemáticas. Sin embargo, la incertidumbre estadística se incrementa. Por lo tanto, el cálculo debe adecuarse a un compromiso entre la incertidumbre estadistica y sistemática.

La eficiencia de tagging ha sido calculada para ambas configuraciones en las primeras resonancias. Para el cálculo, los eventos del TAC fueron reducidos a eventos con m_{cr} >5 y E_{sum} >10 MeV. Para los detectores FTMG, el threshold aplicado fué de A_{th}=40 ADC canales.

Sin embargo, debido a la complejidad del proceso, la mayoria de los observables de fisión están correlacionados. Por ejemplo, el número de neutrones emitidos y las cascadas γ están íntimamente relacionadas con el par de fragmentos de fisión producidos [100]. Esta correlación no permite la detección de forma independendiente los eventos de fisión medidos por el TAC y los FTMG.

Para atajar esta correlación, se ha aplicado una pequeña corrección tál y como se explica en la sección 3.5.4. Los resultados finales para estas cantidades en las dos configuraciones experimentales están en la tabla G.3. La incertidumbre mostrada, es la suma de las componentes estadísticas y sistemáticas.

La eficiencia del TAC para las reacciones (n,γ) fueron determinadas por simulaciones Monte Carlo como en trabajos previos [104, 34, 76]. Las cascadas γ fueron generadas mediante el código DICEBOX [47],

Quantity	2FTMG	10FTMG
ε_f	0.1847(22)	0.842(5)
ε_f^*	0.1847(22)	0.842(5)

Table G.3: Eficiencia de fissión y eficiencia de tagging para ambas configuraciones experimentales.

incluyendo un estado isomérico ($T_{1/2}$ ~100 ns) que distorsiona la señal de captura detectada por el TAC. Las cascadas generadas fueron simuladas en la detallada geometría que incluye el TAC, la cámara de fisión y las muestras de ^{235}U.

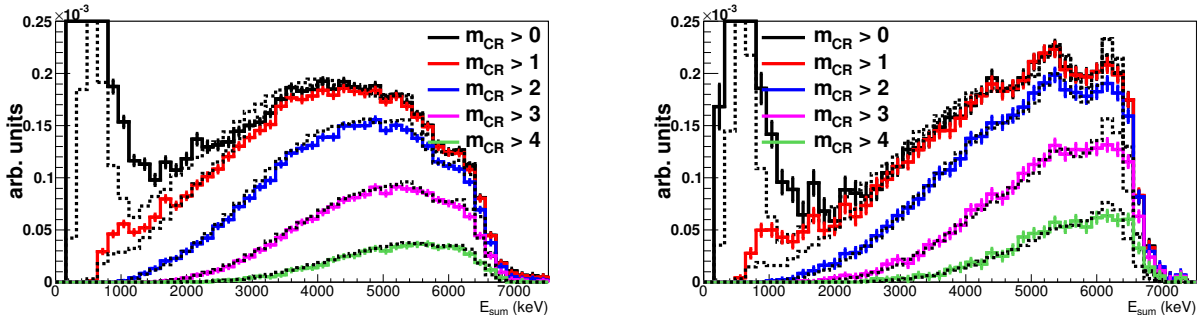

Figure G.6: Espectros de energía depositada del proceso $^{235}U(n,\gamma)$ simulados comparados con los experimentales para diferentes condiciones aplicadas en m_{cr}. En el panel izquierdo, para la configuración experimental con el absorbente neutrónico. En el panel derecho, configuración experimental sin el absorbente neutrónico.

La buena reproducción de los datos experimentales por las cascadas Monte Carlo permiten la determinación de eficiencia del TAC con una precisión del 1.7%.

La normalización de la sección eficaz ^{235}U(n,γ) fué realizada al valor integral de la sección eficaz del ^{235}U(n,f) en el rango de energías desde 7.8 a 11.0 eV, por lo tanto, reduciendo las incertidumbres sistemáticas. La incertidumbre en la normalización es $\Delta(N_{norm})$=2.1%

La alta tasa de contaje registrada por los detectores BaF_2 debida a la gran cantidad de material muerto que intercepta el haz, introduce efectos de pile-up que distorsionan las cascadas γ detectadas en función de la energía del neutrón, cambiando de este modo la eficiencia de detección (n,γ) en función de la energía del neutrón. Para corregir estos efectos, se ha desarrollado un nuevo modelo de tiempo muerto, basado en modelos anteriores [76, 34, 88, 111]. El modelo de tiempo muerto fué validado en las cascadas prompt de fisión detectadas en coincidencia por el TAC y los FTMG. Los excelentes resultados están mostrados en el panel izquierdo de la figura.G.7. En el panel derecho de la misma figura se encuentran las correcciones de tiempo muerto aplicadas para el cálculo de la sección eficaz ^{235}U(n,γ).

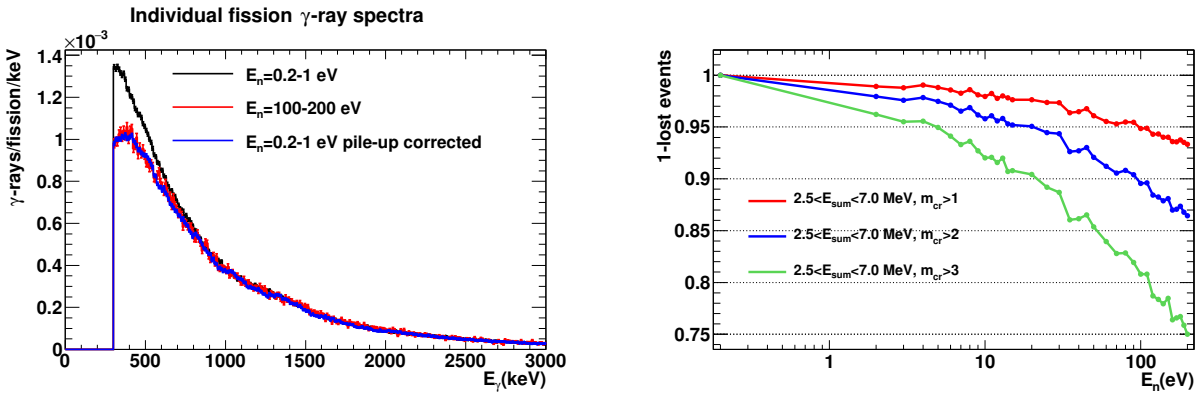

Figure G.7: En el panel izquierdo, comparativa entre la distribución de γs detectados en coincidencia por el TAC-FTMG y los corregidos. En el panel derecho, las correcciones aplicadas a las sección eficaz de captura del ^{235}U.

G.4 Resultados

Se ha calculado y comparado la integral de las resonancias con ENDF/B-VII.1 para diferentes rangos de energía del neutrón como se muestra en la tabla G.4. En la última columna, se muestra la incertidumbre sistemática para cada rango de energía del neutrón.

Figure	Neutron energy period	I(This work)/I(ENDF/B-VII.1)	Sys. uncertainty (%)
4.5	0.2 – 2.2	1.03±0.01	5.1
4.6	2.2 – 20.0	1.088±0.004	4.2
4.7	20.0 – 40.0	1.072±0.007	5.3
4.8	40.0 – 60.0	1.10±0.01	6.1
4.9	60.0 – 100.0	1.09±0.02	6.8
4.10	100.0 – 200.0	1.06±0.02	7.4

Table G.4: Cociente entre las integrales de este trabajo y ENDF/B-VII.1 para los diferentes rangos de energía del neutrón.

Los datos de este trabajo son, en general, mayores que ENDF/B-VII.1. Sin embargo, tomando las incertidumbres sistemáticas, nuestros datos son compatibles con la librerías actuales. Los datos fueron entregados a la colaboración CIELO [31, 12] para la reevaluación del ^{235}U. Como resultado, ha salido a la luz una nueva evaluación(ENDF/B-VIII.0), mejorando el acutal conocimento de las secciones eficaces inducidas por neutrones para el ^{235}U.

G.5 Conclusiones

Se ha medido la sección eficaz de captura neutrónica del ^{235}U en la instalación n_TOF del CERN en el rango de energías del neutrón desde 0.2 a 200 eV.

Debido a la buena resolución de la instalación y el análsis realizado, los resultados han mejorado dicha sección eficaz en la región de resonancias resueltas.

Los datos han sido usados por la colaboración cielo para la producción de una nueva librería evaluada que será usada para el diseño de mejores reactores nucleares.

Bibliography

[1] U.S. DOE Nuclear Energy Research Advisory Committee and the Generation IV International Forum "Generation IV Nuclear Energy Systems "(2002).

[2] Available at *https://ec.europa.eu/research/fp7* .

[3] "Key world energy statistics "Available online at *https://www.iea.org/publications/freepublications/publication/key-world-*

[4] "European Nuclear Society " *http://www.euronuclear.org/1-information/maps.htm*.

[5] "International Energy Outlook 2016 ".

[6] A. J. Knoning *et al.*"CANDIDE: Nuclear data for sustainable nuclear energy "(2009).

[7] Y. Kadi, J. P. Revol "Design of an Accerator-Driven System for the Destruction of Nuclear Waste ", Workshop on Hybrid Nuclear Systems for Energy Production, Utilisation of Actinides and Transmutation of Long-Lived Radioactive Waste (2001).

[8] N. Butler "Literature Review of Partioning and Transmutation "(2011).

[9] M. B. Chadwick *et al.*"ENDF/B-VII.1 Nuclear Data for Science and Technology: Cross Sections, Covariances, Fission Product Yields and Decay Data "Nuclear Data Sheets**112** 2887–2996 (2011).

[10] Keiichi Shibata *et al.*"JENDL-4.0: A New Library for Nuclear Science and Engineering "Journal of Nuclear Science and Technology**48** 1–30 (2011).

[11] The JEFF team "JEFF-3.2: Evaluated nuclear data li-brary "Tech. Rep. (2014).

[12] M. B Chadwick *et al.*"The CIELO Collaboration: Neutron Reactions on ^{1}H, ^{16}O, ^{56}Fe, ^{235,238}U, and ^{239}SPu "Nuclear Data Sheets**118** 1–25 (2014).

[13] H. Palevsky *et al.*"DIRECT MEASUREMENT OF THE ENERGY VARIATION OF ETA FOR U233, U235 AND PU239."J.N.E.**3** 56 (1956).

[14] J. R Smith *et al.*"ETA MEASUREMENTS FOR U-235 "P, IDO**16366** 5707 (1957).

[15] G. de Saussure *et al.*"CONFERENCE PROCEEDINGS NUCLEAR DATA FOR REACTORS (Paris 1966) "**66** 233 (1966).

[16] F. D. Brooks *et al.*"Eta and neutron cross sections of U-235 from 0.03 to 200 eV "C. SDIEGO**2** 196602 (1966).

[17] R. B. Perez *et al.*"Simultaneous Measurements of the Neutron Fission and Capture Cross Sections for Uranium-235 for Neutron Energies from 8 eV to 10 keV "Nuclear Science and Engineering**52** 46 (1973).

[18] G. V. Muradyan "MEASUREMENT OF RADIATION-CAPTURE AND FISSION CROSS-SECTIONS AND THEIR RATIO ALFA FOR URANIUM-235 "C KIEV**77** 119 (1977).

[19] G. V. Muradyan "Multiplicity spectrometer for measuring neutron cross sections "Nuclear Science and Engineering**90** 60–74 (1985).

[20] H. Weigmann "MEASUREMENTS OF ETA OF 235-U FOR SUBTHERMAL NEUTRON ENERGIES "C,90MARSEI**3** 9004 (1990).

[21] Yu. V. Adamchuk "A spectrometer for measurement of the neutron capture gamma multiplicity at a stationary research reactor "Nuclear Instruments and Methods in Physics Research Section A**236** 105–108 (1985).

[22] F. J. Shore and V. L. Sailor "Slow Neutron Resonances in U^{235} " Phys. Rev.**112** 191-202 (1958).

[23] C. Guerrero *et al.*"Simultaneous measurement of neutron-induced capture and fission reactions at CERN "Eur. Phys. J. A**48** 29 (2012).

[24] IAEA EXFOR database *https://www-nds.iaea.org/exfor/exfor.htm*.

[25] Nuclear Energy Agency "Nuclear Data for Improved LEU-LWR reactivity predictions "International Evaluation Co-operation**2**.

[26] Nuclear Energy Agency "Nuclear Data High Priority Request List "Available at .

[27] WPEC Subgroup 18 "Epithermal capture cross-section of ^{235}U "(1999).

[28] WPEC Subgroup 29 "^{235}U capture cross section in the keV to MeV region "(2011).

[29] Japan Atomic Energy Agency "Integral test of evaluated nuclear data files "Available at .

[30] C. Chabert *et al.*"Trends in Nuclear Data Derived from Integral Experiments in Thermal and Epithermal Reactors "Proceedings of International Conference on Nuclear Data for Science and Technology, Tsukuba 868-871 (2001).

[31] Available at *https://www-nds.iaea.org/CIELO/*.

[32] M. Jandel *et al.*"New Precision Measurements of the $^{235}\mathbf{U}(n,\gamma)$ Cross Section "Phys. Rev. Lett.**109** 202506 (2012).

[33] L. Meitner and O. Frish "Desintegration of Uranium by neutrons: a new type of nuclear reaction "Nature**143** 239 (1939).

[34] Emilio Mendoza Cembranos "Measurement of the ^{243}Am capture cross section at the n_TOF facility "

[35] N. Bohr, J. Archibald, "The Mechanism of Nuclear Fission", Phys. Rev.**56**, 426–450 (1939).

[36] G. Breit, E. Wigner "Capture of Slow Neutrons ", Phys. Rev.**49**, 519–531 (1936).

[37] E. P. Wigner "Resonance Reactions ", Phys. Rev.**70**, 606–618 (1946).

[38] E. P. Wigner, L. Eisenbud "Higher Angular Momenta and Long Range Interaction in Resonance Reactions ", Phys. Rev.**72**, 29–41 (1947).

[39] A. M. Lane, R. G. Thomas "R-Matrix Theory of Nuclear Reactions ", Rev. Mod. Phys.**30**, 257–353 (1958).

[40] F. H. Frohner "Evaluation and Analysis of Nuclear Resonance Data. ", JEFF Report**18**, (2000).

[41] J. M. Blatt and L. C. Biedenharn "The Angular Distribution of Scattering and Reaction Cross Sections "Rev. Mod. Phys. **24** 258–272 (1952).

[42] J. Kopecky and M. Uhl "Test of gamma-ray strength functions in nuclear reaction model calculations ", Phys. Rev. C**41** 1941–1955 (1990).

[43] C. H. Johnson "Statistical model radiation widths for $75 < A < 130$ and the enhancement of P-wave neutron capture for $A \approx 90$ "Phys. Rev. C**16** 2238–2248 (1977).

[44] T. A. Brody *et al.*"Random-matrix physics: spectrum and strength fluctuations "Rev. Mod. Phys.**53** 385–479 (1981).

[45] J.C. Hardy *et al.*"The essential decay of pandemonium: β-delayed neutrons "Nuclear Physics A**305** 15 – 28 (1978).

[46] P.O. Hansen *et al.*"Applications of statistical nuclear physics to nuclear spectroscopy "Nuclear Physics A**518** 13 - 34 (1990).

[47] F. Bečvář "Simulation of γ cascades in complex nuclei with emphasis on assessment of uncertainties of cascade-related quantities "Nuc. Inst. and Meth. A**417** 434 – 449 (1998).

[48] Jose L. Tain *et al.*"Accuracy of the Pulse Height Weighting Technique for Capture Cross Section Measurements "Journal of Nuclear Science and Technology**39** 689 – 692 (2002).

[49] J. J. Sakurai "Modern quantum mechanics " (1994).

[50] Till von Egidy *et al.*"Systematics of nuclear level density parameters "Phys. Rev. C**72** 044311 (2005).

[51] A. Gilbert *et al.*"A COMPOSITE NUCLEAR-LEVEL DENSITY FORMULA WITH SHELL CORRECTIONS "Canadian Journal of Physics **43** 1446 – 1496 (1965).

[52] W. Dilg *et al.*"Level density parameters for the back-shifted fermi gas model in the mass range $40 <$ A < 250 "Nuclear Physics A**217**, 269 – 298 (1973).

[53] Niels Bhor "IX. Velocity–Range Relation for Fission Fragments "The Penetration of Charged Particles through Matter (1912–1954) 327–333 (1987).

[54] V. Metag *et al.*"Spectroscopic properties of fission isomers "Physics Reports**65** 1–41 (1980).

[55] H. C. Britt *et al.*"Fission Barriers Deduced from the Analysis of Fission Isomer Results "Phys. Rev. C**7** 801–823 (1973).

[56] Hans J. Specht "Nuclear fission "Rev. Mod. Phys.**46** 773–787 (1974).

[57] S. Bjørnholm and J. E. Lynn "The double-humped fission barrier "Rev. Mod. Phys.**52** 725–931 (1980).

[58] C. Guerrero *et al.*"The n_TOF Total Absorption Calorimeter for neutron capture measurements at CERN "Nuclear Instruments and Methods in Physics Research Section A**608** 424–433 (2009).

[59] S. Andriamonje *et al.*"A new transparent MicroMegas detector for neutron beam monitor at n_TOF "Journal of Korean Physical Society**59** 1597–1600 (2011).

[60] The n_TOF collaboration .

[61] C. Rubbia *et al.*"A high resolution spallation driven facility at the CERN-PS to measureneutron cross sections in the interval from 1 eV to 250 MeV. "CERN/LHC**98** (1998).

[62] N. Colonna "Neutron cross-section measurements at the n_TOF facility at CERN "Nuclear Instruments and Methods in Physics Research Section B: Beam Interactions with Materials and Atoms**213** 49–54 (2004).

[63] F. Gunsing *et al.*"Status and outlook of the neutron time-of-flight facility n_TOF at CERN "Nuclear Instruments and Methods in Physics Research Section B: Beam Interactions with Materials and Atoms**261** 925–929 (2007).

[64] C. Guerrero *et al.*"Performance of the neutron time-of-flight facility n_TOF at CERN "The European Physical Journal A**49** 27 (2013).

[65] E. Chiaveri *et al.*"The CERN n_TOF Facility: Neutron Beams Performances for Cross Section Measurements "Nuclear Data Sheets**119** 1–4 (2014).

[66] N. Colonna *et al.*"Neutron measurements for advanced nuclear systems: The n_TOF project at CERN "Nuclear Instruments and Methods in Physics Research Section B: Beam Interactions with Materials and Atoms**269** 3251–3257 (2011).

[67] C. Weiss *et al.*"The new vertical neutron beam line at the CERN n_TOF facility design and outlook on the performance "Nuclear Instruments and Methods in Physics Research Section A: Accelerators, Spectrometers, Detectors and Associated Equipment**799** 90–98 (2015).

[68] F. Gunsing *et al.*"Nuclear data activities at the n_TOF facility at CERN "The European Physical Journal Plus**131** 371 (2016).

[69] *https://www.ptb.de/cms/* .

[70] M. Barbagallo *et al.*"High-accuracy determination of the neutron flux at n_TOF "The European Physical Journal A**49** 156 (2013).

[71] J. Pancin *et al.*"Measurement of the n_TOF beam profile with a micromegas detector "Nuclear Instruments and Methods in Physics Research Section A**524** 102–114 (2004).

[72] S. Marrone *et al.*"A low background neutron flux monitor for the n_TOF facility at CERN "Nuclear Instruments and Methods in Physics Research Section A: Accelerators, Spectrometers, Detectors and Associated Equipment**517** 389–398 (2004).

[73] The n_TOF collaboration "CERN n_TOF Facility: Performance Report "CERN INTC-2002-037**037** (2003).

[74] U. Abbondanno *et al.*"The data acquisition system of the neutron time-of-flight facility n_TOF at CERN "Nuclear Instruments and Methods in Physics Research Section A**538** 692–702 (2005).

[75] K. Wisshak *et al.*"The Karlsruhe 4π barium fluoride detector "Nuclear Instruments and Methods in Physics Research Section A**292** 595–618 (1990).

[76] C. Guerrero "Measurement of the ^{237}Np and ^{240}Pu neutron cross sections at the CERN n_TOF facility "(2004).

[77] "Pulse shape analysis of signals from BaF2 and CeF3 scintillators for neutron capture experiments "Nuclear Instruments and Methods in Physics Research Section A**568** 904–911 (2006).

[78] Y. Giomataris *et al.*"MICROMEGAS: a high-granularity position-sensitive gaseous detector for high particle-flux environments "Nuclear Instruments and Methods in Physics Research Section A**376** 29 – 35 (1996).

[79] S. Andriamonje *et al.*"Development and performance of Microbulk Micromegas detectors "Journal of Instrumentation**5** 02001 (2010).

[80] S. Andriamonje *et al.*"Experimental studies of a Micromegas neutron detector "Nuclear Instruments and Methods in Physics Research Section A**481** 120–129 (2002).

[81] The n_TOF Collaboration "n-TOF Technical Design Report on Experimental Area "CERN/INTC 2000-018 (2000).

[82] CERN "Casto Facility "*http://castor.web.cern.ch/* .

[83] P. Zugec *et al.*"Pulse processing routines for neutron time-of-flight data "Nuclear Instruments and Methods in Physics Research Section A**812** 134–144 (2016).

[84] Joint Research Center .

[85] J. Heyse *et al.*"Characterization of 235U Targets for the Development of a Secondary Neutron Fluence Standard "Nuclear Data Sheets**119** 407–409 (2014).

[86] C. Guerrero *et al.*"Measurement and resonance analysis of the ^{237}Np neutron capture cross section "Phys. Rev. C**85** 044616 (2012).

[87] E. Mendoza *et al.*"Measurement and analysis of the ^{243}Am neutron capture cross section at the n_TOF facility at CERN "Phys. Rev. C**90** 034608 (2014).

[88] E. Mendoza *et al.*"Pulse pile-up and dead time corrections for digitized signals from a BaF2 calorimeter "Nuclear Instruments and Methods in Physics Research Section A**768** 55–61 (2014).

[89] G.knoll "Radiation Detection and Measurement " Third edition .

[90] S. Agostinelli *et al.*"Geant4—a simulation toolkit "Nuclear Instruments and Methods in Physics Research Section A**506** 250–303 (2003).

[91] J. Allison *et al.*"Recent developemnts in Geant4 "Nuclear Instruments and Methods in Physics Research Section A**835** 186–225 (2016).

[92] K. H. Scmidt *et al.*"General Description of Fission Observables: GEF Model Code "Nuclear Data Sheets**131** 107–221 (2016).

[93] J.L Tain, D. Cano-Ott "Algorithms for the analysis of β-decay total absorption spectra "Nuclear Instruments and Methods in Physics Research Section A**571** 728–738 (2007).

[94] R. Barlow "Extended maximum likelihood "Nuclear Instruments and Methods in Physics Research Section A**297** 496–506 (1990).

[95] Oberstedt *et al.*"Improved values for the characteristics of prompt-fission γ-ray spectra from the reaction ^{235}U($n_{\rm th}$,f) "Phys. Rev. C**87** 051602 (2013).

[96] Patrick Talou *et al.*"Assessing the role of the (n,γf) process in the low-energy fission of actinides "EPJ Web of Conferences**122** 01013 (20116).

[97] V. Stavinsky and M.O. Shaker "The (n,γf) proccess "Nuclear Physics**62** 667–672 (1964).

[98] J. E. Lynn "On the slow neutron, gamma-fission reaction "Physics Letters**18** 31 (1965).

[99] M. Csatlós *et al.*"Resonant tunneling through the triple-humped fission barrier of ^{236}U "Physics Letters B**615** 175–185 (2005).

[100] Sh. Zeynalov Korean Phys. Soc.**59** 1396 (2011).

[101] Marvin M. Hoffman "Directional Correlation of Fission Fragments and Prompt Gamma Rays Associated With Thermal Neutron Fission "Phys. Rev.**133** B714–B723 (1964).

[102] Donald R. Hamilton "On Directional Correlation of sucessive quanta "Phys. Rev.**58** 122 (1940).

[103] OECD Nuclear Energy Agency "Evaluated Nuclear Structure Data File Search and Retrieval "Available at (2016).

[104] C. Guerrero *et al.*"Monte Carlo simulation of the n_TOF Total Absorption Calorimeter "Nuclear Instruments and Methods in Physics Research Section A**671** 108–117 (2012).

[105] N.L. Lark "Spontaneously fissioning isomers in U, Np, Pu and Am isotopes "Nuclear Physics A**139** 481–500 (1969).

[106] J. Pedersen "An investigation of the population of the shape isomer 236mU through the (d, p) reaction "Nuclear Physics A**178** 449–457 (1972).

[107] V. Andersen "The shape isomer in 236U populated by thermal neutron capture "Nuclear Physics A**269** 338–348 (1976).

[108] M. Guttormsen *et al.*"Observation of Large Scissors Resonance Strength in Actinides "Phys. Rev. Lett.**109** 162503 (2012).

[109] M. Guttormsen *et al.*"Scissors resonance in the quasicontinuum of Th, Pa, and U isotopes "Phys. Rev. C**89** 014302 (2014).

[110] T. G. Tornyi *et al.*"Level density and γ-ray strength function in the odd-odd ^{238}Np nucleus "Phys. Rev. C**89** 044323 (2014).

[111] C. Guerrero *et al.*"Correction of dead-time and pile-up in a detector array for constant and rapidly varying counting rates "Nuclear Instruments and Methods in Physics Research Section A **777** 63–69 (2015).

[112] N. M. Larson, Oak Ridge National Laboratory, Oak Ridge, TN, Report No. ORNL/TM-9179/R7, 2006.

[113] Available at *http://www.chanda-nd.eu* .

[114] J. Taieb *et al.*"A new fission chamber dedicated to Prompt Fission Neutron Spectra measurements "Nuclear Instruments and Methods in Physics Research Section A**833** 1–7 (2016).

[115] See for instance *https://en.wikipedia.org/wiki/Lorentz_transformation* .

[116] M. Heil *et al.*"A 4π BaF2 detector for (n,γ) cross-section measurements at a spallation neutron source "Nuclear Instruments and Methods in Physics Research Section A**459** 229–246 (2001).

[117] R. Reifarth *et al.*"(n,γ) measurements on radioactive isotopes with DANCE "Nuclear Instruments and Methods in Physics Research Section B**241** 176–179 (2005).